Doctoral Dissertation

Basis research and development of DNA-targeted radio-platinum agents for Auger electron cancer therapy

（Auger 電子を用いたがん治療創成に向けた DNA を標的とする
放射性白金薬剤の基礎開発研究）

Honoka Obata

Laboratory for Bioanalysis and Molecular Imaging
Biomedical and Pharmaceutical Science Course, Division of Life Science
Graduate School of Life Science, Hokkaido University

March 2023

Table of Contents

Abbreviations 5

Glossary 8

Preface 9

Chapter 1: Development of a Production Method for No-Carrier-Added Radio-Pt and Evaluation of DNA Damage by Auger Electrons using Radio-Cisplatin 21

Chapter 1—Introduction 22

1. Development of Production Methods for No-Carrier-Added Platinum-191, 193m from an Iridium Target 25

Production and chemical purification method 25

Irradiation and dissolution of an iridium target 29

Chemical separation of Pt(IV) and Ir(IV) chloride complexes 31

Production yields of ^{191}Pt by proton irradiation and quality control of the n.c.a. $^{191}Pt^{II}Cl_4^{2-}$ product 32

2. Development of No-Carrier-Added Radio-cisplatin and Evaluation of its DNA-Damaging Efficacy as an Auger-electron emitting agent 36

Radio-synthesis of n.c.a. radio-cisplatin 36

In vitro property of n.c.a. radio-cisplatin 38

Evaluation of the DNA-damaging efficacy of n.c.a. radio-cisplatin with

immunofluorescence staining for γH2AX and gel electrophoresis of plasmid DNA 42
Evaluation of the DNA-damaging efficacy of n.c.a. radio-cisplatin using time-lapse imaging of U2RDP-LE53-21 cells 45
A comprehensive discussion on the DNA-damaging effect induced by Auger electrons from n.c.a. radio-cisplatin 50
In vivo property of n.c.a. radio-cisplatin 52
Chapter 1—Conclusion 57
References 57

Chapter 2: Development of Radio-Pt–Labeled Agents Binding to DNA Efficiently and Inducing DNA Damage Effectively 63
Chapter 2—Introduction 64
1. Development of ^{191}Pt-Labeled Hoechst33258 Targeting DNA 66
Exploring ligands and functional groups that react with n.c.a. ^{191}Pt 66
Synthesis of the DNA-targeting complexes for labeling with ^{191}Pt: DTPA-Hoechst33258 and Cys-Hoechst33258 70
Development of Hoechst33258 labeled with n.c.a. ^{191}Pt via DTPA or Cys 71
Cellular uptake and intracellular distribution of ^{191}Pt- and ^{111}In-labeled Hoechst33258 75
DNA-binding of ^{191}Pt- and ^{111}In-labeled Hoechst33258 77
DNA-damaging efficacy of ^{191}Pt- and ^{111}In-labeled Hoechst33258 78
2. Development of ^{191}Pt-Labeled PI Polyamide Targeting Amplified

Cancer Genes 82
Synthesis of ^{191}Pt-labeled PIP and evaluation of target sequence-binding ability, cell uptake, and DNA binding 82
Cytotoxicity and DNA-damaging efficacy of ^{191}Pt-MYCN-PIP 85
In vivo evaluation of intravenously injected ^{191}Pt-MYCN-PIP in mice bearing neuroblastoma tumors 89
In vivo investigation of intratumoral injection of ^{191}Pt-MYCN-PIP in mice bearing Kelly tumors 92
Chapter 2—Conclusion 96
References 96

Chapter 3: Development of Radio-Pt–Labeled Agents Targeting Tumor Cells *In vivo* 101
Chapter 3—Introduction 102
1. Development of Tumor-Targeting ^{191}Pt-Labeled Agents via Mono-thiol Cysteine and a Tri-thiol Ligand. 104
Synthesis of the tumor-targeting ligands labeled with ^{191}Pt: ^{191}Pt-labeled Nap-Cys-PSMA and Nap-Cys-RGD 104
Cellular uptake and cell-membrane binding of ^{191}Pt-labeled ligands via Cys 106
In vivo evaluation of intravenously injected ^{191}Pt-labeled ligands vis Cys in mice bearing tumors 108
Investigation of ^{191}Pt-labeling via a tri-thiol ligand: ^{191}Pt-Trithiol complex 111

A comprehensive discussion and future directions on radio-Pt drugs design based on all the results in Chapters 1 ~ 3 114
Chapter 3—Conclusion 116
References 116

Conclusion 120

Appendix: Evaluation of the Cytotoxicity by DNA-Targeting and Non-Targeting ^{125}I-Labeled Agents 121
Introduction 121
Results and Discussion 121
Conclusion 125
References 125

Experimental Section 127
Chapter 1. Section 1: 127
Chapter 1. Section 2: 127
Chapter 2. Section 1: 135
Chapter 2. Section 2: 141
Chapter 3. Section 1: 147
Appendix: 151
References: 154

Acknowledgements 156

Abbreviations

AcOH	Acetic acid
Al	Aluminum
AEC	Anion-exchange chromatography
Sb	Antimony
Arb. unit; a.u.	Arbitrary unit
AUC	Area under the curve
Arg (R)	Arginine
RGD	Arginine–glycine–aspartic acid
As	Arsenic
Asp (D)	Aspartic acid
APCI	Atmospheric pressure chemical ionization
APPI	Atmospheric pressure photoionization
ARG	Autoradiograph
BW	Body weight
b.p.	Boiling point
BNCT	Boron neutron capture therapy
BSA	Bovine serum albumin
Calcd	Calculated
c.a.	Carrier-added
Cisplatin; CDDP	Cis-diamminedichloroplatinum(II)
cGAS–STING	Cyclic GMP–AMP synthase–stimulator of interferon genes
Cys	Cysteine
DI water	Deionized water
DNA	Deoxyribonucleic acid
d	Deuteron
DTPA	Diethylenetriaminepentaacetic acid
DMSO	Dimethyl sulfoxide
DMF	Dimethylformamide
DSBs	DNA double strand breaks
EC	Electron capture
ESI	Electrospray ionization
EOB	End of bombardment
EOS	End of synthesis

EtBr	Ethidium bromide
EtOAc	Ethyl acetate
EDDA	Ethylenedithiodiacetic acid
FBS	Fetal Bovine Serum
FISH	Fluorescence in situ hybridization
Glu	Glutamic acid
Gln	Glutamine
Gly (G)	Glycine
Au	Gold
$T_{1/2}$	Half-life
HSAB	Hard and soft acids and bases
HPLC	High-performance liquid chromatography
HPGe	High purity germanium
ICP	Inductively coupled plasma
IT	Internal conversion
i.t.	Intratumoral injection
i.v.	Intravenous injection
Ir	Iridium
LET	Linear energy transfer
Lys	Lysine
Hg	Mercury
MS	Mass spectrometry
Met	Methionine
Nap	Naphthalene
NCS	*N*-Chlorosuccinimide
DIPEA	*N*,*N*-diisopropylethylamine
Nb	Niobium
n.c.a.	No-carrier-added
Boc-Cys(Trt)-OH	*N*-(*tert*-butoxycarbonyl)-*S*-trityl-L-cysteine
NLS	Nuclear localization signal
Os	Osmium
%ID	Percent of the injected dose
	Percent of the incubated dose
PBS	Phosphate-buffered saline
Gamma(γ)-H2AX	Phosphorylated histone H2AX

Pt	Platinum
PGMs	Platinum group metals
Radio-Pt	Platinum radionuclides
PET	Positron emission tomography
PCNA	Proliferating cell nuclear antigen
PSMA	Prostate-specific membrane antigen
p	Proton
PIPs	Pyrrole–imidazole polyamides
RT-qPCR	Quantitative reverse transcription PCR
QMA	Quaternary methyl ammonium
RCP	Radiochemical purity
RCY	Radiochemical yield
SSC	Saline sodium citrate buffer
Ser	Serine
SPECT	Single photon emission computed tomography
SEC	Size exclusion chromatography
H-Cys(Trt)-OH	*S*-trityl-L-cysteine
TRT	Targeted radionuclide therapy
TLC	Thin-layer chromatography
3D	Three-dimensional
R3	Tri-arginine
TBP	Tributyl phosphate
TEA	Triethylamine
TFA	Trifluoroacetic acid
TIPS	Triisopropylsilane
53BP1	Tumor-suppressor p53-binding protein 1
2D	Two-dimensional
UV	Ultraviolet
v.p.	Vapor pressure
DAPI	4',6-diamidino-2-phenylindole
MTT	3-(4,5-dimethylthiazol-2-yl)-2,5-diphenyltetrazolium bromide

Glossary

- **Radiopharmaceuticals**: pharmaceutical agents that contain radionuclides.

- **Targeted radionuclide therapy (TRT)**: a type of internal radiotherapy using a radiopharmaceutical agent that selectively delivers radiation dose to targeted sites such as cancer cells.

- **Auger-electron emitting radionuclides**: radionuclides that release Auger electrons via radioactive decay.

- **Auger-electron emitting agents/compounds/drugs/therapeutics**: substances labeled with Auger-electron emitting radionuclides.

- **Auger electron (cancer) therapy**: TRT using Auger-electron emitting agents (in this dissertation). Auger electron therapy has been commonly demonstrated in TRT, but the Auger effect can be also induced in external radiotherapy using sensitizers.

- **Platinum radionuclides (radio-Pt)**: platinum radionuclides that include several isotopes. In this dissertation, Pt radionuclides were taken together and referred to as “radio-Pt”, which was used in discussion applicable to all Pt radionuclides, or in cases using mixed Pt radionuclides. When using a sample containing a mix of radionuclides, each radionuclide was described in the footnotes and the experimental sections.

Preface

Surgery, chemotherapy, and radiation therapy are widely used as cancer treatments. Surgery is the first-choice approach in many cancer types; unfortunately, sometimes the patient's conditions, like the malignant tumor type/size/location and the degree of metastasis/invasion, make a surgical treatment insufficient or incapable for the patients. To destroy as many cancer cells as possible, chemotherapy and/or radiation therapy are mostly applied in addition to or instead of surgical approaches.[1] Chemotherapy is commonly performed before and/or after surgery to kill even invisible cancer cells that cannot be removed by surgery throughout the body. A variety of anticancer drugs and regimens are now being developed to achieve high therapeutic effects even against drug-resistant cancers while minimizing adverse effects. Radiation therapy is also essential in clinics as a low-invasive treatment applicable to various cancers. The therapeutic effect of radiotherapy is normally based on the irradiated dose on tumors, where the malignant tissues need to be irradiated sufficiently keeping the normal tissue dose as low as possible. Effective and uniform irradiation of the tumors leads to a reliable therapeutic efficacy derived from physio-chemical damage. The well-established external radiotherapy using γ-rays, X-rays, or particle beams like protons and heavier ions is employed in radiation-sensitive cancers, pre/post-treatment of large tumors before/after surgery, and situations where normal tissues must be maintained as much as possible.[2] There are other radiotherapies, like brachytherapy, using a sealed radiation source placed inside or next to tumors,[3] or boron neutron capture therapy (BNCT) using alpha-rays emitted from neutron capture reaction of boronic agents.[4] However, these external radiation therapy approaches are available only for the tumors of which the location is defined.

Radiopharmaceuticals have been widely used in single photon emission computed tomography (SPECT) and positron emission tomography (PET) techniques as a non-invasive imaging modality in diagnosis procedures,[5] and also used for targeted radionuclide therapy (TRT) in therapeutic procedures. As an internal radiotherapy using radiopharmaceuticals, TRT is emerging because it can target even invisible cancer cells. In TRT, targeted malignant tissues are irradiated and damaged efficiently with short-range radiation emitted from radionuclides in low chemical doses (ng–μg). An ideal delivery system of radionuclides to tumors potentially achieves a low-invasive treatment modality to target and treat all of the cancer cells throughout the body.

β^--rays, α-rays, or Auger electrons are the candidate sources for TRT (**Table 1** and **Fig. 1**).[6] β^--rays are the most commonly used in the clinic, exhibiting cytotoxicity for widespread cancer cells because of their emission in a moderate range of energetic electrons (0.05–12 mm).[6] However, recently, α-rays have attracted a great deal of interest due to their high therapeutic efficacy, e.g., ^{225}Ac-PSMA-617 for metastatic castration-resistant prostate cancer.[7] α-rays have a high linear energy transfer (LET) (80 keV/μm) in a short range (2–500 nm),[6] which can minimize extra doses to normal

cells compared to β^--rays. Additionally, Auger electrons, the third candidate, are also expected to be used in TRT because of a high LET (4–26 keV/μm) in a nano-scale range (2–500 nm).[6] Auger electrons are capable of damaging predominately the targeted molecules in cancer cells, causing the least but critical damage to the cells as a whole. This makes Auger electrons an ideal source for internal radiotherapy without any adverse effects. This dissertation focused on the TRT using Auger-electron emitting radionuclides, hereafter referred to as "Auger electron therapy."

Table 1. General characteristics of short-range radiation in TRT.[6]

	β^--ray	α-ray	Auger electrons
Decay	β^-	α	IT/EC
Energy	50–2300 keV	5–9 MeV	eV–keV
Path range in water	0.05–12 mm	40–100 μm	2–500 nm
LET	0.2 keV/μm	80 keV/μm	4–26 keV/μm
Cytotoxicity	Moderate ~ high	High	Low ~ moderate

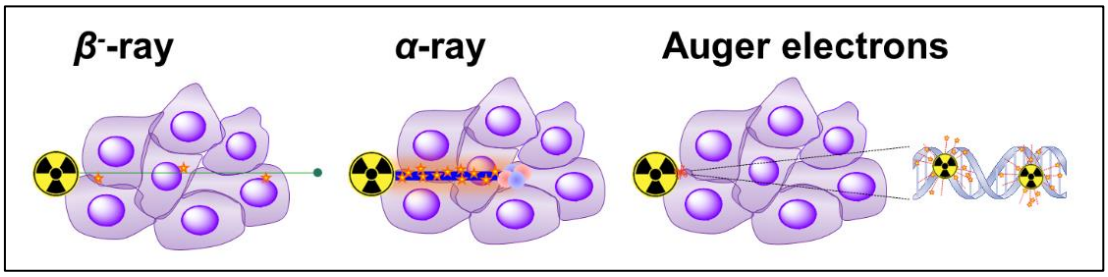

Figure 1. Illustration of short-range radiation in TRT.

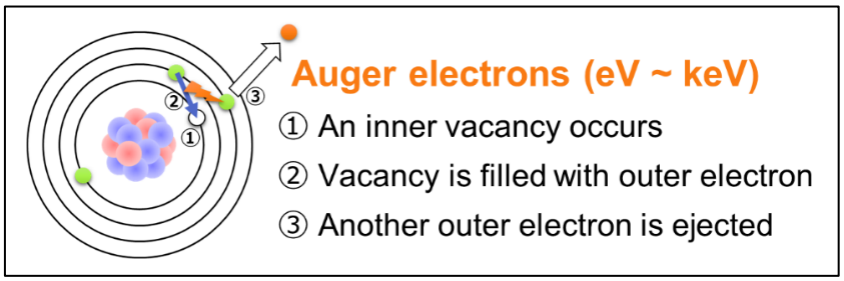

Figure 2. Illustration of Auger electron emission.

Auger electron emission (Auger effect) is a physical phenomenon initiated by a vacancy of an inner (K) orbital electron of an atom (①, **Fig. 2**).[8] This primary vacancy is filled by a higher orbital electron with lower energy (②, **Fig. 2**). The difference in the electronic binding energy of these two orbitals is transferred to either X-ray or another electron of the outer orbital with lower binding energy (③, **Fig. 2**). A specific Auger effect, in which a vacancy is filled by an electron in the same shell and

another electron in the higher shell is ejected, is defined as Coster–Kronig transition. When a vacancy, a transferred electron, and an ejected electron are in the same shell, it is called super Coster–Kronig transition. Furthermore, the primary Auger electron emission leads to a secondary vacancy of orbital electrons and subsequential Auger electron emission. Such a cascade-like multiple emission of low energy electrons occurs and results in the high LET in a nano-scale range (**Table 1**).[6]

Auger electron emission from radionuclides is initiated by decaying via electron capture (EC) or internal conversion (IC).[9] Almost all radionuclides also emit not only Auger electrons/X-rays but also IC electrons/γ-rays. IC electrons at a keV level are mostly taken together with Auger electrons as low energetic electrons to contribute to damaging effects. Both proton-rich radionuclides decaying via EC and excited radionuclides decaying via IC can be produced in an accelerator more readily than β^-- and α-ray–emitting radionuclides.[9] Almost all elements have Auger-electron emitting radionuclides that can be produced practically,[9] leading to a prospective variety of TRT agents. **Table 2** summarizes candidate radionuclides.[10,11] Iodine-123, 125, and In-111 have been commonly used in Auger electron therapy. Gallium-67, Tc-99m, and Tl-201 are generally used as SPECT imaging radionuclides, but also repurposed for Auger electron therapy. There have been many attempts to develop agents labeled with Auger-electron emitting radionuclides, especially $^{123, 125}$I, and ^{111}In, to apply Auger electrons to TRT (e.g., ^{111}In-DTPA-octreotide,[12] ^{111}In-DTPA-EGFR,[13] $^{123, 125}$I-UdR,[14] and ^{125}I-huA33[15]). However, the therapeutic efficacy has been modest or low in clinical trials performed to date. The causes and solutions are under investigation, and development is still ongoing.

Table 2. Properties of Auger electron/IC electron-emitting radionuclides.[11]

Classification	Radionuclides	Decay	Half-life ($T_{1/2}$)	Auger electrons /decay	IC electrons /decay
Commonly used	^{111}In	EC	67 h	7.4	0.2
	^{123}I	EC	13 h	13.7	0.2
	^{125}I	EC	57 d	23.0	0.9
Repurposed from SPECT	^{67}Ga	EC	78 h	5.0	0.3
	^{99m}Tc	IT	6 h	4.4	1.1
	^{201}Tl	EC	73 h	20.9	0.9
Interested as a suitable radionuclide	^{191}Pt	EC	2.8 d	13.3	1.0
	^{193m}Pt	IT	4.3 d	27.4	3.0
	^{195m}Pt	IT	4.0 d	36.6	2.8
	^{197}Hg	EC	64.1 h	23.2	0.8
	^{197m}Hg	IT	23.8 h	19.4	1.6
	^{119}Sb	EC	38.2 h	23.7	0.8

One possible cause would be the effective range of Auger electrons that is much smaller than a single cell. Since the effective range of β^--rays and α-rays covers at least a few cells, tumor cells are killed by delivering more radionuclides, depositing higher radiation doses, and inducing multiple damage to targeted cancer cells. This principle also goes with conventional external radiation therapy. However, the range of Auger electrons is extremely short, yielding a high LET of 4–26 keV/μm in the limited nano-scale range.[3] For example, the locally absorbed radiation dose around a ^{125}I decay site was estimated to be 1.6 MGy within a radius of 2 nm (**Fig. 3**).[16] This physiochemical property of Auger electrons suggests that it is necessary to transport radiopharmaceuticals to intracellular regions that are sensitive to radiation in TRT with Auger electrons. To kill cancer cells with Auger electrons, increasing the number of radionuclides delivered to the tumor cells must be combined with targeted and damaged factors within the cells for best results. Such an intracellular targeting strategy has not been considered in TRT with β^--rays and α-rays; therefore, the ideal therapeutic potential of Auger electrons has yet to be revealed in the present state. From another perspective, the basic difference between Auger electrons and other radiation becomes a unique advantage. Auger electrons that can induce damage predominately to key targets of cancer cells, may be an ideal, smart radiotherapy without any adverse effects, which cannot be accomplished with β^-/α-rays. However, there is also a possibility that only damaging minimum targets by Auger electrons is insufficient to kill cancer cells. To judge whether Auger electrons are indeed useful or not in TRT, further development of adequate targeted agents and their biological evaluation are crucial considering every prospect.

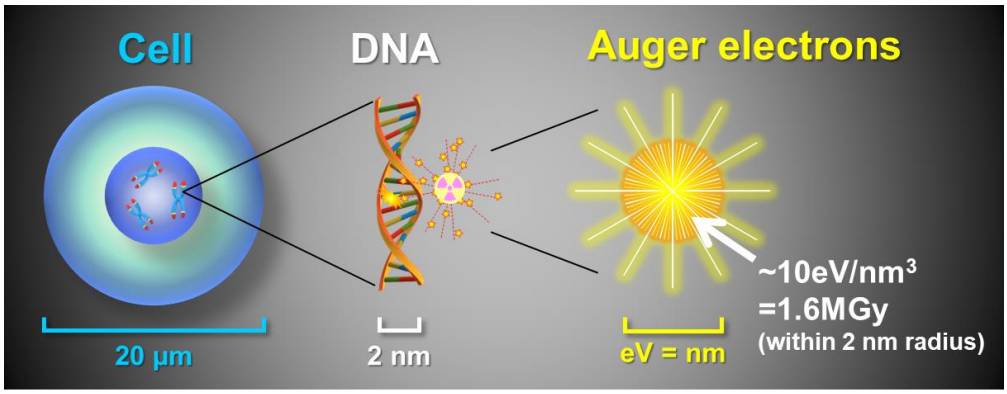

Figure 3. The effective range of Auger electron.

Among a variety of cellular organelles and other components, DNA is supposed to be the primary target of Auger electrons.[17] In radiation therapy, although high doses cause multiple and complex damage to cells, DNA damage like double-strand breaks (DSBs) is widely known as a major factor leading to cell death.[18] To induce serious damage by Auger electrons that leads to cell death, targeting DNA would be one of the most efficient strategies. The range of Auger electrons is equivalent

to the diameter of genomic DNA strands (~2 nm). According to some studies, Auger-electron emitting radionuclides closer to the DNA can induce more DSBs;[19] delivery of the radionuclides as close as possible to the DNA is essential in order to maximize interaction between Auger electrons and the DNA in the nano-scale range. Collectively, DNA-targeting agents labeled with Auger-electron emitting radionuclides are promising tools to induce fatal DNA damage and kill cancer cells.

Unfortunately, such drugs have yet to be established. In attempts at DNA-targeting radiopharmaceutical to date, Auger-emitting radionuclides of $^{123, 125}$I, and ^{111}In were labeled to DNA-targeting molecules, e.g., a nucleic acid derivative such as deoxyuridine (UdR),[20] a nuclear localization signal (NLS),[21] or a DNA-binding molecule,[22] to ensure their transport to DNA. Although antimetabolites based on nucleic acid derivatives are incorporated into DNA, they are limited for use in TRT treatment due to their distribution in the intestinal tract, which is radiosensitive. Due to these risks, only a combination therapy in early clinical trials was performed and thereafter further progress has not been reported.[14] Although the agent conjugated with a NLS signal or a DNA-binding molecule has also been developed, the targeting and damaging efficiency has not been fully elucidated and effective therapeutic agents remain unestablished. In addition, most works have used common $^{123, 125}$I, and ^{111}In; however, the decay properties of these radionuclides are not the most ideal for therapeutic uses.[23] The short half-life of ^{123}I ($T_{1/2}$ = 13 h) and the long half-life of ^{125}I ($T_{1/2}$ = 57 d)[24] cause difficulties in practical clinical application for therapeutic purposes. While a certain amount of deiodination from labeled agents is present, the long half-life of ^{125}I may lead to a high risk of adverse effects. In the case of ^{111}In, the number of Auger/internal conversion electrons is expected to be less than other candidates. As shown in **Table 2**, there are other potential radionuclides; as the atomic number increases, the number of Auger electron emissions also tends to increase because of the increase in the number of orbital electrons. Additionally, to achieve the maximum DNA-damaging effect of Auger electrons, it is ideal for radionuclides to directly bind to DNA on their own. Irrespective of this point, not only commonly-used $^{123, 125}$I, and ^{111}In, but also most radionuclides are not combined with DNA by themselves. Therefore, when being transported to DNA, Auger-electron emitting radionuclides should be labeled to intermediary DNA-targeting molecules. Such drug design is unalterable, inevitably creating separation between the DNA and the radionuclide; consequently, the exact distance between the DNA and the radionuclide can be variable. Auger-electron emitting radionuclides directly combined with DNA may be most efficient at inducing DNA damage.

Hereby, the present research focuses on platinum (Pt) having a natural property that is useful in DNA targeting. Many antineoplastic Pt complexes (e.g., cisplatin, carboplatin, and oxaliplatin) have been used in conventional chemotherapy.[25] Their value is supported by a large number of basic and clinical uses over the years. Platinum complexes with appropriate leaving groups are known to

translocate into nuclei and form direct DNA adducts between Pt and nucleobases.[26] Such action potentially inhibits DNA replication, leading to cell damage and therapeutic efficacy. Thus, Pt binds to DNA directly unlike other radionuclides, suggesting that Pt radionuclides (also written as radio-Pt) have the advantage in DNA-targeting radiopharmaceuticals. Pt-191 ($T_{1/2}$ = 2.80 d, EC = 100%), Pt-193m ($T_{1/2}$ = 4.33 d, IT = 100%), and Pt-195m ($T_{1/2}$ = 4.01 d, IT = 100%), summarized in **Table 2**,[24] are promising candidate radionuclides that have a suitable half-life and a high Auger electron yield. Given the unique characteristics of Pt bound to DNA, Pt complexes labeled with radio-Pt as the center metal allow many Auger electrons to be released very close to DNA. Radio-Pt–based agents targeting DNA have the potential to cause effective DNA damage efficiently, which can be a breakthrough in Auger electron therapy.

To summarize research backgrounds, DNA-targeting radiopharmaceuticals that bind to DNA efficiently and induce DNA damage effectively, have yet to be achieved, and development is still ongoing. As several studies substantiated the distance between DNA and Auger-electron emitting radionuclides was crucial, agents should bind to DNA as close as possible to make DNA damage more serious. Auger-electron emitting radio-Pt is a promising source to deliver Auger electrons closest to DNA efficiently because Pt itself binds to DNA directly. Radio-Pt–based agents directly combined with DNA would induce DNA damage most efficiently, which may make DNA-targeted Auger electron therapy useful.

Here, for Auger electron cancer therapy, basis research and development of DNA-targeted radio-Pt agents were conducted. This dissertation has three chapters including a few sections as follows. First, it was necessary to determine the potential degree of the DNA-damaging effect by Auger electrons released from radio-Pt that binds to DNA. In *Chapter 1*, before the development of radio-Pt–labeled compounds, a production method for n.c.a. radio-Pt from an Ir target using accelerators was developed to prepare a radio-Pt precursor. Thereafter, the DNA damaging effect of Auger electrons was evaluated using n.c.a. radio-cisplatin with the negligible chemical effect of nonradioactive Pt. Second, to deliver radio-Pt to DNA more efficiently than radio-cisplatin, radio-Pt needed to be incorporated into DNA-targeting modules. In *Chapter 2*, the DNA-intercalator Hoechst33258 labeled with ^{191}Pt and the MYCN gene-targeting pyrrole–imidazole polyamide compound labeled with ^{191}Pt were developed for inducing DNA damage and cell damage efficiently. Ultimately, radio-Pt–labeled compounds should work *in vivo* for uses as TRT agents. In *Chapter 3*, regarding *in vivo* characteristics of the ^{191}Pt-labeled agents, radio-Pt–labeled tumor-targeting ligands were developed and their *in vivo* properties were investigated.

◆ **Chapter 1: Development of a Production Method for No-Carrier-Added Radio-Pt and Evaluation of DNA Damage by Auger Electrons using Radio-Cisplatin**

1. Development of Production Methods for No-Carrier-Added Platinum-191, 193m from an Iridium Target
2. Development of No-Carrier-Added Radio-cisplatin and Evaluation of its DNA-Damaging Efficacy as an Auger-electron emitting agent

◆ **Chapter 2: Development of Radio-Pt–Labeled Agents Binding to DNA Efficiently and Inducing DNA Damage Effectively**

1. Development of ^{191}Pt-Labeled Hoechst33258 Targeting DNA
2. Development of ^{191}Pt-Labeled PI Polyamide Targeting Amplified Cancer Genes

◆ **Chapter 3: Development of Radio-Pt–Labeled Agents Targeting Tumor Cells *In vivo***

1. Development of Tumor-Targeting ^{191}Pt-Labeled Agents via Mono-thiol Cysteine and a Tri-thiol Ligand

References

1. (a) Albain KS, Swann RS, Rusch VW, Turrisi AT, Shepherd FA, Smith C, Chen Y, Livingston RB, Feins RH, Gandara DR, Fry WA, Darling G, Johnson DH, Green MR, Miller RC, Ley J, Sause WT, Cox JD. Radiotherapy plus chemotherapy with or without surgical resection for stage III non-small-cell lung cancer: a phase III randomised controlled trial. *The Lancet* **2009**; 374(9687): 379–386. (b) Brunelli A, Charloux A, Bolliger CT, Rocco G, Sculier JP, Varela G, Licker M, Ferguson MK, Finn CF, Huber RM, Clini EM, Win T, Ruysscher DD, Goldman L. ERS/ESTS clinical guidelines on fitness for radical therapy in lung cancer patients (surgery and chemo-radiotherapy). *Eur Respir J* **2009**; 34(1): 17–41. (c) Breugom AJ, Swets M, Bosset JF, Collette L, Sainato A, Cionini L, Jones RG, Counsell N, Bastiaannet E, Broek CBM, Liefers GJ, Putter H, Velde CJH. Adjuvant chemotherapy after preoperative (chemo)radiotherapy and surgery for patients with rectal cancer: a systematic review and meta-analysis of individual patient data. *Lancet Oncol* **2015**; 16(2): 200–207. (d) Ronellenfitsch U, Schwarzbach M, Hofheinz R, Kienle P, Kieser M, Slanger TE, Jensen K. Perioperative chemo(radio)therapy versus primary surgery for resectable adenocarcinoma of the stomach, gastroesophageal junction, and lower esophagus. *Cochrane Database Syst Rev* **2013**; 31(5):CD008107.
2. Baskar R, Lee KA, Yeo R, Yeoh KW. Cancer and radiation therapy: current advances and future directions. *Int J Med Sci* **2012**; 9(3): 193–199.
3. Chargari C, Deutsch E, Blanchard P, Gouy S, Martelli H, Guérin F, Dumas I, Bossi A, Morice P, Viswanathan AN, Meder CH. Brachytherapy: An overview for clinicians. *CA Cancer J Clin* **2019**; 69(5): 386–401.
4. Suzuki M. Boron neutron capture therapy (BNCT): a unique role in radiotherapy with a view to entering the accelerator-based BNCT era. *Int J Clin Oncol* **2020**; 25: 43–50.
5. (a) Gambhir SS. Molecular imaging of cancer with positron emission tomography. *Nat Rev Cancer* **2002**; 2(9): 683–693. (b) Rohren EM, Turkington TG, Coleman RE. Clinical applications of PET in oncology. *Radiology* **2004**; 231(2): 305–332. (c) Fletcher JW, Djulbegovic B, Soares HP, Siegel BA, Lowe VJ, Lyman GH, Coleman RE, Wahl R, Paschold JC, Avril N, Einhorn LH, Suh WW, Samson D, Delbeke D, Gorman M, Shields AF. Recommendations on the use of ^{18}F-FDG PET in oncology. *J Nucl Med* **2008**; 49(3): 480–508. (d) Pimlott SL, Sutherland A. Molecular tracers for the PET and SPECT imaging of disease. *Chem Soc Rev* **2011**; 40(1): 149–162. (e) Nordberg A. PET imaging of amyloid in Alzheimer's disease. *Lancet Neurol* **2004**; 3(9): 519–527. (f) Hamaoka T, Madewell JE, Podoloff DA, Hortobagyi GN, Ueno NT. Bone imaging in metastatic breast cancer. *J Clin Oncol* **2004**; 22(14): 2942–2953.
6. Kassis AI, Adelstein SJ. Radiobiologic principles in radionuclide therapy. *J Nucl Med* **2005**; 46: 4S–12S.
7. (a) Kratochwil C, Bruchertseifer F, Giesel FL, Weis M, Verburg FA, Mottaghy F, Kopka K,

Apostolidis C, Haberkorn U, Morgenstern A. ^{225}Ac-PSMA-617 for PSMA-targeted α-radiation therapy of metastatic castration-resistant prostate cancer. *J Nucl Med* **2016**; **57**: 1941–1944. (b) Kratochwil C, Bruchertseifer F, Rathke H, Bronzel M, Apostolidis C, Weichert W, Haberkorn U, Giesel FL, Morgenstern A. Targeted α-therapy of metastatic castration-resistant prostate cancer with ^{225}Ac-PSMA-617: dosimetry estimate and empiric dose finding. *J Nucl Med* **2017**; 58(10): 1624–1631. (c) Kratochwil C, Bruchertseifer F, Rathke H, Hohenfellner M, Giesel FL, Haberkorn U, Morgenstern A. Targeted α-therapy of metastatic castration-resistant prostate cancer with ^{225}Ac-PSMA-617: swimmer-plot analysis suggests efficacy regarding duration of tumor control. *J Nucl Med* **2018**; 59(5): 795–802.

8. (a) Walter Bambynek, Bernd Crasemann, R.W. Fink, H.U. Freund, Hans Mark. X-Ray fluorescence yields, Auger, and Coster-Kronig transition probabilities. *Rev Mod Phys* **1972**; 44: 716–813. (b) McGuire EJ. Atomic L-shell Coster-Kronig, Auger, and radiative rates and flourescence yields for Na-Th. *Phys Rev A* **1971**; 3(2): 587–594. (c) McGuire EJ. Atomic M-shell Coster-Kronig, Auger, and radiative rates and fluorescence yields for Ca-Th. *Phys Rev A* **1972**; 5(3): 1043–1047.
9. Qaim SM. Nuclear data for production and medical application of radionuclides: Present status and future needs. *Nucl Med Biol* **2017**; 44: 31–49.
10. (a) Howell RW. Radiation spectra for Auger-electron emitting radionuclides: Report No.2 of AAPM Nuclear Medicine Task Group No.6. *Med Phys* **1992**; 19(6): 1371–1383. (b) Pomplun E, Booz J, Charlton DE. A Monte Carlo simulation of Auger cascades. *Radiat Res* **1987**; 111(3): 533–552. (c) Pomplun E. Monte Carlo simulation of Auger electron cascades versus experimental data. *Biomed Phys Eng Express* **2016**; 2(1): 015014. (d) Pomplun E. Auger electron spectra - the basic data for understanding the Auger effect. *Acta Oncol* **2000**; 39(6): 673–679.
11. (a) Eckerman KF, Endo A. MIRD: Radionuclide Data and Decay Schemes. 2nd ed. Reston, VA: Society of Nuclear Medicine; 2008. (b) (b) Ku A, Facca VJ, Cai Z, Reilly RM. Auger electrons for cancer therapy – a review. *EJNMMI Radiopharm Chem* **2019**; 4: 27.
12. (a) Jong M, Valkema R, Jamar F, Kvols LK, Kwekkeboom DJ, Breeman WAP, Bakker WH, Smith C, Pauwels S, Krenning EP. Somatostatin receptor-targeted radionuclide therapy of tumors: preclinical and clinical findings. *Semin Nucl Med* **2002**; 32(2): 133−140. (b) Delpassand ES, Samarghandi A, Mourtada JS, Zamanian S, Espenan GD, Sharif R, MacKenzie S, Kosari K, Barakat O, Naqvi S, Seng JE, Anthony L. Long-term survival, toxicity profile, and role of F-18 FDG PET/CT scan in patients with progressive neuroendocrine tumors following peptide receptor radionuclide therapy with high activity In-111 pentetreotide. *Theranostics* **2012**; 2(5): 472−480. (c) Janson ET, Westlin JE, Ohrvall U, Oberg K, Lukinius A. Nuclear localization of ^{111}In after intravenous injection of [^{111}In-DTPA-D-Phe1]-octreotide in patients with neuroendocrine tumors. *J Nucl Med* **2000**; 41(9): 1514−1518.
13. Vallis KA, Reilly RM, Scollard D, Merante P, Brade A, Velauthapillai S, Caldwell C, Chan I,

Freeman M, Lockwood G, Miller NA, Cornelissen B, Petronis J, Sabate K. Phase I trial to evaluate the tumor and normal tissue uptake, radiation dosimetry and safety of ^{111}In-DTPA-human epidermal growth factor in patients with metastatic EGFR-positive breast cancer. *Am J Nucl Med Mol Imaging* **2014**; 4(2): 181–192.

14. (a) Rebischung C, Hoffmann D, Stéfani L, Desruet MD, Wang K, Adelstein SJ, Artignan X, Vincent F, Gauchez AS, Zhang H, Fagret D, Vuillez J, Kassis AI, Balosso J. First human treatment of resistant neoplastic meningitis by intrathecal administration of MTX Plus ^{125}IUdR. *Int J Radiat Biol* **2008**; 84(12): 1123–1129. (b) Kassis AI, Tumeh SS, Wen PY, Kortylewicz JB, Abbeele AD, Zimmerman RE, Carvalho PA, Garada BM, DeSisto WC, Bailey NO, Castronovo FP, Mariani G, Black PM, Adelstein SJ. Intratumoral administration of 5-[^{123}I]iodo-2′-deoxyuridine in a patient with a brain tumor. J Nucl Med **1996**; 37(4 Suppl):19S–22S. (c) Mariani G, Cei A, Collecchi P, Kortylewicz JB, Abbeele AD, Luca LD, Stefano RD, Viacava P, Ferdeghini EM, Sacco SD, Salvadori PA, Bevilacqua G, Adelstein SJ, Mosca F, Kassis AI. Tumor targeting in vivo and metabolic fate of 5-[iodine-125]iodo-2′-deoxyuridine following intratumoral injection in patients with colorectal cancer. *J Nucl Med* **1993**; 34(7): 1175–1183.
15. (a) Welt S, Scott AM, Divgi CR, Kemeny NE, Finn RD, Daghighian F, Germain JS, Richards EC, Larson SM, Old LJ. Phase I/II study of iodine 125-labeled monoclonal antibody A33 in patients with advanced colon cancer. *J Clin Oncol* **1996**; 14: 1787−1797. (b) Quang TS, Brady LW. Radioimmunotherapy as a novel treatment regimen: ^{125}I-labeled monoclonal antibody 425 in the treatment of high-grade brain gliomas. *Int. J. Radiation Oncology Biol Phys* **2004**; 58(3): 972–975.
16. (a) Kassis AI, Fayad F, Kinsey BM, Sastry KS, Taube RA, Adelstein SJ. Radiotoxicity of ^{125}I in mammalian cells. *Radiat Res* **1987**; 111: 305–318. (b) Buchegger F, Adamer FP, Dupertuis YM, Delaloye AB. Auger radiation targeted into DNA: a therapy perspective. *Eur J Nucl Med Mol Imaging* **2006**; 33: 1352–1363.
17. (a) Martina RF, Feinendegend LE. The quest to exploit the Auger effect in cancer radiotherapy – a reflective review. *Int J Radiat Biol* **2016**; 92(11): 617–632. (b) Imstepf S, Pierroz V, Raposinho P, Bauwens M, Felber M, Fox T, Shapiro AB, Freudenberg R, Fernandes C, Gama S, Gasser G, Motthagy F, Santos IR, Alberto R. Nuclear targeting with an auger electron emitter potentiates the action of a widely used antineoplastic drug. *Bioconjugate Chem* **2015**; 26: 2397−2407.
18. Lomax ME, Folkes LK, O'Neill P. Biological consequences of radiation-induced DNA damage: Relevance to radiotherapy. *Clin Oncol* **2013**; 25: 578–585.
19. (a) Balagurumoorthy P, Xu X, Wang K, Adelstein SJ, Kassis AI. Effect of distance between decaying ^{125}I and DNA on Auger-electron induced double-strand break yield. *Int J Radiat Biol* **2012**; 88(12): 998–1008. (b) Pereira E, Quental L, Palma E, Oliveira MC, Mendes F, Raposinho P, Correia I, Lavrado J, Maria SD, Belchior A, Vaz P, Santos I, Paulo A. Evaluation of acridine orange derivatives as DNA-targeted radiopharmaceuticals for auger therapy: influence of the

radionuclide and distance to DNA. *Sci Rep* **2017**; 7: 42544. (c) Reissig F, Mamat C, Steinbach J, Pietzsch HJ, Freudenberg R, Retamal CN, Caballero J, Kotzerke J, Wunderlich G. Direct and auger electron-induced, single and double-strand breaks on plasmid DNA caused by ^{99m}Tc-labeled pyrene derivatives and the effect of bonding distance. *PLoS ONE* **2016**; 11(9): e0161973.

20. (a) Thisgaard H, Halle B, Jessen CA, Olsen BB, Therkelsen ASN, Dam JH, Langkjær N, Munthe S, Någren K, Carlsen PFH, Kristensen BW. Highly effective Auger-electron therapy in an orthotopic glioblastoma xenograft model using convection-enhanced delivery. *Theranostics* **2016**; 6(12): 2278–2291. (b) Kassis AI, Wen PY, Abbeele AD, Kortylewicz JB, Makrigiorgos GM, Metz KR, Matalka KZ, Cook CU, Sahu SK, Black PM, Adelstein SJ. 5-[^{125}I]iodo-2'-deoxyuridine in the radiotherapy of brain tumors in rats. *J Nucl Med* **1998**; 39(7): 1148–1154. (c) Kassis AI, Dahman BA, Adelstein SJ. In vivo therapy of neoplastic meningitis with methotrexate and 5-[^{125}I]iodo-2'-deoxyuridine. *Acta Oncol* **2000**; 39(6): 731–737.
21. (a) Rosenkranz AA, Slastnikova TA, Karmakova TA, Vorontsova MS, Morozova NB, Petriev VM, Abrosimov AS, Khramtsov YV, Lupanova TN, Ulasov AV, Yakubovskaya RI, Georgiev GP, Sobolev AS. Antitumor activity of auger electron emitter ^{111}In delivered by modular nanotransporter for treatment of bladder cancer with EGFR overexpression. *Front Pharmacol* **2018**; 9: 1331. (b) Rosenkranz AA, Slastnikova TA, Georgiev GP, Zalutsky MR, Sobolev AS. Delivery systems exploiting natural cell transport processes of macromolecules for intracellular targeting of Auger electron emitters. *Nucl Med Biol* **2020**; 80: 45–56.
22. (a) Yasui LS, Chen K, Wang K, Jones TP, Caldwell J, Gusea D, Kassis AI. Using hoechst 33342 to target radioactivity to the cell nucleus. *Radiat Res* **2007**; 167: 167–175. (b) Sato N, Kobayashi H, Saga T, Nakamoto Y, Ishimori T, Togashi K, Fujibayashi Y, Konishi J, Brechbiel MW. Tumor targeting and imaging of intraperitoneal tumors by use of antisense oligo-DNA complexed with dendrimers and/or avidin in mice. *Clin Cancer Res* **2001**; 7: 3606–3612. (c) Dahmen V, Pomplun E, Kriehuber R. Iodine-125-labeled DNA-Triplex-forming oligonucleotides reveal increased cyto- and genotoxic effectiveness compared to Phosphorus-32. *Int J Radiat Biol* **2016**; 92(11): 679–685.
23. Filosofov D, Kurakina E, Radchenko V. Potent candidates for Targeted Auger Therapy: Production and radiochemical considerations. *Nucl. Med. Biol.* **2021**; 94–95: 1–19.
24. NuDat 3.0, available online at (https://www.nndc.bnl.gov/nudat3/) [accessed 24 December 2022].
25. Johnstone TC, Suntharalingam K, Lippard SJ. The next generation of platinum drugs: targeted Pt(II) agents, nanoparticle delivery, and Pt(IV) prodrugs. *Chem Rev* **2016**; 116(5): 3436–3486.
26. (a) Jamieson ER, Lippard SJ. Structure, recognition, and processing of cisplatin-DNA adducts. *Chem Rev.* **1999**; 99: 2467−2498. (b) Wang D, Lippard SJ. Cellular processing of platinum anticancer drugs. *Nat Rev Drug Discovery* **2005**; 4: 307−320. (c) Zamble DB, Lippard SJ. Cisplatin and DNA repair in cancer chemotherapy. *Trends Biochem Sci* **1995**; 20(10): 435–439.

Chapter 1: Development of a Production Method for No-Carrier-Added Radio-Pt and Evaluation of DNA Damage by Auger Electrons using Radio-Cisplatin

Chapter 1—Introduction

Platinum radionuclides, e.g., $^{191, 193m, 195m}$Pt have been readily produced in a nuclear reactor via the (n,x) reaction.[1] Since $^{191, 193m}$Pt are quite difficult to produce with high yields because of the relatively low isotopic abundances of their respective target isotopes (^{190}Pt, 0.014%; ^{192}Pt, 0.782%; ^{194}Pt, 32.967%; ^{195}Pt, 33.832%; ^{196}Pt, 25.242%; ^{198}Pt, 7.163%), mainly ^{195m}Pt has been used in applications.[2] However, the nuclear reactor-produced carrier-added (c.a.) radio-Pt has low specific activity (in MBq/mg), due to the use of non-radioactive Pt targets. Particle accelerators enable no-carrier-added (n.c.a.) radio-Pt production, but the production method has yet to be established at a practical level. These production backgrounds have made radio-Pt–based research not only limited but also done only using c.a. radio-Pt.[3,4] Although some studies reported a certain degree of therapeutic efficacy when using c.a. radio-cisplatin with low specific activity,[4] it was doubtful whether the fundamental potential of Auger electrons alone was investigated without being masked by the chemotherapeutic effects of a large amount of non-radioactive Pt carriers. To evaluate the therapeutic potential of Auger electrons, n.c.a. radio-Pt–labeled agents need to be used.

There are available routes to produce radio-Pt at the n.c.a. level using particle accelerators as follows:

(1) via high-energy proton irradiation on a gold (Au) target[5]
$^{197}Au(p,xpyn)^{191}Pt/^{191}Au/^{191}Hg \rightarrow ^{191}Pt$

(2) via photonuclear reaction associated with electron acceleration on an Au target[6]
$^{197}Au(\gamma,np)^{195m}Pt$

(3) via alpha-particle bombardment on an osmium (Os) target[7,8]
$^{nat}Os(\alpha,xn)^{191, 193m}Pt$ (^{nat}Os: ^{184}Os, 0.02%; ^{186}Os, 1.59%; ^{187}Os, 1.96%; ^{188}Os, 13.24%; ^{189}Os, 16.15%; ^{190}Os, 26.26%; ^{192}Os, 40.78%)

(4) via light-charged particle (proton, deuteron) irradiation on an iridium (Ir) target[9,10]
$^{nat}Ir(p/d,xn)^{191, 193m}Pt$ (^{nat}Ir: ^{191}Ir, 37.3%; ^{193}Ir, 62.7%)

Although the indirect production route ^{nat}Pt(p,xn)^{191}Au $\rightarrow$^{191}Pt (^{nat}Pt: ^{190}Pt, 0.014%; ^{192}Pt, 0.782%; ^{194}Pt, 32.967%; ^{195}Pt, 33.832%; ^{196}Pt, 25.242%; ^{198}Pt, 7.163%) is available,[11] it has rarely been used because rapid chemical separation is needed before ^{191}Au decay ($T_{1/2}$ = 3.18 h), and radiation exposure resulting from high energy proton irradiation is an obstacle. In the case of $^{197}Au(p,xpyn)^{191}Pt/^{191}Au/^{191}Hg \rightarrow ^{191}Pt$ (1), the chemical separation procedure of radio-Pt from a bulk Au target has already been established, but facilities are limited where 75–65 MeV proton beam is available.[5] In the case of $^{197}Au(\gamma,np)^{195m}Pt$ (2), the production yield was reported to be 0.15–0.31 MBq/μA h in the photonuclear reaction induced by electron energy of 34 MeV.[6] It is necessary to irradiate a relatively thick target with a high beam current for this reaction. Practical production needs a suitable irradiation chamber with a cooling system to reduce overheating of the target and avoid

unwanted radiation exposure. In the case of $^{nat}Os(\alpha,xn)^{193m,\ 195m}Pt$ (3), the chemical separation procedure of radio-Pt from a bulk Os target has already been established, and a separation efficiency of 90% was reported.[7] According to Uddin *et al.*, the batch production yield of ^{193m}Pt was 2.1 MBq/μA h from a 40 MeV α-particle bombardment of an enriched ^{192}Os target.[7] The production yield of ^{191}Pt is 3.24 MBq/μA h from a 38–16 MeV α-particle bombardment of a ^{nat}Os target.[7,8] However, there are other significant drawbacks to the use of an Os target. Osmium is readily oxidized, and its oxide (OsO_4) is highly toxic and very volatile (v.p. 15 hPa, 27℃; b.p. 129.7 °C). This chemical property also places a limit on the applicable beam current, leading to low yields.

On the other hand, in the case of $^{nat}Ir(p/d,xn)^{191,\ 193m}Pt$ (4), the production is achieved with 30–15 MeV proton beam for ^{191}Pt production or 20–5 MeV deuteron beam for $^{191,\ 193m}$Pt.[9,10,12] These conditions are available using medium to large accelerators, which are relatively common. Furthermore, an iridium target can be handled safely with moderate radiation exposure. Unfortunately, a production method has yet to be established. A literature search revealed that there were two problems: (1) the dissolution of the irradiated iridium target, and (2) the chemical separation of the two similar complexes – Pt(IV) and Ir(IV) chloride.[9,10,13] Generally, to enhance the solubility of elemental iridium, several steps of thermal treatment are necessary to convert iridium into soluble species. Alkali fusion is one of the most effective thermal treatments. It is based on the oxidation of iridium by an alkali salt (e.g., KOH and KNO_3, or Na_2O_2 alone) under extremely high temperatures.[10,14] However, this method needs an apparatus for achieving the appropriate conditions for efficient melting and treatment. Since it is also difficult to do efficient alkali fusion for an Ir foil as a usual target shape, alkali fusion has rarely been utilized thus far for practical radio-Pt production. In methods of chemical separation, Pt(IV) and Ir(IV) chloride complexes are usually extracted by the same agent and their retention times in column chromatography are very similar, making their separation more difficult.[13] Although solvent extraction has been commonly used for the chemical separation of platinum group metals (PGMs) in the precious metal industry, detailed techniques are proprietary. In the works above, radio-Pt was separated from the iridium targets by liquid-liquid extraction and adsorption chromatography,[9] or anion-exchange chromatography.[10] Still, iridium species were found in the final products after radiochemical processing, and the chemical form of radio-Pt was not determined in either study. In all cases, the conditions for precise chemical separation of n.c.a. radio-Pt from bulk iridium targets needs to be investigated.

To summarize, a safe method to produce a sufficient amount of n.c.a. radio-Pt is necessary for the potential evaluation of radio-Pt and its medical applications. In this regard, an Ir target is a more practical target material for radio-Pt production, under the condition that radio-Pt can be separated from a bulk iridium target. Apart from the production method, it is also necessary to deliver Auger-electron emitting radionuclides as close to DNA as possible and to evaluate the DNA-damaging effect of Auger electrons without causing chemical damage to the DNA. A generic Pt-based

antineoplastic drug cisplatin is a suitable example agent because it can directly bind to DNA on its own without intermediary DNA-binding compounds;[15] therefore, n.c.a. radio-cisplatin emitting Auger electrons will be an ideal choice as a source. Herein, the research objective of *Chapter 1* was to establish a production method for n.c.a. $^{191, 193m}$Pt from an Ir target using accelerators (section 1), and to evaluate the DNA damaging effect of Auger electrons using n.c.a. radio-cisplatin with the minimum chemical effect of nonradioactive Pt (section 2). *Chapter 1* included the following 2 topics: **(1) Development of Production Methods for No-Carrier-Added Platinum-191, 193m from an Iridium Target**, and **(2) Development of No-Carrier-Added Radio-cisplatin and Evaluation of its DNA-Damaging Efficacy as an Auger-electron emitting agent**. Platinum-191 can be detected readily from its γ-ray intensities while ^{193m}Pt emits a 135.5 keV γ-ray with a low intensity (0.0115%). Therefore, the present study mostly focuses on ^{191}Pt, but section 1 demonstrates that the established production method for ^{191}Pt can be employed for ^{193m}Pt.

C*hapter 1* is based on the following papers that are referred to in the text.

1. Obata H, Khandaker MU, Furuta E, Nagatsu K, Zhang MR. Excitation functions of proton- and deuteron-induced nuclear reactions on natural iridium for the production of ^{191}Pt. *Appl Radiat Isot* **2018**; 137: 250–260.
2. Obata H, Minegishi K, Nagatsu K, Zhang MR, Shinohara A. Production of ^{191}Pt from an iridium target by vertical beam irradiation and simultaneous alkali fusion. *Appl Radiat Isot* **2019**; 149: 31–37.
3. Obata H, Minegishi K, Nagatsu K, Ogawa M, Zhang MR. Synthesis of no-carrier-added [$^{188, 189, 191}$Pt]cisplatin from a cyclotron produced $^{188, 189, 191}PtCl_4^{2-}$ complex. *Sci Rep* **2021**; 11: 8140.
4. Obata H, Tsuji AB, Sudo H, Sugyo A, Minegishi K, Nagatsu K, Ogawa M, Zhang MR. In vitro evaluation of no-carrier-added radiolabeled cisplatin ([$^{189, 191}$Pt]cisplatin) emitting Auger electrons. *Int J Mol Sci* **2021**; 22: 4622.
5. Obata H, Tsuji AB, Sudo H, Sugyo A, Minegishi K, Nagatsu K, Ogawa M, Zhang MR. Precise quantitative evaluation of pharmacokinetics of cisplatin using a radio-platinum tracer in tumor-bearing mice. *Nucl Med Commun* **2022**; 43(11): 1121–1127.
6. Obata H, Kurimasa A, Muraoka T, Tsuji AB, Kondo K, Kuwahara Y, Minegishi K, Nagatsu K, Ogawa M, Zhang MR. Dynamic imaging analysis reveals Auger electron-emitting radio-cisplatin induces DNA damage depending on the cell cycle. *BBRC* **2022**; 637: 286–293.

1. Development of Production Methods for No-Carrier-Added Platinum-191, 193m from an Iridium Target

Production and chemical purification method

The production and purification scheme was shown in **Fig. 1-1-1**, and the details of this scheme and photos of actual targets were presented in the following.

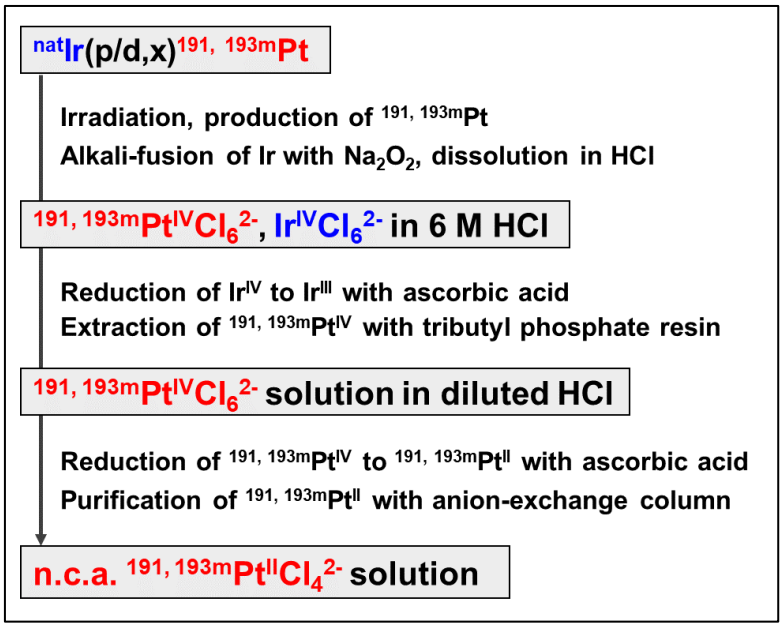

Figure 1-1-1. Scheme for the production and purification of $^{191, 193m}$Pt.

Target preparation, irradiation, and dissolution

Platinum-191 and -193m were produced via proton- and deuteron-induced nuclear reactions on iridium targets in the following accelerator facilities (**Table 1-1-1**). The beam energy was based on the maximum limit of each facility and the cross-section for the ^{nat}Ir(p/d,xn)$^{191, 193m}$Pt nuclear reaction.[12] Pt-191 was produced via the ^{nat}Ir(p, xn)^{191}Pt nuclear reaction with a 30 MeV proton beam, and $^{188, 189}$Pt were co-produced via the ^{nat}Ir(p, xn)$^{188, 189}$Pt nuclear reaction. The proton irradiation of an Ir target was performed using the AVF-930 cyclotron at National Institutes for Quantum Science and Technology (QST), the 930 AVF cyclotron at the Tohoku University Cyclotron and Radioisotope Center (CYRIC), or the CS-30 cyclotron at Duke University Medical Center (DUMC). Platinum-191 and -193m were co-produced via the ^{nat}Ir(d, xn)$^{191, 193m}$Pt nuclear reaction with a deuteron beam below 20 MeV accelerated with the AVF-930 cyclotron at QST, the CS-30 cyclotron at DUMC, or the FN tandem Van de Graaff accelerator at Triangle Universities Nuclear Lab (TUNL).

Table 1-1-1. Facilities and accelerators used in this work.

Facilities	Accelerators	Beam energy on a target		Beam	Target
		Proton	Deuteron		
QST (Japan)	AVF-930 cyclotron	30 MeV	20 MeV	Vertical	Mixture (Ir and Na_2O_2) Ir powder
CYRIC (Japan)	AVF-930 cyclotron	30 MeV	-	Horizontal	Ir coin
DUMC (USA)	CS-30 cyclotron	30 MeV	15 MeV	Horizontal	Ir coin
TUNL (USA)	FN tandem Van de Graaff accelerator	-	14 MeV	Horizontal	Ir coin

Vertical beam irradiation at QST (small scale)

The target irradiation was performed in a vertical beam irradiation system at QST. In this system, the target can be irradiated with an external vertical beam in a semi-sealed target vessel, which is convenient for using a powder target. Additionally, this system makes it possible to irradiate substances with a low melting point, allowing the melting of target materials in the target vessel during irradiation.

A mixture of natural iridium powder (120 mg) and sodium peroxide (98 mg) (molar ratio $^{nat}Ir : Na_2O_2 = 1 : 2$ was used for the irradiation target (**Fig. 1-1-2**). The mixture was put in a Nb target vessel (10 mm diameter and 10 mm depth) which was sealed with Nb foil (99+%, thickness of 127 μm, Nilaco, Tokyo, Japan). Considering the melting of Na_2O_2, the Nb target vessel and foil were used as a highly corrosion-resistant but less expensive material. The irradiation of the target was performed immediately after target preparation to avoid the decomposition of Na_2O_2 due to its moisture absorption. The target was irradiated with a 30 MeV proton beam for 1–3 hours at a beam current of 9–10 μA. The semi-sealed target vessel containing the mixture was placed in a target holder which was cooled by water circulation, and the sealing Nb foil was directly cooled by chilled helium.

The irradiated mixture seemed to form a fused salt (Na-Ir-O compound) due to the high temperature that resulted from the irradiation. The mixture was readily dissolved in 6 M HCl (6 mL) by heating at 130–140°C for 30 minutes. The Nb target vessel containing the fused mixture was put into the HCl solution, and the vessel was taken out from the solution after heating. After heating, the deep blue solution of the crude mixture turned to a dark reddish-brown color, suggesting that the Na-Ir-O compound was converted into $Ir^{IV}Cl_6^{2-}$ in concentrated HCl.

After dissolution, the solution was filtered through quartz wool packed in a cartridge equipped with a 20 μm polyethylene frit (Tomoe Engineering, Tokyo, Japan), and a 0.2 μm PTFE filter (DISMIC, ADVANTEC, Tokyo, Japan). These filtering arrangements were then rinsed with a small volume of 6 M HCl in each process. After filtering the solution, a stock solution containing mostly $Ir^{IV}Cl_6^{2-}$ with trace amounts of radio-$Pt^{IV}Cl_6^{2-}$ was prepared.

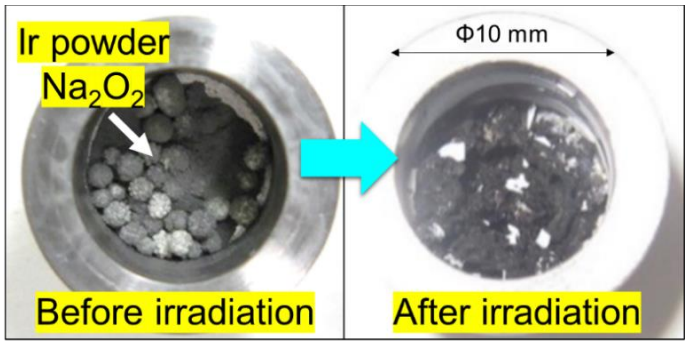

Figure 1-1-2. Photos of a mixed target of Ir and Na_2O_2 before and after irradiation, showed that the irradiated Ir powder was alkali-fused with Na_2O_2 due to heating by the beam.

Vertical beam irradiation at QST (large scale)

The natural iridium powder (250 mg) was put in an Al target vessel (10 mm diameter and 10 mm depth) which was sealed with Al foil (99+%, thickness of 20 μm, Nilaco, Tokyo, Japan) (**Fig. 1-1-3**). The inexpensive Al vessel and foil were used in irradiation for only iridium. The target was irradiated with a 30 MeV proton beam or a 20 MeV deuteron beam for 7 hours at both beam currents of 9–10 μA. The target vessel containing the mixture was placed in a target holder which was cooled by water circulation, and the sealing Al foil was directly cooled by chilled helium. After that, the irradiated Ir powder was alkali-fused by mixing Na_2O_2 (250 mg) and heating at 650°C for 3–4 h inside the alumina vessel (AS ONE, Osaka, Japan) using the original electric furnace. The fused compound was dissolved in 6 M HCl (12 mL) by heating at 130–140°C for 30 minutes. After dissolution, the solution was filtered as described above.

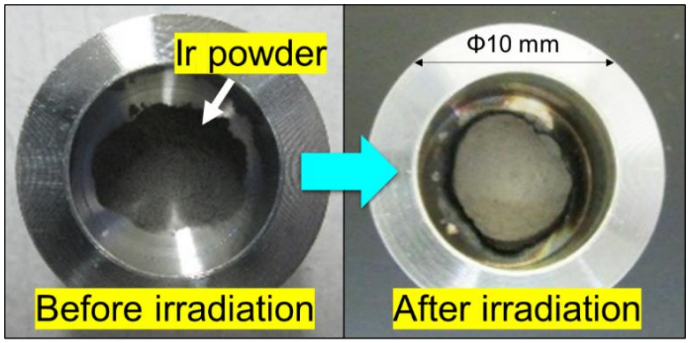

Figure 1-1-3. Photos of an Ir target in an Al vessel before and after irradiation, showed that the Ir target was irradiated in powder form.

Horizontal beam irradiation at CYRIC, DUMC, and TUNL

The natural Ir powder (250 mg) was pressed in a 10 mm diameter like a coin at 10–15 MPa using a pressing machine (SMT-200AF, Sansho Industry, Osaka, Japan). The Ir-coin target was wrapped with an Al foil (10–12 μm) (**Fig. 1-1-4**), and irradiated with a horizontal proton or deuteron beam for 1–7 hours at a beam current of 1–3.5 μA at CYRIC, DUMC, or TUNL. The target was placed in a target holder cooled by water circulation in both irradiation systems at all facilities, and the Al foil was directly cooled by chilled helium only at CYRIC. The irradiated Ir coin was readily crushed, thereafter alkali-fused with Na_2O_2, and dissolved in 6 M HCl as described above.

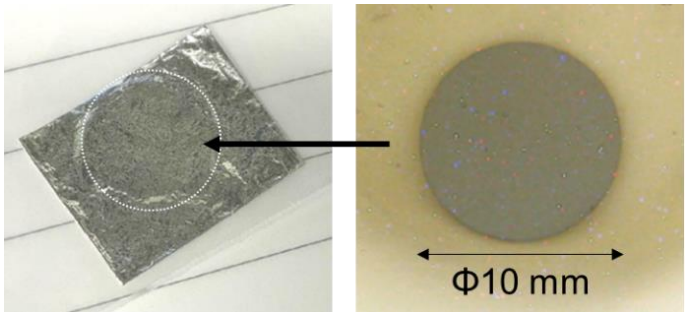

Figure 1-1-4. Photos of an Ir-coin target for horizontal beam irradiation. Ir powder was pressed to make it stand in a vertical direction and wrapped with an Al foil to prevent irradiated materials from shattering.

Chemical separation and preparation of n.c.a. radio-$Pt^{II}Cl_4^{2-}$

A reducing solution (250 mg/mL sodium L-ascorbate and 2 mg/mL sodium sulfite, 0.1–0.2 mL) was added to the filtered solution (6 mL) to selectively reduce $Ir^{IV}Cl_6^{2-}$. During this procedure, the dark reddish-brown solution turned greenish-yellow (**Fig. 1-1-5**), as the $Ir^{IV}Cl_6^{2-}$ was reduced to $Ir^{III}Cl_6^{3-}$ whereas the radio-$Pt^{IV}Cl_6^{2-}$ remained. After the reduction, the mixture was loaded onto a tributyl phosphate (TBP) resin column made by connecting three TBP-resin cartridges (2 mL cartridge, TrisKem International, Rennes, France), as the radio-$Pt^{IV}Cl_6^{2-}$ was selectively extracted into the resin. The column was rinsed with 3.5 M HCl (5 mL), and then DI water (6 mL) was used to elute the radio-$Pt^{IV}Cl_6^{2-}$. To reduce the radio-$Pt^{IV}Cl_6^{2-}$ to radio-$Pt^{II}Cl_4^{2-}$, the reducing agent (187.5 mg/mL sodium L-ascorbate and 1.5 mg/mL sodium sulfite, 12 mL) was added to the eluted solution containing the radio-$Pt^{IV}Cl_6^{2-}$, yielding a crude radio-$Pt^{II}Cl_4^{2-}$ solution. The HCl concentration of this mixed solution was estimated to be <1 M.

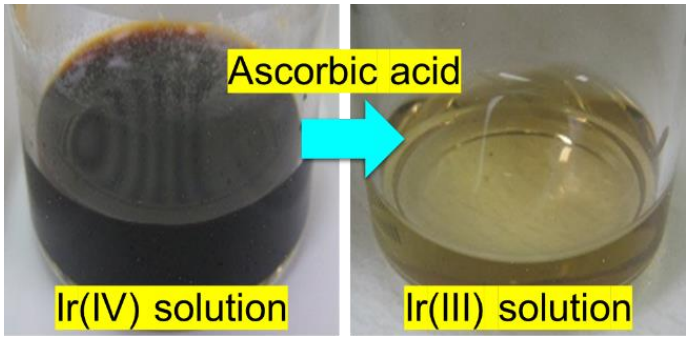

Figure 1-1-5. Photos of an Ir solution before and after reduction with ascorbic acid, showed that the dark reddish-brown solution turned greenish-yellow.

For further purification, the resultant crude radio-$Pt^{II}Cl_4^{2-}$ solution (18 mL) was loaded onto a column of quaternary methyl ammonium (QMA) (Φ15×40 mm, AccellPlus QMA, Waters, Milford, MA, USA), and the column was rinsed with 0.01 M HCl (12 mL). An aqueous solution containing 1.5 M HCl and 0.01–0.02 M KCl, was used to elute the radio-$Pt^{II}Cl_4^{2-}$. The elution was collected in 12 fractions (2 mL each), and the fractions containing radio-$Pt^{II}Cl_4^{2-}$ (f5–10) were combined based on their radioactivity.

Irradiation and dissolution of an iridium target

To dissolve the insoluble Ir efficiently after irradiation, different Ir targets and irradiation methods were evaluated depending on the accelerator facilities (QST, CYRIC, DUMC, and TUNL) and the radioactivity required for biological experiments. First, a mixture of natural iridium (insoluble metal) and sodium peroxide (fusing agent) was combined as a target material for a small-scale production (~100 MBq of ^{191}Pt) using the vertical beam irradiation system at QST. As shown in **Fig. 1-1-2**, the irradiated mixture was observed to form a fused salt (Na-Ir-O compound) due to strong heating by the intense proton beam, suggesting the iridium target was successfully alkali-fused during irradiation. Na_2O_2 as a fusing agent allowed the mixed target to remain soluble after irradiation at 10 μA beam current. Considering the melting point of Na_2O_2 (460°C), the result implied that the temperature inside the target vessel exceeded 460°C. Thus, the present method achieved both radioactivation and alkali fusion of the mixed target simultaneously, and the mixed iridium target became soluble after irradiation for only 30 min, while alkali-fusion processing usually took several hours to achieve similar results.[14] The dissolution efficiencies varied between 40–60% at a beam current of 9–10 μA, and the temperature of the target being irradiated possibly exceeded the decomposition temperature of Na_2O_2 (657°C) locally and/or over a wide area. The appropriate range of temperature would be preferred for alkali fusion, but the beam focusing and the beam spot temperature in the target vessel were difficult to

control in this system. Further improvement in controlling the temperature at the beam spot in the target vessel would give more consistent results for the efficient fusion of the mixed target.

Next, a natural Ir powder was used target material to expand to the large-scale production (>102 MBq of ^{191}Pt) using the vertical beam irradiation at QST. For efficient alkali fusion and dissolution of the irradiated Ir, the surface area of Ir and Na_2O_2 solids will need to be increased. Therefore, an Ir powder target was employed and irradiated with a vertical beam at a beam current of 9–10 μA. The irradiated Ir powder was successfully alkali-fused with Na_2O_2 using the original electric furnace and subsequently dissolved in HCl. In some cases, a small Ir metal piece was observed after the irradiation of Ir powder. This was most likely due to Ir powder melting at a beam spot during the irradiation, which led to a decrease in dissolution efficiency. However, almost all Ir was dissolved by repeating the alkali-fusion process for such insoluble residues.

At CYRIC, DUMC, and TUNL, the horizontal beam irradiation was also evaluated using coin targets which were made by pressing Ir powder. At CYRIC, the Ir coin was irradiated at ~3 μA of beam current. The beam-target contact interface was cooled with chilled helium while the target backside was water-cooled. After irradiation, the Ir coin target was broken apart into powder and granules, resulting in efficient alkali fusion with Na_2O_2 and subsequent dissolution. At DUMC and TUNL, the similar Ir coin target was irradiated at ~3.5 μA while the target was only cooled at the backside with cooling water. After irradiation, the Ir coin target melted and remained a tight disk regardless of efforts to break it apart into powder and granules. The targets were crushed, alkali-fused, and dissolved. This process was repeated for the insoluble residues several times in order to attain the most target dissolution. These results suggest that better cooling will be needed to irradiate the Ir powder coin targets with the increased beam current to avoid the prolonged dissolution process.

Deuteron irradiation of the iridium targets was also investigated to evaluate the possibility of ^{193m}Pt production. The Ir powder was irradiated with 20 MeV deuteron at a beam current of 9–10 μA in the vertical beam irradiation at QST, and the Ir coin target was irradiated with 14–15 MeV deuteron at a beam current of 0.5–1 μA at DUMC and TUNL. Extensive Ir target melting was observed in every deuteron irradiation at all facilities, leading to an inefficient dissolution. Most deuteron energies were expected to be transferred to the target, and in that condition, the current target cooling would be insufficient, especially in deuteron irradiation. The cooling system of iridium targets needs further improvement for efficient target dissolution.

Chemical separation of Pt(IV) and Ir(IV) chloride complexes

By a combination of resin extraction and anion-exchange chromatography (AEC), n.c.a. radio-$Pt^{II}Cl_4^{2-}$ was successfully prepared as a precursor for the synthesis of Pt complexes like cisplatin. First, radio-$Pt^{IV}Cl_6^{2-}$ was separated from the bulk Ir target material through a TBP-resin–based solid-phase extraction. There are a variety of extracting agents for $Pt^{IV}Cl_6^{2-}$ and other PGMs, e.g., TBP and some commercial extracting agents of the Cyanex series, the Alamine series, and the Aliquat series. Among these candidates, the TBP is commonly used as a neutral extraction agent, and it does not alter the chemical form of $Pt^{IV}Cl_6^{2-}$ according to Eq. (1).

$$2H^+{}_{aq} + PtCl_6{}^{2-}{}_{aq} + 2TBP_{org} = (TBP)_2H_2PtCl_6{}_{org} \qquad (1)$$

Since both $Pt^{IV}Cl_6^{2-}$ and $Ir^{IV}Cl_6^{2-}$ are co-extracted by TBP in any solvent conditions, the selective reduction of $Ir^{IV}Cl_6^{2-}$ to $Ir^{III}Cl_6^{3-}$ is essential in the separation of $Pt^{IV}Cl_6^{2-}$ and $Ir^{IV}Cl_6^{2-}$ through extraction. The comprehensive evaluation of reducing agents indicated that ascorbic acid enabled the selective reduction of $Ir^{IV}Cl_6^{2-}$ and facilitated the separation processes. Ascorbic acid exhibited the highest selectivity for the reduction of $Ir^{IV}Cl_6^{2-}$ in 6 M HCl. In contrast, radio-$Pt^{IV}Cl_6^{2-}$ was not reduced at all in 6 M HCl but was readily reduced in diluted HCl (<1 M). As a result, only radio-$Pt^{IV}Cl_6^{2-}$ was extracted from the bulk $Ir^{III}Cl_6^{3-}$ solution onto the TBP resin. The solid-phase extraction was advantageous because of its potential to allow the automation of this separation process. Hence, radio-$Pt^{IV}Cl_6^{2-}$ was extracted onto the TBP resin in the presence of HCl, and then quickly eluted with H_2O. The extraction efficiency for radio-Pt varied between 80–100%.

While only $Ir^{IV}Cl_6^{2-}$ was reduced by ascorbic acid in 6 M HCl, it was found that ascorbic acid could also reduce radio-$Pt^{IV}Cl_6^{2-}$ to radio-$Pt^{II}Cl_4^{2-}$ in diluted HCl (<1 M). For the reduction of n.c.a. radio-$Pt^{IV}Cl_6^{2-}$ (<0.1 nmol), an equivalent amount of a reducing agent as well as its concentration is very small (nM). In that condition, the reducing reaction of n.c.a. radio-$Pt^{IV}Cl_6^{2-}$ did not proceed by conventional reducing agents used for $Pt^{IV}Cl_6^{2-}$ in aqueous solutions (e.g., hydrazine, oxalate, and sulfite). Although excessive reducing agents would promote the reduction of n.c.a. radio-$Pt^{IV}Cl_6^{2-}$ to radio-$Pt^{II}Cl_4^{2-}$ in a neutral solution, hydrolysis and/or ligand exchange of n.c.a. radio-Pt complexes could generate unknown species. Therefore, different reducing agents were evaluated for n.c.a. radio-$Pt^{IV}Cl_6^{2-}$ in HCl, showing that ascorbic acid was the most suitable agent.

After elution from the TBP resin, radio-$Pt^{IV}Cl_6^{2-}$ was reduced by ascorbic acid rapidly in <1 M HCl. After that, the crude radio-$Pt^{II}Cl_4^{2-}$ solution was purified by AEC with a QMA column. The chromatography profile of the QMA-AEC purification was shown in **Fig. 1-1-6**. Although radio-$Pt^{II}Cl_4^{2-}$ was predominantly observed in fractions #4–12, some radio-Pt species passed through the column without any interaction (in fraction #0) while some strongly retained on the column, as shown in **Fig. 1-1-6**. Additionally, the early fractions (fractions #1–4) were removed from the product because HPLC analysis observed impurities that would be derived from ascorbic acid. The yield of AEC

purification for radio-Pt varied between 50–70%.

In summary, a total of 40–70% recovery yield was achieved for the present separation method. The recovery yield likely varied due to the very small amount of n.c.a. radio-Pt that can be changed to unknown species by slight impurities. Nevertheless, the separation method for n.c.a. radio-$Pt^{II}Cl_4^{2-}$ from bulk Ir targets was established in this study, and can function under a variety of irradiation parameters.

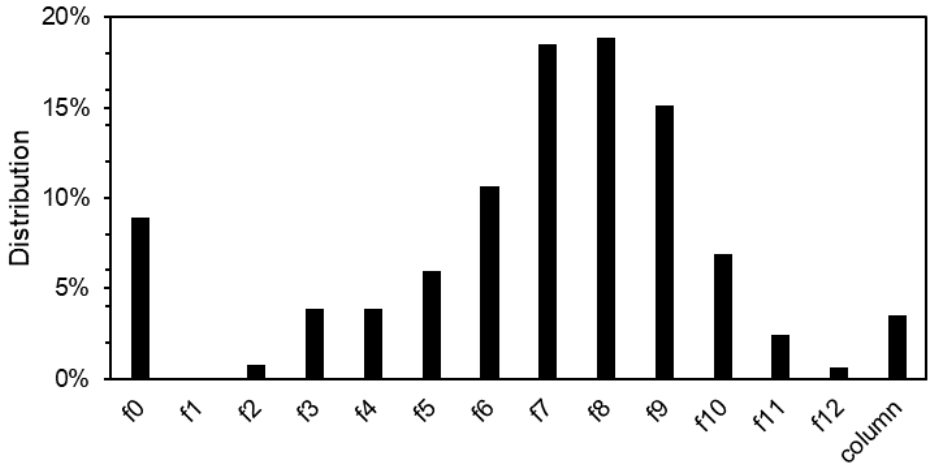

Figure 1-1-6. Radiochromatogram obtained during QMA-purification (f0: non-retaining fraction before elution, column: residual on the column). Fractions from f5 to f10 were collected.

Production yields of ^{191}Pt by proton irradiation and quality control of the n.c.a. $^{191}Pt^{II}Cl_4^{2-}$ product

The theoretical and experimental yields were summarized in **Table 1-1-2**. Platinum-191 was produced from a ^{nat}Ir target with sufficient production yields (~17 MBq/μA*h for the mixed target (Ir and Na_2O_2), and ~37 MBq/μA*h for the pure target at the end of bombardment (EOB)). The production yield for the pure ^{nat}Ir target was about 2-fold higher, compared with the mixed target. The powder target exhibited a similar production yield as the coin target, suggesting both methods were practical depending on the irradiation systems in different facilities.

The chemical form of the radio-Pt product after QMA-AEC was identified by HPLC analysis with an anion-exchange column, as shown in **Fig. 1-1-7**, where the chromatographic profile of radio-Pt using a radio-detector showed identical retention time with the reference standard sample $K_2Pt^{II}Cl_4^{2-}$, indicating the majority of the n.c.a. radio-Pt were $Pt^{II}Cl_4^{2-}$, and it was speculated that the minimum impurity resulted from the hydrolysis of $Pt^{II}Cl_4^{2-}$ leading to the formation such as

$[PtCl^{4-n}(H_2O)_n]^{(2-n)-}$. The n.c.a. radio-Pt(II) product was successfully prepared as the tetra-chloride form and provided a reasonable starting point for radiolabeling chemistry.

Table 1-1-2. Theoretical and production yields for ^{191}Pt.

EOB	Theoretical yield (MBq/μA*h)	Production yield† (MBq/μA*h)
^{nat}Ir thick target (p, 29.6–17.5 MeV)	108[16]	-
^{nat}Ir powder and Na_2O_2 (p, 30 MeV)‡		~17[17]
^{nat}Ir powder (p, 30 MeV)‡		~37
^{nat}Ir coin target (p, 29.2–26.2 MeV)	37[a]	~37

† Corrected with 100% dissolution efficiency and 100% separation efficiency.

‡ The precise exit energy was not calculated for powder targets due to their unknown target thickness in this system.

[a] Calculated from the formula of thick target yield.[16]

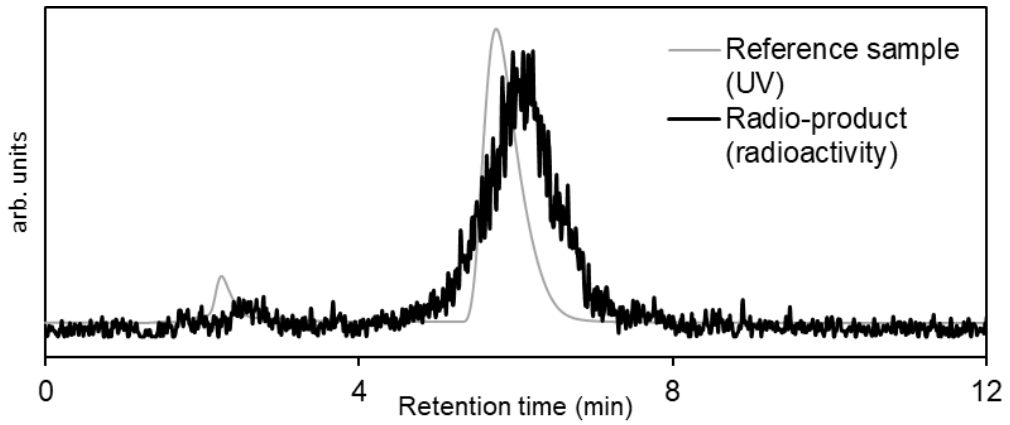

Figure 1-1-7. HPLC profile of a radio-$Pt^{II}Cl_4^{2-}$ product on the radio-detector. (HPLC conditions: a Nucleosil SB anionic exchange column (Chemco Plus Scientific, Osaka, Japan); flow rate, 1.5 mL/min; eluent, perchlorate solution (CH_3CN/H_2O = 40/60 (v/v) containing 0.1 M $NaClO_4$ and 0.04 M $HClO_4$). Reference sample: $K_2Pt^{II}Cl_4$.)

The radionuclidic purity of the radio-$Pt^{II}Cl_4^{2-}$ product was evaluated with HPGe gamma-ray spectrometry. A previous study showed that the excitation functions for the ^{nat}Ir(p,xn)$^{188,\ 189,\ 191}$Pt nuclear reactions overlap with each other,[16] and therefore, ^{188,189}Pt were possible by-products for the production of ^{191}Pt. The radionuclidic purity was determined over 99% for the total Pt radionuclides, 81.7% ^{189}Pt, 17.6% ^{191}Pt, and 0.7% of ^{188}Pt, corrected to the EOB, while $^{190g,\ 192g}$Ir were below the detection limit, for the production with the mixed target. It is possible to reduce the amount of ^{189}Pt by introducing a cool-down period before target dissolution because the half-life of ^{189}Pt ($T_{1/2}$ = 10.87 h)

is shorter than that of ^{191}Pt ($T_{1/2}$ = 2.83 d), and the radionuclidic purity of ^{191}Pt was estimated to be 95% about 4 days after EOB. The other impurity of ^{188}Pt ($T_{1/2}$ = 10.2 d) can be removed by decreasing the initial proton beam energy to 26 MeV or less. However, the production rate of ^{191}Pt will also reduce in both methods. On the other hand, it is possible to obtain high radionuclidic purity of ^{191}Pt using a mono-isotopically enriched ^{193}Ir target with an optimal energy window of proton beam (30–15 MeV), based on each excitation function for the ^{nat}Ir(p,xn)$^{188, 189, 191}$Pt nuclear reactions (^{nat}Ir: ^{191}Ir, 37.3 atom%; ^{193}Ir, 62.7 atom%).[16] The enriched ^{193}Ir target seems to be the logical option for ^{191}Pt production with high radionuclidic purity. In an examination using an enriched ^{193}Ir coin target, pure ^{191}Pt was successfully produced as expected (gamma-ray spectrum was shown in **Fig. 1-1-8**, upper panel). Any other contaminants derived from the target vessel and foil were also below the detection limit in the final product.

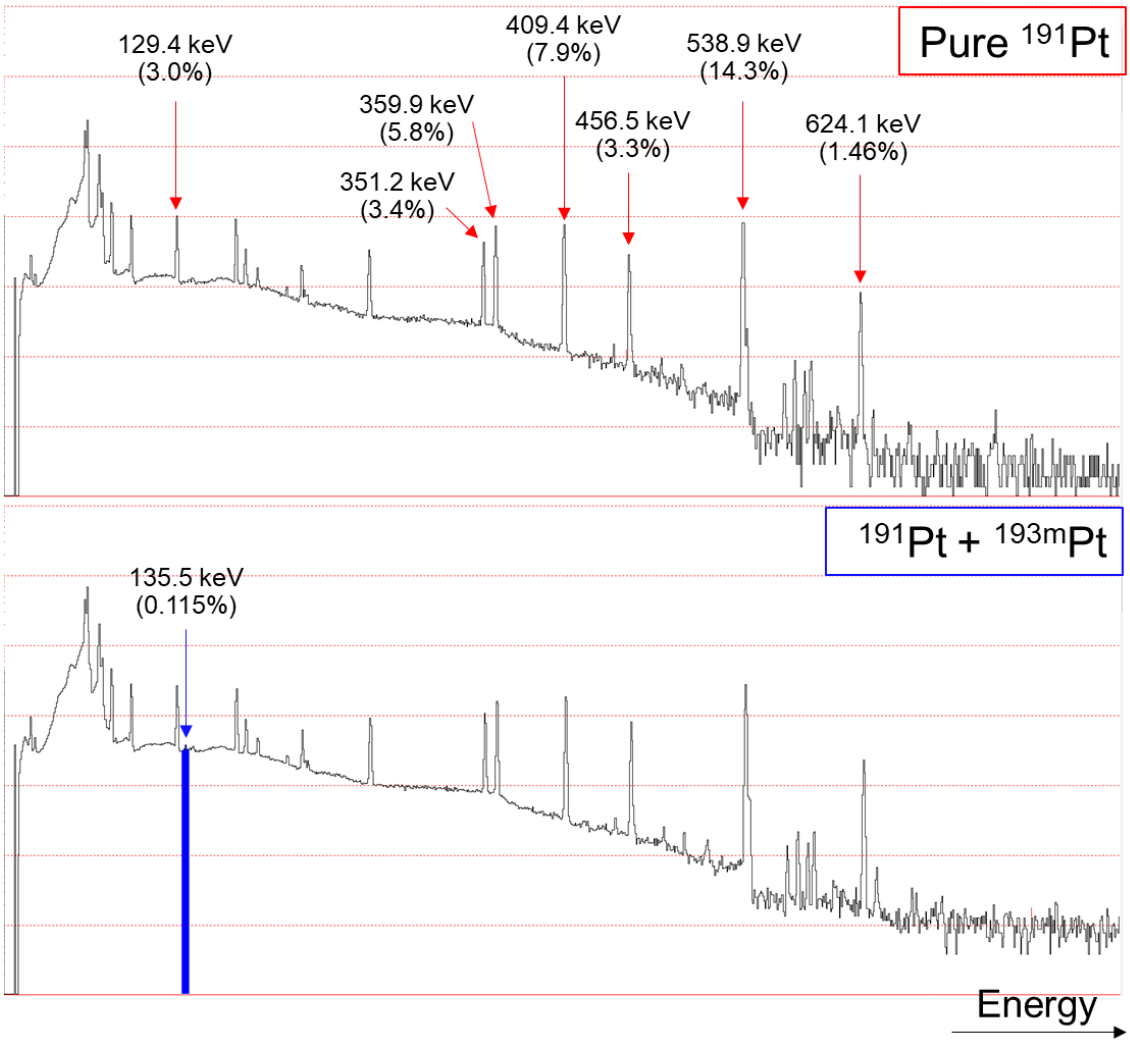

Figure 1-1-8. γ-ray spectrum of ^{191}Pt and ^{193m}Pt products (upper panel, pure ^{191}Pt; lower panel, mixed ^{191}Pt and ^{193m}Pt).

Production of mixed $^{191,\ 193m}$Pt by deuteron irradiation

Platinum-193m emits a 135.5 keV γ-ray with low intensity (0.0115%), which makes it extremely difficult to accurately measure its radioactivity before separation from the target material. After purification, HPGe spectrometry showed the presence of ^{193m}Pt along with co-produced ^{191}Pt (**Fig. 1-1-8**, lower panel). The radioactivity ratio of ^{191}Pt to ^{193m}Pt is around 1–2 at EOB, which was consistent with the theoretical yield.[12]

Due to the extensive melting of the Ir powder target during the deuteron irradiations, the Ir target did not dissolve completely. The radioactivity measurement was complicated due to the target state and the solid target shielding the radioactivity in combination with the physical properties of ^{193m}Pt. Hence, the production yield at EOB could not be measured.

Table 1-1-3. Irradiation conditions for ^{191}Pt/^{193m}Pt production and yield ratio of ^{191}Pt/^{193m}Pt.

Deuteron energy, Target	Facilities	^{191}Pt/^{193m}Pt (EOB, n = 1)
20 MeV, Ir powder	QST	1.25/1
15 MeV, Ir coin	DUMC	1.91/1
14 MeV, Ir coin	TUNL	1.86/1

2. Development of No-Carrier-Added Radio-cisplatin and Evaluation of its DNA-Damaging Efficacy as an Auger-electron emitting agent

Radio-synthesis of n.c.a. radio-cisplatin

The mixed $^{189, 191}$Pt were used in the following section, and the total radionuclidic purity of $^{189, 191}$Pt was 90–95%, containing small amounts of ^{188}Pt (described as radio-Pt). A one-pot radiosynthesis of n.c.a. radio-cisplatin from radio-$Pt^{II}Cl_4^{2-}$ in solution was developed (**Fig. 1-2-1**), and the product was purified by preparative HPLC. Pt(II) iodide species facilitate ligand exchanges that generate cis-trans isomers better than chloride species. The traditional synthetic scheme of cisplatin involves the conversion of K_2PtCl_4 to K_2PtI_4 prior to ligand-exchange reaction with NH_3.[18] Additionally, bulk cisplatin is commonly produced by inducing precipitation and crystallization in an aqueous solution.[18,19] However, this method is not applicable for n.c.a. radionuclides (pg–ng), and efforts are needed to streamline the synthesis to avoid losses. Therefore, n.c.a. radio-cisplatin was directly synthesized from radio-$Pt^{II}Cl_4^{2-}$ in solution and separated by HPLC, as shown in **Fig. 1-2-2**. The radio-cisplatin was detected at a retention time of 28–30 min, in good agreement with the nonradioactive cisplatin. The trans-isomer (transplatin) was not observed in this radiosynthesis (retention time: 47–49 min). The radiochemical yield (RCY) for radio-cisplatin was 5–15%.

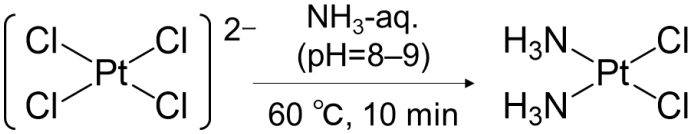

Figure 1-2-1. Scheme of the synthesis of radio-cisplatin.

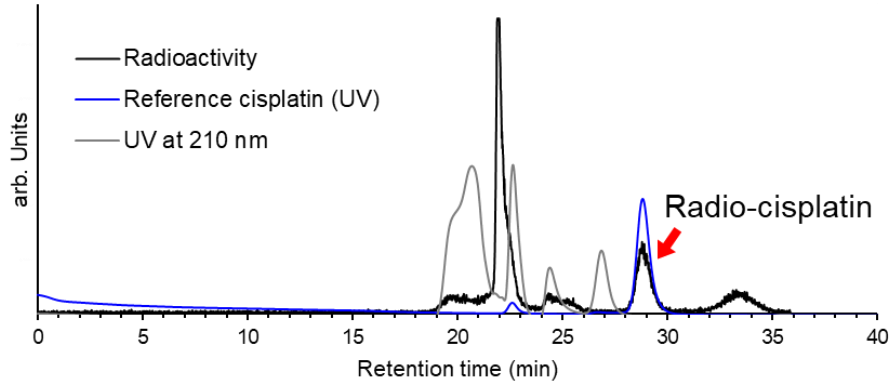

Figure 1-2-2. Radiochromatogram obtained during preparative HPLC. HPLC conditions: column,

OHpak SB-2004 (Shodex, Showa Denko, Tokyo, Japan); flow rate, 3.0 mL/min; eluent, physiological saline solution.

The low RCY of the n.c.a. radio-cisplatin partially resulted from a decrease in radio-$Pt^{II}Cl_4^{2-}$ purity during solvent evaporation, in addition to the low yield of the ligand-exchange reaction between Cl and NH_3. In HPLC analyses using an anion-exchange column, the peak intensity of radio-$Pt^{II}Cl_4^{2-}$ decreased over time, while an unknown peak (no interaction with the column) and the peak of radio-$Pt^{IV}Cl_6^{2-}$ grew. The purity of radio-$Pt^{II}Cl_4^{2-}$ was determined 60% or in some cases less in the concentrated solution after solvent evaporation, suggesting that the n.c.a. radio-$Pt^{II}Cl_4^{2-}$ was unstable during the process. Evidently, the RCY increased to 30–40% when the collected elution (1 M HCl and 0.5 M KCl) from the QMA column was used immediately without solvent evaporation.

Apart from that, the RCY of n.c.a. radio-cisplatin was less than 50% despite the relatively high purity of radio-$Pt^{II}Cl_4^{2-}$ in some cases. In the conventional synthetic method for bulk cisplatin, the synthetic yield was reported at ~60% when $K_2[Pt^{II}Cl_4]$ was treated directly with NH_3 at the ratio of two equivalents of NH_3 to Pt to prevent excess ligand exchange.[19,20] In this study, n.c.a. radio-$Pt^{II}Cl_4^{2-}$ was treated with an excess of NH_3, likely resulting in the low RCY. Nevertheless, it should be noted that heating was essential to promote the ligand exchange reaction between the n.c.a. radio-$Pt^{II}Cl_4^{2-}$ and excess NH_3. It was shown that without heating, ~50% of radio-$Pt^{II}Cl_4^{2-}$ remained at a pH of 9, indicating that both NH_3 and elevated temperature promoted ligand exchange for radio-Pt at nanomolar concentration. Although it is quite difficult to accurately control the stoichiometric balance of NH_3 and n.c.a. radio-$Pt^{II}Cl_4^{2-}$, the concentration of NH3 can be optimized to improve the RCY.

The radiochemical purity (RCP) and *in vitro* stability of radio-cisplatin were investigated by HPLC analyses. As shown in **Fig. 1-2-3(a1)**, a single peak of radio-cisplatin was observed with a retention time of 14–15 min. The RCP of n.c.a. radio-cisplatin was over 99% in the final product at the end of synthesis (EOS). In the sample with low radioactivity concentration shown in **Fig. 1-2-3(a1, 2)** (0.37 (^{189}Pt), 0.31 (^{191}Pt), and 0.01 (^{188}Pt) MBq/mL at EOS), radio-cisplatin exhibited good stability in the solution, and RCP was constant up to 15 h after EOS. In contrast, at a high radioactivity concentration shown in **Fig. 1-2-3(b1, 2)** (1.76 (^{189}Pt), 1.40 (^{191}Pt), and 0.05 (^{188}Pt) MBq/mL at EOS), radio-cisplatin decomposed as time passed. In this higher concentration, the RCP decreased to 84% (6 h) and 54% (24 h) after EOS. Nonradioactive transplatin was observed with a retention time of 22 min. Therefore, the decomposition product at 11–12 min of **Fig. 1-2-3(b1, 2)** was not transplatin, which was thermodynamically more stable than cisplatin. In summary, radio-cisplatin could decompose due to hydrolysis or ligand exchange followed by radiolysis induced by γ-ray, X-ray, and Auger electrons emitted from radio-Pt.

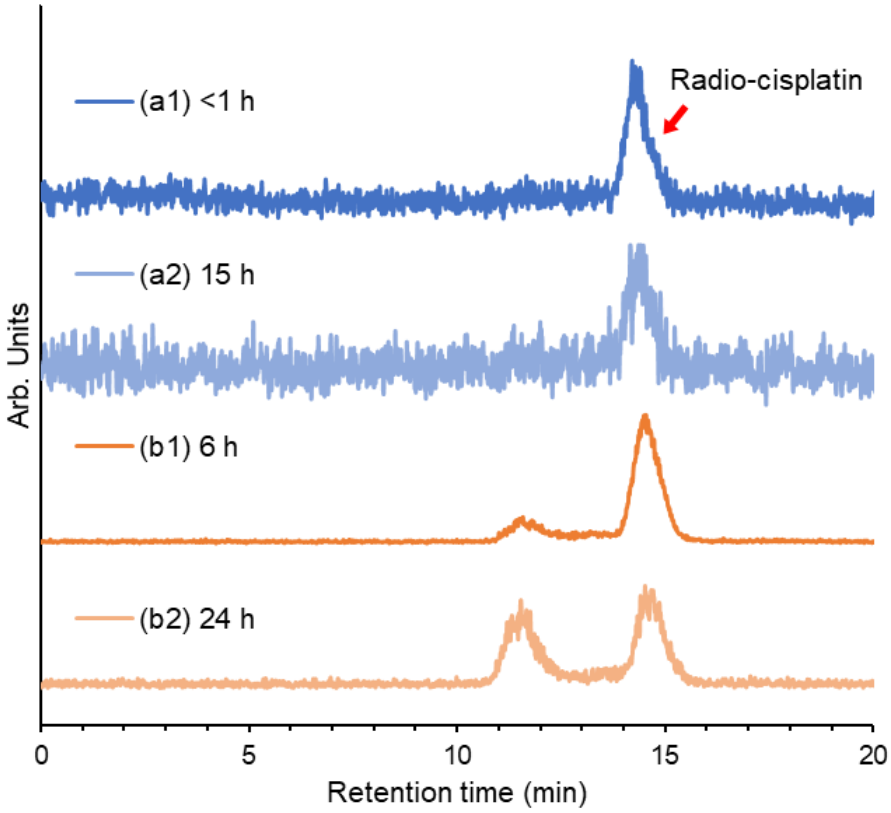

Figure 1-2-3. Radiochromatograms of a radio-cisplatin product (a) 0.37 (^{189}Pt), 0.31 (^{191}Pt), and 0.01 (^{188}Pt) MBq/mL at EOS, (b) 1.76 (^{189}Pt), 1.40 (^{191}Pt), and 0.05 (^{188}Pt) MBq/mL at EOS. HPLC conditions: column, OHpak SB-804 HQ (Shodex, Showa Denko, Tokyo, Japan); flow rate, 1.0 mL/min; eluent, saline solution.

In vitro property of n.c.a. radio-cisplatin

The *in vitro* behavior and distribution of n.c.a. radio-cisplatin (cellular uptake, intracellular distribution, and DNA binding) were evaluated. First, its cellular uptake in five different cell lines (H226, LN319, U87MG, H460, and U2OS) was investigated. The total uptake of n.c.a. radio-cisplatin was less than 1% of total radioactivity added to the cells after 1-d incubation in all cell lines mentioned above, likely due to the hydrophilic nature of cisplatin resulting in less penetration of the cell membrane.

Figure. 1-2-4 showed the cellular uptake in H226 and LN319 cells including seven-time points from 30 min to 25 h. The uptake in both cells increased over time, but the maximum uptake of n.c.a. radio-cisplatin was 0.56%ID in H226 and 0.57%ID in LN319 cells after 25-h incubation in FBS-free medium (**Fig. 1-2-4**). In the medium containing 10% FBS, the uptake rate of n.c.a. radio-cisplatin was similarly low, <1%ID, indicating that the addition of FBS had no significant effect on the uptake. In LN319 cells, the uptake of c.a. radio-cisplatin was 2-fold higher than the n.c.a. radio-cisplatin after

5-h incubation ($p < 0.0001$). In contrast, this was not observed in H226 cells where similar uptake was seen for both c.a. and n.c.a. agents (**Fig. 2-4**). It is speculated that the cellular uptake of radio-cisplatin is correlated to carrier concentration in some cell lines.

The uptake and its time dependency were similar between H226 and LN319 cells, but the carrier dependency was different. There are likely to be two pathways of cellular uptake of cisplatin: passive diffusion through the plasma membrane and active transport mediated by membrane proteins,[21] which supports the idea that the uptake of cisplatin is time- and dose-dependent and is proportional to the administered concentration of cisplatin.[22] In the present study, the time dependency was observed in both H226 and LN319 cells under the n.c.a. condition, but the concentration dependency differed somewhat between the two cell lines (**Fig. 1-2-4**). The cisplatin concentration was 70 pM for n.c.a. and 33 μM for c.a., a 10^6-fold difference. The higher uptake in LN319 cells under the c.a. condition was consistent with several studies.[22] The uptake in H226 cells, in contrast, did not differ significantly between the two conditions. Although the mechanism is unclear, differences in the activity of related active transporters, e.g., copper transporters and organic cation transporters, [23] may explain the differences in carrier dependency between the cell lines.

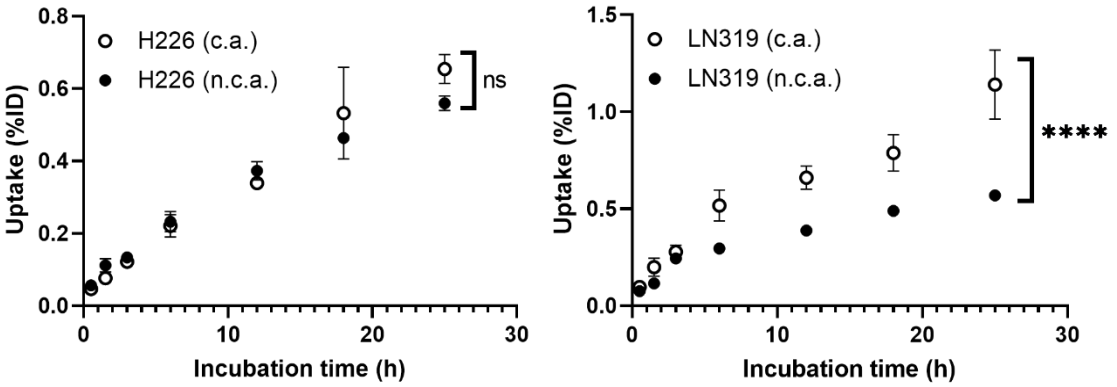

Figure 1-2-4. Cellular uptake of radio-cisplatin in H226 (left) and LN319 (right) cells. Data were expressed as the percentage of the incubated dose (%ID) ($n = 3$). Incubated dose: 31 kBq/^{189}Pt and 25 kBq/^{191}Pt of radio-cisplatin with 0 (n.c.a.) or 2.5 μg (c.a.) of nonradioactive cisplatin. ns: not significant, ****$p < 0.0001$. H226 (4×10^4 cells/well) and LN319 (1×10^5 cells/well) cells were seeded 1 day before the assay.

Second, to confirm that n.c.a. radio-cisplatin penetrates into nuclei and binds to DNA, the intracellular distribution and DNA-binding fraction of radio-cisplatin were evaluated. The intracellular distribution of radio-cisplatin was investigated by dividing cells into four subcellular fractions: F1, cytosolic; F2, membrane/organelle protein; F3, nuclear protein; F4, cytoskeletal fraction. **Figure 1-2-5** showed the intracellular distribution in LN319 cells, which were incubated continuously with radio-

cisplatin in FBS-medium without any medium change or washing. The F3 fraction was almost constant, containing about 20% of the total radio-Pt in the cells, indicating nuclear translocation of n.c.a. radio-cisplatin (**Fig. 1-2-5**). To determine to what extent radio-cisplatin in nuclei targets genomic DNA, genomic DNA was isolated from LN319 cells incubated with radio-Pt, and then measured its concentration and radioactivity. The DNA binding fraction of radio-Pt was 0.28 ± 0.02%ID/mg DNA. Based on the cellular uptake, ~0.4% of intracellular radio-cisplatin (2% of intra-nucleus radio-cisplatin) was estimated to bind to DNA.

The intra-nuclear fraction of 20% was consistent with an experiment by Groessl *et al*. (**Fig. 1-2-5**).[24] Another study reported that approximately 1% of intracellular Pt bound to DNA, which was a little higher than but still consistent with the present result (0.4%).[25] Thus, the intra-nuclear and binding fractions of n.c.a. radio-cisplatin were almost the same as those for c.a., as reported by other researchers, while the n.c.a. dose level (pM) was 10^6-fold lower than the standard c.a. level (μM). The results suggested that both reaction rates of translocation to nuclei and binding to DNA were independent of Pt concentration.

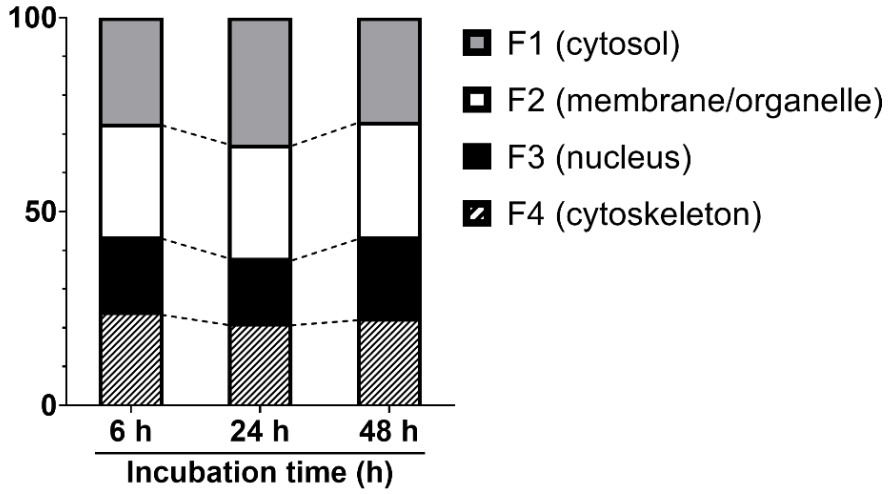

Figure 1-2-5. Intracellular distribution of radio-cisplatin in LN319 cells after incubation for 6–48 h in medium containing FBS. F1, cytosolic fraction; F2, membrane/organelle protein fraction; F3: nucleic protein fraction; F4: cytoskeletal fraction.

Based on the intracellular distribution and DNA binding fraction, the number of radio-cisplatin per cell was roughly estimated assuming homogeneous uptake in individual cells: uptake of 0.1%ID of radio-cisplatin, intranuclear localization of 0.02%ID (20% of intracellular radio-cisplatin), and DNA binding of 0.0004%ID (2% of intra-nucleus radio-cisplatin) (**Table 1-2-1**). When 3.5×10^{10} (1×10^5 Bq) of [^{191}Pt]cisplatin was added to 2×10^5 cells (1.75×10^5/cell), 175 [^{191}Pt]cisplatin molecules were estimated to be in each cell, 35 in each nucleus, and one bound to DNA (**Table 1-2-1**). Thus, the

estimated number of Pt per cell, few Pt atoms bound to DNA in each cell. This number was obtained by assuming equal uptake in individual cells, as a single-cell ICP-MS of nonradioactive cisplatin previously observed almost identical uptake of the standard dose of cisplatin, i.e., cellular uptake of cisplatin was independent of the cell cycle.[26]

Table 1-2-1. Estimated distribution of [^{191}Pt]cisplatin in 2×10^5 LN319 cells.

Fraction of ^{191}Pt (%ID)		[^{191}Pt]cisplatin *	
		Number per cell	Radioactivity (Bq) per cell
Cell	0.1*	175	5×10^{-4}
Nucleus	0.02	35	1×10^{-4}
DNA	0.0004	1	2×10^{-6}

Uptake at 3 h after incubation. ID: incubated dose = 1×10^5 Bq.

In the cell proliferation assay (SRB cell proliferation assay and Live/Dead cell staining assay) as shown in **Tables 1-2-2 and 1-2-3**, no cytotoxicity of n.c.a. radio-cisplatin was observed in either assay; there was no statistically significant difference between saline, nonradioactive cisplatin (1 ng), and radio-cisplatin. These results would be due to almost all radio-Pt decaying without binding to DNA (**Table 1-2-1**). Meanwhile, a few studies reported that the cytotoxicity of c.a. [^{191}Pt]cisplatin containing much more nonradioactive carrier (> μg) was greater than that of nonradioactive cisplatin alone,[4] whereas nonradioactive cisplatin could decrease cell survival significantly. Taken together with a low cytotoxic effect of n.c.a. radio-cisplatin alone in the present result, it was suggested that the cytotoxicity of c.a. [^{191}Pt]cisplatin was mainly due to chemical damage by nonradioactive cisplatin. Due to the small DNA-binding fraction of n.c.a. radio-cisplatin, n.c.a. radio-cisplatin had only a small effect on cell survival.

Table 1-2-2. Cell proliferation SRB assay for H226 and LN319 cells.

Treatment	Survival (%)*	
	H226	LN319
Saline	100 ± 7	100 ± 11
Cisplatin		
1 ng (17 nM)	100 ± 9	95 ± 14
1 μg (17 μM)	63 ± 7	48 ± 8
Radio-cisplatin		
^{189}Pt, 58 kBq; ^{191}Pt, 34 kBq	113 ± 18	92 ± 4
^{189}Pt, 120 kBq; ^{191}Pt, 70 kBq	91 ± 15	87 ± 13

* Survival was expressed as means ± SD (n = 6). There was no statistically significant difference.

Table 1-2-3. Fluorescence intensity in live/dead viability/cytotoxicity assay for LN319 cells.

Treatment	Live*	Dead*	D/L ratio
Saline	900	6.77	1.00
Cisplatin 2.5 ng (11 nM)	862	6.94	1.07
Radio-cisplatin ^{189}Pt, 75 kBq; ^{191}Pt, 50 kBq	829	7.27	1.17

* Fluorescence intensity (arbitrary units: a.u.).

Evaluation of the DNA-damaging efficacy of n.c.a. radio-cisplatin with immunofluorescence staining for γH2AX and gel electrophoresis of plasmid DNA

An immunohistostaining assay of γH2AX as a reporter of DSBs was conducted to evaluate the DNA damage induced by Auger electrons released very close to DNA. In addition, to assess direct DNA damage by Auger electrons, DNA damage analysis was performed by gel electrophoresis of plasmid DNA.

Immunofluorescence assay for γH2AX was conducted in LN319 cells treated with n.c.a. radio-cisplatin (1200 kBq, ^{189}Pt; 600 kBq, ^{191}Pt), saline (untreated control), or nonradioactive cisplatin (7.5 ng) to compare with the chemical damage of cisplatin. Representative microphotographs were shown in **Fig. 1-2-6**, and quantitative analysis was shown in **Fig. 1-2-7**. An increase in γH2AX signals was observed in nuclei treated with n.c.a. radio-cisplatin compared with those treated with saline or nonradioactive cisplatin (**Fig. 1-2-6**). Quantitative analysis of images exhibited more γH2AX-positive nuclei (**Fig. 1-2-7**, left) and 2-fold greater relative γH2AX intensity (**Fig. 1-2-7**, right) on average in cells treated with radio-cisplatin than those in the other groups. Although the difference was not statistically significant, radio-cisplatin tended to induce more γH2AX foci with greater fluorescence intensity than saline or nonradioactive cisplatin. To perform image analysis of DSBs induced by Auger electrons, high-resolution two-dimensional (2D) and three-dimensional (3D) images were obtained with a 100× objective lens (**Fig. 1-2-8**). The 2D images indicated γH2AX aggregation in nuclei treated with radio-cisplatin (**Fig. 1-2-8**, upper and middle panels), and the 3D images revealed their spatial dispersion (**Fig. 1-2-8**, lower panels). These γH2AX aggregates with high fluorescence intensity corresponded to the quantitative results described above.

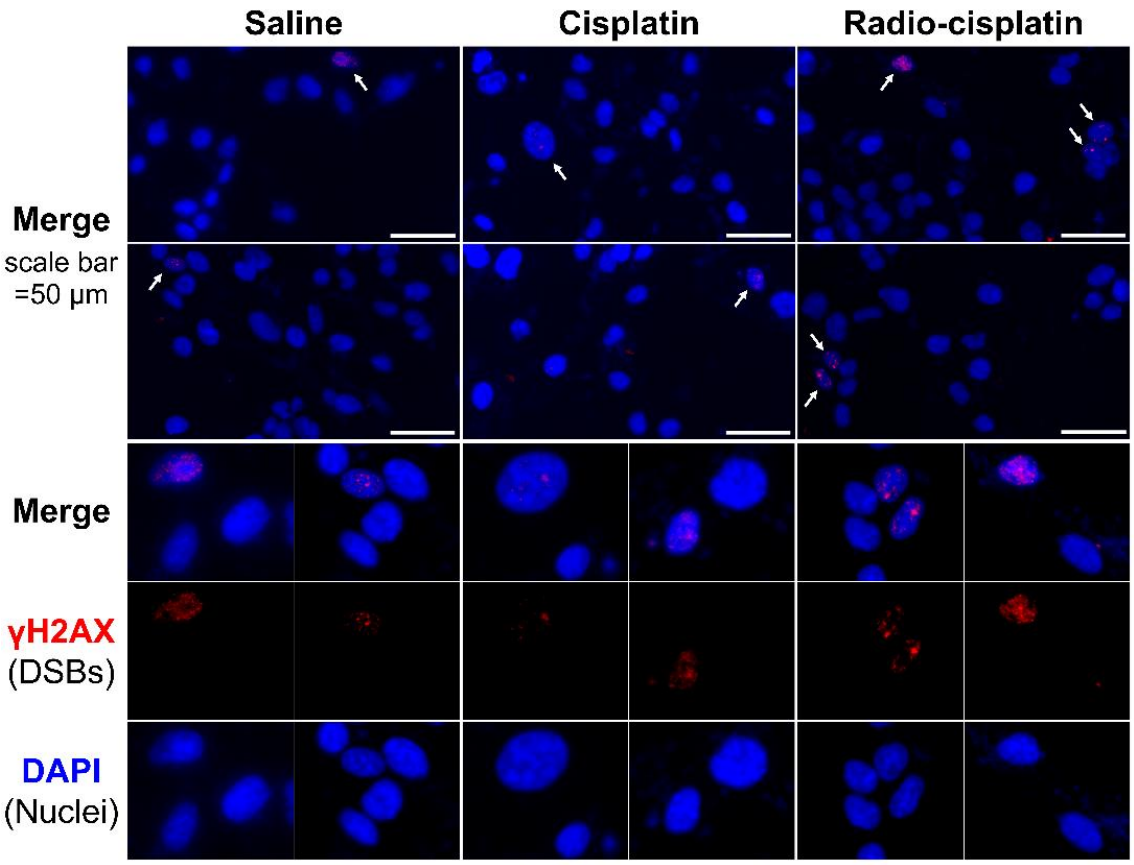

Figure 1-2-6. Representative microphotographs of γH2AX staining in LN319 cells treated with saline, nonradioactive cisplatin (7.5 ng), and n.c.a. radio-cisplatin (1200 kBq, ^{189}Pt; 600 kBq, ^{191}Pt). Cell nuclei were indicated in blue and γH2AX foci in red. Cells (4×10^5 /well) were seeded 1 day before the assay. Objective lens: 40×.

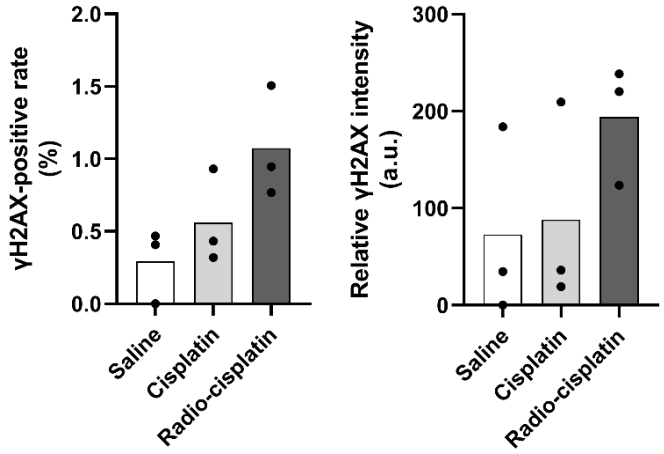

Figure 1-2-7. The fraction of LN319 cells with γH2AX-positive nuclei (left). Relative γH2AX intensity was expressed as the ratio of the total fluorescence intensity of γH2AX in the nuclei to all

nuclei counts (right). Data were obtained from three different images, including 199–274 nuclei per image, and expressed as means ± SD (n = 3). No significant difference was observed.

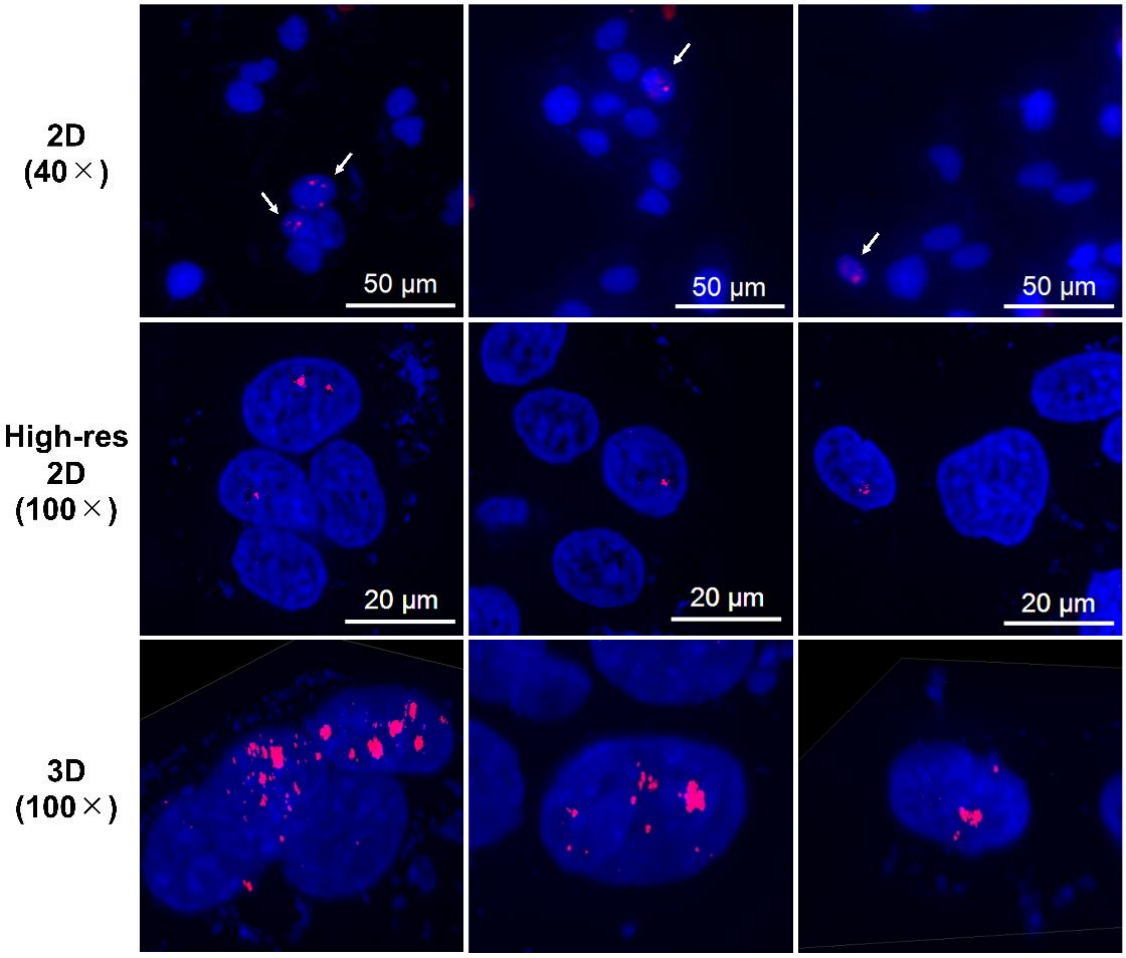

Figure 1-2-8. Representative high-resolution 2D and Z-stacked 3D images of cells with strong γH2AX foci (aggregations), observed in samples treated with n.c.a. radio-cisplatin. γH2AX-positive nuclei were indicated by arrows in the upper panels, and high-resolution 2D and 3D images were shown in the middle and lower panels.

To explore the possibility that the observed DSBs in the γH2AX assay were directly induced by Auger electrons, gel electrophoresis of plasmid DNA treated with radio-cisplatin was conducted (**Fig. 1-2-9**). The original plasmid that was purchased, included circular and supercoiled forms, and the purified plasmid was only supercoiled. The restriction enzyme *Hin*dIII cuts one site in the plasmid, yielding the linear form. Dimethyl sulfoxide (DMSO) was used as an OH-radical scavenger to determine the effect of radicals. Treatment with radio-cisplatin generated circular and linear forms (**Fig. 1-2-9**, lane 5). The formation of the circular form was inhibited by DMSO (**Fig. 1-2-9**, lane 8).

Radio-HPLC analysis of plasmid and autoradiography of the gel revealed almost no DNA binding to n.c.a. [^{191}Pt]cisplatin on day 1. Due to the slow binding between Pt and DNA, it was likely that most of the DNA damage was due to radicals induced by radio-Pt, and the band corresponding to the circular plasmid (indirect DNA damage) was observed. Meanwhile, the band corresponding to the linear plasmid (direct DNA damage) was observed at the same intensity ratio both in the presence and absence of DMSO (**Fig. 1-2-9**, lanes 5 and 8), suggesting that radio-cisplatin also caused direct plasmid breakage, possibly by Auger electrons released from radio-Pt binding to DNA.

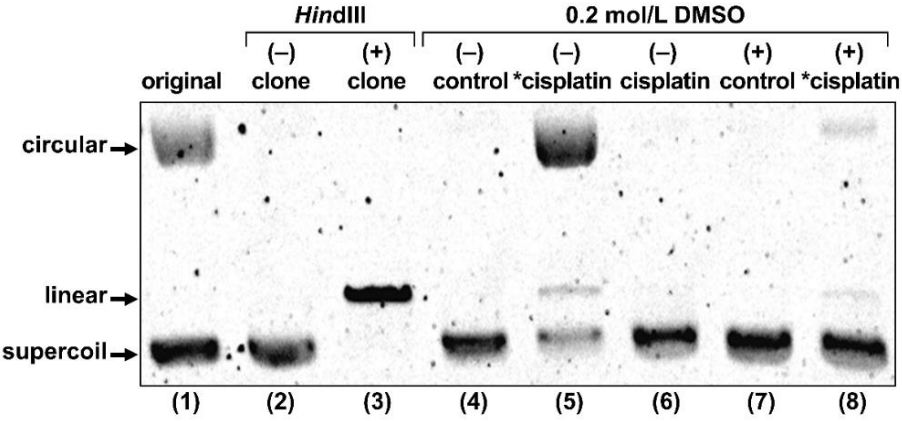

Figure 1-2-9. Gel electrophoresis of plasmid treated with no agent (control), radio-cisplatin (*cisplatin), or nonradioactive cisplatin (cisplatin). "original" refers to plasmid as purchased from the company. "Clone" refers to the plasmid purified after cultivation of the original clone. Each lane was loaded with 50 ng of plasmid in 10 μL of buffer.

Evaluation of the DNA-damaging efficacy of n.c.a. radio-cisplatin using time-lapse imaging of U2RDP-LE53-21 cells

As mentioned above, the low cellular uptake and the small DNA-binding fraction of n.c.a. radio-cisplatin made it difficult to precisely evaluate the cellular and DNA damage in a mass of cells. In order to clarify the low-probability DNA damage, it is necessary to analyze individual cells over time. Furthermore, γH2AX-positive cells were evidently observed as neighboring cells in the immunofluorescence staining (**Fig. 1-2-6 and 1-2-8**). Neighboring cells were supposed to have been in the postmitotic state, suggesting that radio-cisplatin-induced DSBs were related to the cell cycle. This is most likely because of the cell-cycle–dependent variation of the DNA repair capacity. However, the previous static analysis of immunofluorescence staining provided only the featured data at one non-consecutive time point and could not directly support this hypothesis. Therefore, to quantitatively

evaluate DSBs for individual cells and determine the relevance of DSBs and the cell cycle in the treatment with radio-cisplatin, a dynamic evaluation of DNA damage and the cell cycle was conducted using time-lapse imaging analysis. For the real-time detection of DNA damage and the cell cycle, the present study used the U2OS-derived cancer cell line U2RDP-LE53-21 expressing two different fluorescent proteins: a green fluorescent protein fused with tumor-suppressor p53 binding protein 1 (53BP1), which was a response factor of DSBs, and a red fluorescent protein fused with proliferating cell nuclear antigen (PCNA), which was an important DNA clamp involved in DNA replication. A systematic evaluation of huge microscopy images was performed using an analysis system based on the ImageJ software and deep learning, where deep learning-based segmentation enabled each nucleus with different fluorescent intensities to be extracted simultaneously from the images. Here, the numbers of 53BP1 and PCNA foci, and the cell cycle were evaluated over time for each nucleus treated with n.c.a. radio-cisplatin or a control agent (radio-cisplatin, 134 nuclei; saline, 133 nuclei; nonradioactive cisplatin, 95 nuclei). They were summarized and discussed in the following subsections: (a) the change in 53BP1 foci over time corresponding to the cell cycle and (b) the length of the cell-cycle phase, comparing those between treatments. The methodological details and representative images were described in the *experimental section*.

(a) Radio-cisplatin promoted DSBs induction, especially around the G1→S phase transition

To evaluate the DNA-damaging efficacy of n.c.a. radio-cisplatin, the DNA-repairing protein 53BP1, which could be recruited to the sites of DSBs, was used.[27] The number of 53BP1 foci was counted for each nucleus and summarized for each cell-cycle phase. Because the starting phase of the cell cycle differed for each nucleus in the imaging timeline, the data were separated by each cell-cycle phase and the number of 53BP1 foci was evaluated. **Figure 1-2-10(a)** showed the average number of 53BP1 foci before and after each phase transition of the cell cycle. For the control nuclei, approximately 0–10 foci of 53BP1 were present as a background in the G1, G2, and M phases. The dark background in these phases clarified the observed change in small foci numbers per nucleus. However, DNA damage, including DSBs, appeared naturally in the S phase of DNA synthesis, leading to an increase in the number of 53BP1 foci to ~20 over time in the control treatment with saline or nonradioactive cisplatin.

The systematic results indicated an increase in 53BP1 foci in the treatment of radio-cisplatin compared with the controls at the middle-to-late G1 phase and around the G1→S phase transition (**Fig. 1-2-10(a)**, upper panels). Statistical analysis was conducted by dividing every 10 hours of the period of the G1→S phase transition (G1(a), −20 → −10.25 hr; G1(b), −10 → −0.25 hr; S(a), 0 → 9.75 hr; S(b), 10 → 19.75 hr; S(c), 20 → 29.75 hr), which showed a significant difference in the period in the G1(a), G1(b), and S(a) between the radio-cisplatin and the controls. Ten hours after the G1→S phase transition, the radio-cisplatin treatment caused a decrease in the 53BP1 foci, which was not observed

for the other treatments. Additionally, some nuclei with numerous foci were observed in the radio-cisplatin treatment in the G2 phase, resulting in a wide range, while the 53BP1 foci were approximately consistent under the background level over time in the G2 phase of the controls. The average number of PCNA foci before and after each phase transition of the cell cycle was also shown in **Fig. 1-2-10(b)**; the results of the three treatments were similar. From the middle-to-late S phase (**Fig. 1-2-10(b)**, upper panels) after the G1→S phase transition, PCNA foci in the cells treated with radio-cisplatin decreased compared with those in the cells subjected to control treatments.

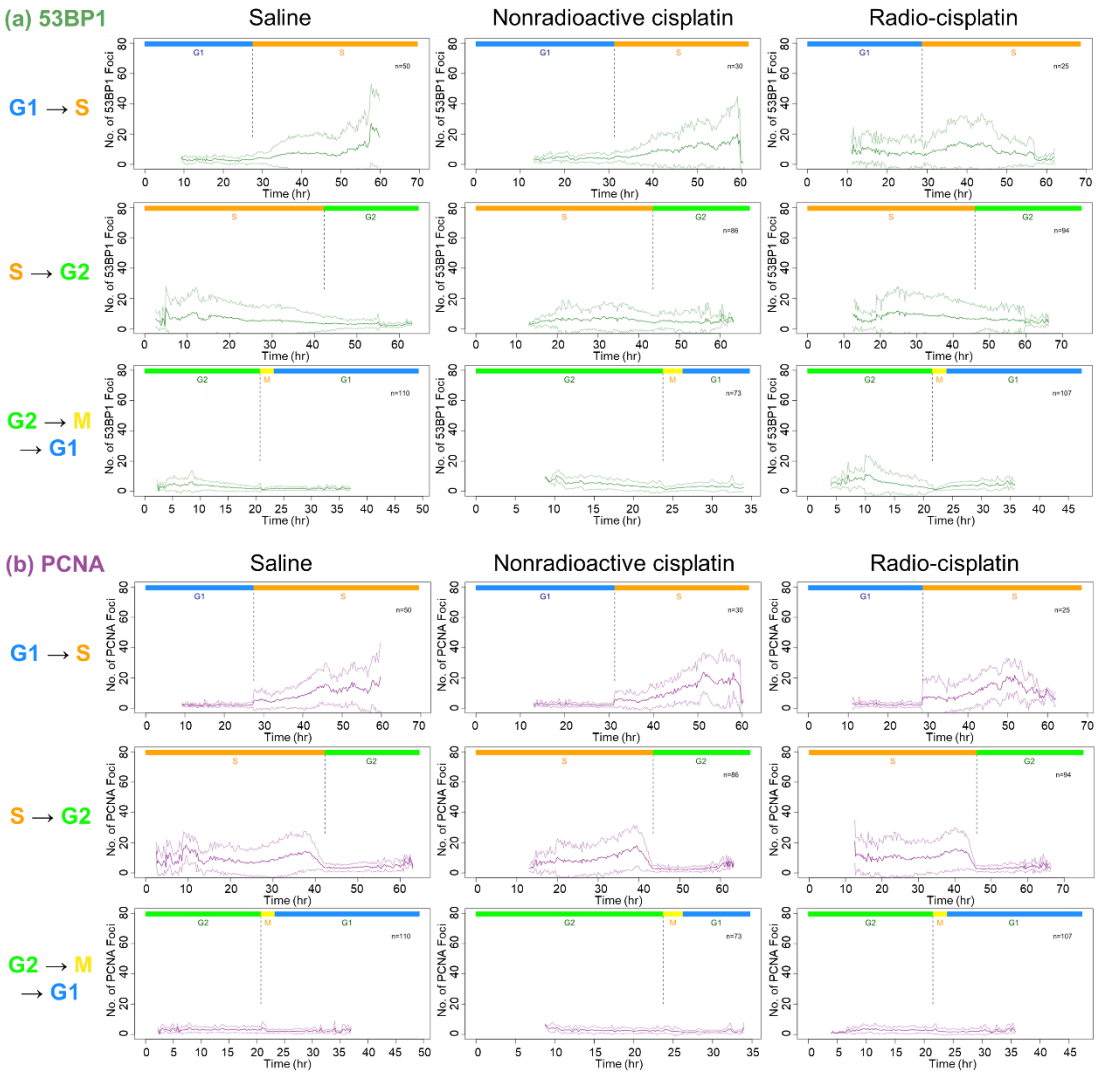

Figure 1-2-10. The numbers of (a) 53BP1 foci and (b) PCNA foci per nucleus before and after the phase transition of the cell cycle in the treatment with saline, nonradioactive cisplatin (0.5 ng), and n.c.a. radio-cisplatin (886 kBq, ^{189}Pt; 759 kBq, ^{191}Pt). The middle line was the mean; the upper and lower lines were the standard deviation (SD). Each mean was calculated for the case of $n \geq 4$; when $n < 4$, the result was treated as a missing data point.

Only the data for each phase of the cell cycle were extracted from all the raw data on the 53BP1 foci number and plotted under the same imaging timeline in **Fig. 1-2-11**, where the starting/ending time of the phase of each nucleus was different during the imaging time course. When the whole trend of each phase of the cell cycle was considered, the radio-cisplatin treatment increased the 53BP1 foci in the G1 phase, whereas the 53BP1 foci in the controls were only a few foci observed as a background. In contrast, the background foci of 53BP1 in the S phase were low-contrast and no difference was observed among the treatments. In addition, no obvious increase in the 53BP1 foci was observed in the G2 phase after the radio-cisplatin treatment.

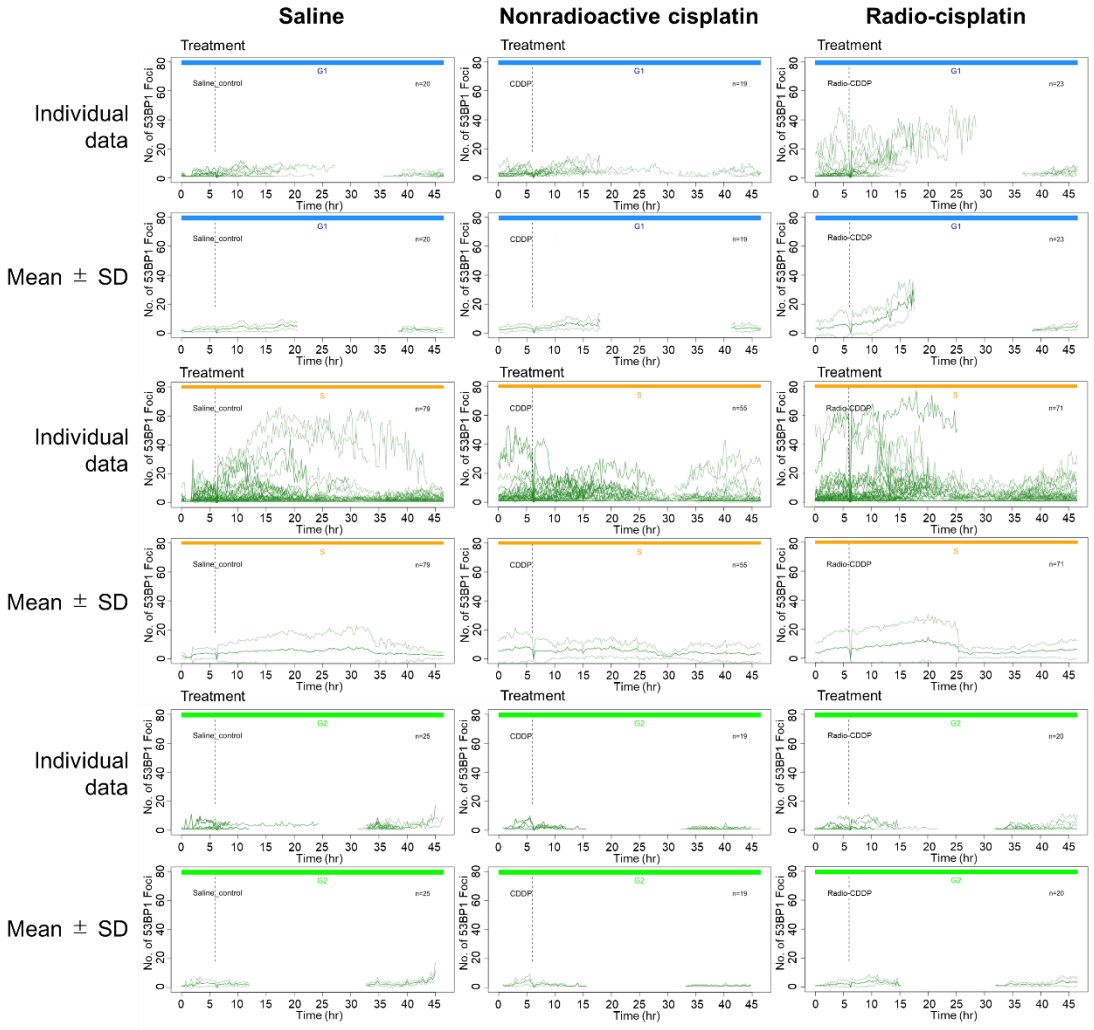

Figure 1-2-11. The number of 53BP1 foci per nucleus for each phase of the cell cycle under the same imaging timeline. Each mean was calculated in the case of $n \geq 4$; when $n < 4$, the result was treated as a missing data point.

(b) Radio-cisplatin influenced DNA synthesis and delayed the cell cycle in the late time points

The cell cycle of all nuclei was summarized in **Fig. 1-2-12**. For all the treatments, 1–2 nuclei without cell division were observed and their cell-cycle phase of G1 or G2 was not judged (**Fig. 1-2-12**; G1/G2). Little cell death was observed after the treatments with saline, nonradioactive cisplatin, and radio-cisplatin. A few nuclei were not able to be tracked in the middle of imaging because of huge migration and flame out. The average length of each phase of the cell cycle was shown in **Fig. 1-2-13**, which represents only the data with the full cell-cycle phase.

The average length of each cell cycle tended to decrease slightly over time. Although there were not any specific causes for this effect, poor performance of the simple incubating container and sustained fluorescent exposure might have affected the cell cycle. The length of each phase in the first cell cycle was similar among the three treatments, and there was no significant difference. In the second to third cell cycle (i.e., the late imaging points), the length of the G1 and G2 phases was longer in the treatment of radio-cisplatin than in the control treatments (**Fig. 1-2-13**). A significant difference was observed, suggesting that radio-cisplatin affected the progress of the cell cycle.

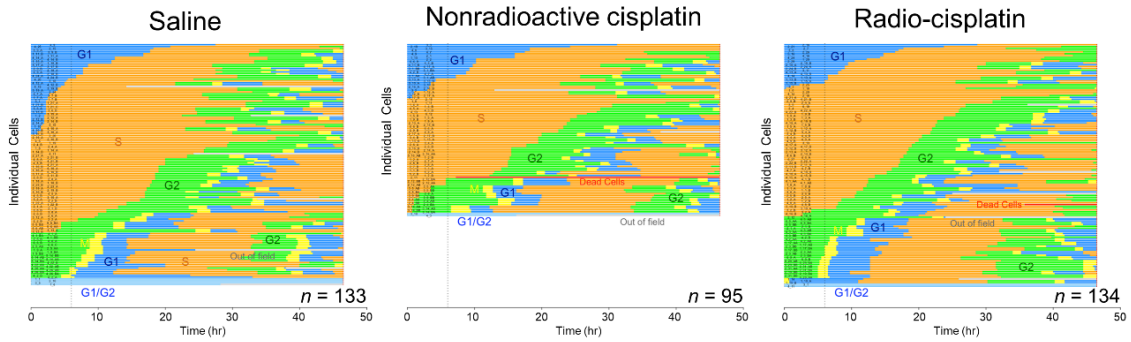

Figure 1-2-12. Summary of the cell-cycle profile for each cell.

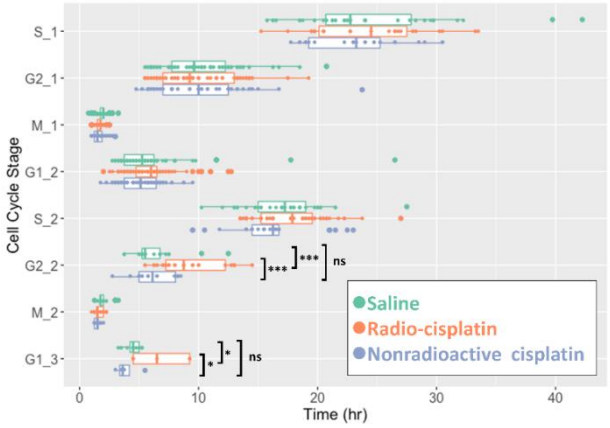

Figure 1-2-13. The length of the cell-cycle phase. Data were expressed as the mean ± standard deviation. Each dot indicates a value of a nucleus. *$p < 0.05$, **$p < 0.01$, ***$p < 0.001$.

A comprehensive discussion on the DNA-damaging effect induced by Auger electrons from n.c.a. radio-cisplatin

First, γH2AX staining revealed DNA damage induced by Auger electrons from n.c.a. radio-cisplatin that bound to DNA directly, with a negligible chemical effect. Representative microphotographs of γH2AX staining and its quantitative analysis found more γH2AX foci with stronger fluorescence in nuclei treated with n.c.a. radio-cisplatin than in those treated with saline or nonradioactive cisplatin (**Figs. 1-2-6 and 1-2-7**), indicating that n.c.a. radio-cisplatin induced more DSBs in nuclei. It was reported that more cisplatin induced more DSBs at microgram doses,[28] whereas no increase in γH2AX intensity was observed in cells treated with nonradioactive cisplatin (25 pmol), which was 100-fold higher than n.c.a. radio-cisplatin (0.46 pmol) in the present result. Therefore, it was suggested that most DSBs in cells treated with n.c.a. radio-cisplatin would be due to the effects of radiation, rather than the chemical effects as Pt.

High-resolution 2D and 3D images revealed local aggregation of γH2AX in the nucleus (**Fig. 1-2-8**). These highly fluorescent γH2AX aggregates were specifically observed in cells treated with n.c.a. radio-cisplatin, which likely corresponds to DSBs induced by Auger electrons released very close to DNA. Gel electrophoresis of the plasmids also supports the idea that DSBs were formed directly by radio-cisplatin, as DNA breakage was observed at the same level in the presence and absence of OH scavenger (**Fig. 1-2-9**). On the other hand, there was a low probability of direct plasmid breakage and a high probability of indirect damage (**Fig. 1-2-9**). Auger electrons are expected to directly induce DNA damage when released close to DNA. The low probability would be due to slow binding to the plasmid, causing Auger electrons to be emitted prior to DNA binding. Covalent binding between Pt and DNA would be unlikely to proceed efficiently due to the very low concentration of both plasmid and n.c.a. radio-cisplatin (1–3 fmol/μL). Due to the low rate of covalent binding, the amount of direct DNA breakage by n.c.a. radio-cisplatin would be small.

The frequency of γH2AX positivity *in vitro* was also low, at most 1% of all nuclei (**Fig. 1-2-7**). Meanwhile, this low probability of the γH2AX-positive nuclei was reasonable considering the amount of radio-Pt binding to DNA, as expected from the low DNA binding rate (0.0004%ID) (**Table 1-2-1**). According to this calculation, in 1×10^6 nuclei, 7×10^4 atoms of radio-Pt were expected to decay while bound to DNA, i.e., the proportion of nuclei with one radio-Pt decay in DNA was 7%. Therefore, this estimation suggests that only a small amount of radio-Pt binding to DNA can induce the formation of DSBs.

Second, the time-lapse imaging and its quantitative image analysis with deep learning enabled a sequential and quantitative investigation of such low-probability DNA damage by Auger electrons released from n.c.a. radio-cisplatin for individual cells with respect to the cell cycle.

Systematic image analysis revealed that n.c.a. radio-cisplatin induced more DSBs depending on the cell cycle compared with nonradioactive controls (**Figs. 1-2-10(a) and 1-2-11**). From the middle-to-late G1 phases, around the phase transition of G1 to S, and in the middle G2 phase, 53BP1 foci increased in cells treated with n.c.a. radio-cisplatin. N.c.a. radio-cisplatin efficiently caused DSBs in cells, especially in the G1 phase. The late G1 phase exhibits high sensitivity to radiation.[29] Similar to radiation, unlabeled cisplatin is also more cytotoxic to cells in the G1 phase than to cells in the other phases even though its action mechanism is not cell-cycle specific.[30] Taken together, the high sensitivity of the G1 phase to radio-cisplatin is reasonable. The DNA repair in cells in the G1 phase might be error-prone to radio-cisplatin-induced damage. 53BP1 recruited to DSBs in the G1 phase could be retained for the extended phase, leading to the observed increase in 53BP1 foci. Thus, such a different sensitivity to DNA damage in each cell cycle would explain the correlation between radio-cisplatin-induced damage and the cell cycle.

An unexpected decrease in 53BP1 foci by the radio-cisplatin treatment was observed in the middle S phase while an increase in 53BP1 foci was observed in the controls because of natural DNA strand break during progressive DNA replication in the S phase (**Fig. 1-2-10(a)**). Because a decrease in PCNA foci was observed to correspond with a decrease in 53PB1 foci, the DNA replication might be inhibited by damage caused by radio-cisplatin in the S phase, resulting in a low background of 53BP1 foci because of a decrease in natural DSBs. Moreover, the S phase is generally resistant to DNA-damaging radiation and drugs because of homologous recombination repair. The late S phase is particularly well known to express radiation resistance.[29] The DNA-repairing system in the S phase might have been activated in cells treated with radio-cisplatin and might have repaired 53BP1-recruited DSBs efficiently.

Regarding the cell cycle, radio-cisplatin extended the length of the cell-cycle period in the second G2 and third G1 phases after radio-cisplatin was added (**Fig. 1-2-13**). In the first cell-cycle phases, no obvious effect of accelerating or delaying the progress of the cell cycle was observed. In general, radiation damage tends to occur after several cell divisions post-radiation exposure (i.e., reproductive cell death).[31] Taken together with a continuous cisplatin uptake over time in tumor cells,[22] the delayed effect on the cell cycle is reasonable. The lack of a difference in the second S phase suggests that the G1 and G2 phases might be more sensitive than the S phase to radio-cisplatin. This assumption could be clarified by evaluating the cell cycle at later time points after 2 days. Continuous imaging for several days is necessary to introduce a medium reflux system and to reduce the phototoxicity of the image-capture process toward the current system.

Collectively, γH2AX staining and 53BP1 imaging successfully evaluated the small amount of DNA damage induced by Auger electrons released from n.c.a. radio-cisplatin with the minimum chemical effect of nonradioactive Pt. These methods indicated DSBs induced by Auger electrons from n.c.a. radio-cisplatin. Unfortunately, due to its low cellular uptake, only a small fraction of radio-

cisplatin bound to DNA, leading to a low probability of DSBs. To reveal the ideal potential of Auger electrons, it is necessary to modify radio-Pt with proper targeting modules for increasing the fraction of radio-Pt bound to DNA and inducing DNA damage by Auger electrons efficiently.

In vivo property of n.c.a. radio-cisplatin

Chemical analysis methods (HPLC, atomic absorption analysis, or ICP-MS) are common for the evaluation of the pharmacokinetics of Pt drugs, but they require at least nanogram quantities of Pt for precise quantification.[32] Because of this limitation in precisely quantifying small amounts of Pt, these studies have mainly focused on blood or urine retention in the case of high injection doses for humans.[32] The biodistribution data, especially in the case of long-term tracing or low-uptake tissue retention, are rare.[33] This suggests that a comprehensive biodistribution assay using radio-Pt will contribute to the further development of Pt-based drugs, particularly regarding their *in vivo* characteristics. Herein, the quantitative pharmacokinetics of cisplatin was evaluated for 7 d after the intravenous injection of the radio-cisplatin tracer in a xenograft mouse model bearing subcutaneous tumors. A lung cancer cell line, H460, was used in this study since cisplatin is commonly used as a chemotherapy agent for lung cancer.[34] The preliminary experiment showed that the pharmacokinetics was almost the same for n.c.a. and c.a. radio-cisplatin. To compare with the reference data conducted previously by other researchers,[33] nonradioactive carriers were mixed with a solution of radio-cisplatin and then injected into mice (2 mg cisplatin/kg BW) in this work.

The retention of cisplatin in the whole body and blood was investigated, as shown in **Fig. 1-2-14**, where data were shown as %ID for the whole body (**Fig. 1-2-14**, left) and %ID per gram for blood (**Fig. 1-2-14**, right). These results showed rapid clearance of cisplatin from the whole body and blood, consistent with the biphasic exponential curve including the alpha and beta phases (**Fig. 1-2-14**: alpha, white; beta, black). Cisplatin in the whole body was excreted quickly to ~24% of the injected dose within 19 h after injection, corresponding to the alpha phase of the retention curve (**Fig. 1-2-14**, left, white). After that, cisplatin was cleared slowly during the beta phase, and ~10% of the injected dose remained in the body 7 d after injection (**Fig. 1-2-14**, left, black). The blood concentration also decreased mainly within 19 h after injection, which corresponds to the alpha phase of the retention curve (**Fig. 1-2-14**, right, white). Although the blood concentration was ~1%ID/g in the beta-phase of the retention curve, the radiotracer enabled a quantitative evaluation (**Fig. 1-2-14**, right, black). Thus, a biphasic retention curve in the whole body and blood was observed, and the biological half-life was calculated to be $T_{1/2}(\alpha)$ = 1.14 h and $T_{1/2}(\beta)$ = 5.33 d for the whole body and $T_{1/2}(\alpha)$ = 23.9 min and $T_{1/2}(\beta)$ = 4.72 d for blood (**Fig. 1-2-14**). This half-life in the blood was acceptably consistent with the results of several studies.[33]

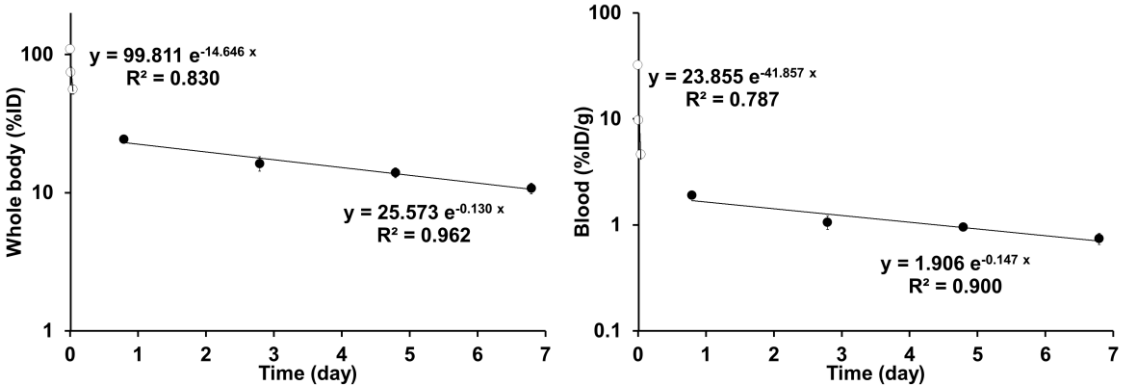

Figure 1-2-14. Percentage of the injected dose for the whole body (left, %ID) and percentage of the injected dose per gram of blood (right, %ID/g), corrected to those with a body weight (BW) of 20 g. Mice were intravenously injected with radio-cisplatin (50 kBq, ^{189}Pt; 35 kBq, ^{191}Pt) and with nonradioactive cisplatin (2 mg/kg BW) in 100 μL of saline. Data were presented as the mean ± SD (*n* = 4). The alpha phase was indicated in white, and the beta phase was in black.

The biodistribution of cisplatin was shown in **Fig. 1-2-15**, where the data were presented as %ID/g of tissues. From the data in **Fig. 1-2-15**, the uptake ratio of each tissue to blood was summarized in **Table 1-2-4** to evaluate the effect of blood on the accumulation in tissues. The uptake of cisplatin was high in the lungs and kidneys in the early time points after injection. The accumulation of radioactivity in the lungs was related to blood clearance (**Table 1-2-4**), considering the constant uptake ratio of the lung to blood was approximately ~1 at each time point. Renal accumulation of cisplatin was observed in the early time points (27.2%ID/g at 15 min), and its excretion was observed thereafter (**Fig. 1-2-15**). Hepatic accumulation was also observed, and the cisplatin uptake in the liver was relatively higher than that in the kidneys in the late time points (kidney, 1.7%ID/g; liver, 2.6%ID/g at 7 d). There was a slight increase in the accumulation of cisplatin in the bone 5 d after injection (**Fig. 1-2-15**).

The accumulation in H460 tumors was not high, and the peak was 4.7%ID/g 15 min after injection (**Fig. 1-2-15**). The area under the curve ($AUC_{0–7\ days}$) was calculated on the basis of the biodistribution data (**Fig. 1-2-15**); the ratios of the tumor to each tissue were shown in **Table 1-2-5**. Compared with the $AUC_{0–7\ days}$ in the pancreas, stomach, intestine, and muscle, that in H460 tumors was approximately the same. The $AUC_{0–7\ days}$ in the kidneys and liver were almost three times higher and that in the bone was almost two times higher than that in H460 tumors (**Table 1-2-5**).

In separate experiments, to clarify the blood stability of cisplatin, radio-cisplatin uptake in blood, the red blood cell partitioning rate of radio-cisplatin in blood cells, and the plasma protein binding rate of cisplatin were also evaluated at 2 min, 1 h, and 19 h after injection (**Table 1-2-6**) The

uptake in blood was ~35%ID/g at 2 min after injection and quickly decreased thereafter, consistent with the results in the right panel of **Fig. 1-2-14**. The red blood cell partitioning rate of cisplatin increased gradually over the experimental period after injection and reached ~50%. The plasma protein binding rate of cisplatin increased to ~80% within 1 h after injection. From the end of the alpha phase to the beginning of the beta phase, the plasma protein binding rates remained high.

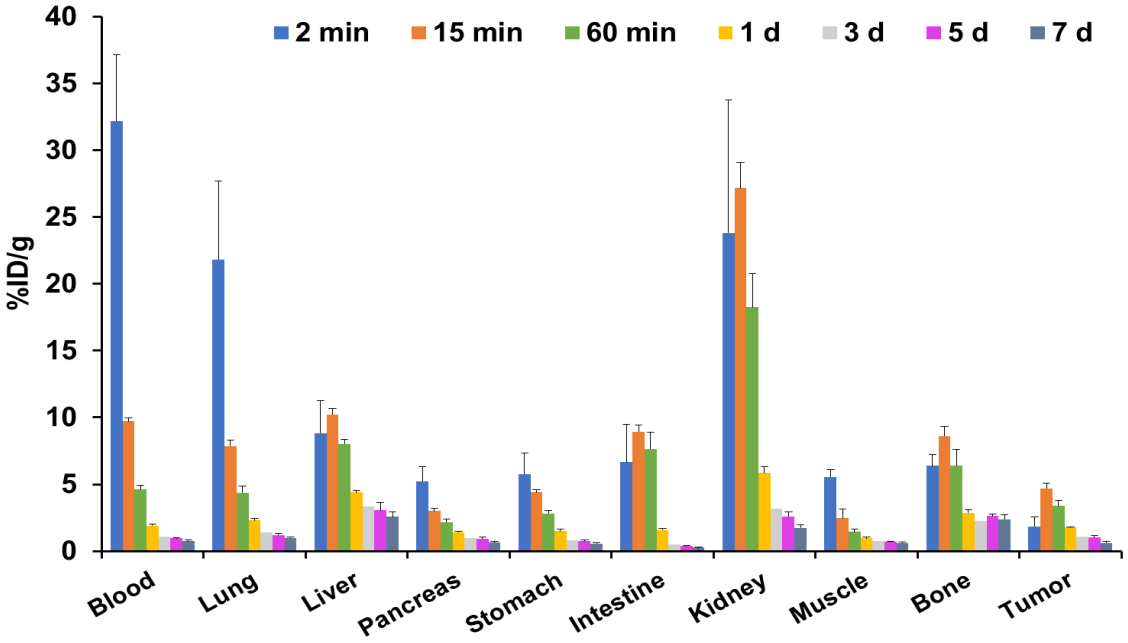

Figure 1-2-15. Biodistribution of radio-cisplatin in mice bearing H460 tumors. Data were represented as the percentage of the injected dose per gram (%ID/g) of tissue, corrected to those with a body weight of 20 g (mean ± SD, $n = 4$). The data for blood were the same as in the right panel of **Fig. 1-2-14**.

Table 1-2-4. Uptake ratios of each tissue to blood.

Ratio	2 min	15 min	60 min	1 d	3 d	5 d	7 d
Lung	0.68	0.81	0.94	1.21	1.34	1.26	1.34
Liver	0.27	1.05	1.74	2.30	3.13	3.20	3.48
Pancreas	0.16	0.31	0.47	0.75	0.94	0.98	0.87
Stomach	0.18	0.45	0.61	0.79	0.77	0.77	0.76
Intestine	0.21	0.92	1.65	0.83	0.44	0.39	0.38
Kidney	0.74	2.79	3.95	3.07	2.98	2.72	2.35
Muscle	0.17	0.25	0.31	0.50	0.70	0.72	0.82
Bone	0.20	0.89	1.38	1.51	2.13	2.74	3.20
Tumor	0.06	0.48	0.73	0.93	1.02	1.07	0.83

The ratios were calculated on the basis of the biodistribution data in **Fig. 1-2-15**.

Table 1-2-5. Area under the curve ($AUC_{0–7\ days}$) ratios of tumor to each tissue.

Tumor/Tissue	$AUC_{0–7\ days}$ ratio
Blood	0.91
Lung	0.76
Liver	0.35
Pancreas	1.17
Stomach	1.24
Intestine	1.18
Kidney	0.30
Muscle	1.59
Bone	0.46

The ratios were calculated on the basis of the biodistribution data in **Fig. 1-2-15**.

Table 1-2-6. Uptake in whole blood (%ID/g), red blood cell partitioning rate (%), and plasma protein binding rate (%) ($n = 2$).

Time	Whole blood uptake (%ID/g)	Red blood cell partitioning rate (%)	Plasma protein binding rate (%)
2 min	33.7, 35.5	1.5, 8.8	35.5, 28.6
1 h	4.5, 5.0	27.3, 23.2	82.8, 79.5
19 h	1.9, 2.2	51.8, 55.7	91.6, 92.2

The biodistribution experiments with radio-cisplatin over 7 d provided comprehensive pharmacokinetics data showing high accumulation in the kidneys, liver, and bone. Some literature demonstrated that cisplatin was rapidly excreted via the kidneys although a part of it remained intact.[33] Considering this, most of the intact cisplatin was expected to be excreted via the kidneys rapidly after injection before working in the body. Some intact cisplatin could be uptaken into renal cells, leading to the renal disorder recognized as the main side effect of cisplatin.[35] On the other hand, uptake in the liver was relatively higher than in the kidneys in the late time points from 3 d after injection (**Fig. 1-2-15**). This result might be related to the plasma protein binding of cisplatin. The plasma protein binding rate increased immediately after intravenous injection (**Table 1-2-6**), which was consistent with the general understanding of the behavior of cisplatin.[33,35] Cisplatin readily reacts with sulfur-containing cysteine or methionine of proteins such as serum albumin, leading to an irreversible increase of protein-bound cisplatin.[36] The protein-bound cisplatin is known to not be excreted predominately by the kidneys, to be retained longer in the blood, and to be accumulated in the liver.[37] This tendency might be responsible for the moderate retention in the liver in the late time points (**Fig. 1-2-15**), suggesting that the protein-bound cisplatin would be re-accumulated partly in the liver while

remaining and circulating in the blood (**Fig. 1-2-15**). Numerous studies on cisplatin treatments have shown that high-dose administration of cisplatin causes hepatoxicity,[38] and the oxidative stress derived from the metal toxicity of Pt has been suggested to be the main cause.[39] As some authors have also reported a high accumulation of cisplatin in the liver,[40] the radio-Pt tracer could provide insights enabling the elucidation of the relationship between hepatoxicity and cisplatin. Moreover, only the bone uptake of cisplatin increased slightly on day 5 (**Fig. 1-2-15**). Cisplatin remaining in the blood or excreted from tissues appeared to be taken into bones. This effect is speculated to correspond to cisplatin side effects such as myelosuppression.

In summary, the comprehensive and quantitative biodistribution indicated *in vivo* properties of the small Pt complex cisplatin, which was consistent with literature reporting the biodistribution of non-radioactive cisplatin. These results suggest risks of unwanted accumulation of radio-Pt in normal tissues. For less adverse effects, it is warranted to modify radio-Pt using tumor-targeting motifs having high *in vivo* stability and tumor-targeting specificity.

Chapter 1—Conclusion

Chapter 1 described the n.c.a. radio-Pt production from an Ir target using accelerators, evaluating DNA damage induced by Auger electrons released from n.c.a. radio-Pt bound to DNA without the chemical effect of nonradioactive Pt.

First, a novel method for radio-Pt production was established using Ir powder as a target material. The Ir powder target and alkali fusion process with Na_2O_2 led to the efficient dissolution of the irradiated Ir. The production yield of ^{191}Pt for both powder and coin targets of pure ^{nat}Ir was around ~37 MBq (1 mCi)/μA h at EOB before separation, which enabled sufficient production for biological application. By the selective reduction of $Ir^{IV}Cl_6^{2-}$ with ascorbic acid and two-step separation with TBP resin extraction and AEC, n.c.a. radio-$Pt^{II}Cl_4^{2-}$ was successfully prepared in a useful chemical form as a precursor for the synthesis of Pt drugs. From n.c.a. radio-$Pt^{II}Cl_4^{2-}$, n.c.a. radio-cisplatin was also successfully synthesized not via forming a crystal precipitate and used for DNA damage evaluation.

Second, the observations of the DNA-damaging efficacy of n.c.a. radio-cisplatin indicated that DSBs induced by Auger electrons released from radio-Pt bound to DNA, as shown in immunofluorescence staining for γH2AX. A dynamic evaluation of 53BP1-related DNA damage and the cell cycle revealed that n.c.a. radio-cisplatin increased DSBs, especially in the G1 phase, and also delayed the cell cycle. Thus, both γH2AX- and 53BP1-based evaluation as DBS markers showed that n.c.a. radio-cisplatin induced more DSBs than nonradioactive cisplatin, which found the damaging effect of Auger electrons, not the chemical effect of nonradioactive Pt carriers. Unfortunately, due to its low cellular uptake, only a small fraction of radio-cisplatin bound to DNA, making DSB probability and cytotoxicity low. To maximize the damaging effect of Auger electrons and reveal their ideal potential, it was necessary to develop a more efficient system for delivering radio-Pt to DNA by modifying radio-Pt with proper targeting modules. In addition, biodistribution studies revealed that tumor-targeting ligands should also be attached to radio-Pt for *in vivo* uses because cisplatin itself was not targeted to tumors sufficiently.

References

1. Qaim SM. Nuclear data for production and medical application of radionuclides: Present status and future needs. *Nucl Med Biol* **2017**; 44: 31–49.
2. (a) Hoeschele JD, Butler TA, Roberts JA, Guyer CE. Analysis and refinement of the microscale synthesis of the ^{195m}Pt-labeled antitumor drug, *cis*-Dichlorodiammineplatinum(II), *cis*-DDP. *Radiochim Acta* **1982**; 31: 27–36. (b) Zeevaart JR, Wagener J, Painter BM, Sathekge M, Soni N,

Zinn C, Perkins G, Smith SV. Production of high specific activity ^{195m}Pt-cisplatinum at South African Nuclear Energy Corporation for Phase 0 clinical trials in healthy individual subjects. *J Label Compd Radiopharm* **2013**; 56: 495–503. (c) Akaboshi M. Platinum 195m: in manual for reactor produced radioisotopes. IAEA-TECDOC-1340 **2003**; 171–178. (d) Howell RW, Kassis AI, Adelstein SJ, Rao DV, Wright HA, Hamm RN, Turner JE, Sastry KSR. Radiotoxicity of ^{195m}Pt labeled trans-platinum(II) in mammalian cells. *Radiat Res* **1994**; 140: 55–62. (e) Smith PHS, Taylor DM. Distribution and retention of the antitumor agent ^{195m}Pt-cis-dichlorodiammine platinum (II) in man. *J Nucl Med* **1974**; 15: 349–351. (f) Lange RC, Spencer RP, Harder HC. The antitumor agent cis-Pt$(NH_3)_2Cl_2$: distribution studies and dose calculations for ^{193m}Pt and ^{195m}Pt. *J Nucl Med* **1973**; 14: 191–195. (g) Aalbersberg EA, Wit BJ, Zwaagstra O, Codée K, Vegt E, Vogel WV. Preclinical imaging characteristics and quantification of Platinum-195m SPECT. *Eur J Nucl Med Mol Imaging* **2017**; 44: 1347–1354. (h) Buckley SE, Ali PA, Evans CJ, El-Sharkawi AM. Gamma camera scintigraphy of tumours using ^{195m}Pt-cisplatin. *Phys Med Biol* **2006**; 51: 1325.

3. (a) Deconti RC, Toftness BR, Lange RC, Creasey WA. Clinical and pharmacological studies with cis-diamminedichloroplatinum (II). *Cancer Res* **1973**; 33: 1310–1315. (b) Lange RC, Spencer RP, Harder HC. Synthesis and distribution of a radiolabeled antitumor agent: cis-diamminedichloroplatinum (II). *J Nucl Med* **1972**; 13: 328-330. (c) Norrgren K, Sjölin M, Björkman S, Areberg J, Johnsson A, Johansson L, Mattsson S. Comparative renal, hepatic, and bone marrow toxicity of cisplatin and radioactive cisplatin (^{191}Pt) in wistar rats. *Cancer Biother Radiopharm* **2006**; 21(5): 528–534. (d) Bates PI, Sharma HL, Murrer BA, Bernard CFJ, McAuliffe CA. The synthesis of ^{191}Pt labelled JM216, an orally active platinum anti-tumour agent. *Appl Radiat Isot* **1997**; 48(4): 469–476.
4. (a) Areberg J, Johnsson A, Wennerberg J. In vitro toxicity of ^{191}Pt-labeled cisplatin to a human cervical carcinoma cell line (ME-180). *Int J Radiation Oncol Biol Phys* **2000**; 46(5): 1275–1280. (b) Areberg J, Wennerberg J, Johnsson A, Norrgren K, Mattsson S. Antitumor effect of radioactive cisplatin (^{191}Pt) on nude mice. *Int J Radiation Oncol Biol Phys* **2001**; 49(3): 827–832. (c) Azure MT, Sastry KSR, Archer RD, Howell RW, Rao DV. Microscale synthesis of carboplatin labeled with the Auger emitter Pt-193m: Radiotoxicity versus chemotoxicity of the antitumor drug in mammalian cells. *Biophysical Aspects of Auger Processes, AAPM Symposium Series No.8* **1992**; 46(5): 336–351.
5. Areberg J, Björkman S, Einarsson L, Frankenberg B, Lundqvist H, Mattsson S, Norrgren K, Scheike O, Wallin R. Gamma camera imaging of platinum in tumours and tissues of patients after administration of ^{191}Pt-cisplatin. *Acta Oncol* **1999**; 38(2): 221-8.
6. Bodnar EN, Dikiy MP, Medvedeva EP. Photonuclear production and antitumor effect of radioactive cisplatin (^{195m}Pt). *J Radioanal Nucl Chem* **2015**; 305: 133–138.

7. (a) Hilgers K, Coenen HH, Qaim SM. Production of the therapeutic radionuclides ^{193m}Pt and ^{195m}Pt with high specific activity via α-particle-induced reactions on ^{192}Os. *Appl Radiat Isot* **2008**; 66: 545–551. (b) Uddin MS, Scholten B, Hermanne A, Sudár S, Coenen HH, Qaim SM. Radiochemical determination of cross sections of α-particle induced reactions on ^{192}Os for the production of the therapeutic radionuclide ^{193m}Pt. *Appl Radiat Isot* **2010**; 68: 2001–2006. (c) Uddin MS, Hermanne A, Scholten B, Spellerberg S, Coenen HH, Qaim SM. Small scale production of high purity ^{193m}Pt by the ^{192}Os(α, 3n)-process. *Radiochim Acta* **2011**; 99: 131–135.
8. (a) Bonardi M, Birattari C, Gallorini M, Groppi F, Arginelli D, Gini L. Cyclotron production, radiochemical separation and quality control of platinum radiotracers for toxicological studies. *J Radioanal Nucl Chem* **1998**; 236(1–2): 159–164. (b) Groppi F, Birattari C, Bonardi M, Gallorini M, Gubu L. Thin target excitation functions for (α, *x*n) reactions on osmium targets for platinum radiotracer production. *J Radioanal Nucl Chem* **2001**; 249(2): 289–293. (c) Qaim SM, Hilgers K, Sudár S, Coenen HH. Excitation function of the ^{192}Os(^{3}He,4n)-reaction for production of ^{191}Pt. *Appl Radiat Isot* **2009**; 67: 1074–1077.
9. Parent, M., Strijckmans, K., Cornelis, R., Dewaele, J., Dams, R., 1994. Production of ^{191}Pt radiotracer with high specific activity for the development of preconcentration procedures. *Nucl. Instrum. Methods Phys. Res., Sect. B* 86, 355–366.
10. Tinker, N.D., Zweit, J., Sharma, H. L., Downey, S., McAuliffe, C.A., 1991. Production of no-carrier added ^{191}Pt, a radiolabel for the synthesis and biological investigations of platinum anti-tumour compounds. *Radiochim. Acta.* 54, 29–34.
11. Tárkányi F, Ditrói F, Takács S, Hermanne A, Ignatyuk AV. Experimental and theoretical cross section data of deuteron induced nuclear reactions on platinum. *J Radioanal Nucl Chem* **2019**; 321: 747–764.
12. (a) Tárkányi F, Király B, Ditrói F, Takács S, Csikai J, Hermanne A, Uddin MS, Hagiwara M, Baba M, Ido T, Shubin YN, Dityuk AI. Activation cross section of proton induced nuclear reactions on iridium. *Nucl Instrum Methods Phys Res Sect B* **2005**; 239: 293–302. (b) Tárkányi F, Király B, Ditrói F, Takács S, Csikai J, Hermanne A, Uddin MS, Hagiwara M, Baba M, Ido T, Shubin YN, Kovalev SF. Cross sections of deuteron induced nuclear reactions on iridium. *Nucl Instrum Methods Phys Res Sect B* **2006**; 247: 210–216. (c) Obata H, Khandaker MU, Furuta E, Nagatsu K, Zhang MR. Excitation functions of proton- and deuteron-induced nuclear reactions on natural iridium for the production of ^{191}Pt. *Appl Radiat Isot* **2018**; 137: 250–260.
13. Bernardis FL, Grant RA, Sherrington DC. A review of methods of separation of the platinum-group metals through their chloro-complexes. *React Funct Polym* **2005**; 65: 205–217.
14. Lee J, Kim Y. Chemical dissolution of iridium powder using alkali fusion followed by high-temperature leaching. *Materials Transactions* **2011**; 52: 2067–2070.
15. Johnstone TC, Suntharalingam K, Lippard SJ. The next generation of platinum drugs: targeted

Pt(II) agents, nanoparticle delivery, and Pt(IV) prodrugs. *Chem Rev* **2016**; 116(5): 3436–3486.

16. Obata H, Khandaker MU, Furuta E, Nagatsu K, Zhang MR. Excitation functions of proton- and deuteron-induced nuclear reactions on natural iridium for the production of ^{191}Pt. *Appl Radiat Isot* **2018**; 137: 250–260.
17. Obata H, Minegishi K, Nagatsu K, Zhang MR, Shinohara A. Production of ^{191}Pt from an iridium target by vertical beam irradiation and simultaneous alkali fusion. *Appl Radiat Isot* **2019**; 149: 31–37.
18. Alderden RA, Hall MD, Hambley TW. The Discovery and Development of Cisplatin. *J. Chem. Educ.* 2006;**83**(5):728.
19. Kleinberg J. *Inorganic Syntheses*, Volume 7. New York: John Wiely & Sons; 1963. 239 p.
20. Darensbourg MY. *Inorganic. Syntheses*, Volume 32. New York: John Wiely & Sons; 1998. 141–144 p.
21. (a) Gately DP, Howell SB. Cellular accumulation of the anticancer agent cisplatin: A review. *Br J Cancer* **1993**; 67: 1171–1176. (b) Eljack ND, Ma HM, Drucker J, Shen C, Hambley TW, New EJ, Friedrich T, Clarke RJ. Mechanisms of cell uptake and toxicity of the anticancer drug cisplatin. *Metallomics* **2014**; 6: 2126–2133.
22. (a) Gale GR, Morris CR, Atkins LM, Smith AB. Binding of an antitumor platinum compound to cells as influenced by physical factors and pharmacologically active agents. *Cancer Res* **1973**; 33: 813–818. (b) Ogawa M, Gale GR, Keirn SS. Effects of cis-diamminedichloroplatinum (NSC 119875) on murine and human hemopoietic precursor cells. *Cancer Res* **1975**; 35: 1398–1401. (c) Binks SP, Dobrota M. Kinetics and mechanism of uptake of platinum-based pharmaceuticals by the rat small intestine. *Biochem Pharmacol* **1990**; 40: 1329–1336. (d) EI-Kareh AW, Secomb TW. A mathematical model for cisplatin cellular pharmacodynamics. *Neoplasia* **2003**; 5: 161–169.
23. (a) Ishida S, Lee J, Thiele DJ, Herskowitz I. Uptake of the anticancer drug cisplatin mediated by the copper transporter Ctr1 in yeast and mammals. *Proc Natl Acad Sci U S A* **2002**; 99: 14298–14302. (b) Howell, S.B.; Safaei, R.; Larson, C.A.; Sailor, M.J. Copper transporters and the cellular pharmacology of the platinum-containing cancer drugs. Mol. Pharmacol. 2010, 77, 887–894. (c) Yonezawa, A.; Masuda, S.; Yokoo, S.; Katsura, T.; Inui, K. Cisplatin and oxaliplatin, but not carboplatin and nedaplatin, are substrates for human organic cation transporters (SLC22A1–3 and multidrug and toxin extrusion family). *J Pharmacol Exp Ther* **2006**; 319: 879–886.
24. Groessl M, Zava O, Dyson PJ. Cellular uptake and subcellular distribution of ruthenium-based metallodrugs under clinical investigation versus cisplatin. *Metallomics* **2011**; 3: 591–599.
25. Andrews, P.A.; Howell, S.B. Cellular pharmacology of cisplatin: Perspectives on mechanisms of acquired resistance. *Cancer Cells* **1990**; 2: 35–43.
26. (a) Rodríguez MC, García RÁF, Blanco E, Bettmer J, Bayón MM. Quantitative evaluation of

cisplatin uptake in sensitive and resistant individual cells by single-cell ICP-MS (SC-ICP-MS). *Anal Chem* **2017**; 89: 11491–11497. (b) Drewinko B, Brown B, Gottlieb JA. The effect of cis-diamminedichloroplatinum(II) on cultured human lymphoma cells and its therapeutic implications. *Cancer Res* **1973**; 33: 3091–3095.

27. FitzGerald JE, Grenon M, Lowndes NF. 53BP1: function and mechanisms of focal recruitment. *Biochem Soc Trans* **2009**; 37: 897e904.
28. Olive PL, Banáth JP. Kinetics of H2AX phosphorylation after exposure to cisplatin. *Cytom Part B Clin Cytom J Int Soc Anal Cytol* **2009**; 76: 79–90.
29. (a) Pawlik TM, Keyomarsi K. Role of cell cycle in mediating sensitivity to radiotherapy. *IJROBP* **2004**; 59(4): 928e942. (b) Sia J, Szmyd R, Hau E, Gee HE. Molecular mechanisms of radiation-induced cancer cell death: a primer. *Front Cell Dev Biol* **2020**; 8: 41.
30. Donaldson KL, Goolsby GL, Wahl AF. Cytotoxicity of the anticancer agents cisplatin and taxol during cell proliferation and the cell cycle. *Int J Cancer* **1994**; 57: 847e855.
31. Eriksson D, Stigbrand T. Radiation-induced cell death mechanisms. *Tumour Biol* **2010**; 31(4): 363e372.
32. (a) Falta T, Koellensperger G, Standler A, Buchberger W, Maderc RM, Hann S. Quantification of cisplatin, carboplatin and oxaliplatin in spiked human plasma samples by ICP-SFMS and hydrophilic interaction liquid chromatography (HILIC) combined with ICP-MS detection. *J Anal At Spectrom* **2009**; 24: 1336–1342. (b) Hennik MB, Vijgh WJF, Klein I, Elferink F, Vermorken JB, Winograd B, *et al*. Comparative pharmacokinetics of cisplatin and three analogues in mice and humans. *Cancer Res* **1987**; 47: 6297-6301. (c) Urien S, Lokiec F. Population pharmacokinetics of total and unbound plasma cisplatin in adult patients. *Br J Clin Pharmacol* **2004**; 57(6): 756–763. (d) Hermann G, Heffeter P, Falta T, Berger W, Hann S, Koellensperger G. In vitro studies on cisplatin focusing on kinetic aspects of intracellular chemistry by LC-ICP-MS. Metallomics **2013**; 5: 636–647.
33. (a) Deconti RC, Toftness BR, Lange RC, Creasey WA. Clinical and pharmacological studies with cis-diamminedichloroplatinum (II). *Cancer Res* **1973**; 33: 1310–1315. (b) Panteix G, Beaujard A, Garbit F, Chaduiron-Faye C, Guillaumont M, Gilly F, *et al*. Population pharmacokinetics of cisplatin in patients with advanced ovarian cancer during intraperitoneal hyperthermia chemotherapy. *Anticancer Res* **2002**; 22(2B): 1329–36. (c) Vermorken JB, Vijgh WJF, Klein I, Gall HE, Groeningen GJ, Hart GAM, *et al*. Pharmacokinetics of free and total platinum species after rapid and prolonged infusions of cisplatin. *Clin Pharmacol Ther* **1986**; 39(2): 136–144.
34. (a) Schiller JH, Harrington D, Belani CP, Langer C, Sandler A, Krook J, et al. Comparison of four chemotherapy regimens for advanced bib-small-cell lung cancer. *N Engl J Med* **2002**; 346(2): 92–98. (b) Teme JS, Greer JA, Muzikansky A, Gallagher ER, Admane S, Jackson VA, et al. Early Palliative Care for Patients with Metastatic Non–Small-Cell Lung Cancer. *N Engl J Med* **2010**;

363(8): 733–742.

35. Crona DJ, Faso A, Nishijima TF, Mcgraw KA, Galsky MD, Milowsky MI. A systematic review of strategies to prevent cisplatin-induced nephrotoxicity. *The Oncologist* **2017**; 22: 609–619.
36. (a) Wang X, Guo Z. The role of sulfur in platinum anticancer chemotherapy. *Anti-Cancer Agents Med Chem* **2007**; 7:19−34. (b) Ivanov AI, Christodoulou J, Parkinson JA, Barnham KJ, Tucker A, Woodrowi J, *et al*. Cisplatin binding sites on human albumin. *J Biol Chem* **1998**; 273(24): 14721–14730. (c) Zimmermann T, Zeizinger M, Burda JV. Cisplatin interaction with cysteine and methionine, a theoretical DFT study. *J Inorg Biochem* **2005**; 99(11): 2184–2196.
37. (a) Wolf WC. Preparation and metabolism of a cisplatin/serum protein complex. *Chemico-Biological Interactions* **1980**; 30(2): 223–235. (b) Holding JD, Lindup WE, Laer C, Vreeburg GC, Schilling V, Wilson JA, *et al*. Phase I trial of a cisplatin-albumin complex for the treatment of cancer of the head and neck. *Br J Clin Pharmacol* **1992**; 33(1): 75–81.
38. (a) Cersosimo RJ. Hepatotoxicity associated with cisplatin chemotherapy. *Ann Pharmacother* **1993**; 27(4): 438–41. (b) Lu Y, Cederbaum AI. Cisplatin-Induced Hepatotoxicity Is Enhanced by Elevated Expression of Cytochrome P450 2E1. *Toxicological Sciences* **2006**; 89(2): 515–523. (c) Liu J, Liu Y, Habeebu SS, Klaassen CD. Metallothionein (MT)-null mice are sensitive to cisplatin-induced hepatotoxicity. *Toxicol Appl Pharmacol* **1998**; 149: 24–31.
39. (a) Rashid NA, Halim SASA, Teoh SL, Budin SB, Hussan F, Ridzuan NRA, *et al*. The role of natural antioxidants in cisplatin-induced hepatotoxicity. *Biomed Pharmacother* **2021**; 144: 112328. (b) Naziroglu M, Karaoglu A, Aksoy AO. Selenium and high dose vitamin E administration protects cisplatin-induced oxidative damage to renal, liver and lens tissues in rats. *Toxicology* **2004**; 195: 221–230. (c) Christova TY, Gorneva GA, Taxirov SI, Duridanova DB, Setchenska MS. Effect of cisplatin and cobalt chloride on antioxidant enzymes in the livers of Lewis lung carcinoma-bearing mice: Protective role of heme oxygenase. *Toxicol Lett* **2003**; 138: 235–242.
40. (a) Lange RC, Spencer RP, Harder HC. The antitumor agent cis-$Pt(NH_3)_2Cl_2$: distribution studies and dose calculations for ^{193m}Pt and ^{195m}Pt. *J Nucl Med* **1973**; 14: 191–195. (b) Lange RC, Spencer RP, Harder HC. Synthesis and distribution of a radiolabeled antitumor agent: cis-diamminedichloroplatinum (II). *J Nucl Med* **1972**; 13: 328-330. (c) Areberg J, Björkman S, Einarsson L, Frankenberg B, Lundqvist H, Mattsson S, *et al*. Gamma camera imaging of platinum in tumours and tissues of patients after administration of ^{191}Pt-cisplatin. *Acta Oncologica* **1999**; 38(2): 221–228. (d) Smith PHS and Taylor DM. Distribution and retention of the antitumor agent ^{195m}Pt-cis-dichlorodiammine platinum (II) in man. *J Nucl Med* **1974**; 15: 349–351.

Chapter 2: Development of Radio-Pt–Labeled Agents Binding to DNA Efficiently and Inducing DNA Damage Effectively

Chapter 2—Introduction

In *Chapter 1*, DSBs were induced by Auger electrons released from n.c.a. radio-cisplatin without chemical damage of nonradioactive Pt. Unfortunately, the low cellular uptake and the small DNA-binding fraction of radio-cisplatin led to a low probability of DSBs. To cause DNA damage efficiently, the amount of DNA-bound radio-Pt needs to be increased by enhancing its cellular uptake and DNA-binding rate. Therefore, *Chapter 2* investigated the incorporation of radio-Pt into hydrophilic DNA-targeting modules with membrane permeability and DNA-binding ability.

To date, common antineoplastic drugs labeled with radio-Pt had been developed using c.a. radio-Pt including a large amount of nonradioactive Pt.[1] They were synthesized in milligram-scale syntheses involving precipitation steps as well as conventional methods for nonradioactive Pt drugs. Few radio-Pt–labeled compounds other than common antineoplastic drugs were developed and synthesized using c.a. radio-Pt.[2] Literature review found few to no publications on compounds labeled with n.c.a. radio-Pt. This lack of radio-Pt–labeled complexes could be due to the limited availability of n.c.a. radio-Pt. Since the production of n.c.a. radio-Pt had not been established at a practical level, the radiolabeling chemistry of n.c.a. radio-Pt also remained under-developed, leading to the absence of established labeling methods for n.c.a. radio-Pt.

Multidentate chelating agents are useful for labeling targeting modules with metallic radionuclides in a simple scheme;[3] however, no suitable ligands have been reported for n.c.a. radio-Pt. Apart from such chelators, other labeled moieties that less substantially affect the chemical structure of targeting modules need to be considered, especially for labeling small molecules. Sulfur-containing amino acids are candidates applicable to n.c.a. radio-Pt because of their high reactivity toward Pt.[4] In order to expand radio-Pt drug development, labeling methods suitable for n.c.a. radio-Pt are critical. Therefore, at first, labeling methods with n.c.a. radio-Pt (^{191}Pt) via multidentate ligands and cysteine (Cys) were investigated in section 1 of *Chapter 2*. Thereafter, a DNA-targeting molecule, Hoechst33258 that binds to the minor groove of double-stranded DNA particularly rich in adenine and thymine, was employed as an example for DNA-targeting complexes labeled with radio-Pt. Radio-Pt–labeled Hoechst33258 via DTPA or Cys; [^{191}Pt]Pt-DTPA-Hoechst33258 and [^{191}Pt]Pt-Cys-Hoechst33258 were developed, and their *in vitro* properties were evaluated.

It is necessary to cause cell death from DNA damage by Auger electrons more efficiently; targeting specific sites of the genome that are involved in the survival mechanism in living cells may be a crucial strategy for novel Auger electron therapy. Key oncogenes involved in cancer survival are potential targets and would be targeted with Auger-electron emitting radionuclides coupled with agents that recognize specific DNA sequences. However, the development and application of such drugs have remained elusive.[5] In section 2 of *Chapter 2*, the delivery of radio-Pt to a specific site of the genome and the biological effect induced by the delivered radio-Pt are first investigated as a demonstration, to

advance TRT agents targeting key oncogenes.

Dysregulated transcription factors of cancer cells are the focus as a target in the genome. The genome of cancer cells is maintained under abnormal cancer-related transcription factors, genome regulators, etc. Therefore, the survival of cancer cells often depends on such specific gene amplification and overexpression.[6] Transcription-related genes that are amplified and overexpressed in cancer cells are potential targets for Auger electron therapy, and there is an unmet need to develop a module that delivers radio-Pt to targeted genes. By combining imidazole and pyrrole, sequence-specific pyrrole–imidazole polyamides (PIPs) are produced. PIPs are used for gene-targeting compounds that can deliver radio-Pt to a specific site of the genome. Numerous PIPs that target cancer-related genes have been developed, and some have been substantiated to have therapeutic efficacy in preclinical studies with mice and marmosets.[7] In the case of the MYCN gene, a MYCN-targeting PIP developed by Yoda *et al*. showed specific targeting ability and therapeutic effects in MYCN-amplified cells.[8] The oncogene MYCN is a transcription factor that is amplified in human neuroblastoma, and related to the prognosis.[9] This MYCN-PIP is well-established to demonstrate the concept of gene-targeted Auger electron therapy with radio-Pt. Hereby, a novel ^{191}Pt-labeled conjugate based on the MYCN-targeting PIP (^{191}Pt-MYCN-PIP) was demonstrated. ^{191}Pt-MYCN-PIP was developed and then evaluated for its *in vitro* and *in vivo* properties in MYCN-amplified and unamplified neuroblastoma models.

As a summary of *Chapter 2*, the research objective was to explore efficient DNA targeting and damaging agents labeled with n.c.a. ^{191}Pt, using DNA-targeting modules: the DNA-intercalator Hoechst33258 (section 1) and the sequence-specific DNA-binding molecule PIP (section 2). *Chapter 2* included the following 2 topics: **(1) Development of ^{191}Pt-Labeled Hoechst33258 Targeting DNA**, and **(2) Development of ^{191}Pt-Labeled PI Polyamide Targeting Amplified Cancer Genes**. The *in vitro* properties that were discovered provided an insight into the adequate chemical modification and targeting strategy of Auger-electron emitting radionuclides.

C*hapter 2* is based on the following papers that are referred to in the text.

1. **Obata H**, Tsuji AB, Kumata K, Sudo H, Minegishi K, Nagatsu K, Takakura H, Ogawa M, Kurimasa A, Zhang M R. Development of novel ^{191}Pt-labeled Hoechst33258: ^{191}Pt is more suitable than ^{111}In for targeting DNA. *J Med Chem* **2022**; 65(7) 5690–5700.
2. **Obata H**, Tsuji AB, Sudo H, Sugyo A, Hashiya K, Ikeda H, Itoh M, Minegishi K, Nagatsu K, Ogawa M, Bando T, Sugiyama H, Zhang MR. Novel Auger electron-emitting ^{191}Pt-labeled pyrrole–imidazole polyamide targeting MYCN induces gene damage and cytosolic dsDNA stress in neuroblastoma models. *In review*.

1. Development of ^{191}Pt-Labeled Hoechst33258 Targeting DNA

Exploring ligands and functional groups that react with n.c.a. ^{191}Pt

As shown in section 1 of *Chapter 1*, n.c.a. ^{191}Pt has been prepared as a chloride complex since Pt(II) chloride has been commonly used as a useful precursor for the synthesis of common Pt(II) complexes like cisplatin.[10] Most of the n.c.a. ^{191}Pt was prepared as $^{191}Pt^{II}Cl_4^{2-}$ (60–80%) for radio-labeling; some of it was hydrolyzed to neutral complexes such as $[^{191}Pt^{II}Cl_{4-n}(H_2O)_n]^{(2-n)-}$. After the concentration process by solvent evaporation and redissolution, the hydrolysis of $^{191}Pt^{II}Cl_4^{2-}$ was present due to the presence of numerous H_2O molecules to n.c.a. ^{191}Pt. Nevertheless, hydrolyzed Pt in the form $[PtCl_{4-n}(H_2O)_n]^{(2-n)-}$ was expected to be reactive toward amines or sulfur-containing agents because both chloro group (Cl) and aquo group (H_2O) were labile leaving groups for Pt(II) complex, according to the mechanism of Pt-based drugs[10] and HSAB theory.[11] Therefore, mixtures of $^{191}PtCl_4^{2-}$ and $[^{191}PtCl_{4-n}(H_2O)_n]^{(2-n)-}$ were hereafter referred to as "free ^{191}Pt" and were used as the precursor.

As a general method, chloro ligands of Pt(II) were replaced with aquo groups via chloride precipitation by silver nitrate before ligand exchange with any other functional groups. To synthesize cis or trans isomers precisely, aquo ligand needs to be further exchanged to other functional groups like iodine, as mentioned in section 1 of *Chapter 1* on radio-cisplatin synthesis, whereas the present labeling for n.c.a. radio-Pt did not do these processes to avoid loss of RCY. Bose *et al*. reported that an aquo ligand of a Pt(II) complex was very labile and substituted with a thiol group of Cys fast.[12] This knowledge possibly suggests that Pt(II) aquo complexes can be labeled via ligand exchange with other functional groups more rapidly than chloro complexes. N.c.a. ^{191}Pt(II) aquo complex, however, would be more susceptible to inactivation by even slight impurities. As silver nitrate leads to co-precipitation of n.c.a. radio-Pt with silver chloride, the preparation of Pt(II) aquo complexes also needs to be investigated. Considering such practical causes, the present research employed a chloride complex as a precursor and investigated radio-labeling of n.c.a. $^{191}Pt^{II}Cl_4^{2-}$ using sulfur and amine-containing ligands.

A general understanding of Pt complexes[4] and the HSAB theory[11] suggest that sulfur and amine-containing ligands have high affinity to n.c.a. radio-Pt(II), enabling efficient radio-labeling. Thus, two approaches to radio-Pt labeling were investigated: labeling via a polycarboxylic acid multidentate ligand and labeling via an amino acid (**Fig. 2-1-1**). The multidentate ligands were diethylenetriaminepentaacetic acid (DTPA) and ethylenedithiodiacetic acid (EDDA); the amino acids were L-cysteine (Cys), L-methionine (Met), L-serine (Ser), and L-glutamine (Gln); and the protected Cys analogs were *N*-(*tert*-butoxycarbonyl)-*S*-trityl-L-cysteine (Boc-Cys(Trt)-OH) and *S*-trityl-L-

cysteine (H-Cys(Trt)-OH). In the preliminary experiments, a certain heat treatment (45–80°C, 0.5–1 h) was critical to promoting the reaction of $\leq 10^0$ ng-scale radio-Pt quantitatively.

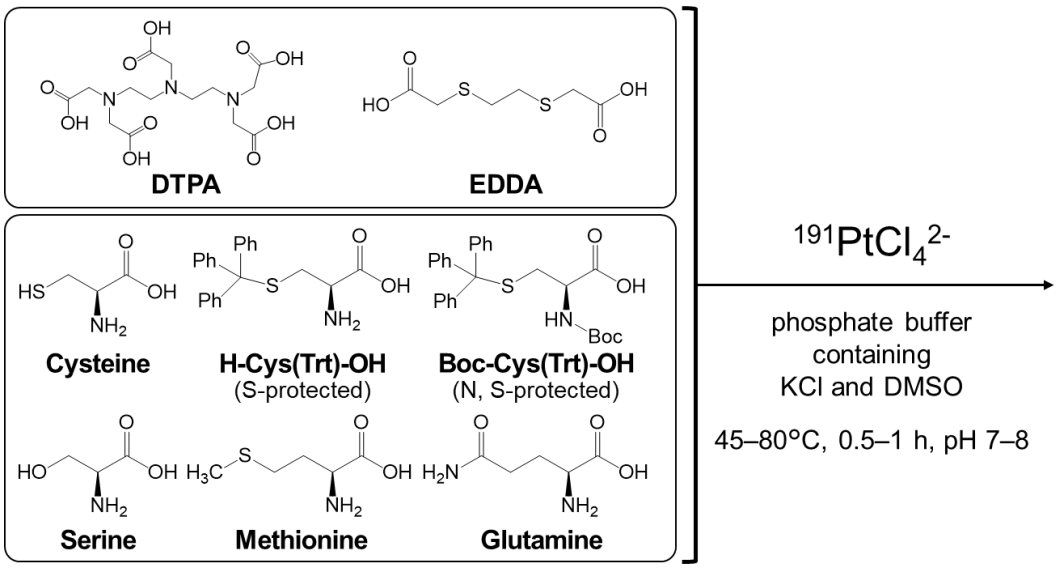

Figure 2-1-1. Amine- and/or sulfur-containing ligand candidates for radio-Pt.

First, the chelation of ^{191}Pt with the multidentate ligands DTPA and EDDA was investigated. **Figure 2-1-2** showed the radio thin-layer chromatogram for the reaction mixture of ^{191}Pt in the absence and presence of 5 mM DTPA or EDDA after the mixture was heated at 60°C for 1 h. Most of the ^{191}Pt chelated with DTPA or EDDA was observed at retention factor (R_f) 0.65–0.66 and a small amount of ^{191}Pt was observed at the origin and at R_f 0.11–0.12 (**Fig. 2-1-2**, lanes b-1 and c-1). The relative intensity corresponds to rough RCYs of 70–80%. These RCYs were high but slightly overestimated because of the overlapped peak from free ^{191}Pt (**Fig. 2-1-2**, lane a-1). The spots of the chelated ^{191}Pt at R_f 0.65–0.66 of DTPA and EDDA remained in the chromatogram of the ultrafiltered solution after co-incubation with fetal bovine serum (FBS) (**Fig. 2-1-2,** lanes b-2 and c-2), suggesting the component at R_f 0.65–0.66 corresponds to chelated ^{191}Pt. Although free ^{191}Pt was bound to protein at a high fraction of ~68%, chelating via DTPA or EDDA effectively reduced the protein binding of ^{191}Pt (DTPA, ~42%; EDDA, ~30%) (**Table 2-1-1**). The amount of ^{191}Pt chelated with DTPA in the ultrafiltered solution was less than the amount with EDDA (**Fig. 2-1-2**, lanes b-1 and c-1). This result was likely attributable to de-chelation or the formation of composites. EDDA, which has sulfur-based functional groups, can form a more stable complex with ^{191}Pt than DTPA, which binds via an amine group.

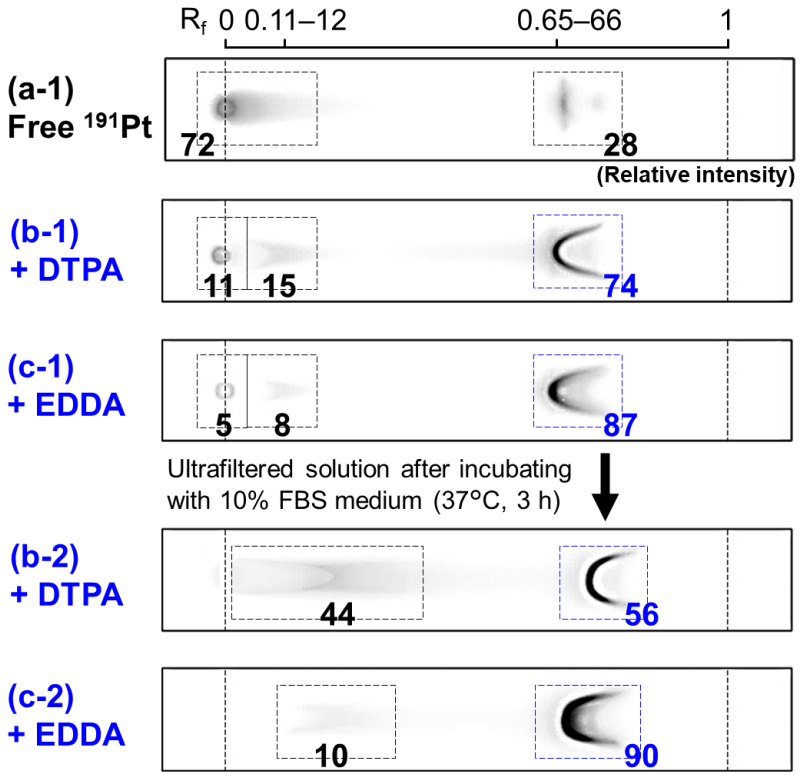

Figure 2-1-2. Radio-TLC analysis for the reaction mixtures (chelating agent: none, 5 mM DTPA, and 5 mM EDDA; 1 MBq of ^{191}Pt in 100 μL), which were detected using an imaging plate. TLC conditions: solvent, 100% methanol; stationary phase, silica gel.

Second, another labeling method of radio-Pt via the sulfur-containing amino acid Cys was evaluated. Based on the classical HSAB theory,[11] Pt(II) complexes have a high affinity and bind to sulfur-containing amino acids, especially Cys.[4,12] Incorporating Cys into a compound would provide a labeling site for radio-Pt instead of chelators. To assess the binding ability of sulfur groups to radio-Pt, a protein-binding assay of the reaction mixture was conducted for four amino acids (Cys, Met, Ser, and Gln) and two protected Cys analogs (H-Cys(Trt)-OH and Boc-Cys(Trt)-OH) after the mixtures were heated in the presence of ^{191}Pt at 45 or 60°C for 1 h (**Table 2-1-1**). The protein-binding of free ^{191}Pt was more inhibited by the reaction of ^{191}Pt and Cys containing a thiol group (–SH) than by the reaction of ^{191}Pt and Met containing a sulfide group (–SR) and Cys analogs containing protected S (–S-Trt). These results indicate that the thiol group in Cys reacted with n.c.a. ^{191}Pt, leading to a stable ^{191}Pt-Cys complex. Other amino acids containing no sulfur groups were almost equivalent to free ^{191}Pt. For the reaction mixture of Cys, the protein-binding was reduced substantially at 60°C (~10%) compared with that at 45°C (~42%) (**Table 2-1-1**). The number of ligands bound to ^{191}Pt possibly changed by heating, and their conditions affected the reactivity of ^{191}Pt complexes to proteins. Met containing a sulfide group (–SR) will be more reactive to n.c.a. ^{191}Pt at higher reaction temperatures.

Table 2-1-1. Protein-binding fraction of ^{191}Pt.

Agent (5 mM)	Reaction conditions	Functional groups	Protein-binding fraction (%)*
Free ^{191}Pt			68.2, 68.4
+ DTPA	60°C for 1 h ^{191}Pt 1 MBq/100 µL	–NR_2×3, –COOH×5	42.4, 42.0
+ EDDA		–SR×2, –COOH×2	30.2, 26.0
+ Cysteine (Cys)		–SH, –NH_2, –COOH	9.9, 5.8
Free ^{191}Pt			74.0, 74.3
+ Cysteine (Cys)		–SH, –NH_2, –COOH	39.0, 42.5
+ H-Cys(Trt)-OH		–S-Trt, –NH_2, –COOH	62.0, 63.1
+ Boc-Cys(Trt)-OH	45°C for 1 h ^{191}Pt 1 MBq/150 µL	–S-Trt, –N-Boc, -COOH	64.6, 68.0
+ Methionine (Met)		–SR, –NH_2, –COOH	58.6. 60.2
+ Glutamine (Gln)		–NH_2×2, –COOH	70.5, 69.5
+ Serine (Ser)		–NH_2, –COOH	70.2, 70.6

*After the reaction mixture was incubated in 10% FBS medium at 37°C for 3 h. All experiments were performed in duplicate.

A comparison of all the results of the protein-binding assays indicated that the affinity of functional groups to n.c.a. ^{191}Pt decreased in the order of thiol (–SH) > sulfide (–SR) > primary amine (–NH_2) > carboxy (–COOH), suggesting that Cys was the best agent for labeling with ^{191}Pt. Cys is one of the 20 amino acids found in living organisms; thus, radio-Pt labeling via Cys is suitable for biological applications. The method developed in the present work can be readily applied to polypeptide-based pharmaceuticals such as modular nanotransporters,[13] which are used in mainstream TRT agents using Auger-electron emitting radionuclides. To summarize, novel labeling methods were demonstrated for n.c.a. radio-Pt in the picogram-to-nanogram scale via amino/thio-polycarboxylic acids (DTPA and EDDA) and a sulfur-containing amino acid (Cys), whereas other research groups used carrier-added radio-Pt in milligram-scale syntheses involving precipitation steps.[1,2] Thereafter, radio-Pt–labeled DNA-targeting compounds were developed and evaluated.

Synthesis of the DNA-targeting complexes for labeling with ^{191}Pt: DTPA-Hoechst33258 and Cys-Hoechst33258

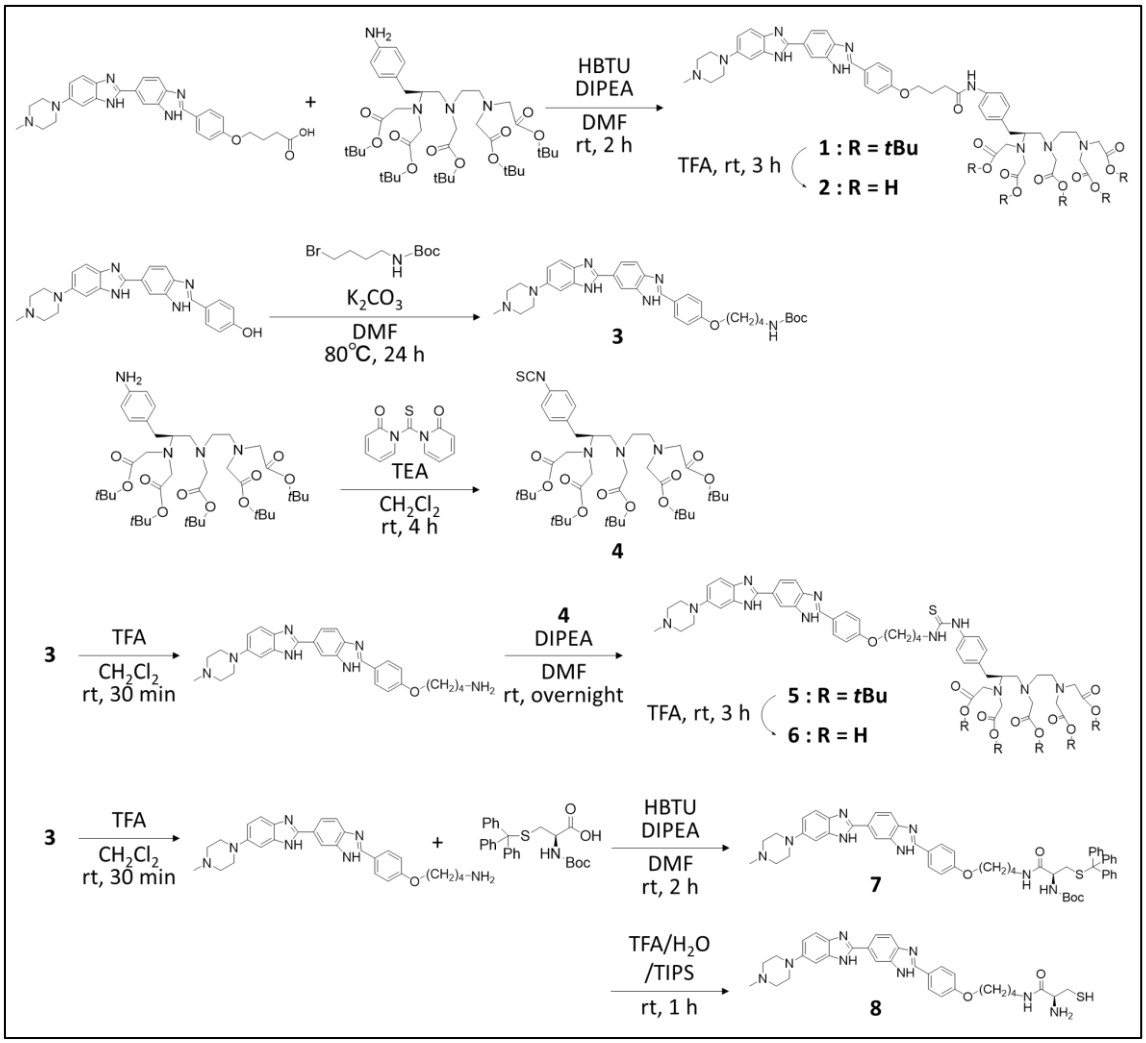

Figure 2-1-3. Scheme of the synthesis of DTPA-Hoechst33258 (**2**, **6**) and Cys-Hoechst33258 (**8**).

Three DNA-targeting complexes, DTPA-Hoechst33258 (amide analog (**2**) and thiourea analog (**6**)) and Cys-Hoechst33258 (**8**) were designed and synthesized as illustrated in **Fig. 2-1-3**. These complexes were based on Hoechst33258 labeled with ^{191}Pt via DTPA or Cys, [^{191}Pt]Pt-DTPA-Hoechst33258 and [^{191}Pt]Pt-Cys-Hoechst33258, which were synthesized by conjugating Hoechst33258 with DTPA or Cys via an amide or a thiourea bond, respectively. Although EDDA showed a higher affinity to ^{191}Pt than DTPA (**Fig. 2-1-2**), DTPA was used as a general chelator to enable a direct comparison to the common Auger-electron emitting radionuclide ^{111}In.[3] The protected conjugates *t*Bu-DTPA-Hoechst33258 (**1**, **5**) and Boc-Cys(Trt)-Hoechst33258 (**7**) were >95% pure, as

determined by C18 HPLC (conditions were specified in the *Experimental Section*). Although the deprotected conjugates DTPA-Hoechst33258 (**2**, **6**) and Cys-Hoechst33258 (**8**) contained decomposition products, an additional purification was conducted by HPLC after the labeling reaction with radio-materials.

Development of Hoechst33258 labeled with n.c.a. ^{191}Pt via DTPA or Cys

Preliminary experiments of ^{191}Pt labeling via DTPA showed the thiourea linkage was reactive toward Pt, leading to uncontrollable coordination forms other than DTPA. A broad peak of the labeled product of [^{191}Pt]Pt-DTPA-Hoechst (thiourea analog) was observed in the HPLC chromatogram (**Fig. 2-1-4**) and observed a time lag between the radioactivity and UV peaks, suggesting that the thiourea analog (**6**) was unsuitable for n.c.a. ^{191}Pt labeling via DTPA. Considering the high reactivity of Pt toward sulfur-containing groups, not only DTPA but also the thiourea bond would bind to ^{191}Pt. Therefore, the amide analog of DTPA-Hoechst33258 (**2**) was used for ^{191}Pt labeling in the following experiments. In contrast, both the amide and thiourea analogs of DTPA-Hoechst33258 were labeled with ^{111}In without problems, as shown in the radiochromatograms in **Fig. 2-1-5**.

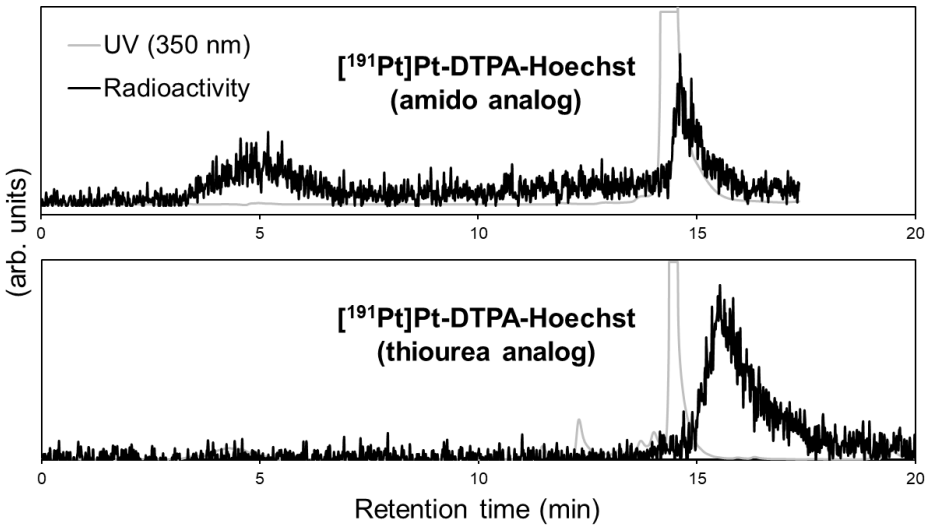

Figure 2-1-4. Radiochromatograms of preparative HPLC for [^{191}Pt]Pt-DTPA-Hoechst33258 (amide and thiourea analogs). HPLC conditions: column, COSMOSIL 5C18-MS-II (Nacalai Tesque, Kyoto, Japan); gradient elution, A/B = 0.1% TFA in H_2O/CH_3CN = 90/10 → 50/50 (20 min).

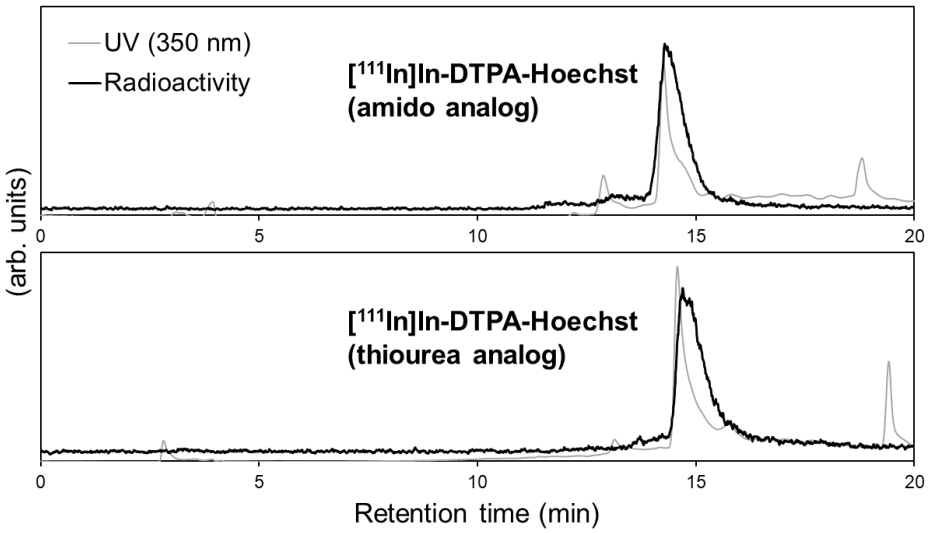

Figure 2-1-5. Radiochromatograms of analytical HPLC for [^{111}In]In-DTPA-Hoechst33258 (amide and thiourea analog). HPLC conditions: column, COSMOSIL 5C18-MS-II (Nacalai Tesque, Kyoto, Japan); gradient elution, A/B = 0.1% TFA in H_2O/CH_3CN = 90/10 → 50/50 (20 min) → 5/95 (30 min).

The radiolabeling conditions for n.c.a. ^{191}Pt were summarized in **Table 2-1-2**, and representative radiochromatograms (preparative HPLC of the reaction mixtures and analytical HPLC analysis of the purified products) were shown in **Fig. 2-1-6**. The UV peak of DTPA-Hoechst33258 (**2**) appeared at a retention time of 14–15 min in **Fig. 2-1-6(a)**, and that of Cys-Hoechst33258 (**8**) appeared at a retention time of 13–14 min in **Fig. 2-1-6(b)**. Each radioactive peak of both conjugates labeled with ^{191}Pt was observed to immediately follow the corresponding UV peak. The heating temperature and concentration of conjugates were varied in the n.c.a. ^{191}Pt labeling experiments, and the area percentages based on the radiochromatograms (**Fig. 2-1-6**) were roughly calculated for ^{191}Pt-labeled product peaks under each condition (**Table 2-1-2**).

It was found that labeling via DTPA should be performed at a high temperature (80°C) and a high concentration of conjugates (450 μM) (**Table 2-1-2**). DTPA appeared to exhibit a slightly low affinity to Pt (**Fig. 2-1-3**); such a condition was necessary for the rapid formation of a stable coordination state. Nevertheless, numerous peaks of byproducts were observed and extensive tailing and adsorption onto the column resulted in a low area percentage of ~27% (**Fig. 2-1-6(a)**). As a result of the repeated trials of radiosynthesis under a concentration of 450 μM and temperature of 80°C, the yield was approximately 12–22%, as determined by preparative HPLC (n = 3). In contrast, a sharp peak of [^{111}In]In-DTPA-Hoechst33258 was observed irrespective of the analogs (**Fig. 2-1-7**), resulting in a high yield of approximately 60–80% (n = 6). These results suggest that the chelation of n.c.a. ^{191}Pt via DTPA cannot proceed as quickly as the chelation of ^{111}In. The stable coordination number and structure, therefore, differ between ^{191}Pt and ^{111}In.

Thiol-containing Cys reacted with n.c.a. radio-Pt readily and formed strong Pt–S bonds (**Fig. 2-1-6(b)**). To avoid multivalent coordination when labeling via Cys, ^{191}Pt needed to be labeled with a low concentration of conjugates (45 μM) by being heated at a moderate temperature (45°C) (**Table 2-1-2**). Higher concentrations of conjugates, a higher temperature, or a greater activity of ^{191}Pt (~0.5 MBq/μL) resulted in more multivalent peaks (**Fig. 2-1-6(b)**), which made the yield uncertain at 10–80%, as determined by preparative HPLC (n = 4, 0.05–0.5 MBq/μL); the yield was also affected by the fractionation period.

[^{191}Pt]Pt-DTPA-Hoechst33258 and [^{191}Pt]Pt-Cys-Hoechst33258 were isolated successfully and prepared in the solution after the CH_3CN was removed and the pH was adjusted to neutral. In radio-HPLC analyses of the products after purification, the RCPs of [^{191}Pt]Pt-DTPA-Hoechst33258 (amide analog) and [^{111}In]In-DTPA-Hoechst33258 (amide and thiourea analogs) were >95% (**Figs. 2-1-6(a) and 2-1-7**). [^{191}Pt]Pt-Cys-Hoechst33258 contained a few multivalent byproducts, leading to a RCP of ~90% (**Fig. 2-1-6(b)**). Comparing the peak shape in the radiochromatograms of [^{191}Pt]Pt-DTPA-Hoechst33258 (amide analog) and [^{191}Pt]Pt-Cys-Hoechst33258 after HPLC purification, [^{191}Pt]Pt-DTPA-Hoechst33258 (amide analog) led to a sharper main product peak and fewer byproduct peaks than [^{191}Pt]Pt-Cys-Hoechst33258. These results suggest that multidentate ligands are likely to unify the coordination number and structure of ^{191}Pt.

Table 2-1-2. Conditions of labeling DTPA-Hoechst33258 (**2**) and Cys-Hoechst33258 (**8**) with ^{191}Pt.

Conjugates	Concentration	Temperature	Heating time	Labeling properties Area percentages of the labeled product* (n = 1)
DTPA-Hoechst33258 (**2**)	450 μM	80°C	60 min	A main peak of the product (**Fig. 2-1-6(a1)**) 27%
	450 μM	45°C	60 min	Multiple peaks (**Fig. 2-1-6(a2)**) 21%
	45 μM	80°C	60 min	No labeled peaks (**Fig. 2-1-6(a3)**) 11%
Cys-Hoechst33258 (**8**)	45 μM	45°C	60 min	A main peak of the product (**Fig. 2-1-6(b1)**) 45%
	450 μM	45°C	60 min	Multiple peaks (**Fig. 2-1-6(b2)**) 24%

*Calculated on the basis of the radiochromatograms in **Fig. 2-1-6**.

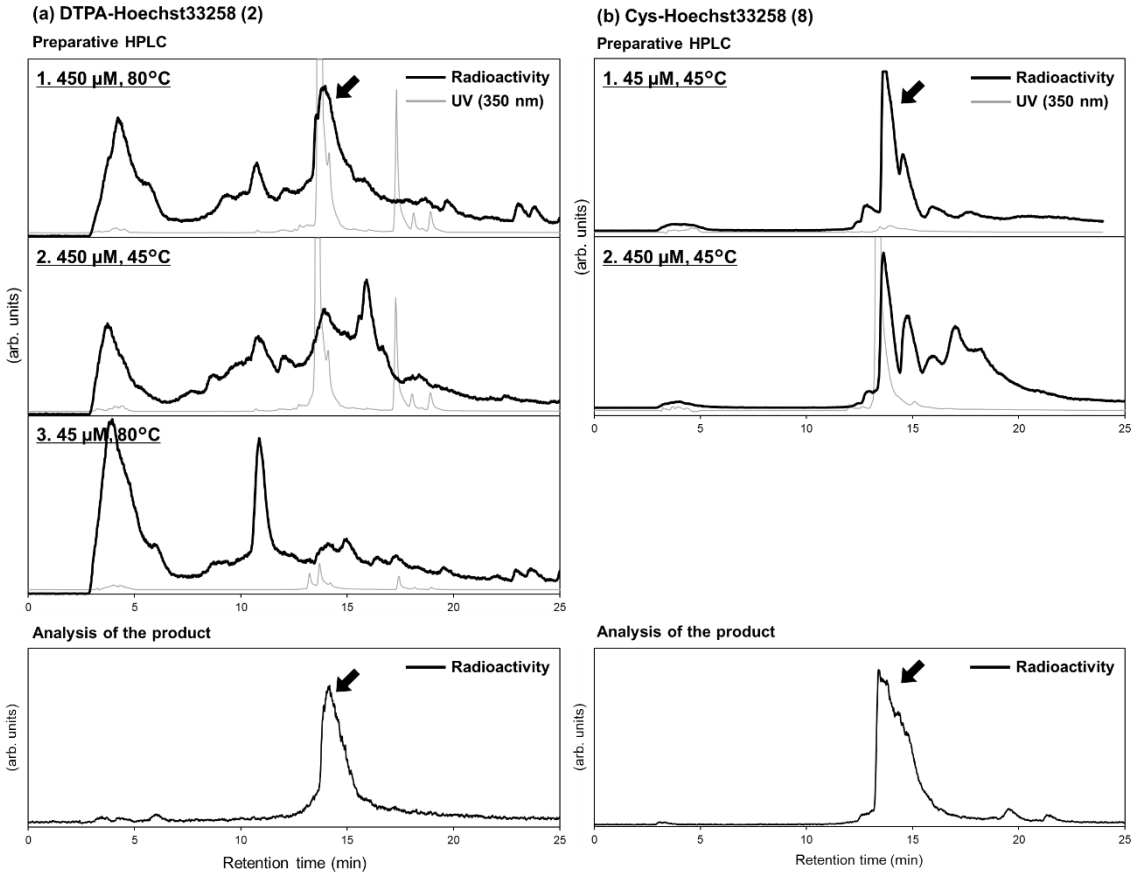

Figure 2-1-6. Radiochromatograms of preparative and analytical HPLC for (a) DTPA-Hoechst33258 (**2**) and (b) Cys-Hoechst33258 (**8**) labeled with ^{191}Pt. Labeling conditions: 45–450 μM conjugates and 50 kBq/μL ^{191}Pt in a buffer solution (200 μL) containing 0.1 M phosphate, 0.1–0.2 M KCl, and 7 M DMSO, pH 7–8. HPLC conditions: column, COSMOSIL 5C18-MS-II (Nacalai Tesque, Kyoto, Japan); gradient elution, A/B = 0.1% TFA in H_2O/CH_3CN = 90/10 → 50/50 (20 min) → 5/95 (30 min). Arrows indicated the peak of the labeled product.

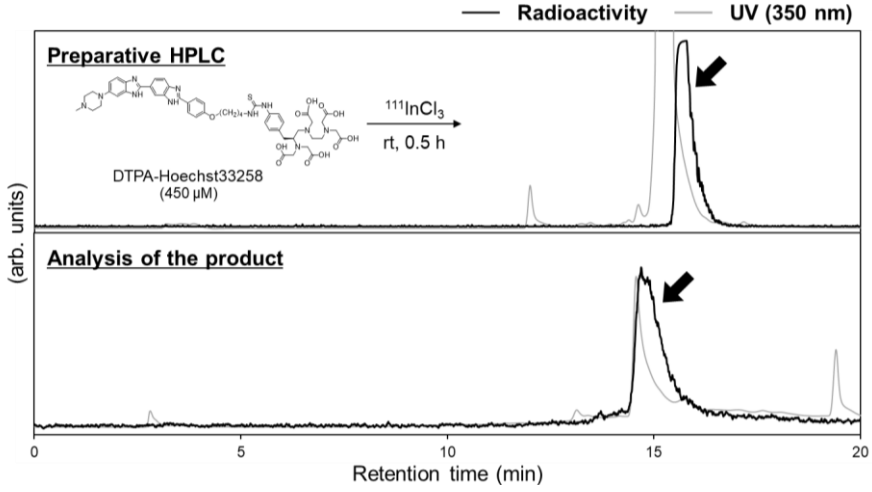

Figure 2-1-7. Radiochromatograms of preparative and analytical HPLC for [^{111}In]In-DTPA-Hoechst33258 (thiourea analog). Labeling conditions: 450 μM conjugates in a buffer solution containing 0.7 w/v% saline and 1.8 M DMSO. HPLC conditions: column, COSMOSIL 5C18-MS-II (Nacalai Tesque, Kyoto, Japan); gradient elution, A/B = 0.1% TFA in H_2O/CH_3CN = 90/10 → 50/50 (20 min) → 5/95 (30 min). Arrows showed the peak of the labeled product.

Cellular uptake and intracellular distribution of ^{191}Pt- and ^{111}In-labeled Hoechst33258

The cellular uptake and intracellular distribution of [^{191}Pt]Pt-DTPA-Hoechst33258 (amide analog) and [^{191}Pt]Pt-Cys-Hoechst33258 were evaluated using the human osteosarcoma cell line U2OS-53BP1 by measuring the activity of ^{191}Pt and comparing it to the activities of free ^{191}Pt, [^{111}In]In-DTPA-Hoechst33258 (thiourea and amide analogs), and free ^{111}In ($^{111}InCl_3$). The cellular uptakes (percent of the incubated dose per milligram of protein; %ID/mg protein) of [^{191}Pt]Pt-DTPA-Hoechst33258 (amide analog) and [^{111}In]In-DTPA-Hoechst33258 (thiourea analog) were similar (0.42–0.65%ID/mg) and relatively higher than those of free ^{191}Pt/^{111}In (0.17–0.23%ID/mg) (**Fig. 2-1-8(a)**). [^{191}Pt]Pt-Cys-Hoechst33258 was taken into U2OS-53BP1 cells at a greater rate than the others (1.5%ID). Interestingly, a comparison of the two ^{191}Pt-labeled Hoechst33258 samples reveals that [^{191}Pt]Pt-Cys-Hoechst33258 exhibited two to three times greater cellular uptake than [^{191}Pt]Pt-DTPA-Hoechst33258 (**Fig. 2-1-8(a)**), suggesting that Hoechst33258 did not enhance the membrane permeability of ^{191}Pt and ^{111}In efficiently in the case of the DTPA analog.

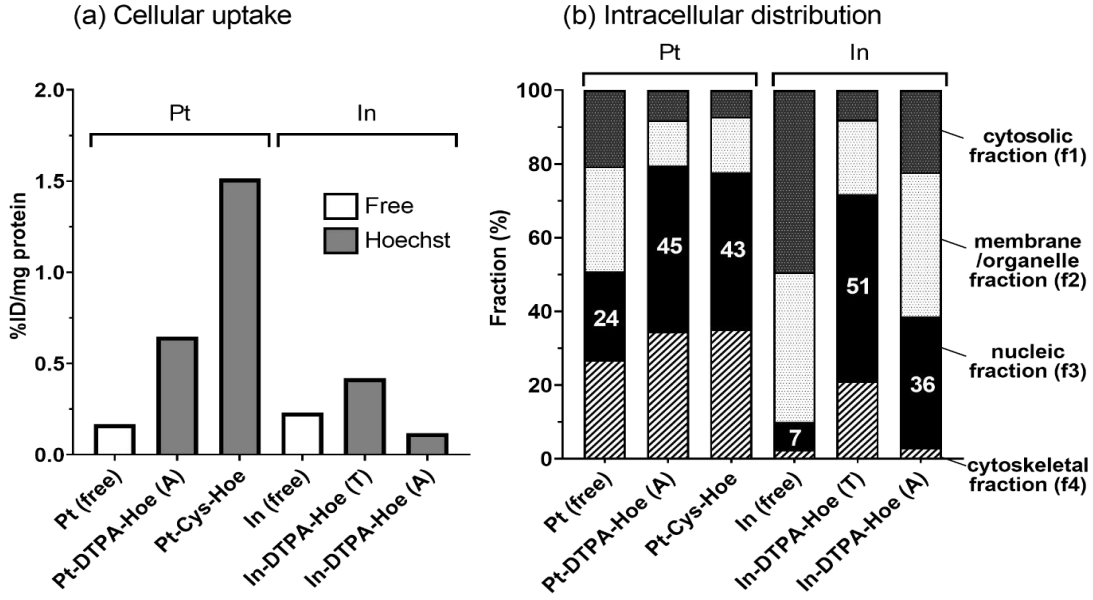

Figure 2-1-8. (a) Cellular uptake (%ID/mg protein) and (b) intracellular distribution (%) of ^{191}Pt and ^{111}In in U2OS-53BP1 cells after incubation for 18 h (f1, cytosolic fraction; f2, membrane/organelle protein fraction; f3, nucleic protein fraction; f4, cytoskeletal fraction; A, amide analog; T, thiourea analog).

To characterize the difference between the DTPA and Cys analogs, the lipophilicity of the Hoechst33258 analogs was evaluated on the basis of log $D_{7.4}$, which was defined as the logarithm of the distribution coefficient in 1-octanol/PBS, as determined by the shaking-flask method (pH = 7.4 at room temperature) (**Table 2-1-3**). The results showed that both the thiourea and amide analogs of DTPA-Hoechst33258 were significantly more polar than the original Hoechst33258, whereas the Cys-Hoechst33258 remained hydrophobic. Thus, the maintained hydrophobicity of the Cys-Hoechst33258 enabled the complexed ^{191}Pt to pass through the cell membrane efficiently; these results suggest that radio-Pt labeling via Cys was more effective for drug applications than radio-Pt labeling via DTPA.

Table 2-1-3. Log $D_{7.4}$ values of the Hoechst analogs.

Compounds	Log D (pH = 7.4, room temperature)
Hoechst33258	2.2
Cys-Hoechst33258	2.0
DTPA-Hoechst33258 (amide analog)	−0.5
DTPA-Hoechst33258 (thiourea analog)	−1.4

The intracellular fractions of ^{191}Pt and ^{111}In were evaluated by dividing the cells in **Fig. 2-1-8(b)** into four subcellular fractions: f1, cytosolic; f2, membrane/organelle protein; f3, nuclear protein; and f4, cytoskeletal fraction. In U2OS-53BP1 cells, the nucleic fraction (f3) of ^{191}Pt- and ^{111}In-labeled Hoechst33258 was 40–50%, which was higher than the fractions of the free ^{191}Pt and ^{111}In (24% and 7%, respectively) (**Fig. 2-1-8(b)**). Nuclear translocation between the two ^{191}Pt-labeled Hoechst33258 was similar. These results suggested that ^{191}Pt labeling via either DTPA or Cys effectively produced radio-Pt–based agents that can function in living cells. In addition, the intracellular distribution differed between free ^{191}Pt and ^{111}In. The nuclear translocation of the free ^{191}Pt was greater than that of the free ^{111}In, consistent with the tendency of many Pt complexes to transport to nuclei and bind directly to DNA.[10]

A comparison of the two ^{111}In-labeled analogs showed that both the cellular uptake and the nuclear fraction (f3) of the amide analog were lower than those of the thiourea analog (**Figs. 2-1-8(a) and (b)**). The cellular uptake of the ^{111}In-labeled amide analog was also lower than that of free ^{111}In, indicating that the behavior of Hoechst33258 was not sufficiently imparted to the ^{111}In-labeled analog.

The f1 and f2 fractions of the ^{111}In-labeled amide analog were higher than those of the thiourea analog. The ^{111}In-labeled amide analog might be less stable in the cells than the thiourea analog.; however, the reasons why both the cellular uptake and the nuclear fraction (f3) of the amide analog were lower than those of the thiourea analog in **Figs. 2-1-8(a) and (b)** were not revealed in the present work. The aforementioned results indicate that the thiourea analog of [^{111}In]In-DTPA-Hoechst33258 is more suitable than the amide analog for comparison with ^{191}Pt-labeled Hoechst33258 in further biological evaluation. In the following assays, different analogs, [^{111}In]In-DTPA-Hoechst33258 (amide analog) and [^{111}In]In-DTPA-Hoechst33258 (thiourea analog) were used, to evaluate the DNA-targeting and -damaging ability under the compatible nuclear translocation between ^{191}Pt- and ^{111}In-labeled Hoechst.

DNA-binding of ^{191}Pt- and ^{111}In-labeled Hoechst33258

A DNA-binding assay was conducted for two cell lines (U2OS-53BP1 and NB69) to evaluate the DNA-targeting ability of the ^{191}Pt-labeled Hoechst33258. **Figures 2-1-9(a), (b), and (c)** showed the cell fraction (%ID), the DNA-binding rate (%ID/μg genomic DNA), and the ratio of DNA-binding to cell fraction (%), respectively. The cell fraction was obtained from the radioactivity of the collected cells for DNA extraction (**Fig. 2-1-9(a)**), and the DNA-binding rate was obtained from that of the extracted DNA (**Fig. 2-1-9(b)**); the ratio of the DNA-binding rate (%ID) to cellular uptake (%ID) was indicated by the percent value in **Fig. 2-1-9(c)**. The cell fractions of ^{191}Pt- and ^{111}In-labeled DTPA-Hoechst33258 were similar to those of free ^{191}Pt and ^{111}In (0.4–1.0%ID) (**Fig. 2-1-9(a)**). [^{191}Pt]Pt-Cys-Hoechst33258, in contrast, was taken into U2OS-53BP1 and NB69 cells at a rate greater than the others (3.8 and 1.6%ID). These results were consistent with those of cellular uptake discussed in the preceding subsection.

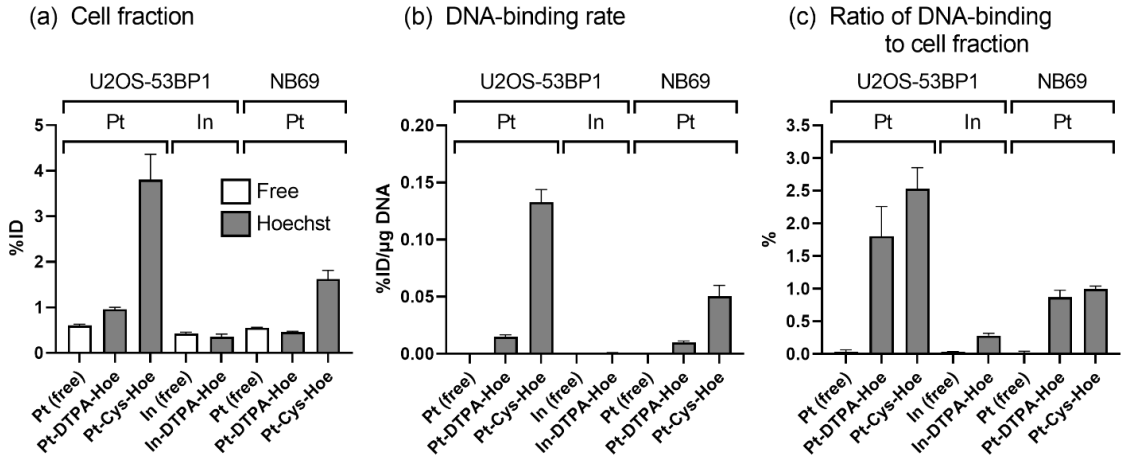

Figure 2-1-9. (a) Cellular fraction (%ID), (b) DNA-binding rate (%ID/μg DNA), and (c) the ratio of

DNA-binding to cell fraction (%) of ^{191}Pt and ^{111}In in U2OS-53BP1 and NB69 cells after incubation for 16 h.

The DNA-binding fractions of free ^{191}Pt and ^{111}In were near the detection limit (**Fig. 2-1-9(b)**), and the intracellular ^{191}Pt and ^{111}In were bound to DNA at a low rate of ≤0.01% (**Fig. 2-1-9(c)**). The DNA-binding of ^{191}Pt- and ^{111}In-labeled Hoechst33258 increased compared with that of free ^{191}Pt and ^{111}In, and the rate was quite different between ^{191}Pt and ^{111}In. Despite the ^{191}Pt- and ^{111}In-labeled Hoechst33258 having the same DNA-targeting module, DNA-binding rates of ^{191}Pt-labeled Hoechst33258 were 10- to 100-fold higher (via DTPA, 0.015 ± 0.002%ID/μg; via Cys, 0.13 ± 0.01%ID/μg for U2OS-53BP1) than those of [^{111}In]In-DTPA-Hoechst33258 (0.0010 ± 0.0001%ID/μg for U2OS-53BP1) (**Fig. 2-1-9(b)**). A comparison of Hoechst33258 labeled with ^{191}Pt via DTPA with that labeled with ^{191}Pt via Cys showed a difference in the DNA-binding rate in both U2OS-53BP1 and NB69 cells, which was mainly due to the difference in cellular uptake. The ratio of DNA-binding to cell fraction was approximately the same between [^{191}Pt]Pt-DTPA-Hoechst33258 and [^{191}Pt]Pt-Cys-Hoechst33258 (~2% for U2OS-53BP1 and ~1% for NB69) and was much higher than the 0.3% of ^{111}In-DTPA-Hoechst for U2OS-53BP1 (**Fig. 2-1-9(c)**). These results confirm that ^{191}Pt labeling via DTPA and Cys is workable in living cells and suggest that ^{191}Pt-labeled agents are more suitable than ^{111}In-labeled agents for targeting DNA. The superior DNA affinity of ^{191}Pt-labeled Hoechst33258 compared with ^{111}In-labeled Hoechst33258 would be attributable to the DNA-binding ability of ^{191}Pt. Pt can directly bind to DNA after being delivered to DNA by Hoechst33258. This direct binding may result in the formation of stable ^{191}Pt–DNA adducts, leading to substantial interaction between DNA and Auger electrons. Rather than the ^{111}In commonly used in the development of Auger-electron emitting therapeutics, radio-Pt has a greater potential in Auger electron cancer therapy targeting DNA.

DNA-damaging efficacy of ^{191}Pt- and ^{111}In-labeled Hoechst33258

To assess whether the high DNA-binding fraction of ^{191}Pt-labeled Hoechst33258 leads to DNA damage by Auger electrons, fluorescent imaging of 53BP1 was conducted for evaluating DSBs induced by [^{191}Pt]Pt-DTPA-Hoechst33258 and [^{191}Pt]Pt-Cys-Hoechst33258 in the stably 53BP1-EGFP–expressing U2OS-53BP1 cells. The representative fluorescent microphotographs and their quantitative analysis were shown in **Figs. 2-1-10 and 2-1-11**. The number of foci of 53BP1-EGFP per nucleus and the area ratio of foci to nuclei were quantified from five different images with 16–24 nuclei per image.

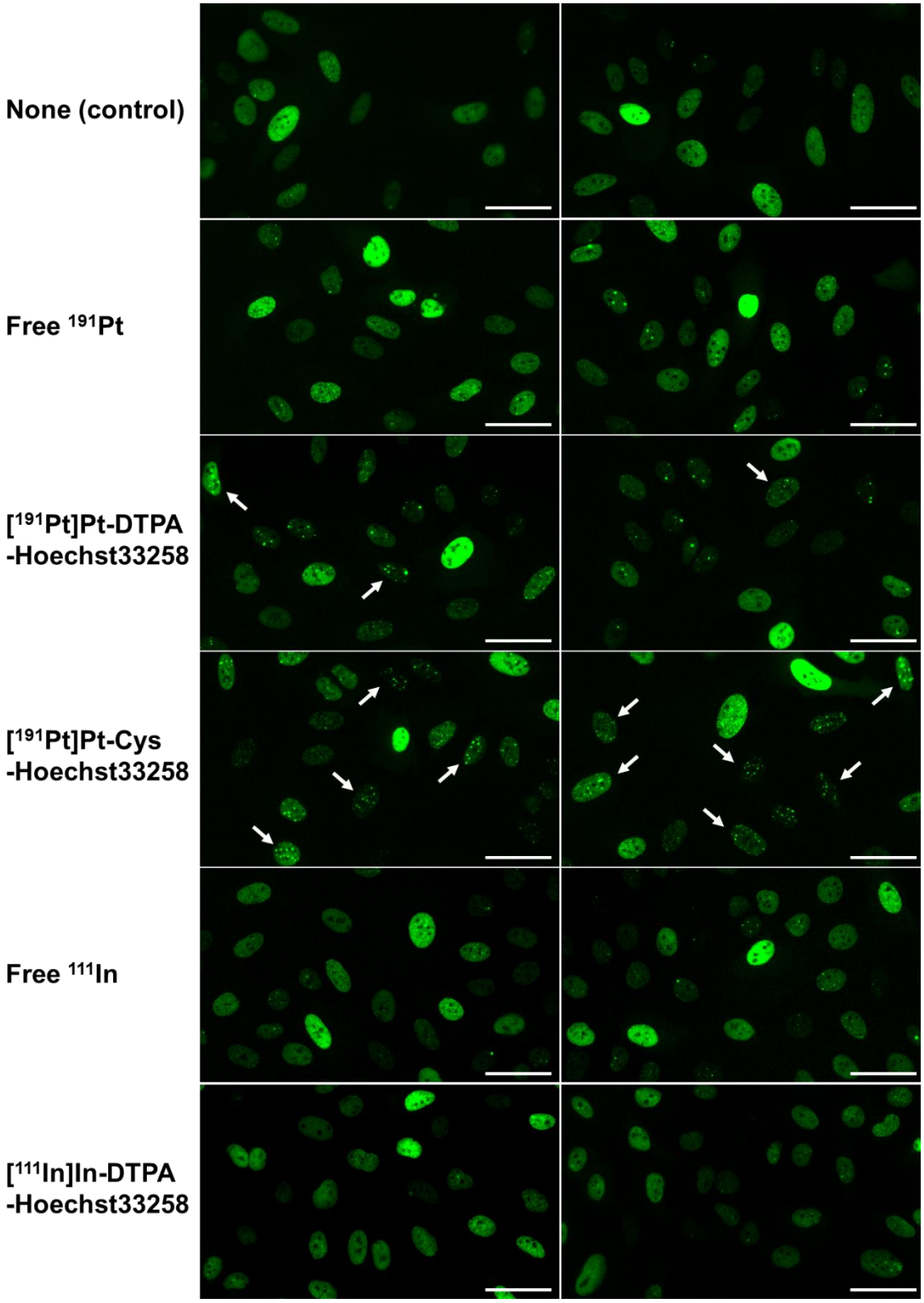

Figure 2-1-10. Representative microphotographs of U2OS-53BP1 cells 1.5 d after the treatment with free ^{191}Pt (410 kBq), [^{191}Pt]Pt-DTPA-Hoechst33258 (360 kBq), [^{191}Pt]Pt-Cys-Hoechst33258 (420 kBq), free ^{111}In (430 kBq), [^{111}In]In-DTPA-Hoechst33258 (440 kBq), or none (control). Signals of

53BP1-EGFP were indicated in green. Objective lens: 20×; scale bar: 50 μm. Arrows showed the cells with 53BP1 foci.

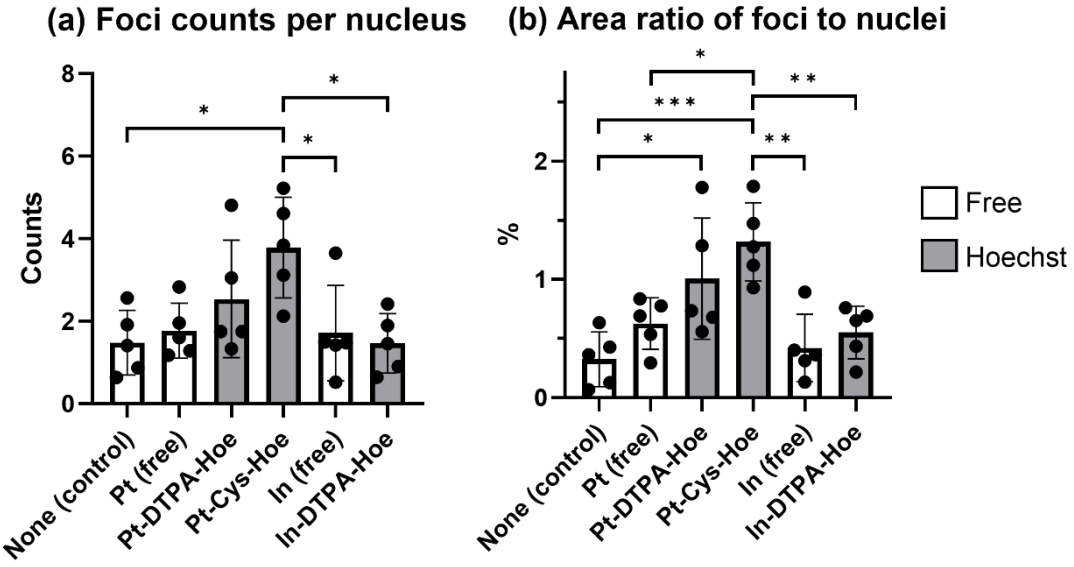

Figure 2-1-11. (a) The number of 53BP1 foci per nucleus. (b) The area ratio of 53BP1 foci to nuclei. Data were obtained from five different images with 16–24 nuclei per image and were expressed as the mean ± SD (n = 5). Each dot indicates a value per image. * $p < 0.05$, ** $p < 0.01$, *** $p < 0.001$.

The results found almost no increase of the 53BP1-EGFP foci in the treatment of free ^{191}Pt and ^{111}In compared to the control (first, second, and fifth panels in **Fig. 2-1-10**; **Fig. 2-1-11**). [^{191}Pt]Pt-DTPA-Hoechst33258 and [^{191}Pt]Pt-Cys-Hoechst33258, in contrast, induced more foci of 53BP1-EGFP than the control, whereas almost no increase was observed in the treatment of [^{111}In]In-DTPA-Hoechst33258 compared to the control (third, fourth, and sixth panels in **Fig. 2-1-10**; **Fig. 2-1-11**). The statistical results of multiple comparisons in the analysis of variance (ANOVA) showed that the 53BP1-EGFP foci were increased significantly in the treatment with [^{191}Pt]Pt-Cys-Hoechst33258 compared with the control, the free ^{191}Pt/^{111}In, and the [^{111}In]In-DTPA-Hoechst33258 (**Fig. 2-1-11**). The [^{191}Pt]Pt-DTPA-Hoechst33258 appeared to have relatively more foci of 53BP1-EGFP than the free ^{191}Pt/^{111}In and [^{111}In]In-DTPA-Hoechst33258 (**Fig. 2-1-11**). This result indicated that [^{191}Pt]Pt-Cys-Hoechst33258 caused DNA damage in the form of DSBs more efficiently than the other agents, consistent with [^{191}Pt]Pt-Cys-Hoechst33258 exhibiting the highest DNA-binding rate (**Fig. 2-1-9(b)**).

The greater DNA damage of the ^{191}Pt-labeled Hoechst33258 compared with that of the ^{111}In-labeled Hoechst33258 might be caused by a difference in not only the number of radionuclides delivered to DNA but also Auger electron emission yields between ^{191}Pt and ^{111}In (e.g., a calculated average of 13.3 e^- emitted per decay for ^{191}Pt and 7.4 e^- for ^{111}In, summarized in **Table 2** of *Preface*).

Although a rigorous discussion based solely on such Auger electron data from simulations is difficult, the suitability of radionuclides for therapeutic use in Auger electron therapy will be a matter for consideration from the perspective of not only chemical but also physical properties.

To summarize the biological evaluation of the labeled agents, the two ^{191}Pt-labeled Hoechst33258 showed more than 1 order of magnitude greater DNA-binding ability than [^{111}In]In-DTPA-Hoechst33258, suggesting the superior DNA-targeting effect of radio-Pt. [^{191}Pt]Pt-Hoechst33258 labeled via Cys led to a very high DNA-binding fraction and induced extensive DNA damage such as DSBs. Labeling the proper targeting module with ^{191}Pt via Cys would lead to DNA-targeting radio-Pt agents applicable in Auger electron therapy targeting DNA.

2. Development of ^{191}Pt-Labeled PI Polyamide Targeting Amplified Cancer Genes

Synthesis of ^{191}Pt-labeled PIP and evaluation of target sequence-binding ability, cell uptake, and DNA binding

The chemical designs of MYCN-Cys-R3-coumarin (MYCN-PIP) and GCC-Cys-R3-coumarin (GCC-PIP) were shown in **Fig. 2-2-1(a)**. The original MYCN-targeting PIP motif was established by Yoda *et al*.[8] The molecules consisting of MYCN-targeting PIP or short GCC-targeting PIP as a negative control were conjugated with cysteine (Cys) as a labeling site of ^{191}Pt, tri-arginine (R3) as a cell penetration module,[14] and the fluorescent compound coumarin. The representative radiochromatograms (preparative HPLC of the reaction mixtures and analytical HPLC analysis of the purified products) were shown in **Fig. 2-2-1(b)**. ^{191}Pt-labeled MYCN-PIP and GCC-PIP were obtained in a high RCY of 50–70%. After purification by preparative HPLC, ^{191}Pt-MYCN-PIP and ^{191}Pt-GCC-PIP were achieved with a RCP greater than 95% at the end of synthesis, as shown in the analytical HPLC chromatogram (**Fig. 2-2-1(b)**).

In the preceding section 1 on another ^{191}Pt-labeled compound via Cys (Cys-Hoechst33258), multiple labeled products were observed leading to low RCY and RCP, because of the high reactivity of Pt toward the thiol group. Additionally, the excess ligands to n.c.a. ^{191}Pt could contribute to this phenomenon. However, in the present compound, changing the molecular size and the position of Cys in the compounds led to high RCYs and RCPs for ^{191}Pt-MYCN-PIP and ^{191}Pt-GCC-PIP. ^{191}Pt-MYCN-PIP and ^{191}Pt-GCC-PIP were observed mainly as a single peak, and their tailing and fronting were slight. Cysteine was positioned next to the PIP molecule and tri-Arg; these middle molecules might create steric hindrance and suppress multivalent coordination of ^{191}Pt. Additionally, the product peak of ^{191}Pt-MYCN-PIP was sharper than that of ^{191}Pt-GCC-PIP in the analysis after preparative HPLC. These results may be due to the difference in molecular size of larger MYCN-PIP and smaller GCC-PIP. Thus, the current design would be suitable for further drug development of ^{191}Pt-labeled compounds via Cys.

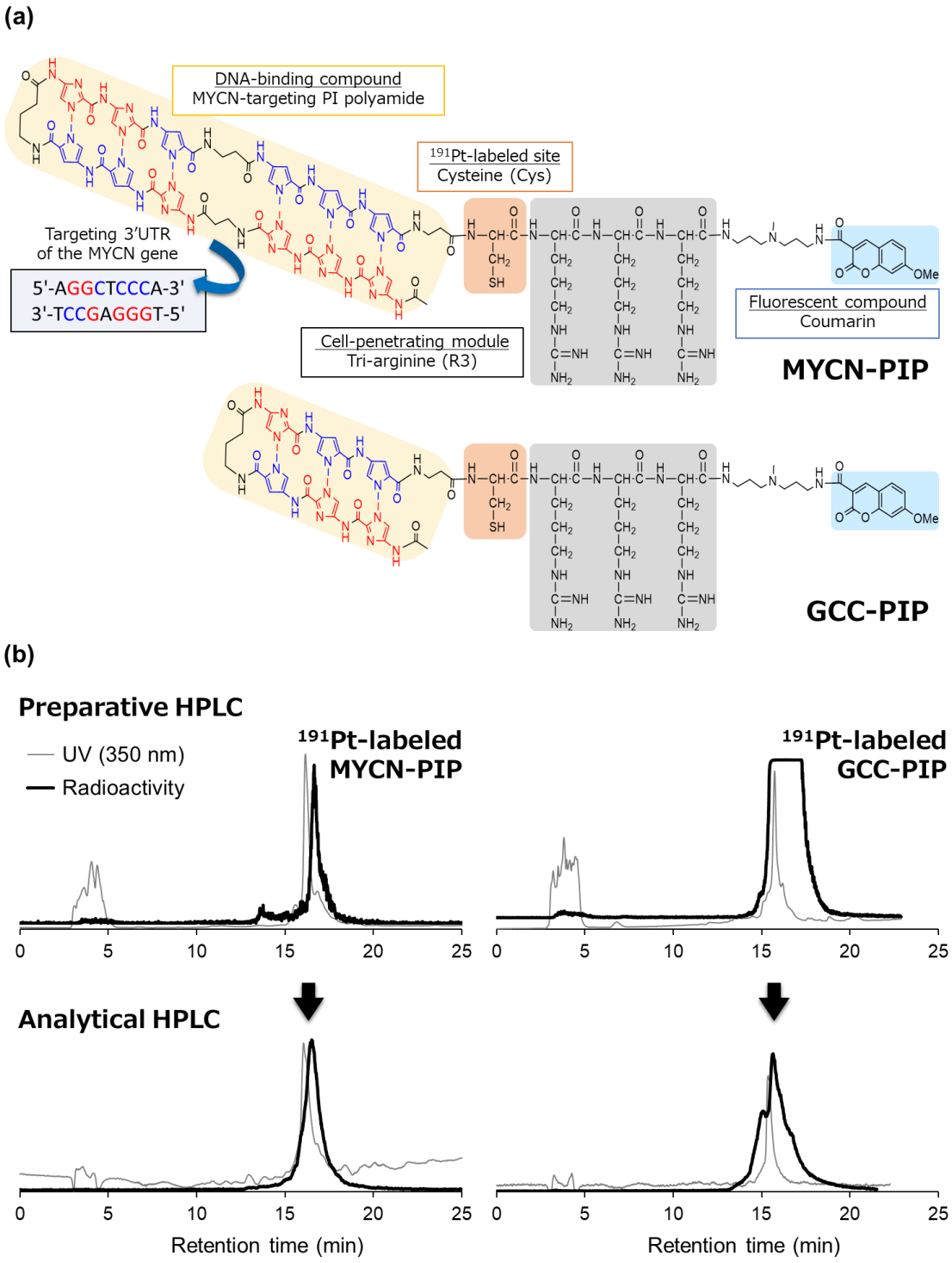

Figure 2-2-1. (a) Compound designs of MYCN-PIP and GCC-PIP. (b) Radiochromatograms of preparative and analytical HPLC for the product of [^{191}Pt]Pt-MYCN-Cys-R3-coumarin (^{191}Pt-MYCN-PIP) and [^{191}Pt]Pt-GCC-Cys-R3-coumarin (^{191}Pt-GCC-PIP). HPLC conditions: column, COSMOSIL 5C18-MS-II; gradient elution, A/B = 0.1%TFA in H_2O/CH_3CN = 95/5 → 30/70 (25 min).

The MYCN-targeting ability of MYCN-PIP was determined by gel electrophoretic mobility shift assay after it was labeled with ^{191}Pt. **Figure 2-2-2(a)** showed the fluorescence images of EtBr-stained oligonucleotides (lanes 1–5) and the autoradiograph of ^{191}Pt radioactivity (lane 6). Untreated oligonucleotides were observed in a single band (lane 1), and treatment with GCC-PIP and MYCN-PIP generated mobility-shifted bands (lanes 2 and 3). MYCN-PIP (lane 3) resulted in a much more intense shifted band than GCC-PIP (lane 2), suggesting that MYCN-PIP exhibits greater targeting ability than GCC-PIP, as expected from the compound design. ^{191}Pt-MYCN-PIP also generated the mobility-shifted bands observed for unlabeled MYCN-PIP (lanes 3, 5, and 6). In the autoradiograph, ^{191}Pt radioactivity was observed in the shifted band but not in the unshifted original band (lane 6). These results suggested that ^{191}Pt-MYCN-PIP maintained the MYCN-targeting ability of unlabeled MYCN-PIP, and ^{191}Pt-MYCN-PIP would form stable complexes with DNA.

The cellular uptake and DNA-binding behavior of ^{191}Pt-MYCN-PIP in cultured human neuroblastoma cells with different levels of MYCN gene amplification (amplified: Kelly; unamplified: SK-N-AS) was subsequently evaluated. The cellular uptake of ^{191}Pt-MYCN-PIP was saturated within 3 h after incubation and was similar between the two cell lines (**Fig. 2-2-2(b)**, left). ^{191}Pt-MYCN-PIP exhibited the greatest cellular uptake, followed by ^{191}Pt-GCC-PIP and free ^{191}Pt (**Fig. 2-2-2(b)**, right). The amount of ^{191}Pt bound to DNA was approximately the same in both the Kelly and SK-N-AS cell lines with different copy numbers of the MYCN gene (**Fig. 2-2-2(c)**). Both the cellular uptake and the DNA-binding fraction of ^{191}Pt-MYCN-PIP were one order of magnitude greater than those of ^{191}Pt-GCC-PIP. These results indicated ^{191}Pt-MYCN-PIP was more readily transported into cells, retained longer in the cells, and more stably bound to DNA than ^{191}Pt-GCC-PIP. Therefore, the hydrophobicity, membrane affinity, and binding strength of PIP-DNA for MYCN-PIP would be greater than those of GCC-PIP. Unfortunately, no differences in cell uptake and DNA-binding ability of ^{191}Pt-MYCN-PIP were observed between MYCN-amplified Kelly and nonamplified SK-N-AS cell lines (**Fig. 2-2-2(b) and (c)**). This result means that ^{191}Pt-MYCN-PIP bound to not only the target sequence but also other genomic regions, thus raising concerns about off-target effects.

To evaluate DNA double-strand breaks (DSBs) induced by ^{191}Pt-MYCN-PIP, the DSB marker 53BP1 was fluorescently imaged (**Fig. 2-2-2(d)**). A substantial increase of the 53BP1-EGFP foci was observed in the treatment of ^{191}Pt-MYCN-PIP, whereas almost no increase was observed in the treatment of MYCN-PIP; the DSBs were expected to be caused by Auger electrons emitted from ^{191}Pt-MYCN-PIP.

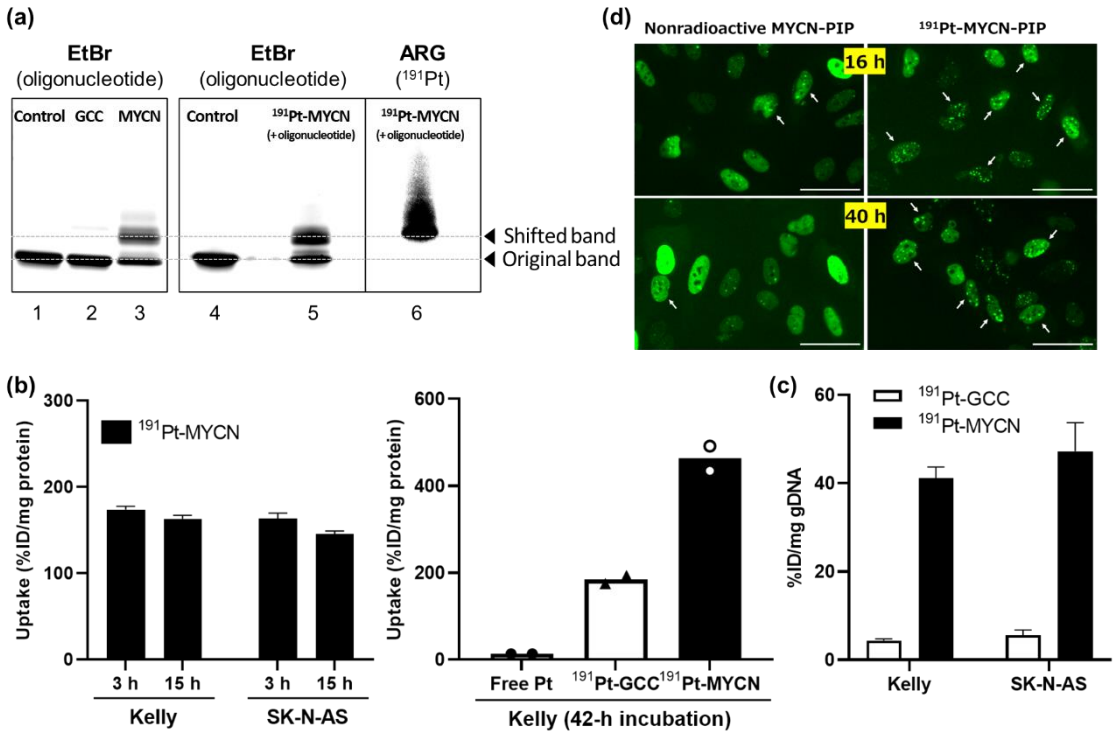

Figure 2-2-2. (a) Gel electrophoretic mobility shift assay of oligonucleotides treated with no agent (control), nonradioactive GCC-PIP (GCC), and nonradioactive MYCN-PIP (MYCN) or with ^{191}Pt-MYCN-PIP (^{191}Pt-MYCN) and nonradioactive MYCN-PIP. Lanes 1–5, fluorescence images of EtBr-stained oligonucleotides; lane 6, an autoradiograph (ARG) of ^{191}Pt radioactivity. Lanes 5 and 6 of the same experiment and sample were detected by fluorescence and radioactivity, respectively. (b) Cellular uptake (%ID/mg protein) of ^{191}Pt-MYCN-PIP (80–90 kBq/mL) in Kelly and SK-N-AS cells after 3 and 15 h of incubation ((8–9) × 10^5 cells/6-wells were seeded 1 day before the assay; n = 3, left). Cellular uptake (%ID/mg protein) of free ^{191}Pt, ^{191}Pt-GCC-PIP, ^{191}Pt-MYCN-PIP (160–180 kBq/mL) in Kelly cells after 42 h of incubation (1 × 10^5 cells/24-wells were seeded 1 day before the assay; n = 2, right). (c) DNA-binding rate (%ID/mg genomic DNA) of ^{191}Pt-GCC-PIP (80 kBq/mL) and ^{191}Pt-MYCN-PIP (65 kBq/mL) in Kelly cells after 1 d of incubation (n = 3). (d) Representative microphotographs of U2OS-53BP1 cells 16 and 40 h after the treatment with nonradioactive MYCN-PIP (1.5 nmol) with or without ^{191}Pt-MYCN-PIP (290 kBq). Signals of 53BP1-EGFP were indicated in green. Objective lens: 20×; scale bars: 50 μm. Arrows showed the cells with 53BP1 foci.

Cytotoxicity and DNA-damaging efficacy of ^{191}Pt-MYCN-PIP

The cytotoxicity was evaluated via a cell viability assay using three different cell lines (amplified: Kelly, SK-N-DZ; unamplified: SK-N-AS) treated with ^{191}Pt-MYCN-PIP, MYCN-PIP, or PBS. The

copy number of the MYCN gene in Kelly cells is greater than that in SK-N-DZ cells.[15] As expected, the cytotoxicity of ^{191}Pt-MYCN-PIP differed among the three cell lines (**Fig. 2-2-3(a)**). For highly MYCN-amplified Kelly cells, ^{191}Pt-MYCN-PIP decreased cell viability substantially more than only nonradioactive MYCN-PIP or PBS. A moderate effect of ^{191}Pt-MYCN-PIP on slightly amplified SK-N-DZ cells and no significant effect of ^{191}Pt-MYCN-PIP on unamplified SK-N-AS cells were observed when compared with the effects of only nonradioactive MYCN-PIP or PBS. Thus, the cytotoxicity of ^{191}Pt-MYCN-PIP was greater in Kelly cells (highly amplified) than in SK-N-DZ (moderately amplified) and SK-N-AS (unamplified) cells (**Fig. 2-2-3(a)**), although the DNA-binding fraction of ^{191}Pt-MYCN-PIP was approximately the same in all the cell lines with the different MYCN copy numbers (**Fig. 2-2-2(c)**). Since Kelly is one of the highest expressions of MYCN in human neuroblastoma cell lines,[15] its survival hallmark depends on MYCN-related transcription.[9] The present results expect that Auger-electron emitting ^{191}Pt-MYCN-PIP damaged the target MYCN gene and the cytotoxicity could depend on the role of the MYCN gene in each cell line.[9]

This speculation is supported by the results of the RT-qPCR analysis and the FISH analysis. The RT-qPCR analysis of the MYCN gene showed that the MYCN gene expression differed substantially among the cell lines (**Fig. 2-2-3(b)**, left). The highest expression was observed in Kelly cells, approximately one-tenth expression was observed in SK-N-DZ cells, and little expression was observed in SK-N-AS cells. In all the cells, treatment with ^{191}Pt-MYCN-PIP decreased the expression of MYCN when compared with treatment with MYCN-PIP (**Fig. 2-2-3(b)**, right), suggesting that Auger-electron emitting ^{191}Pt affected MYCN gene expression. As another evaluation of the damaging effect of ^{191}Pt-MYCN-PIP on the MYCN gene, FISH imaging in Kelly cells was conducted. In highly MYCN-amplified Kelly cells, many signals of the MYCN gene were observed (**Fig. 2-2-3(c)**). Approximately the same number of signals observed in nuclei treated with PBS was also observed in nuclei treated with MYCN-PIP. In contrast, a significant decrease in MYCN signaling was observed in nuclei treated with ^{191}Pt-MYCN-PIP. These results were consistent with the previously discussed RT-qPCR results. Collectively, the therapeutic ability of ^{191}Pt-MYCN-PIP depended on the copy number and expression of the MYCN gene, suggesting a potential strategy of targeting key genes involved in the survival mechanism of cancer in Auger electron therapy.

To evaluate DNA replication stress following damage to the transcription factor MYCN gene, immunostaining with anti-dsDNA was carried out. The cytosolic dsDNA released by cell damage and DNA cleavage can be recognized by anti-DNA and compose immune complexes.[16] Free ^{191}Pt did not induce a change; the cells were similar to those in PBS (**Fig. 2-2-3(d)**). MYCN-PIP and ^{191}Pt-GCC-PIP resulted in a few cytosolic dsDNA granules outside the cell nuclei. However, ^{191}Pt-MYCN-PIP resulted in numerous cytosolic dsDNA granules, and the fluorescence signal was significantly stronger after treatment with ^{191}Pt-MYCN-PIP than treatments with MYCN-PIP and ^{191}Pt-GCC-PIP. Such cytosolic dsDNA granules are known to induce type I interferons such as IFN-α

and IFN-β by activating the cGAS-STING pathway.[17] The RT-qPCR analysis also found more IFN-α and IFN-β released in Kelly cells treated with ^{191}Pt-MYCN-PIP than in Kelly cells treated with PBS or nonradioactive MYCN-PIP (**Fig. 2-2-3(e)**).

Interestingly, damage to MYCN and its related transcription system using ^{191}Pt-MYCN-PIP led to an increase in cytosolic dsDNA granules and IFN-α/β. These results are likely because the mechanism for maintaining DNA replication and genome stability significantly depends on the MYCN gene in MYCN-amplified cells.[9] Compared with the control conditions at a low background level, the fluorescent intensity of anti-dsDNA also increased for nucleic dsDNA in the treatment of ^{191}Pt-MYCN-PIP in addition to the increase for cytosolic dsDNA. This result means that damage to the MYCN gene by ^{191}Pt-MYCN-PIP might lead to (1) genomic structural changes that make antigens open, (2) DNA fragmentations, and (3) a release of cytosolic dsDNA fragments. Additionally, although recent studies have mentioned intercellular interaction such as the bystander effect in Auger electron therapy,[18] the DNA damage and its response factors induced by Auger-electron emitting ^{191}Pt-MYCN-PIP could propagate the neighbor cells.

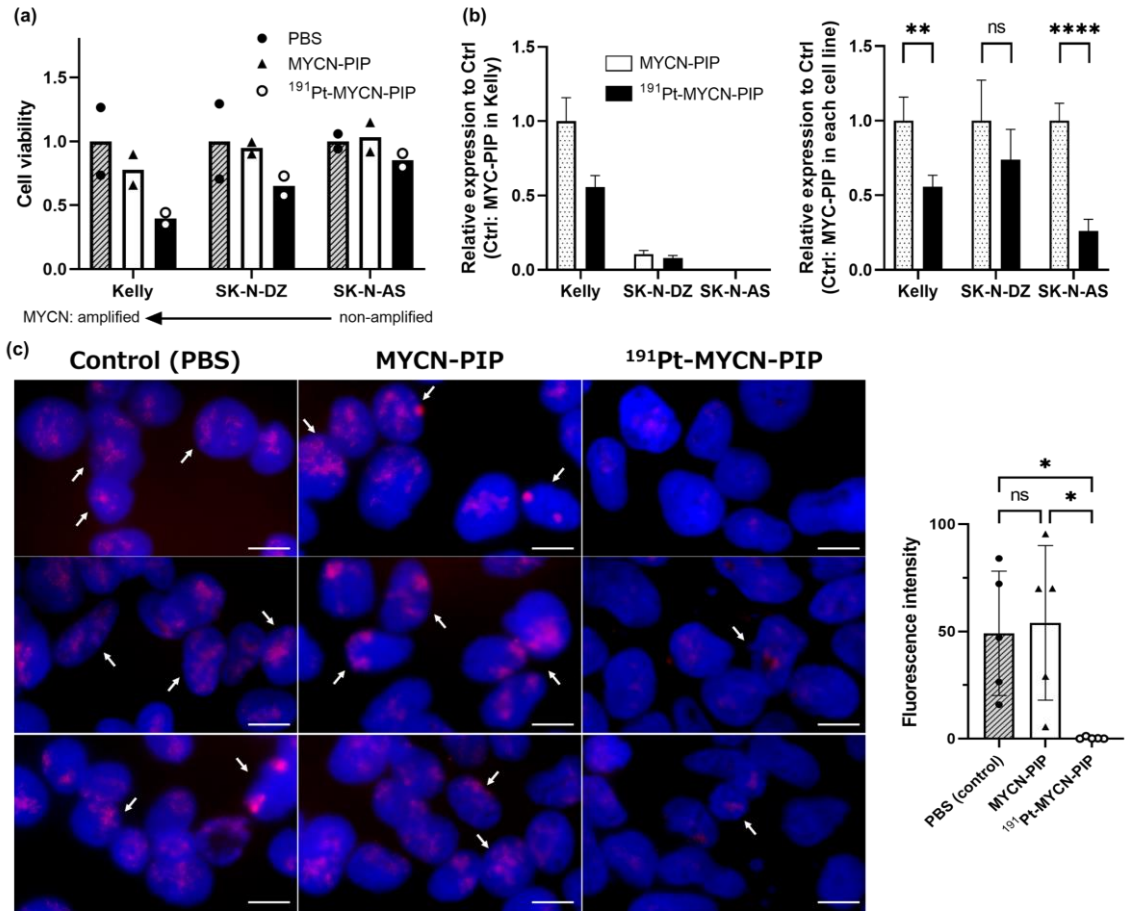

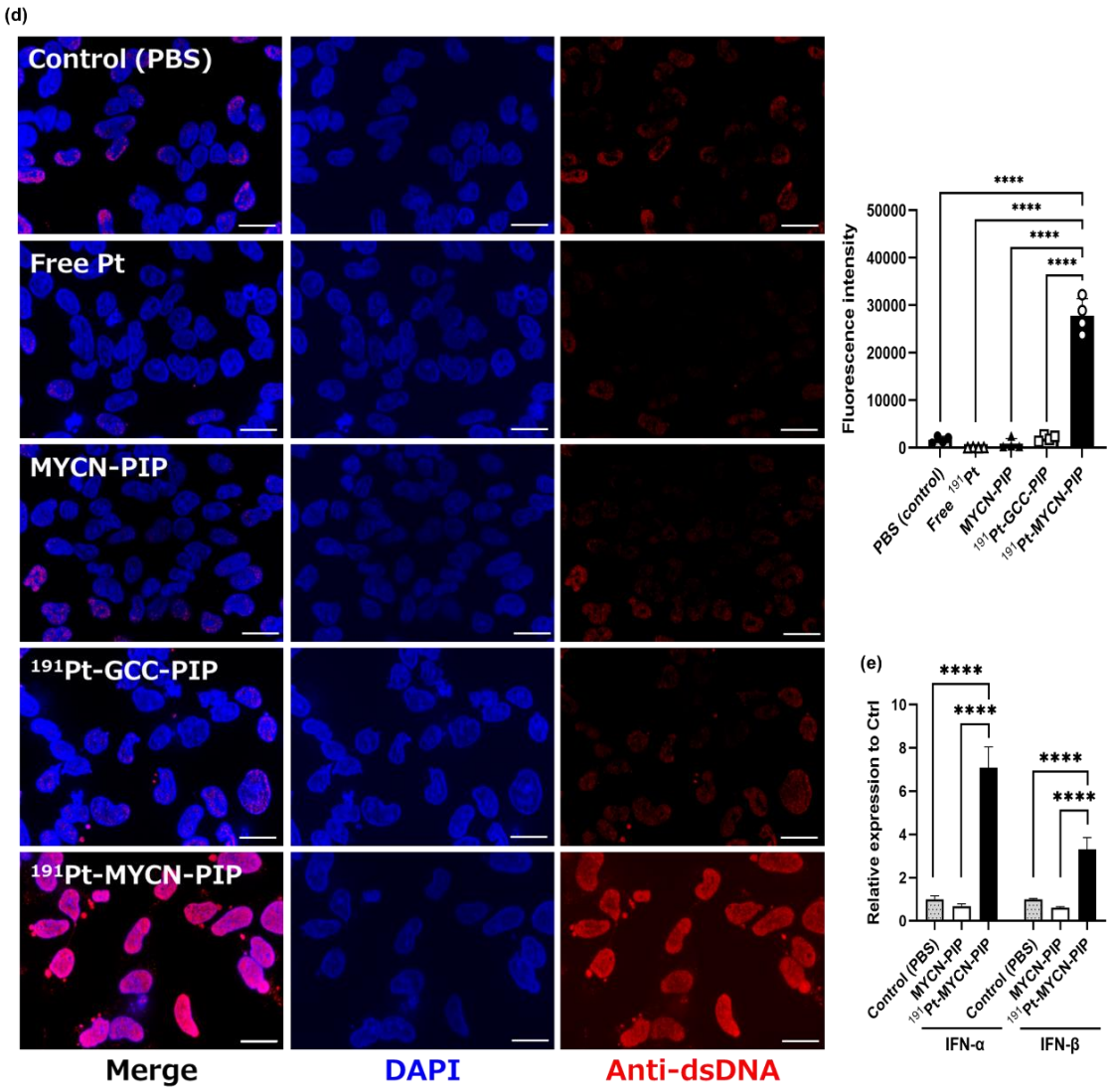

Figure 2-2-3. (a) Cell viability evaluated by live-cell staining. ^{191}Pt-MYCN-PIP (457 kBq) and nonradioactive MYCN-PIP (0.05 nmol), only nonradioactive MYCN-PIP (0.05 nmol), or PBS was added to the cells, and the cells were incubated for 1.5 d (n = 2). (b) Relative expression of the MYCN gene in RT-qPCR for MYCN in Kelly, SK-N-DZ, and SK-N-AS cells (left, Ctrl = MYCN-PIP in Kelly; right, Ctrl = MYCN-PIP in each cell line; Ctrl column filled with dots and defined as relative expression = 1). ^{191}Pt-MYCN-PIP (457 kBq for 24-well, 732 kBq for 6-well) and nonradioactive MYCN-PIP (0.05 nmol for 24-well, 0.08 nmol for 6-well), only nonradioactive MYCN-PIP (0.05 nmol for 24-well, 0.08 nmol for 6-well), or PBS was added to the cells, and the cells were incubated for 2 d (n = 4). (c) Representative fluorescence images of FISH imaging in Kelly cells. ^{191}Pt-MYCN-PIP (274 kBq) and nonradioactive MYCN-PIP (0.03 nmol), only nonradioactive MYCN-PIP (0.03 nmol), or PBS was added to the cells, and the cells were incubated for 1.5 d. Cell nuclei were indicated in blue (DAPI), and the MYCN gene was indicated in red. Scale bar: 10 μm. The quantitative data

were expressed as the ratio of the total fluorescence intensity of the MYCN gene to the nucleus area. (d) Representative images of immunofluorescent staining of double-strand DNA (dsDNA) in Kelly cells. ^{191}Pt-MYCN-PIP (836 kBq) and nonradioactive MYCN-PIP (0.1 nmol), ^{191}Pt-GCC-PIP (872 kBq) and nonradioactive GCC-PIP (0.1 nmol), free ^{191}Pt (899 kBq), only nonradioactive MYCN-PIP (0.1 nmol), or PBS was added to the cells, and the cells were incubated for 2 d. Cell nuclei were indicated in blue (DAPI), and dsDNA was indicated in red. Scale bar: 20 μm. Arrows showed the cytosolic dsDNA. The quantitative data were expressed as the ratio of the total fluorescence intensity of dsDNA to the nucleus area. (e) Relative expression of the MYCN gene in RT-qPCR for IFN-α and IFN-β in Kelly cells. The treatment of PBS was defined as a control (relative expression = 1). ^{191}Pt-MYCN-PIP (457 kBq for 24-well) and nonradioactive MYCN-PIP (0.05 nmol for 24-well), only nonradioactive MYCN-PIP (0.05 nmol for 24-well), or PBS was added to the cells, and the cells were incubated for 2 d (n = 4).

In vivo evaluation of intravenously injected ^{191}Pt-MYCN-PIP in mice bearing neuroblastoma tumors

The biodistribution of ^{191}Pt-MYCN-PIP was evaluated in a xenograft mouse model bearing Kelly tumors after intravenous injection (**Fig. 2-2-4(a)**). The whole-body retention and blood concentration agreed with the biphasic decay curve with two main components (**Fig. 2-2-4(b)**: early time points, blue; late time points, red), and ~50% of the injected dose remained in the mice's bodies 7 d after injection (**Fig. 2-2-4(b)**, upper panel). The blood concentration decreased to ~1 %ID/g, mainly within 1 d after injection (**Fig. 2-2-4(b)**, lower panel).

The biodistribution was represented in the upper panel of **Fig. 2-2-4(c)** (lung, liver, spleen, kidney, and bone) and the lower panel of **Fig. 2-2-4(c)** (blood, brain, intestine, muscle, and tumor). A high accumulation of ^{191}Pt-MYCN-PIP in the lungs was observed in the early time points; the peak was 342 %ID/g at 2 min after injection (**Fig. 2-2-4(c)**, upper panel). Such high accumulation in the lungs was temporary, as evidenced by the uptake (30–40 %ID/g) in the late time points. The accumulation in the spleen increased over time until 1 d (100 %ID/g) and then decreased in the late time points (**Fig. 2-2-4(c)**, upper panel). Relatively high hepatic accumulation was observed; the peak was 26 %ID/g at 1 d (**Fig. 2-2-4(c)**, upper panel). Consequently, little accumulation of ^{191}Pt-MYCN-PIP was observed in tumors: less than 1 %ID/g (**Fig. 2-2-4(c)**, lower panel). The red blood cell (RBC) partitioning proceeded rapidly after the injection; the rate was 85% at 2 min and 55% thereafter at 1–4 d (**Fig. 2-2-4(d)**). In contrast, the plasma protein-binding rate was 50% at 2 min and increased to 83% at 1 d after injection.

Yoda *et al*. reported that the parental MYCN-targeting PIP expressed therapeutic efficacy and damaged the MYCN gene in mice bearing Kelly tumors when administered by intravenous injection,[8] suggesting high tumor uptake of the parental PIP. However, the current ^{191}Pt-MYCN-PIP was mainly distributed in the RBCs instantly after intravenous injection (**Fig. 2-2-4(d)**), resulting in low tumor uptake and high uptake in the lungs, spleen, and liver (**Fig. 2-2-4(c)**). Almost no renal excretion of ^{191}Pt was observed even though small Pt agents such as radio-cisplatin have been shown to be excreted via the kidneys rapidly after intravenous injection, as shown in **Fig. 1-2-15** in section 2 of *Chapter 1*. Therefore, the labeled form of ^{191}Pt was maintained stably *in vivo* and the *in vivo* properties reflected the nature of hydrophilic and cationic R3-coumarin attached to the PIP scaffold. High hydrophilic and cationic poly-bases readily interact with plasma proteins or the membrane of RBCs,[19] inducing their agglutination and an acute pulmonary embolism (PE).[20] The high accumulation of ^{191}Pt-MYCN-PIP in the lungs is likely due to the acute PE. For ^{191}Pt-MYCN-PIP to work via intravenous injection, the drug design should be improved by the replacement of R3-coumarin with tumor-targeting modules.

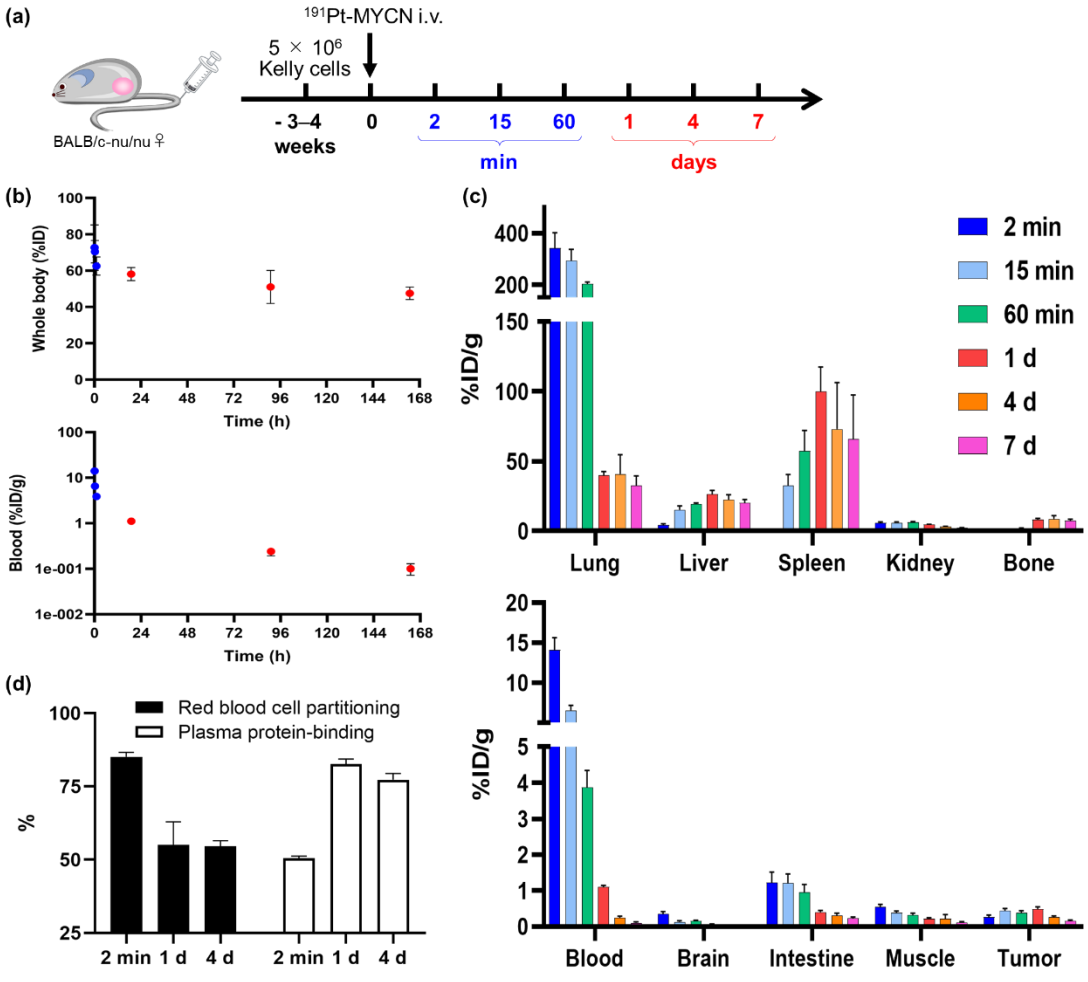

Figure 2-2-4. (a) Experimental schedule of *in vivo* experiments using mice bearing Kelly tumors to evaluate the biodistribution of ^{191}Pt-MYCN-PIP. Mice were intravenously (i.v.) injected with ^{191}Pt-MYCN-PIP (168 kBq) and nonradioactive MYCN-PIP (0.1 nmol, 5 nmol/kg BW). (b) Percentage of the injected dose for the whole body (upper panel, %ID) and percentage of the injected dose per gram of blood (lower panel, %ID/g), corrected to those with a body weight of 20 g (n = 5). (c) Biodistribution of ^{191}Pt-MYCN-PIP at 2 min to 7 d after intravenous injection (i.v.) in mice bearing Kelly tumors (n = 5). The data for blood were the same as in the lower panel of **Fig. 2-2-4(b)**. (d) Red blood cell partitioning rate (%) and plasma protein-binding rate (%) (n = 4).

Experimental therapy with intravenous injection of ^{191}Pt-MYCN-PIP was also conducted, and mice bearing Kelly and SK-N-AS tumors were compared (**Fig. 2-2-5(a)**). Due to the negligible tumor uptake of ^{191}Pt-MYCN-PIP (**Fig. 2-2-4(c)**), no therapeutic efficacy was observed (**Fig. 2-2-5(b)**). Although this work used mice bearing tumors with volumes of 100–600 mm^3, such tumors might be too large for Auger electron therapy. The uses of Auger-electron emitting agents may be limited to small-volume tumors (<1 mm diameter) because of the effective range of Auger electrons that is much smaller than a single cell. The whole-body retention was approximately the same; however, the uptake in the Kelly tumors was slightly greater than that in the SK-N-AS tumors (**Figs. 2-2-5(c) and (d)**). ^{191}Pt-MYCN-PIP might be retained longer in MYCN-amplified tumors than in the unamplified ones (**Fig. 2-2-5(d)**), likely because it bound to the target gene. If the compound is delivered more to tumors, the difference may be more apparent.

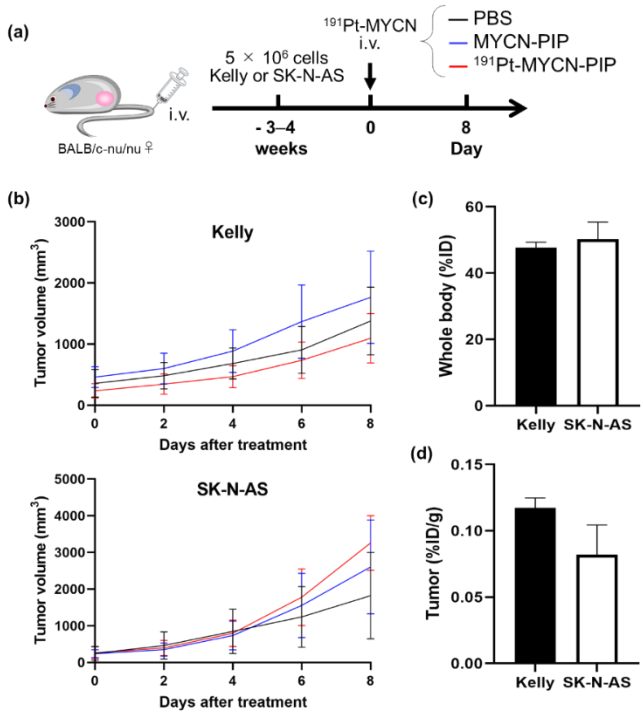

Figure 2-2-5. (a) Experimental schedule of *in vivo* experiments using mice bearing Kelly or SK-N-AS tumors for experimental therapy of ^{191}Pt-MYCN-PIP. PBS, only nonradioactive MYCN-PIP (0.3 nmol), or ^{191}Pt-MYCN-PIP (690 kBq) and nonradioactive MYCN-PIP (0.3 nmol) was intravenously injected into mice (n = 5). (b) Tumor growth curves in experimental therapy of ^{191}Pt-MYCN-PIP for mice bearing the Kelly or SK-N-AS tumors. (c) Percentage of the injected dose for the whole body (%ID), corrected to those with a body weight of 20 g (n = 5). (d) Percentage of the injected dose per 1 g of Kelly or SK-N-AS tumor at 8 d after intravenous injection, corrected to those with a body weight of 20 g (n = 5).

In vivo investigation of intratumoral injection of ^{191}Pt-MYCN-PIP in mice bearing Kelly tumors

The results presented thus far suggested that the compound design should be improved to enable its delivery to a tumor via intravenous injection. Nevertheless, to evaluate whether ^{191}Pt-MYCN-PIP works after being delivered to a tumor, intratumoral injection to mice bearing Kelly tumors was evaluated *in vivo* (**Fig. 2-2-6(a)**). The whole-body retention and tumor uptake in Kelly tumor-bearing mice were shown in **Fig. 2-2-6(b)**, where the intravenous and intratumoral injections were compared; the biodistribution after the intratumoral injection was summarized in **Fig. 2-2-6(c)**.

At 4 d after intratumoral injection of ^{191}Pt-MYCN-PIP, the whole-body uptake was approximately 60%ID and high accumulation in Kelly tumors was observed (**Fig. 2-2-6(b)**). Most of the ^{191}Pt-MYCN-PIP was retained in the Kelly tumors and not excreted (357 %ID/g at 4 d) (**Fig. 2-2-6(b)**). ^{191}Pt-MYCN-PIP hardly diffused to other organs at 2 min (**Fig. 2-2-6(c)**). At 1 d, slight hepatic uptake and renal excretion were observed (**Fig. 2-2-6(c)**). These results were attributed to leakage into subcutaneous tissues outside the tumor or to extracellular excretion of the tumor after its uptake. The *in vivo* DNA-binding rate and the DNA-binding-to-cell-uptake ratio were comparable to those in the *in vitro* experiments (**Table 2-2-1**).

To investigate whether ^{191}Pt-MYCN-PIP causes DNA damage *in vivo*, γH2AX as a DSB marker and dsDNA as a radiation-mediated DNA damage response and replication stress marker were immunohistochemically evaluated in dissected Kelly tumors (**Figs. 2-2-6(e) and (f)**). Compared with unlabeled MYCN-PIP and PBS, the ^{191}Pt-MYCN-PIP tended to increase the number of γH2AX-positive cells at 1 d, although the difference was not statistically significant (**Fig. 2-2-6(e)**). More cytosolic dsDNA granules were observed in cells treated with ^{191}Pt-MYCN-PIP compared with the amounts observed in cells treated with PBS or nonradioactive MYCN-PIP (**Fig. 2-2-6(f)**).

To summarize, in the *in vivo* evaluation with intratumoral injection, ^{191}Pt-MYCN-PIP was

uptaken into tumor cells and bound to DNA, causing DNA damage and cytosolic dsDNA, which was consistent with the *in vitro* evaluation of ^{191}Pt-MYCN-PIP. In recent years, the cGAS-STING pathway has been attracting interest in cancer therapy involving DNA damage and the natural antitumor immune system.[17] Several studies reported that radiation sometimes activates the antitumor immune system related to the cGAS-STING pathway.[21] Therefore, damage to key oncogenes by Auger electrons might not only induce cell death but also activate the antitumor immune system via the cGAS–STING pathway.

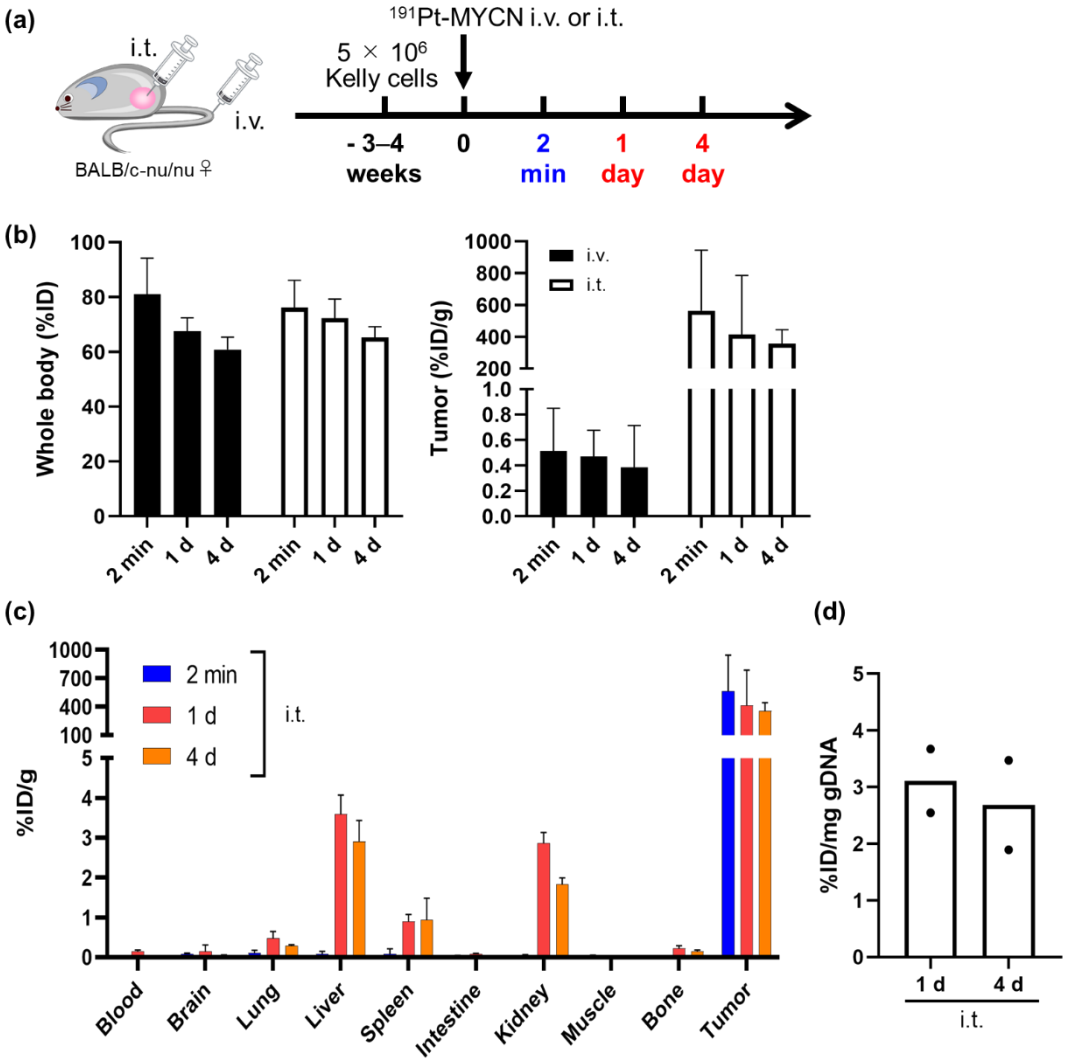

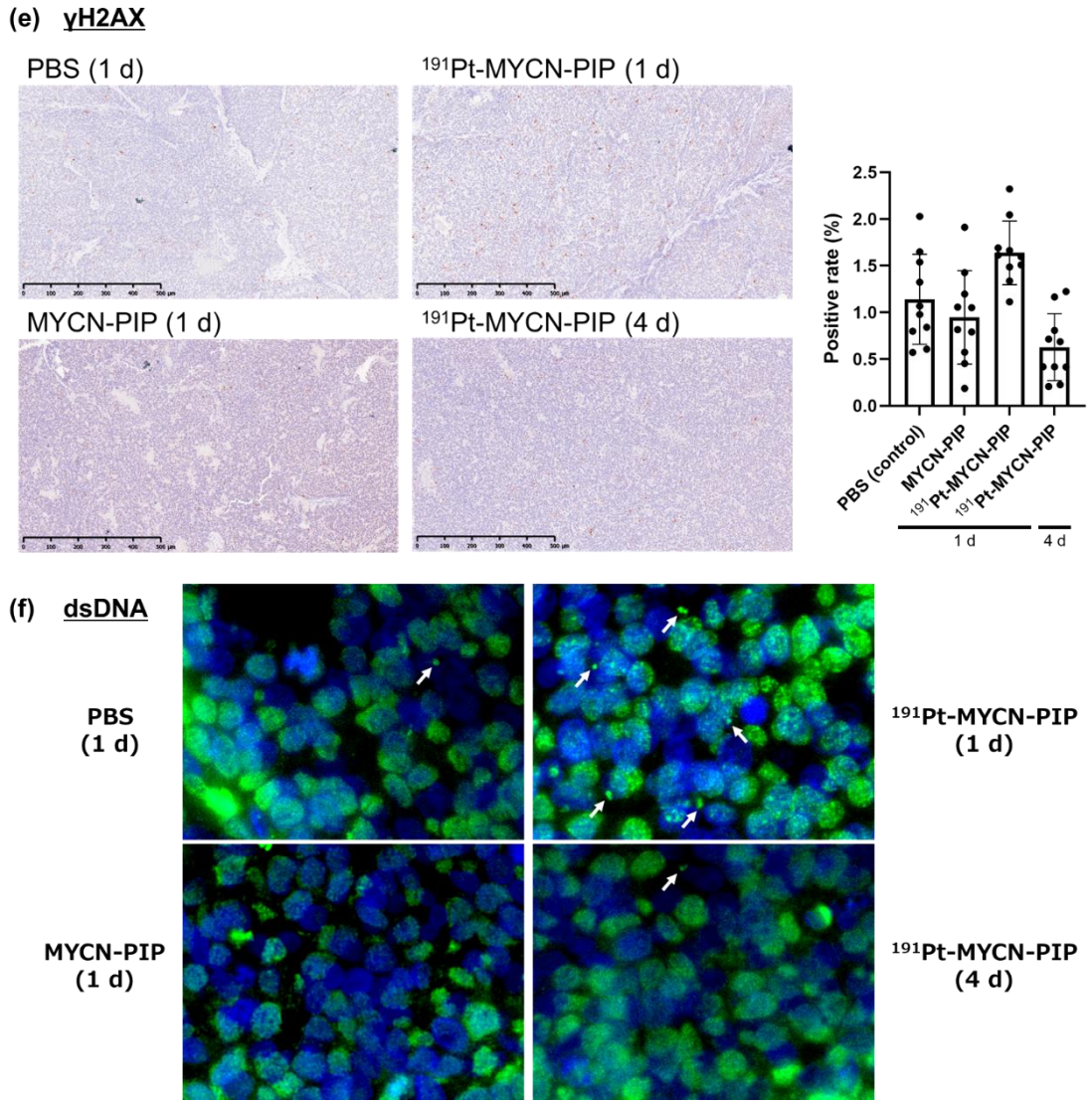

Figure 2-2-6. (a) Experimental schedule of *in vivo* experiments using mice bearing Kelly tumors (n = 4 for distribution analyses; n = 3 for histological analyses), where intravenous (i.v.) and intratumoral (i.t.) injections were compared (^{191}Pt-MYCN-PIP: 229 kBq for distribution analyses; 975 kBq for histological analyses. Nonradioactive MYCN-PIP: 0.1 nmol, 5 nmol/kg BW for distribution analyses; 0.4 nmol, 20 nmol/kg BW for histological analyses). (b) Percentage of the injected dose for the whole body (corrected to those with a body weight of 20 g, n = 4), percentage of the injected dose per 1 g of the Kelly tumors (%ID/g). (c) Biodistribution of ^{191}Pt-MYCN-PIP at 2 min, 1 d, and 4 d after intratumoral injection in mice bearing Kelly tumors (n = 4). The data for the tumor were the same as the data shown in the right panel of **Fig. 2-2-6(b)**. The values were corrected to those with a body weight of 20 g. (d) DNA-binding fraction of ^{191}Pt per mg of tumor gDNA (%ID/mg gDNA) (n = 2). (e) Representative images of γH2AX in histological analyses. Tumors were dissected at 1 d and 4 d after the intratumoral injection of ^{191}Pt-MYCN-PIP, nonradioactive MYCN-PIP, or PBS. γH2AX-

positive nuclei were indicated in red. Scale bar: 50 μm. The number of γH2AX-positive nuclei was counted from five different images including approximately 500 nuclei per image from each of two mice, and quantitative data were expressed as the ratio of positive nuclei to total nuclei. (f) Representative fluorescence images of dsDNA in histological analyses. Cell nuclei were indicated in blue (DAPI), and dsDNA was indicated in green. Arrows showed the cytosolic dsDNA.

Table 2-2-1. DNA-binding rate (%ID/mg DNA) and the ratio of DNA binding to cell fraction (%) of ^{191}Pt in Kelly cells at 1 d after the incubation or injection of ^{191}Pt-MYCN-PIP.

	In vitro (n = 3)	*In vivo* (n = 2)
Cell or tumor fraction (%ID)	24 ± 1	56; 64
DNA-binding/cell fraction (%)	0.38 ± 0.04	0.30; 0.46
DNA-binding rate (%ID/mg gDNA)	41 ± 3	3.7; 2.5
DNA volume per fraction (μg)	2.2 ± 0.4	17; 34

Chapter 2—Conclusion

Chapter 2 demonstrated the two ^{191}Pt-labeled DNA-targeting compounds, ^{191}Pt-labeled Hoechst33258 and ^{191}Pt-MYCN-PIP. These compounds successfully increased the DNA-binding fraction of ^{191}Pt, DNA damage like DSBs, and cytotoxicity under certain conditions.

First, it was shown that labeling the proper DNA targeting module with ^{191}Pt increased the DNA-binding fraction of ^{191}Pt and DNA damage efficiently. Two labeling methods for n.c.a. radio-Pt via the multidentate-ligand polycarboxylic acids DTPA and EDDA and via the sulfur-containing amino acid Cys were developed. These methods successfully produced DNA-targeting complexes [^{191}Pt]Pt-DTPA-Hoechst33258 and [^{191}Pt]Pt-Cys-Hoechst33258. The two radio-Pt–based agents indicated more than one order of magnitude greater DNA-binding ability than [^{111}In]In-DTPA-Hoechst33258. The higher DNA-binding fraction of [^{191}Pt]Pt-Cys-Hoechst33258 caused DNA damage more efficiently than [^{191}Pt]Pt-DTPA-Hoechst33258, suggesting that radio-Pt is efficiently delivered to DNA when labeled via Cys. The superior DNA affinity of ^{191}Pt-labeled Hoechst33258 compared with ^{111}In-labeled Hoechst33258 might be attributable to the direct DNA-binding of ^{191}Pt. To summarize the biological evaluation of the labeled agents, [^{191}Pt]Pt-Hoechst33258 labeled via Cys showed a very high DNA-binding fraction and induced extensive DNA damage such as DSBs.

Second, the oncogene MYCN-targeting compound labeled with ^{191}Pt via Cys: ^{191}Pt-MYCN-PIP was first developed. ^{191}Pt-MYCN-PIP bound to DNA efficiently and caused DNA damage, decreasing MYCN gene expression and cell viability, especially in MYCN-amplified Kelly cells. Thus, Auger-electron emitting drugs that target key genes in cell survival have the potential to be a novel therapy for various tumor types. ^{191}Pt-MYCN-PIP also induced a substantial increase in cytosolic dsDNA granules and generated proinflammatory cytokines, IFN-α/β, in Kelly cells. These findings may open a new strategy of gene-targeted Auger electron therapy not only to induce cell death but also to activate a DNA-damage response as an anticancer immune system.

References

1. (a) Smith PHS, Taylor DM. Distribution and retention of the antitumor agent ^{195m}Pt-cis-dichlorodiammine platinum (II) in man. *J Nucl Med* **1974**; 15: 349–351. (b) Lange RC, Spencer RP, Harder HC. The antitumor agent cis-Pt$(NH_3)_2Cl_2$: distribution studies and dose calculations for ^{193m}Pt and ^{195m}Pt. *J Nucl Med* **1973**; 14: 191–195. (c) Areberg J, Björkman S, Einarsson L, Frankenberg B, Lundqvist H, Mattsson S, Norrgren K, Scheike O, Wallin R. Gamma camera imaging of platinum in tumours and tissues of patients after administration of ^{191}Pt-cisplatin. *Acta Oncol* **1999**; 38(2): 221-8.

2. (a) Nadar RA, Farbod K, der Schilden KC, Schlatt L, Crone B, Asokan N, Curci A, Brand M, Bornhaeuser M, Iafisco M, Margiotta N, Karst U, Heskamp S, Boerman OC, Beucken JJJP, Leeuwenburgh SCG. Targeting of radioactive platinumbisphosphonate anticancer drugs to bone of high metabolic activity. *Sci Rep* **2020**; 10: 5889. (b) Muns JA, Montserrat V, Houthoff HJ, der Schilden KC, Zwaagstra O, Sijbrandi NJ, Merkul E, Dongen GAMS. In vivo characterization of platinum(II)-based linker technology for the development of antibody−drug conjugates: taking advantage of dual labeling with ^{195m}Pt and ^{89}Zr. *J Nucl Med* **2018**; 59: 1146−1151. (c) Bates PI, Sharma HL, Murrer BA, Bernard CFJ, McAuliffe CA. The synthesis of ^{191}Pt labelled JM216, an orally active platinum anti-tumour agent. *Appl Radiat Isot* **1997**; 48(4): 469–476.
3. (a) Price EW, Orvig C. Matching chelators to radiometals for radiopharmaceuticals. *Chem Soc Rev* **2014**; 43: 260–290. (b) Spang P, Herrmann C, Roesch F. Bifunctional gallium-68 chelators: past, present, and future. *Semin Nucl Med*; **2016**: 46(5): 373–394.
4. (a) Ivanov AI, Christodoulou J, Parkinson JA, Barnham KJ, Tucker A, Woodrow J, Sadler PJ. Cisplatin binding sites on human albumin. *J Biol Chem* **1998**; 273: 14721−14730. (b) Zimmermann T, Zeizinger M, Burda JV. Cisplatin interaction with cysteine and methionine, a theoretical DFT study. *J Inorg Biochem* **2005**; 99: 2184−2196. (c) Ma Z, Rao L, Bierbach U. Replacement of a thiourea-S with an amidine-NH donor group in a platinum−acridine antitumor compound reduces the metal's reactivity with cysteine sulfur. *J Med Chem* **2009**; 52: 3424−3427. (d) Yao X, Tracy CM, Bierbach U. Cysteine-directed bioconjugation of a platinum(II)−acridine anticancer agent. *Inorg Chem* **2019**; 58: 43−46. (e) Wang X, Guo Z. The role of sulfur in platinum anticancer chemotherapy. *Anti-Cancer Agents Med Chem* **2007**; 7: 19−34.
5. Watanabe N, Sawai H, Umeda I O, Tanada S, Kim EE, Yonekura Y, Sasaki Y. Molecular Therapy of Human Neuroblastoma Cells Using Auger Electrons of ^{111}In-Labeled N-myc Antisense Oligonucleotides. *J Nucl Med* **2006**; 47: 1670–1677
6. (a) Stine ZE, Walton ZE, Altman BJ, Hsieh AL, Dang CV. MYC, Metabolism, and Cancer. *Cancer Discov* **2015**; 5(10): 1024–1039. (b) Bradner JE, Hnisz D, Young RA. Transcriptional addiction in cancer. *Cell* **2017**; 168: 629−643. (c) Michalak EM, Burr ML, Bannister AJ, Dawson MA. The roles of DNA, RNA and histone methylation in ageing and cancer. *Nat Rev Molecular Cell Biology* **2019**; 20: 573–589. (d) Allis CD, Jenuwein T. The molecular hallmarks of epigenetic control. *Nat Rev Genetics* **2016**; 17: 487–500.
7. (a) Yu Z, Pandian GN, Hidaka T, Sugiyama H. Therapeutic gene regulation using pyrrole–imidazole polyamides. Advanced Drug Delivery Reviews. 2019; 147: 66–85. (b) Igarashi J, Fukuda N, Inoue T, Nakai S, Saito K, Fujiwara K, Matsuda H, Ueno T, Matsumoto Y, Watanabe T, *et al*. Preclinical study of novel gene silencer pyrrole-imidazole polyamide targeting human TGF-β1 promoter for hypertrophic scars in a common marmoset primate model. PLoS ONE **2015**; 10(5): e0125295.

8. Yoda H, Inoue T, Shinozaki Y, Lin J, Watanabe T, Koshikawa N, Takatori A, Nagase H. Direct targeting of MYCN Gene Amplification by site-specific DNA alkylation in neuroblastoma. *Cancer Res* **2019**; 79(4): 830–840.
9. (a) Huang M, Weiss WA. Neuroblastoma and MYCN. *Cold Spring Harb Perspect Med* **2013**; 3(10): a014415. (b) Durbin AD, Zimmerman MW, Dharia NV, Abraham BJ, Iniguez AB, Leahey NW, He S, Burger JMK, Root DE, Vazquez F, *et al*. Selective gene dependencies in MYCN-amplified neuroblastoma include the core transcriptional regulatory circuitry. *Nat Genetics* **2018**; 50: 1240–1246.
10. (a) Jamieson ER, Lippard SJ. Structure, recognition, and processing of cisplatin-DNA adducts. *Chem Rev* **1999**; 99: 2467−2498. (b) Wang D, Lippard SJ. Cellular processing of platinum anticancer drugs. *Nat Rev Drug Discovery* **2005**; 4: 307−320. (c) Johnstone TC, Suntharalingam K, Lippard SJ. The next generation of platinum drugs: targeted Pt(II) agents, nanoparticle delivery, and Pt(IV) prodrugs. *Chem Rev* **2016**; 116: 3436−3486.
11. (a) Pearson RG. Hard and soft acids and bases, HSAB, part 1: Fundamental principles. *J Chem Educ* **1968**; 45(9): 581. (b) Pearson RG. Hard and soft acids and bases, HSAB, part II: Underlying theories. *J Chem Educ* **1968**; 45: 10, 643.
12. (a) Wang X, Guo Z. The role of sulfur in platinum anticancer chemotherapy. *Anticancer Agents Med Chem* **2007**; 7(1): 19–34. (b) Bose RB, Ghosh SK, Mogbaddas S. Kinetic analysis of the cis-diamminedichloroplatinum(II)-cysteine reaction: implications to the extent of platinum-DNA binding. *J Inorg Biochem* **1997**; 65(3): 199–205.
13. Rosenkranz AA, Slastnikova TA, Georgiev GP, Zalutsky MR, Sobolev AS. Delivery systems exploiting natural cell transport processes of macromolecules for intracellular targeting of Auger electron emitters. *Nucl Med Biol* **2020**; 80: 45–56.
14. Hidaka T, Tsubono Y, Hashiya K, Bando T, Pandian GN, Sugiyama H. Enhanced nuclear accumulation of pyrrole–imidazole polyamides by incorporation of the tri-arginine vector. *Chem Commun* **2020**; 56: 12371.
15. Harenza JL, Diamond MA, Adams RN, Song MM, Davidson H, Hart LS, Dent MH, Fortina P, Reynolds CP, Maris JM. Transcriptomic profiling of 39 commonly-used neuroblastoma cell lines. *Sci Data* **2017**; 4: 170033.
16. Wang X, Xia Y. Anti-double stranded DNA antibodies: origin, pathogenicity, and targeted. therapies. *Front Immunol* **2019**; 10: 1667.
17. (a) Chabanon RM, Rouanne M, Lord CJ, Soria JC, Pasero P, Vinay SP. Targeting the DNA damage response in immuno- oncology: developments and opportunities. *Nat Rev Cancer* **2021**; 21(11): 701–717. (b) Miller KN, Victorelli SG, Salmonowicz H, Dasgupta N, Liu T, Passos JF, Adams PD. Cytoplasmic DNA: sources, sensing, and role in aging and disease. *Cell* **2021**; 184(22): 5506–5526. (c) Shen JZ, Qiu Z, Wu Q, Finlay D, Garcia G, Sun D, Rantala J, Barshop

W, Hope JL, Gimple RC, *et al*. FBXO44 promotes DNA replication-coupled repetitive element silencing in cancer cells. *Cell* **2021**; 184(2): 352–369.e23. (d) Griffin GK, Wu J, Vellve AI, Patti JC, Hsu J, Davis T, Oni DD, Du PP, Halawi AG, Ishizuka JJ, *et al*. Epigenetic silencing by SETDB1 suppresses tumour intrinsic immunogenicity. *Nature* **2021**; 595(7866): 309–314. (e) Chabanon RM, Rouanne M, Lord CJ, Soria JC, Pasero P, Vinay SP. Targeting the DNA damage response in immuno-oncology: developments and opportunities. *Nat Rev Cancer* **2021**; 21(11): 701–717.

18. (a) Paillas S, Ladjohounlou R, Lozza C, Pichard A, Boudousq V, Jarlier M, Sevestre S, Blay ML, Deshayes E, Sosabowski J, *et al*. Localized irradiation of cell membrane by Auger electrons is cytotoxic through oxidative stress-mediated nontargeted effects. *Antioxid. Redox Signal* **2016**; 25: 467–484. (b) Xue LY, Butler NJ, Makrigiorgos GM, Adelstein SJ, Kassis AI. Bystander effect produced by radiolabeled tumor cells in vivo. *Proc Natl Acad Sci U S A* **2002**; 99(21): 13765–13770.
19. (a) Fernandes HP, Cesar CL, Castro MLB. Electrical properties of the red blood cell membrane and immunohematological investigation. *Rev Bras Hematol Hemoter* **2011**; 33(4): 297–301. (b) Danon AKD, Vries ANA. Interaction of basic polyelectrolytes with the red blood cell II. Agglutination of red blood cells by polymeric bases. *Biochimica et Biophysica Acta* **1959**; 33(1): 120–138.
20. (a) Zhou XY, Jeffris KE, Yu EY, Zheng B, Goodwill PW, Nahid P, Conolly SM. First in vivo magnetic particle imaging of lung perfusion in rats. *Phys Med Biol* **2017**; 62(9): 3510–3522. (b) Mortensen J, Gutte H. SPECT/CT and pulmonary embolism. *Eur J Nucl Med Mol Imaging* **2014**; 41(Suppl 1): S81–S90. (c) Anselmo AC, Gupta V, Zern BJ, Pan D, Zakrewsky M, Muzykantov V, Mitragotri S. Delivering nanoparticles to lungs while avoiding liver and spleen through adsorption on red blood cells. *ACS Nano* **2013**; 7(12): 11129–11137. (d) Brenner JS, Pan DC, Myerson JW, Contreras OAM, Villa CH, Patel P, Hekierski H, Chatterjee S, Tao JQ, Parhiz H, Bhamidipati K, Uhler TG, Hood ED, Kiseleva RY, Shuvaev VS, Shuvaeva T, Khoshnejad M, Johnston I, Gregory JV, Lahann J, Wang T, Cantu E, Armstead WM, Mitragotri S, Muzykantov V. Red blood cell-hitchhiking boosts delivery of nanocarriers to chosen organs by orders of magnitude. *Nat Comm* **2018**; 9: 2684.
21. (a) Ruiz MER, Box CV, Melero I, Formenti SC, Demaria S. Immunological mechanisms responsible for radiation-induced abscopal effect. *Trends Immunol* **2018**; 39(8): 644–655. (b) Deng L, Liang H, Xu M, Yang X, Burnette B, Arina A, Li XD, Mauceri H, Beckett M, Darga T, *et al*. STING-dependent cytosolic DNA sensing promotes radiation-induced type I interferon-dependent antitumor immunity in immunogenic tumors. *Immunity* **2014**; 41: 843–852.

Chapter 3: Development of Radio-Pt–Labeled Agents Targeting Tumor Cells *In vivo*

Chapter 3—Introduction

Chapter 2 successfully demonstrated DNA-targeting radio-Pt conjugates, ^{191}Pt-labeled Hoechst33258 (section 1) and ^{191}Pt-MYCN-PIP (section 2). These agents bound to DNA and induced DNA damage like DSBs efficiently. Oncogene-targeting ^{191}Pt-MYCN-PIP caused cytotoxicity in the targeted gene-amplified cells, suggesting a therapeutic potential for DNA-targeted Auger electron therapy. On the other hand, these agents included no tumor-targeting modules for *in vivo* uses. The biodistribution of intravenously-injected ^{191}Pt-MYCN-PIP observed that hydrophilic and cationic R3-coumarin attached to the PIP scaffold led to an extreme accumulation in the lung rapidly after injection and thereafter in the spleen and liver. In order to make ^{191}Pt-MYCN-PIP work *in vivo*, the drug design needed to be improved at least by the replacement of R3-coumarin with tumor-targeting modules. Additionally, in section 2 of *Chapter 1*, the biodistribution of radio-cisplatin as a small Pt complex was also evaluated. Although cisplatin is widely used in clinics as an anti-cancer agent that is injected intravenously, the accumulation in the tumors was not high; the $AUC_{0–7\ days}$ in the kidneys and liver were almost three times higher, and that in the bone was almost two times higher than that in the tumors. Hence, a small ^{191}Pt complex and labeled compounds, which do not target tumors, are not delivered predominately to tumors. For *in vivo* delivery in therapeutic uses of radio-Pt pharmaceuticals, ^{191}Pt-labeled compounds should be redesigned using tumor-targeting ligands.

An ideal radiopharmaceutical for Auger electron therapy would consist of not only a DNA-binding module for intracellular delivery to DNA after cell penetration, but also a tumor-targeting domain for *in vivo* tumor accumulation after intravenous injection. In *Chapter 2*, ^{191}Pt was labeled to several modules via one Cys, but the *in vivo* stability of the labeled products has yet to be evaluated. It is critical, at first, to investigate whether tumor-targeting ligands labeled with ^{191}Pt via Cys are delivered to tumors efficiently.

Integrins mediate adhesive events such as malignant transformation, tumor growth and progression, invasion, and metastasis.[1] Among integrin receptors, the integrin $\alpha_v\beta_3$ plays a crucial role in angiogenesis.[1] A variety of peptides including arginine–glycine–aspartic acid (RGD) motif have been developed and a substantial accumulation in tumors has been supported by a large number of basic research over the years.[1,2] Therefore, a cyclic RGD peptide, c(RGDfK) was used in this research because cyclic peptides are more stable, more potent, and more specific because of the rigidity conferred by cyclization.[1]

Development of prostate-specific membrane antigen (PSMA)-targeting agents has grown rapidly in recent years, particularly since it was reported that ^{225}Ac-PSMA-617 for metastatic castration-resistant prostate cancer expressed a great deal of therapeutic efficacy in clinical studies.[3] A lot of PSMA-targeting ligands including PSMA-617 developed to date, were based on a glutamic acid (Glu)–urea–lysine (Lys) motif.[4] Considering numerous studies to prove the PSMA-targeting

ability, the Glu–urea–Lys motif was used here.

Collectively, the research objective of *Chapter 3* was to develop tumor-targeting ^{191}Pt-labeled agents and evaluate the *in vivo* properties. *Chapter 3* included the following 1 topic: **(1) Development of Tumor-Targeting ^{191}Pt-Labeled Agents via Mono-thiol Cysteine and a Tri-thiol Ligand.** Two couples of tumor targets and targeting ligands were used as a demonstration: integrin $\alpha_v\beta_3$ receptor and RGD peptide, and PSMA and its ligand. Both have been widely used in pharmaceuticals, and their motifs include no Cys. This means that radio-Pt is supposed to be incorporated into not a site of targeting motif but a labeled site of Cys.

1. Development of Tumor-Targeting ^{191}Pt-Labeled Agents via Mono-thiol Cysteine and a Tri-thiol Ligand

Synthesis of the tumor-targeting ligands labeled with ^{191}Pt: ^{191}Pt-labeled Nap-Cys-PSMA and Nap-Cys-RGD

Two tumor-targeting complexes, Nap-Cys-PSMA (**2**) and Nap-Cys-RGD (**3**) were designed and synthesized as illustrated in **Fig. 3-1-1**. The complexes consist of the Glu–urea–Lys motif as a PSMA-targeting ligand (**2**) or the c(RGDfK) peptide as an integrin $\alpha_v\beta_3$ receptor-targeting ligand (**3**), conjugated with Cys as a labeling site of ^{191}Pt, and naphthalene. Considering the results of Cys-Hoechst33258 and MYCN-Cys-R3-coumarin labeling in *Chapter 2*, it is necessary to prevent multivalent coordination of ^{191}Pt to ligands. Naphthalene was incorporated into the present complexes to position Cys in the middle of the complexes like ^{191}Pt-MYCN-PIP in *Chapter 2*. The hydrophobicity of the complexes was supposed to increase by naphthalene because a naphthalene-based linker was widely used in PSMA-targeting agents.[3,4]

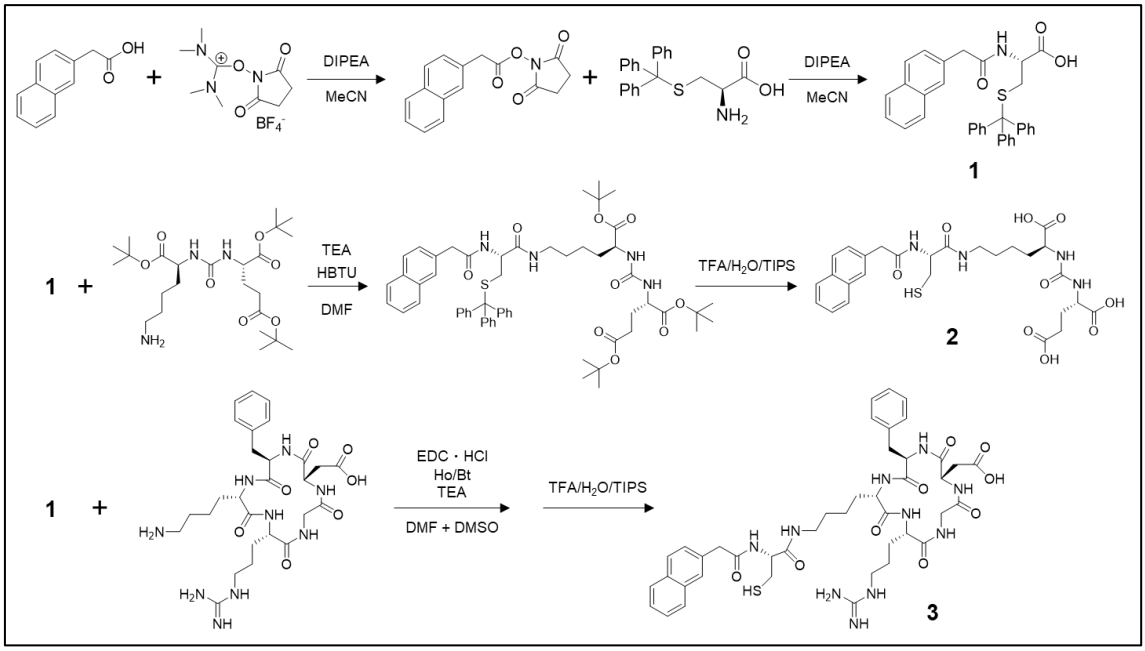

Figure 3-1-1. Scheme of the synthesis of Nap-Cys-PSMA (**2**) and Nap-Cys-RGD (**3**).

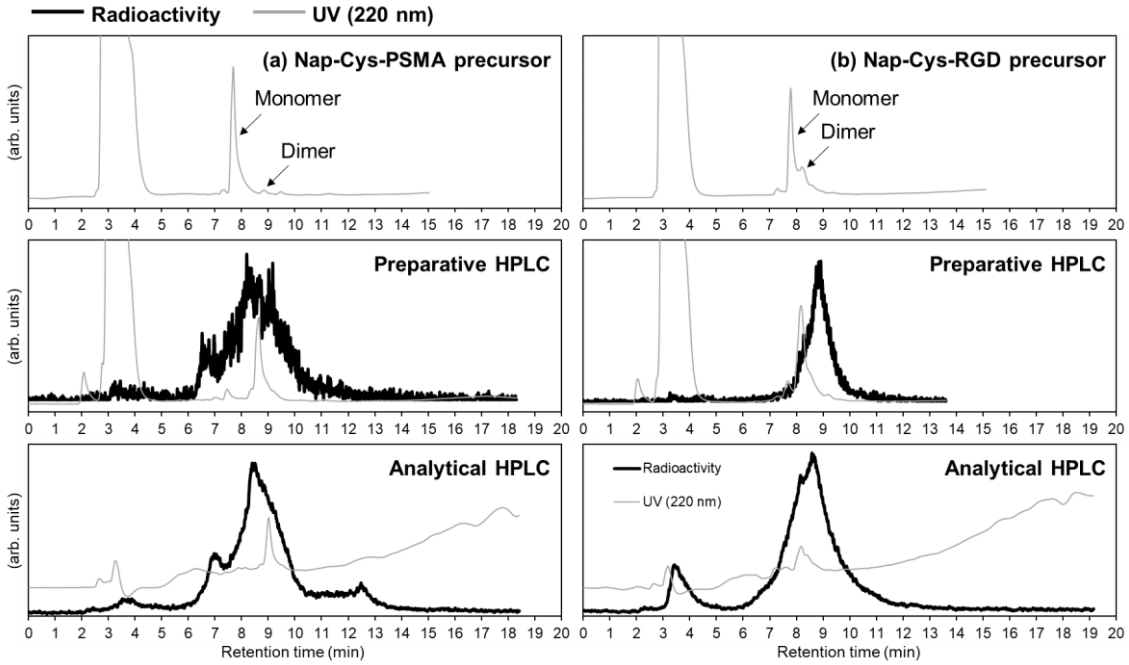

Figure 3-1-2. Chromatograms of precursors (upper panels), and radiochromatograms of preparative (middle panels) and analytical (lower panels) HPLC for Nap-Cys-PSMA (left, **2**) and Nap-Cys-RGD (right, **3**) labeled with ^{191}Pt. Labeling conditions: 100 μM conjugates in a buffer solution (100 μL) containing 0.18 M phosphate, 0.2–0.4 M KCl, and 1.4 M DMSO, pH 7–8. HPLC conditions: column, COSMOSIL 5C18-AR-II (Nacalai Tesque, Kyoto, Japan); gradient elution, A/B = 0.1% TFA in H_2O/CH_3CN = 70/30 → 20/80 (10 min) → 0/100 (15 min). The monomer and dimer of Nap-Cys-PSMA/RGD were identified by ESI-MS.

The precursors Nap-Cys-PSMA and Nap-Cys-RGD were prepared mostly as a monomer (**Fig. 3-1-2**, upper panels) and labeled with n.c.a. ^{191}Pt (**Fig. 3-1-2**, middle and lower panels). Free ^{191}Pt was not retained on the C18 column. As shown in preparative HPLC, n.c.a. free ^{191}Pt reacted with the precursors and was not found after the reaction, resulting in a RCY of over 50%. The precursor was observed as a monomer before the labeling reaction, but in preparative HPLC, the precursor mostly formed a disulfide-bonded dimer in the reaction mixture. In preparative and analytical HPLC, both ^{191}Pt-labeled Nap-Cys-PSMA and Nap-Cys-RGD were observed having multiple, broad peaks in the retention time that covers the peaks of monomer and dimer precursors, like ^{191}Pt-labeled Cys-Hocehst33258 (section 1 of *Chapter 2*). More Nap-Cys-PSMA/RGD precursors seemed dimerized than the Cys-Hoechst33258. Nap-Cys-PSMA/RGD consisted of naphthalene and more oxygen atoms than Cys-Hoechst33258. Such components could enhance intermolecular interactions like π-π stacking by naphthalene or hydrogen bonding by oxygen atoms and promote dimerization. Yang *et al*. reported the self-assembly of conjugates of naphthalene and dipeptides occurred via π-π stacking and

hydrogen bonding,[5] and this speculation was also supported in some studies by other researchers.[6] Although clinically-used PSMA-617 similarly consists of naphthalene and Glu–urea–Lys motif as a PSMA ligand, the current compounds conjugating naphthalene and an amino acid-based motif might promote intermolecular interactions and multivalent labeling. Therefore, the current design is inappropriate at least to prepare a single ^{191}Pt-labeled product.

Additionally, MYCN-Cys-R3-coumarin was not dimerized (section 2 of *Chapter 2*), and the ^{191}Pt-labeled peak looked sharp likely as a product with Pt and precursor, bound at 1/1. Considering a molecule size difference between Nap-Cys-PSMA/RGD and MYCN-Cys-R3-coumarin, steric hindrance would be a cause to suppress the multivalent coordination of Cys-based precursors. Comparing smaller Nap-Cys-PSMA and larger Nap-Cys-RGD, the peak of ^{191}Pt-labeled Nap-Cys-PSMA resulted in broader than that of ^{191}Pt-labeled Nap-Cys-RGD. Thus, it is likely to be difficult to precisely handle the coordination state of ^{191}Pt for especially small compounds containing Cys.

Cellular uptake and cell-membrane binding of ^{191}Pt-labeled ligands via Cys

To confirm whether the ligand specificity was maintained for the ^{191}Pt-labeled ligands, the cellular uptake of ^{191}Pt-labeled Nap-Cys-PSMA and Nap-Cys-RGD in target-positive and -negative cancer cell lines were investigated after 3 h and 24 h incubation, by measuring the activity of ^{191}Pt. The uptake of ^{191}Pt-labeled Nap-Cys-PSMA in PSMA-positive PC3-PIP cells and PSMA-negative PC3-FLU cells[7] was shown in **Fig. 3-1-3(a)**, and that of ^{191}Pt-labeled Nap-Cys-RGD in integrin $\alpha_v\beta_3$-positive U87MG cells and integrin $\alpha_v\beta_3$-negative PC3-FLU cells[8] in **Fig. 3-1-3(b)**. Since U87MG cells tended to peel off and float away in the treatment with 2 μM of Nap-Cys-RGD, the blocking condition (2 μM) could not be examined for Nap-Cys-RGD but only for Nap-Cys-PSMA (**Fig. 3-1-3(a)**).

The uptake of ^{191}Pt-labeled Nap-Cys-PSMA increased over time (**Fig. 3-1-3(a)**). Although the uptake of ^{191}Pt-labeled Nap-Cys-PSMA and free ^{191}Pt was similar for both PC3-PIP and PC3-FLU cells, the uptake of ^{191}Pt-labeled Nap-Cys-PSMA was about six times higher than that of free ^{191}Pt in positive PC3-PIP cells. The uptake of ^{191}Pt-labeled Nap-Cys-PSMA in positive cells was about 10-fold higher than that in negative cells. In the cells blocked with unlabeled Nap-Cys-PSMA in a concentration 10-fold higher than the unblocked cells, the uptake decreased to one-quarter. These results suggested that ^{191}Pt-labeled Nap-Cys-PSMA kept the specificity of PSMA-targeting ligand despite multiple coordination numbers and states. The uptake was not fast, but it increased slowly over time after the treatment, indicating that ^{191}Pt-labeled Nap-Cys-PSMA was stable at least in the FBS-containing cell culture medium. In addition, ^{191}Pt-labeled Nap-Cys-PSMA was not retained on the

membrane for very long and most ^{191}Pt was observed in the internalized fraction.

The uptake of ^{191}Pt-labeled Nap-Cys-RGD also increased over time and the tendency was the same as Nap-Cys-PSMA (**Fig. 3-1-3**). After 3 h and 24 h incubation, the uptake of ^{191}Pt-labeled Nap-Cys-RGD in positive U87MG cells was about two times higher than that of ^{191}Pt-labeled Nap-Cys-RGD in negative PC3-FLU cells, or that of free ^{191}Pt in positive U87MG cells (**Fig. 3-1-3(b)**). Collectively, ^{191}Pt-labeled Nap-Cys-PSMA and Nap-Cys-RGD expressed the ligand specificity and were able to be uptaken into the target-positive cells under the *in vitro* situation.

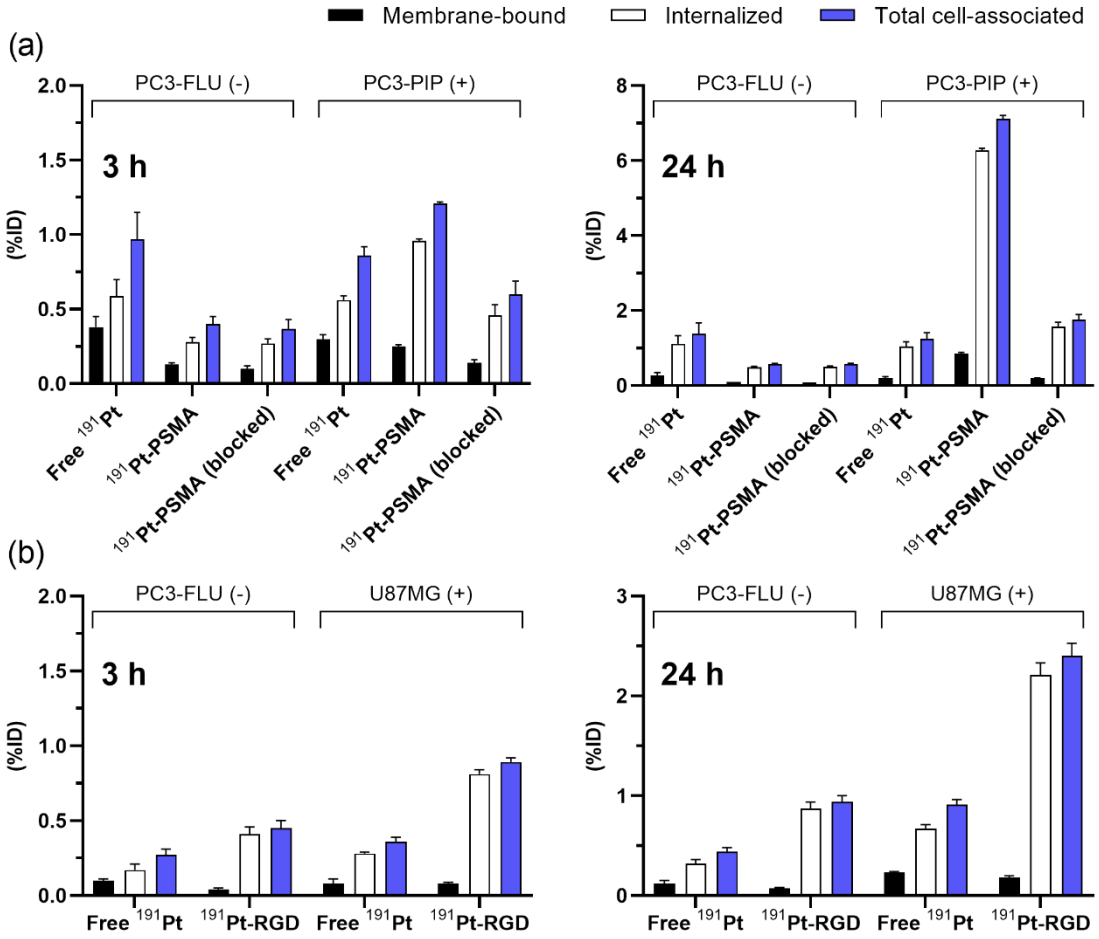

Figure 3-1-3. Cellular fractionation and uptake of (a) ^{191}Pt-labeled Nap-Cys-PSMA in PSMA-negative PC3-FLU cells and PSMA-positive PC3-PIP cells; (b) ^{191}Pt-labeled Nap-Cys-RGD in integrin-negative PC3-FLU cells and integrin-positive U87MG cells (Membrane-bound, Internalized, and total cell-associated radioactivity).

In vivo evaluation of intravenously injected ^{191}Pt-labeled ligands vis Cys in mice bearing tumors

The biodistribution of ^{191}Pt-labeled Nap-Cys-PSMA and Nap-Cys-RGD was investigated after intravenous injection using xenografted mice bearing target-positive and negative tumors (**Fig. 3-1-4** and **Table 3-1-1**). High uptake of both ^{191}Pt-labeled Nap-Cys-PSMA and Nap-Cys-RGD were observed especially in the kidney, livers, and spleens for mice bearing both target-positive and negative tumors. While PSMA ligands were reported to be predominantly excreted by the kidneys,[9] ^{191}Pt-labeled Nap-Cys-PSMA was highly accumulated in the kidney (60 %ID/g at 1 h) and retained at least over 1 d after injection. The accumulation of ^{191}Pt-labeled Nap-Cys-PSMA in the livers and spleens was about 10–30 %ID/g, and there was a slight variation in these uptake values between the two separate experiments (**Fig. 3-1-4(a)** and **Table 3-1-1**). These experiments were conducted at QST in Japan (**Fig. 3-1-4(a)**) and at Duke University in the USA (**Table 3-1-1**), where mice were raised in different countries and environments. The uptake difference would be mainly due to such mice difference mainly in the average body weight of mice (20 g in **Fig. 3-1-4(a)**; 28 g in **Table 3-1-1**). The uptake of ^{191}Pt-labeled Nap-Cys-RGD in the kidneys was about 20 %ID/g, and that in the livers and spleens was the same degree. ^{191}Pt-labeled Nap-Cys-RGD also remained mostly in the kidneys, livers, and spleens at 1 d, and was not excreted (**Fig. 3-1-4(b)**). Collectively, the high accumulation of ^{191}Pt-labeled Nap-Cys-PSMA/RGD in normal tissues including the kidneys, livers, and spleens led to low uptake in the tumors. For both ^{191}Pt-labeled compounds, the uptakes in other tissues like the lungs, intestines, muscles, and bones, were less than a few %ID/g, which was equal to that in the tumors.

Notably, the tumor uptake of both ^{191}Pt-labeled Nap-Cys-PSMA and Nap-Cys-RGD was different between the target-positive and negative tumors, as summarized in **Table 3-1-2**. ^{191}Pt-labeled Nap-Cys-PSMA/RGD was accumulated in the target-positive tumors 4–5 times more than the target-negative tumors 1 h and later after injection. These results indicated that ^{191}Pt-labeled Nap-Cys-PSMA and Nap-Cys-RGD kept the specificity of the ligands *in vivo* to a certain degree.

Assuming that the high accumulation especially in the livers and spleens was attributed to the instability of ^{191}Pt-labeled Nap-Cys-PSMA/RGD in the blood, red blood cell partitioning and plasma protein binding were investigated at 2 min, 1 h, and 1 d after injection for mice bearing target-positive tumors (**Table 3-1-3**). It was found that no ^{191}Pt-labeled Nap-Cys-PSMA/RGD migrated to red blood cells, suggesting no reactivity with blood cells. On the other hand, the plasma protein binding of ^{191}Pt-labeled Nap-Cys-PSMA/RGD showed that unfortunately, both ^{191}Pt-labeled Nap-Cys-PSMA and Nap-Cys-RGD bound to plasma proteins immediately after intravenous injection and the rate is about 70–80% at 2 min. Therefore, ^{191}Pt-labeled Nap-Cys-PSMA/RGD reacted with plasma protein and the complexes were delivered to the livers and spleens more than the target tumors.

Platinum drugs, like cisplatin, readily react with Cys residues-containing serum albumin,[10] which is the main component in blood proteins. Unfortunately, the ^{191}Pt-labeled Nap-Cys-PSMA/RGD could remain reactive to other Cys, suggesting that the reactivity of ^{191}Pt-labeled complexes with serum proteins needs to be reduced. Divalent Pt mostly forms a square planar complex with a coordination number of four. Based on the labeling experiments, in the current labeled products, ^{191}Pt might be labeled to one or two molecules of Nap-Cys-PSMA/RGD. If ^{191}Pt bound to only the thiol of Cys, the coordination number would be one or two and the residual two or three ligands could bind to the proteins. Therefore, to increase the stability of the labeled complexes in the blood and deliver them to the tumors, the coordination number of ^{191}Pt should be increased.

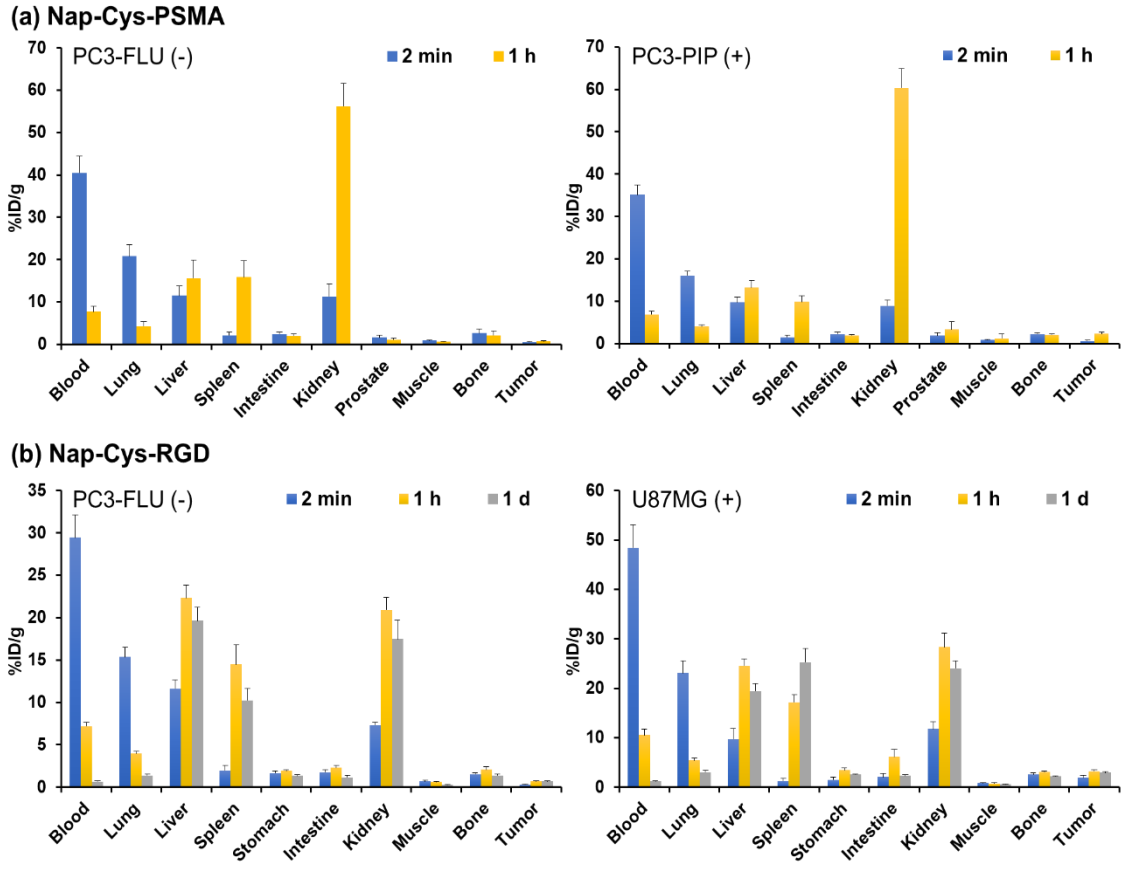

Figure 3-1-4. Biodistribution of (a) ^{191}Pt-labeled Nap-Cys-PSMA in mice bearing PSMA-negative PC3-FLU and PSMA-positive PC3-PIP tumors, and (b) ^{191}Pt-labeled Nap-Cys-RGD in mice bearing integrin-negative PC3-FLU and integrin-positive U87MG tumors. Data were represented as the percentage of the injected dose per gram (%ID/g) of tissue (mean ± SD, n = 5), corrected to those with a body weight of 20 g.

Table 3-1-1. Uptake of ^{191}Pt-labeled Nap-Cys-PSMA at 1 h and 24 h after intravenous injection in mice bearing PSMA-positive PC3-PIP tumors.

Tissues	Uptake (%ID/g)	
	1 h	24 h
Blood	5.24 ± 1.20	0.71 ± 0.42
Brain	0.20 ± 0.04	0.04 ± 0.03
Heart	1.97 ± 0.33	1.13 ± 0.62
Lungs	3.81 ± 0.45	1.65 ± 0.68
Liver	23.40 ± 3.58	28.28 ± 13.61
Spleen	31.94 ± 15.63	34.59 ± 9.87
Kidneys	72.79 ± 19.68	57.78 ± 18.33
Stomach	0.37 ± 0.12	0.41 ± 0.09
Sm. Int.	1.53 ± 0.78	0.59 ± 0.21
Lg. Int.	0.67 ± 0.53	0.66 ± 0.20
Muscle	0.41 ± 0.08	0.30 ± 0.12
Bone	2.35 ± 0.66	1.73 ± 1.23
Skin	1.53 ± 0.30	1.35 ± 0.80
Bladder	0.89 ± 0.17	0.82 ± 0.62
Tumor	1.34 ± 0.46	1.40 ± 0.58

Data were represented as the percentage of the injected dose per gram (%ID/g) of tissue (mean ± SD, n = 4–5), corrected to those with a body weight of 20 g. The data were based on another experiment separate from **Fig. 3-1-4**.

Table 3-1-2. Tumor uptake (%ID/g).

Agents	Time after injection	Positive tumors	Negative tumors
^{191}Pt-labeled	2 min	0.7 ± 0.1	0.5 ± 0.1
Nap-Cys-PSMA	1 h	2.3 ± 0.4	0.8 ± 0.1
	5 h	2.1 ± 0.1†	0.4 ± 0.1†
^{191}Pt-labeled	2 min	1.9 ± 0.4	0.3 ± 0.1
Nap-Cys-RGD	1 h	3.3 ± 0.3	0.7 ± 0.1
	24 h	2.9 ± 0.2	0.7 ± 0.1

Data were corrected to those with a body weight of 20 g and expressed as means ± SD (n = 5, $^{\dagger}n$ = 3). The data were the same as in **Fig. 3-1-4**.

Table 3-1-3. Plasma protein binding rate (%) (n = 3).

Agents	Time after injection	Plasma protein binding rate (%)
^{191}Pt-labeled	2 min	79 ± 4
Nap-Cys-PSMA	1 h	90 ± 1
^{191}Pt-labeled	2 min	68 ± 3
Nap-Cys-RGD	1 d	90 ± 1

The data were obtained from the same experiment in **Fig. 3-1-4**.

Investigation of ^{191}Pt-labeling via a tri-thiol ligand: ^{191}Pt-Trithiol complex

Among a variety of cis/trans-Pt(II, IV) complexes having different ligands, bifunctional Pt(II) complexes that have two labile leaving-group ligands and two inert ligands are the most classical structure in Pt drugs.[11] Meanwhile, several studies developed monofunctional Pt(II) drugs with three inert non-leaving ligands and one labile leaving ligand for DNA binding.[11,12] Such monofunctional Pt(II) complexes were expected to form only one covalent bond to DNA.[12] Interestingly, they bound to serum proteins mostly not via covalent binding but through hydrophobic interaction.[13] Therefore, the monofunctional Pt(II) complex can be stable in the blood. Hereby, ^{191}Pt labeling with a coordination number of three was investigated using a multidentate ligand that consists of three thiol groups (trithiol) (**Fig. 3-1-5**). Considering such a monofunctional Pt(II) complex is less susceptible to inactivation by another thiol ligand, chelation of ^{191}Pt with a trithiol ligand would lead to a product with Pt and precursor bound at 1/1, not multiple products. This ligand has been established and used as an efficient radiolabeling method for various metal radionuclides such as Sb, As, and so on.[14] To avoid the oxidization of thiol, tris(2-carboxyethyl)phosphine (TCEP) was added to the reaction mixture as a reducing agent.[14]

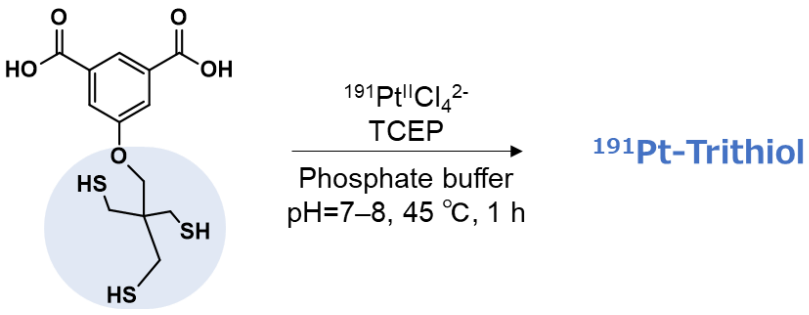

Figure 3-1-5. Chemical structure of a trithiol ligand and ^{191}Pt-labeling scheme.

N.c.a. ^{191}Pt was successfully labeled with the trithiol ligand as shown in **Fig. 3-1-6**. While the precursor was a simple and small molecule, the ^{191}Pt-labeled complex (^{191}Pt-Trithiol) was observed as a sharp and single peak in preparative HPLC, unlike Nap-Cys-PSMA/RGD in **Fig. 3-1-2**. The RCY was about 70%. N.c.a. ^{191}Pt reacted with trithiol in the presence of a 10-fold higher concentration TCEP, suggesting that the trithiol was highly reactive to n.c.a. ^{191}Pt. Thus, the coordination state of ^{191}Pt-labeled complexes would be made uniform with multidentate ligands by increasing the coordination number of ^{191}Pt. Meanwhile, slight tailing and fronting were observed, which may be due to byproducts with different coordination numbers or states. The retention time of the precursor and ^{191}Pt-labeled product differed, likely due to structure change by chelating with trithiol inside of the small precursor. When the labeling test was performed with nonradioactive Pt tetrachloride under the equivalence reaction, the nonradioactive product was also eluted prior to the trithiol precursor.

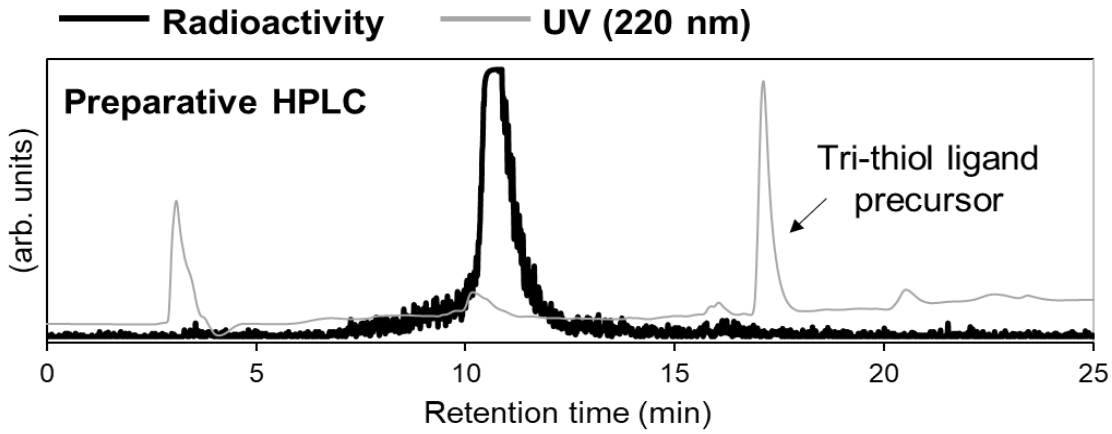

Figure 3-1-6. Radiochromatogram of preparative HPLC for [^{191}Pt]Pt-Trithiol (^{191}Pt-Trithiol). Labeling conditions: 100 μM conjugates in a buffer solution (100 μL) containing 0.18 M phosphate, 0.2–0.4 M KCl, and 1 mM TCEP. pH 7–8. HPLC conditions: column, COSMOSIL 5C18-AR-II (Nacalai Tesque, Kyoto, Japan); gradient elution, A/B = 0.1% TFA in H_2O/CH_3CN = 5/95 → 40/60 (10 min) → 0/100 (15 min).

To confirm whether the trithiol ligand reduces ^{191}Pt-protein binding, the plasma protein binding rate and the biodistribution of ^{191}Pt-Trithiol after intravenous injection were evaluated using xenografted mice bearing PC3-PIP tumors (**Table 3-1-4** and **Fig. 3-1-7**). As expected, the plasma protein binding was mostly suppressed to less than 10% at 2 min after injection. The rate increased to about 20%, but not high, 1 hour after injection. Considering that a monofunctional Pt(II) complex is less susceptible to inactivation by proteins, ^{191}Pt would be chelated with three thiol ligands and have one labile ligand of the chloro or aquo group. Thus, most ^{191}Pt-Trithiol did not bind to protein in the blood rapidly after injection, suggesting that ^{191}Pt-Trithiol complexes can work stably during blood

circulation at a certain level. The biodistribution data showed that ^{191}Pt-Trithiol having no tumor-targeting motif was rapidly excreted and cleared from all organs after intravenous injection (**Fig. 3-1-7**). The low uptake of less than 1 %ID/g for all tissues was observed 1 d after injection. To summarize, the trithiol ligand demonstrated that ^{191}Pt-labeled agents can be intact to proteins in the blood by increasing the coordination number of ^{191}Pt with multidentate ligands and reducing the protein reactivity of ^{191}Pt.

Table 3-1-4. Red blood cell partitioning rate (%), and plasma protein binding rate (%) of ^{191}Pt-Trithiol (n = 3).

Time after injection	Red blood cell partitioning rate (%)	Plasma protein binding rate (%)
2 min	47 ± 2	8 ± 2
1 h	46 ± 5	21 ± 5

The data were obtained from the same experiment in **Fig. 3-1-7**.

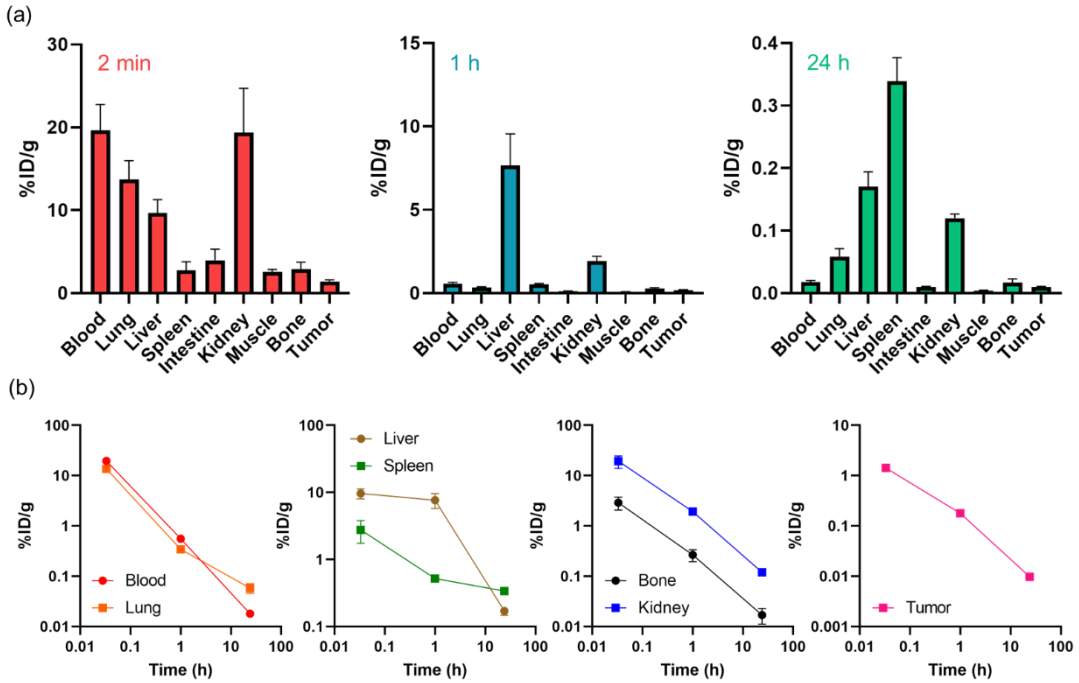

Figure 3-1-7. Biodistribution of [^{191}Pt]Pt-Trithiol in mice bearing PC3-PIP tumors. Data were represented as the percentage of the injected dose per gram (%ID/g) of tissue (mean ± SD, n = 5). (a) data per time point (2 min, 1 h, and 24 h); (b) retention curves per tissue.

A comprehensive discussion and future directions on radio-Pt drugs design based on all the results in *Chapters 1 ~ 3*

The developed radio-Pt–compounds and their properties opened insights into useful radiolabeling methods and workable labeled complexes for *in vitro* cell research and *in vivo* uses. In order to label compounds with n.c.a. radio-Pt and make the labeled compounds work for *in vitro* and *in vivo* uses, the present dissertation suggests the three considerations for complex design: (1) reactive ligands to n.c.a. radio-Pt for efficient radio-labeling, (2) the number and type of labile and inert ligands (a) to form a covalent DNA-Pt bond efficiently, and (b) to keep Pt intact to any biomolecules like serum albumins during blood circulation.

In addition to the classical HSAB theory showing Pt(II) is a soft acid and has a high reactivity to sulfur-containing groups,[15] all the results in the present research showed that sulfur functional groups, especially thiol-containing ligands, were suitable as a labeling module for n.c.a. radio-Pt to incorporate n.c.a. radio-Pt into precursors efficiently. Many experiments on cisplatin, which is one of the most common bifunctional Pt(II) complexes, indicated that the bond of cisplatin and thiol-containing cysteine is irreversible in biological conditions.[10] Such a covalent bond of Pt and thiol would be strong, suggesting thiol ligand may be the first choice for n.c.a. radio-Pt labeling. Notably, the precursors that consist of one thiol-containing cysteine were labeled with n.c.a. radio-Pt and the labeled compounds maintained their original binding ability and specificity as a targeting module. The labeled radio-Pt was delivered to the targeted region, sometimes expressing damaging effects on the targets.

On the other hand, precursors containing one thiol group were not enough to produce uniform labeled products with the same coordination states and numbers and to deliver the labeled compounds to tumors efficiently for *in vivo* application. It should be noted that reactivity to thiol-containing albumins is entirely different between monofunctional and bifunctional Pt(II) complexes.[11,12] Considering this knowledge of monofunctional Pt(II) drugs and the present results of ^{191}Pt-Trithiol, an ideal design may be a monofunctional radio-Pt(II) based complex to produce a single product labeled with radio-Pt while reducing reactivity to protein binding leading to deactivation.

The ligand design has been an important research topic in the development of even nonradioactive Pt-based drugs. However, the design strategies of radio-Pt–labeled agents and nonradioactive Pt-based drugs are partly different. For nonradioactive Pt drugs, chemical action causing steric hindrance of DNA while escaping DNA repair is the most crucial as an effective anti-cancer agent.[11] Only Pt itself is used as a DNA-binding module, and DNA-targeting modules are not incorporated into Pt, unlike the radio-Pt–labeled–agents developed in this research. In the case of radio-Pt–labeled drugs, it is the most critical to deliver radio-Pt to targets and keep it retained there as

efficiently as possible. Therefore, it is essential to determine whether monofunctional radio-Pt(II) based complexes are indeed appropriate as DNA-targeting agents as well as a tumor-targeting agent although nonradioactive monofunctional Pt(II) complexes are known to bind to DNA. Such monofunctional radio-Pt(II) complexes have the potential to reduce off-targets as well as protein binding, and further development and evaluation should be conducted. Collectively, to deliver drugs and form thermodynamically-stable adducts between Pt and DNA efficiently, the structural details of monofunctional radio-Pt(II) compounds conjugates to a DNA-targeting module and a tumor-targeting motif need to be explored and optimized in future studies.

Chapter 3—Conclusion

Chapter 3 described ^{191}Pt-labeled tumor-targeting ligands and their *in vivo* properties. The results showed insights to make ^{191}Pt-labeled compounds workable for *in vivo* uses. First, the two tumor-targeting complexes, Nap-Cys-PSMA and Nap-Cys-RGD were developed, and the ^{191}Pt-labeled compounds were obtained. Although the Nap-Cys-PSMA/RGD precursors were readily dimerized and created multiple labeled products due to the multivalent coordination states of ^{191}Pt, both ^{191}Pt-labeled Nap-Cys-PSMA/RGD expressed high cellular uptake in target-positive cells in the *in vitro* experiments. ^{191}Pt-labeled Nap-Cys-PSMA and Nap-Cys-RGD kept the specificity of the ligands *in vivo* to a certain degree. However, the ^{191}Pt-labeled Nap-Cys-PSMA/RGD could remain reactive to blood proteins like serum albumin containing Cys residues, leading to a high accumulation of ^{191}Pt in the livers and spleens. To reduce the protein reactivity of ^{191}Pt, the trithiol ligand was investigated for increasing the coordination number of ^{191}Pt with multidentate ligands. ^{191}Pt-labeled agents via multidentate trithiol ligands were potentially intact in the blood, suggesting a potential ligand for ^{191}Pt labeling. For future work with ^{191}Pt-labeling drugs targeting both DNA and tumors, suitable multidentate ligands for ^{191}Pt labeling need to be developed in order to maintain the DNA-binding ability of ^{191}Pt after tumor uptake and to keep ^{191}Pt-labeled intact in the blood with low reactivity to serum proteins.

References

1. Danhier F, Breton AL, Préat V. RGD-based strategies to target alpha(v) beta(3) integrin in cancer therapy and diagnosis. *Mol Pharmaceutics* **2012**; 9(11): 2961–2973.
2. (a) Liu S. Radiolabeled cyclic RGD peptides as integrin $\alpha_v\beta_3$-targeted radiotracers: maximizing binding affinity via bivalency. *Bioconjug Chem* **2009**; 20(12): 2199–2213. (b) Liu S. Radiolabeled multimeric cyclic RGD peptides as integrin alphavbeta3 targeted radiotracers for tumor imaging. *Mol Pharm* **2006**; 3(5): 472–487. (c) Wu Y, Zhang X, Xiong Z, Cheng Z, Fisher DR, Liu S, Gambhir SS, Chen X. microPET imaging of glioma integrin {alpha}v{beta}3 expression using ^{64}Cu-labeled tetrameric RGD peptide. *J Nucl Med* **2005**; 46(10): 1707–1718.
3. (a) Kratochwil C, Bruchertseifer F, Giesel FL, Weis M, Verburg FA, Mottaghy F, Kopka K, Apostolidis C, Haberkorn U, Morgenstern A. ^{225}Ac-PSMA-617 for PSMA-targeted α-radiation therapy of metastatic castration-resistant prostate cancer. *J Nucl Med* **2016**; **57**: 1941–1944. (b) Kratochwil C, Bruchertseifer F, Rathke H, Bronzel M, Apostolidis C, Weichert W, Haberkorn U, Giesel FL, Morgenstern A. Targeted α-therapy of metastatic castration-resistant prostate cancer with ^{225}Ac-PSMA-617: dosimetry estimate and empiric dose finding. *J Nucl Med* **2017**; 58(10):

1624–1631. (c) Kratochwil C, Bruchertseifer F, Rathke H, Hohenfellner M, Giesel FL, Haberkorn U, Morgenstern A. Targeted α-therapy of metastatic castration-resistant prostate cancer with ^{225}Ac-PSMA-617: swimmer-plot analysis suggests efficacy regarding duration of tumor control. *J Nucl Med* **2018**; 59(5): 795–802.

4. (a) Perera M, Papa N, Christidis D, Wetherell D, Hofman MS, Murphy DG, Bolton D, Lawrentschuk N. Sensitivity, specificity, and predictors of positive ^{68}Ga-prostate-specific membrane antigen positron emission tomography in advanced prostate cancer: a systematic review and meta-analysis. *Eur Urol* **2016**; 70(6): 926–937. (b) Kozikowski AP, Nan F, Conti P, Zhang J, Ramadan E, Bzdega T, Wroblewska B, Neale JH, Pshenichkin S, Wroblewski JT. Design of remarkably simple, yet potent urea-based inhibitors of glutamate carboxypeptidase II (NAALADase). *J Med Chem* **2001**; 44(3): 298–301. (c) Foss CA, Mease RC, Fan H, Wang Y, Ravert HT, Dannals RF, Olszewski RT, Heston WD, Kozikowski AP, Pomper MG. Radiolabeled small-molecule ligands for prostate-specific membrane antigen: in vivo imaging in experimental models of prostate cancer. *Clin Cancer Res* **2005**; 11(11): 4022–4028. (d) Kopka K, Benešová M, Bařinka C, Haberkorn U, Babich J. Glu-ureido-based inhibitors of prostate-specific membrane antigen: lessons learned during the development of a novel class of low-molecular-weight theranostic radiotracers. *J Nucl Med* **2017**; 58(Suppl 2): 17S–26S.
5. Yang Z, Liang G, Ma M, Gao Y, Xu B. Conjugates of naphthalene and dipeptides produce molecular hydrogelators with high efficiency of hydrogelation and superhelical nanofibers. *J Mater Chem* **2007**; 17: 850–854.
6. (a) Chen L, Morris K, Laybourn A, Elias D, Hicks MR, Rodger A, Serpell L, Adams DJ. Self-assembly mechanism for a naphthalene−dipeptide leading to hydrogelation. *Langmuir* **2010**; 26(7): 5232–5242. (b) Fichman G, Gazit E. Self-assembly of short peptides to form hydrogels: Design of building blocks, physical properties and technological applications. *Acta Biomaterialia* 2014; 10(4), 1671–1682. (c) Debnath S, Roy S, Ulijn RV. Peptide nanofibers with dynamic instability through nonequilibrium biocatalytic assembly. *J Am Chem Soc* **2013**; 135(45): 16789–16792.
7. Kiess AP, Minn I, Vaidyanathan G, Hobbs RF, Josefsson A, Shen C, Brummet M, Chen Y, Choi J, Koumarianou E, Baidoo K, Brechbiel MW, Mease RC, Sgouros G, Zalutsky MR, Pomper MG. (2S)-2-(3-(1-carboxy-5-(4-^{211}At-astatobenzamido)pentyl)ureido)-pentanedioic acid for PSMA-targeted α-particle radiopharmaceutical therapy. *J Nucl Med* **2016**; 57(10): 1569–1575.
8. Zhou Y, Kim YS, Chakraborty S, Shi J, Gao H, Liu S. ^{99m}Tc-labeled cyclic RGD peptides for noninvasive monitoring of tumor integrin $\alpha_V\beta_3$ expression. *Mol Imaging* **2011**; 10(5): 386–397.
9. (a) Gallyamov M, Meyrick D, Barley J, Lenzo N. Renal outcomes of radioligand therapy: experience of ^{177}lutetium—prostate-specific membrane antigen ligand therapy in metastatic castrate-resistant prostate cancer. *Clin Kidney J* **2020**, 13(6), 1049–1055. (b) Rauscher I, Maurer

T, Fendler WP, Sommer WH, Schwaiger M, Eiber M. ^{68}Ga-PSMA ligand PET/CT in patients with prostate cancer: How we review and report. *Cancer Imaging* **2016**; 16: 14.

10. (a) Johnstone TC, Suntharalingam K, Lippard SJ. The next generation of platinum drugs: targeted Pt(II) agents, nanoparticle delivery, and Pt(IV) prodrugs. *Chem Rev* **2016**; 116: 3436−3486. (b) Macquet JP, Butour JL. Platinum-amine compounds: importance of the labile and inert ligands for their pharmacological activities toward L1210 leukemia cells. *J Natl Cancer Inst* **1983**; 70: 899−905. (b) Hollis LS, Miller AV, Amundsen AR, Stern EW, Sundquist WI, Toni J, Burstyn JN, Heiger W, Lippard SJ. Chemical and biological studies of new platinum antitumor agents. *J Inorg Biochem* **1989**; 36, 153.
11. (a) Lovejoy KS, Todd RC, Zhang S, McCormick MS, D'Aquino JA, Reardon JT, Sancar A, Giacomini KM, Lippard SJ. cis-Diammine(pyridine)chloroplatinum(II), a monofunctional platinum(II) antitumor agent: Uptake, structure, function, and prospects. *Proc Natl Acad Sci U S A* **2008**; 105(26): 8902−8907. (b) Park GY, Wilson JJ, Song Y, Lippard SJ. Phenanthriplatin, a monofunctional DNA-binding platinum anticancer drug candidate with unusual potency and cellular activity profile. *Proc Natl Acad Sci U S A* **2012**; 109(30): 11987−11992. (c) Jin S, Guo Y, Guo Z, Wang X. Monofunctional platinum(II) anticancer agents. *Pharmaceuticals (Basel)* **2021**; 14(2): 133.
12. Wang Y, Wang X, Wang J, Zhao Y, He W, Guo Z. Noncovalent interactions between a trinuclear monofunctional platinum complex and human serum albumin. *Inorg Chem* **2011**; 50(24): 12661–12668.
13. (a) Feng Y, Jurisson SS. Chapter 8 - Trithiol compounds—tricky but valuable: the design and synthesis of ligands for stabilizing radioarsenic for radiopharmaceutical development. *Strategies and Tactics in Organic Synthesis* **2019**; 14, Pages 207−224. (b) DeGraffenreid AJ, Feng Y, Barnes CL, Ketring AR, Cutler CS, Jurisson SS. Trithiols and their arsenic compounds for potential use in diagnostic and therapeutic radiopharmaceuticals. *Nucl Med Biol* **2016**; 43(5): 288–295. (c) Khosroshahi FN, Feng Y, Ma L, Manring S, Rold TL, Gallazzi FA, Kelley SP, Embree MF, Hennkens HM, Hoffman TJ, Jurisson SS. A new, second generation trithiol bifunctional chelate for ^{72,77}As: trithiol(b)-(Ser)$_2$-RM2. *Bioconjug Chem* **2021**; 32(7):1364−1373. (d) Ma L, Grant C, Gallazzi F, Watkinson LD, Carmack TL, Embree MF, Smith CJ, Medvedev D, Cutler CS, Li Y, Wilbur DS, Hennkens HM, Jurisson SS. Development and biodistribution studies of 77As-labeled trithiol RM2 bioconjugates for prostate cancer: Comparison of [^{77}As]As-trithiol-Ser-Ser-RM2 vs. [^{77}As]As-trithiol-Glu-Ser-RM2. *Nucl Med Biol* **2022**; 108–109: 61–69. (e) Olson AP, Ma L, Feng Y, Khosroshahi FN, Kelley SP, Sarduy EA, Barnhart TE, Hennkens HM, Ellison PA, Jurisson SS, Engle JW. A third generation potentially bifunctional trithiol chelate, its ^{nat,1XX}Sb(III) complex, and selective chelation of radioantimony (^{119}Sb) from its Sn target. *Inorg Chem* **2021**; 60(20): 15223–15232.

14. (a) Pearson RG. Hard and soft acids and bases, HSAB, part 1: Fundamental principles. *J Chem Educ* **1968**; 45(9): 581. (b) Pearson RG. Hard and soft acids and bases, HSAB, part II: Underlying theories. *J Chem Educ* **1968**; 45: 10, 643
15. (a) Cole WC, Wolf W. Preparation and metabolism of a cisplatin/serum protein complex. *Chem Biol Interact* **1980**; 30(2): 223–235. (b) Zimmermann T, Zeizinger M, Burda JV. Cisplatin interaction with cysteine and methionine, a theoretical DFT study. *J Inorg Biochem* **2005**; 99(11): 2184–2196. (c) Kato R, Sato T, Iwamoto A, Yamazaki T, Nakashiro S, Yoshikai S, Fujimoto A, Imano H, Ijiri Y, Mino Y, Chikuma M, Tanaka K, Hayashi T. Interaction of platinum agents, cisplatin, carboplatin and oxaliplatin against albumin in vivo rats and in vitro study using inductively coupled plasma-mass spectrometory. *Biopharm Drug Dispos* **2019**; 40(7): 242–249.

Conclusion

In *Chapter 1*, a novel method for n.c.a. radio-Pt production from an Ir target using accelerators was developed. N.c.a. radio-$Pt^{II}Cl_4^{2-}$ was successfully prepared in a useful chemical form as a precursor for the synthesis of Pt drugs. Thereafter, the DNA damaging effect of Auger electrons was evaluated using n.c.a. radio-cisplatin with the negligible chemical effect of nonradioactive Pt. The observations of the DNA damage by Auger electrons released from n.c.a. radio-cisplatin indicated that DSBs were induced by Auger electrons released from radio-Pt bound to DNA, not the chemical effect of nonradioactive Pt carriers. Unfortunately, due to its low cellular uptake, only a small fraction of radio-cisplatin bound to DNA, leading to a low probability of DSBs and low cytotoxicity. To maximize the damaging effect of Auger electrons and reveal their ideal potential, it was necessary to develop a more efficient system for delivering radio-Pt to DNA.

In *Chapter 2*, the DNA-intercalator Hoechst33258 labeled with ^{191}Pt and the MYCN gene-targeting PIP compound labeled with ^{191}Pt were successfully developed. Interestingly, ^{191}Pt exhibited superior DNA binding and damaging ability when being delivered to DNA using DNA-binding modules. The radio-Pt–based agents [^{191}Pt]Pt-DTPA-Hoechst33258 and [^{191}Pt]Pt-Cys-Hoechst33258 demonstrated more than one order of magnitude greater DNA-binding ability than [^{111}In]In-DTPA-Hoechst33258. [^{191}Pt]Pt-Hoechst33258 labeled via Cys showed a very high DNA-binding fraction and induced extensive DNA damage such as DSBs. Additionally, the novel ^{191}Pt-labeled compound ^{191}Pt-MYCN-PIP targeting the oncogene MYCN bound to DNA efficiently and caused DNA damage, decreasing MYCN gene expression and cell viability, especially in MYCN-amplified Kelly cells. Considering these observations, Auger-electron emitting drugs that target key genes in cell survival may be a novel therapy. Collectively, the two ^{191}Pt-labeled DNA-targeting compounds (Hoechst33258 and MYCN-PIP) successfully increased the DNA-binding fraction of ^{191}Pt, DNA damage like DSBs, and cytotoxicity under certain conditions.

In *Chapter 3,* regarding *in vivo* characteristics of the radio-Pt–labeled compounds, the two tumor-targeting complexes ^{191}Pt-labeled Nap-Cys-PSMA and Nap-Cys-RGD were developed, and their properties were investigated. ^{191}Pt-labeled Nap-Cys-PSMA and Nap-Cys-RGD kept the specificity of the ligands *in vivo* to a certain degree. However, the ^{191}Pt-labeled Nap-Cys-PSMA/RGD could remain reactive to other Cys and bound to blood proteins like serum albumin containing Cys residues, which led to a high accumulation of ^{191}Pt in the livers and spleens. ^{191}Pt-labeled agents via multidentate trithiol ligands were intact in the blood with low reactivity to serum proteins, suggesting a suitable ligand for ^{191}Pt labeling.

In summary, this dissertation successfully produced n.c.a. ^{191}Pt and ^{191}Pt-labeled compounds, providing insights into the compound design for ^{191}Pt delivery to DNA and tumors. The results and findings would contribute to the development of DNA-targeted Auger electron cancer therapy.

Appendix: Evaluation of the Cytotoxicity by DNA-Targeting and Non-Targeting ^{125}I-Labeled Agents

Introduction

Several works showed that Auger-electron emitting radionuclides closer to the DNA can maximize interaction between Auger electrons and DNA and induce more DSBs.[1] Such DNA-targeted Auger electrons have been generally expected to induce fatal DNA damage and cell death.[2] However, there are few experimental results to prove that DNA-targeting has a solid advantage in Auger electron therapy.[3] To confirm the therapeutic efficacy of DNA-targeted Auger electrons, here, the cytotoxicity was compared between the three different ^{125}I-labeled compounds: not-internalized anion [^{125}I]NaI, cell-membrane targeting and not DNA-targeting [^{125}I]VK290Lu, and DNA-targeting [^{125}I]1,3,4-SGMIB-Hoechst33258.

Results and Discussion

The ^{125}I-labeled compounds: an uninternalized anion, [^{125}I]NaI; a cell-membrane (PSMA) targeting and not DNA-targeting compound, [^{125}I]VK290Lu; a DNA-targeting compound, [^{125}I]1,3,4-SGMIB-Hoechst33258, were prepared (**Fig. 4-1**). [^{125}I]NaI was purchased from PerkinElmer (Waltham, MA, USA). A PSMA-targeting compound, VK290Lu, was developed by Professor Michael R Zalutsky *et al*. of Duke University and was radio-iodinated in the common scheme using NCS (**Fig. 4-2**).[4] A DNA-targeting compound, 1,3,4-SGMIB-Hoechst33258 was developed in this research. The tin precursor 1,3,4-SGMTB was also developed by Professor Michael R Zalutsky *et al*. and was radio-iodinated (**Fig. 4-3**).[5] After conjugating [^{125}I]1,3,4-SGMIB with Hoechst33258 via an amide bond, [^{125}I]1,3,4-SGMIB-Hoechst33258 was obtained (**Fig. 4-3**). The ^{125}I-labeled products were prepared with a RCP greater than 95% at EOS in the analytical HPLC after purification.

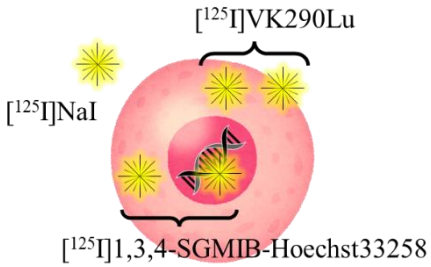

Figure 4-1. Illustration of the distribution of [^{125}I]NaI, [^{125}I]VK290Lu, and [^{125}I]1,3,4-SGMIB-Hoechst33258.

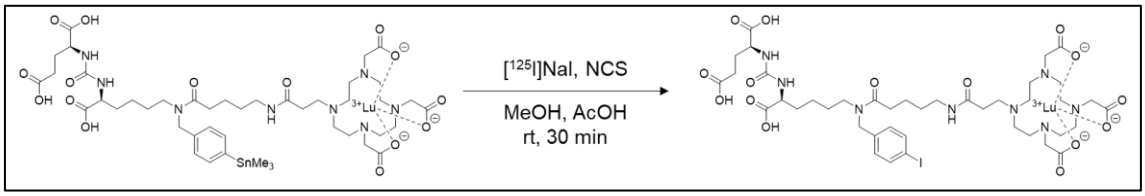

Figure 4-2. Scheme of the synthesis of [^{125}I]VK290Lu.

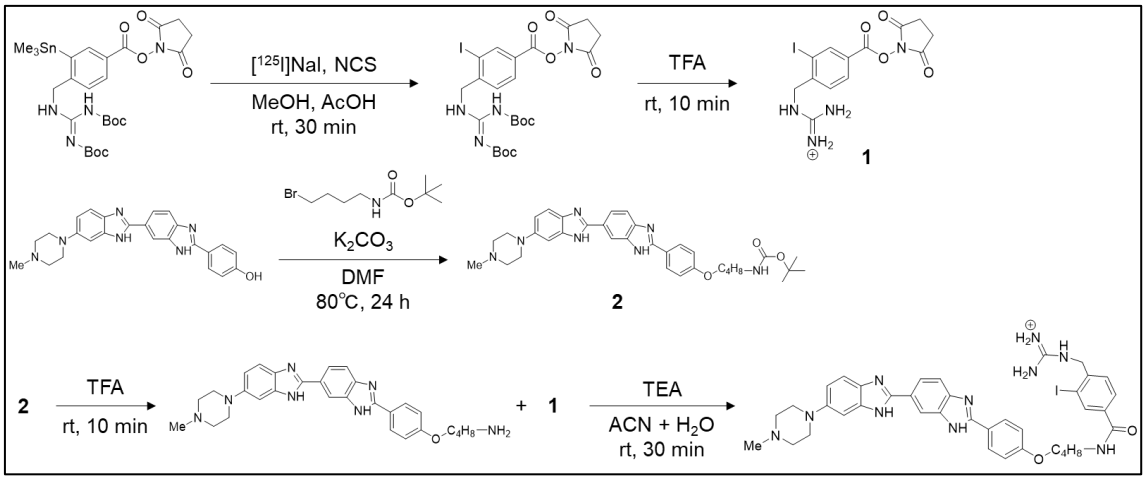

Figure 4-3. Scheme of the synthesis of [^{125}I]1,3,4-SGMIB-Hoechst33258.

The cellular uptake (membrane binding and internalization) and the DNA binding of [^{125}I]NaI, [^{125}I]VK290Lu, and [^{125}I]1,3,4-SGMIB-Hoechst33258 were investigated in PSMA-positive PC3-PIP cells (**Tables 4-1 and 4-2**). As expected, [^{125}I]NaI was not uptaken into cells, and [^{125}I]VK290Lu and [^{125}I]1,3,4-SGMIB-Hoechst33258 were translocated in cell membranes and into cells. This result suggests that [^{125}I]NaI is potentially used as a control condition where Auger-electron emitting ^{125}I is not placed inside the cells. The total cell-associated radioactivity of ^{125}I was similar for [^{125}I]VK290Lu and [^{125}I]1,3,4-SGMIB-Hoechst33258; in contrast, the percentage of membrane-bound fraction and internalized fraction was different. More ^{125}I was measured in the membrane-bound fraction than the internalized fraction for [^{125}I]VK290Lu, whereas more ^{125}I was measured in the internalized fraction than the membrane-bound fraction for [^{125}I]1,3,4-SGMIB-Hoechst33258. The internalized [^{125}I]1,3,4-SGMIB-Hoechst33258 bound to DNA while little DNA binding of the internalized [^{125}I]VK290Lu was observed (**Table 4-2**). The DNA-binding rate of [^{125}I]1,3,4-SGMIB-Hoechst33258 was 20–30 times higher than that of [^{125}I]VK290Lu. Thus, [^{125}I]VK290Lu and [^{125}I]1,3,4-SGMIB-Hoechst33258 expressed different intracellular distributions and were available as not-DNA targeting and DNA-targeting conditions.

Table 4-1. Cellular fractionation and uptake of [^{125}I]NaI, [^{125}I]VK290Lu, and [^{125}I]1,3,4-SGMIB-Hoechst33258 after incubation for 3 and 24 h in PC3-PIP cells (Membrane-bound, Internalized, and total cell-associated radioactivity).

Agents	Fractions	3 h		24 h	
		(%ID)	(%)	(%ID)	(%)
[^{125}I]NaI	Membrane-bound	0.0108 ± 0.0004	71	0.0154 ± 0.0009	78
	Internalized	0.00436 ± 0.00049	29	0.00425 ± 0.00107	22
	Total cell-associated	0.0152 ± 0.0009		0.0196 ± 0.0015	
[^{125}I]VK290Lu	Membrane-bound	2.44 ± 0.05	61	4.38 ± 0.09	55
	Internalized	1.54 ± 0.06	39	3.58 ± 0.13	45
	Total cell-associated	3.97 ± 0.11		7.96 ± 0.18	
[^{125}I]1,3,4-SGMIB-Hoechst	Membrane-bound	4.44 ± 0.19	49	3.64 ± 0.16	34
	Internalized	4.69 ± 0.33	51	6.93 ± 0.39	66
	Total cell-associated	9.13 ± 0.52		10.6 ± 0.5	

Table 4-2. Cellular uptake and DNA-binding of [^{125}I]NaI, [^{125}I]VK290Lu, and [^{125}I]1,3,4-SGMIB-Hoechst33258 for PC3-PIP cells after 24-h incubation.

Agents	Total cell-associated (%ID)	DNA-bound (%ID/mg gDNA)	DNA-bound /Total cell-associated (%)
[^{125}I]NaI	0.0087 ± 0.0016	< DL	< DL
[^{125}I]VK290Lu	14.6 ± 0.4	0.06 ± 0.03	0.002 ± 0.001
[^{125}I]1,3,4-SGMIB-Hoechst	8.4 ± 3.9	1.45 ± 0.83	0.068 ± 0.010

In the cell proliferation MTT assay as shown in **Figure 4-4**, different cytotoxicity was observed for PC3-PIP cells treated with [^{125}I]NaI, [^{125}I]VK290Lu, and [^{125}I]1,3,4-SGMIB-Hoechst33258. The proliferation of PC3-PIP cells was not inhibited in the treatment of [^{125}I]NaI up to 1 MBq for 10^3 cells. On the other hand, [^{125}I]VK290Lu and [^{125}I]1,3,4-SGMIB-Hoechst33258 decreased cell survival in the treatment of 100–1000 kBq of ^{125}I, compared with the untreated control well. That means that X-rays and γ-rays were not critical to cell survival and the damage of [^{125}I]VK290Lu and [^{125}I]1,3,4-SGMIB-Hoechst33258 could be due to Auger electrons. The relative cell survival rate was lower in the treatment with [^{125}I]1,3,4-SGMIB-Hoechst33258 than [^{125}I]VK290Lu (**Fig. 4-4**, middle and lower panels). These results suggested that DNA-targeting ^{125}I was capable of damaging cell proliferation more efficiently than non-DNA–targeting. On the other hand, PC3-PIP cells highly express PSMA antigens, and [^{125}I]VK290Lu targets them, leading to some degree of cytotoxicity. The membrane-targeted Auger-electron emitting radionuclides potentially damage cells as demonstrated in a few studies,[6] but they would be less efficient than DNA-targeted ones that the present results indicate.

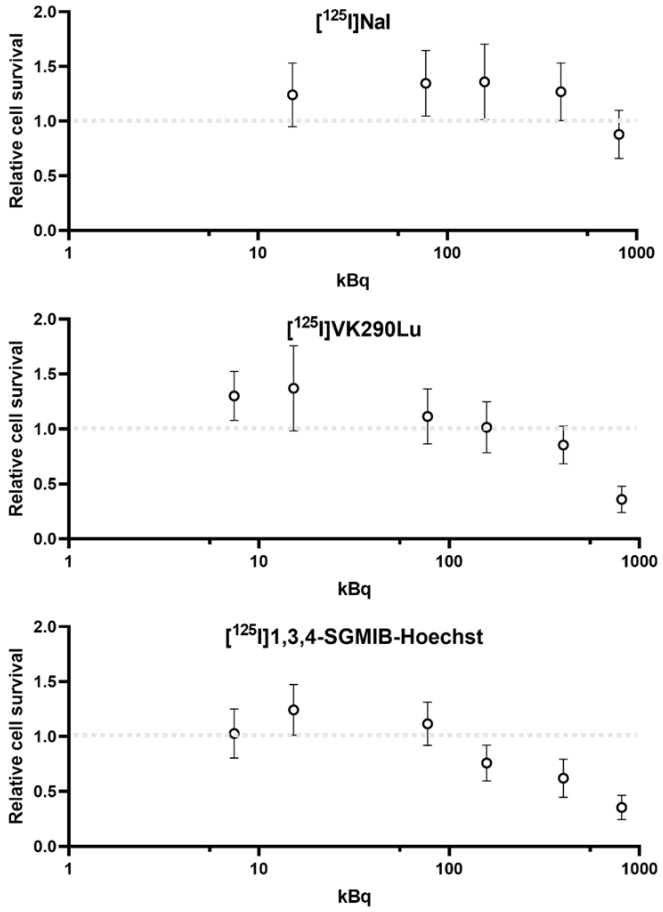

Figure 4-4. Cell proliferation MTT assay for PC3-PIP cells treated with [^{125}I]NaI, [^{125}I]VK290Lu, and

[^{125}I]1,3,4-SGMIB-Hoechst33258. 2000 cells/well were seeded onto a 96-well plate 1 d before the treatment. After adding radioactivity to the medium and incubating the cells for 3 days, the MTT assay was conducted. Survival was expressed as means ± SD (n = 6).

Conclusion

[^{125}I]NaI, distributed outside cells, and [^{125}I]VK290Lu and [^{125}I]1,3,4-SGMIB-Hoechst33258 which were distributed differently inside cells, were compared at the point of cytotoxicity. The DNA-targeting [^{125}I]1,3,4-SGMIB-Hoechst33258 decreased cell proliferation more efficiently than non-internalized [^{125}I]NaI and non-DNA–targeting [^{125}I]VK290Lu. The present experimental work indicates that DNA targeting is an effective way to cause cell damage by Auger electrons.

References

1. (a) Balagurumoorthy P, Xu X, Wang K, Adelstein SJ, Kassis AI. Effect of distance between decaying ^{125}I and DNA on Auger-electron induced double-strand break yield. *Int J Radiat Biol* **2012**; 88(12): 998–1008. (b) Pereira E, Quental L, Palma E, Oliveira MC, Mendes F, Raposinho P, Correia I, Lavrado J, Maria SD, Belchior A, Vaz P, Santos I, Paulo A. Evaluation of acridine orange derivatives as DNA-targeted radiopharmaceuticals for auger therapy: influence of the radionuclide and distance to DNA. *Sci Rep* **2017**; 7: 42544. (c) Reissig F, Mamat C, Steinbach J, Pietzsch HJ, Freudenberg R, Retamal CN, Caballero J, Kotzerke J, Wunderlich G. Direct and auger electron-induced, single and double-strand breaks on plasmid DNA caused by ^{99m}Tc-labeled pyrene derivatives and the effect of bonding distance. *PLoS ONE* **2016**; 11(9): e0161973.
2. (a) Buchegger F, Adamer FP, Dupertuis YM, Delaloye AB. Auger radiation targeted into DNA: a therapy perspective. *Eur J Nucl Med Mol Imaging* **2006**; 33: 1352–1363. (b) Imstepf S, Pierroz V, Raposinho P, Bauwens M, Felber M, Fox T, Shapiro AB, Freudenberg R, Fernandes C, Gama S, Gasser G, Motthagy F, Santos IR, Alberto R. Nuclear targeting with an auger electron emitter potentiates the action of a widely used antineoplastic drug. *Bioconjugate Chem* **2015**; 26: 2397−2407.
3. Yasui LS, Chen K, Wang K, Jones TP, Caldwell J, Gusea D, Kassis AI. Using hoechst 33342 to target radioactivity to the cell nucleus. *Radiat Res* **2007**; 167: 167–175.
4. Mease RC, Kang CM, Kumar V, Banerjee SR, Minn I, Brummet M, Gabrielson KL, Feng Y, Park A, Kiess AP, Sgouros G, Vaidyanathan G, Zalutsky MR, Pomper MG. An improved ^{211}At-labeled agent for PSMA-targeted α-therapy. *J Nucl Med* **2022**; 63(2): 259−267.
5. (a) Vaidyanathan G, McDougald D, Choi J, Koumarianou E, Weitzel D, Osada T, Lyerly HK,

Zalutsky MR. Preclinical evaluation of ^{18}F-labeled anti-HER2 nanobody conjugates for imaging HER2 receptor expression by immuno-PET. *J Nucl Med* **2016**; 57(6): 967−73. (b) Feng Y, Zhou Z, McDougald D, Meshaw RL, Vaidyanathan G, Zalutsky MR. Site-specific radioiodination of an anti-HER2 single domain antibody fragment with a residualizing prosthetic agent. *Nucl Med Biol* **2021**; 92: 171−183.

6. (a) Kiess AP, Minn I, Chen Y, Hobbs R, Sgouros G, Mease RC, Pullambhatla M, Shen CJ, Foss CA, Pomper MG. Auger radiopharmaceutical therapy targeting prostate-specific membrane antigen. *J Nucl Med* **2015**; 56(9): 1401–1407. (b) Santoro L, Boutaleb S, Garambois V, Mollevi CB, Boudousq V, Kotzki PO, P`elegrin M, Teulon IN, P`elegrin A, Pouget JP. Noninternalizing monoclonal antibodies are suitable candidates for ^{125}I radioimmunotherapy of small-volume peritoneal carcinomatosis. *J Nucl Med* **2009**; 50: 2033–2041. (c) Borgna1 F, Haller S, Rodriguez JMM, Ginj M, Grundler PV, Zeevaart JR, Köster U, Schibli1 R, Meulen1 NP, Müller C. Combination of terbium-161 with somatostatin receptor antagonists—a potential paradigm shift for the treatment of neuroendocrine neoplasms. *Eur J Nucl Med Mol Imaging* **2022**; 49(4): 1113–1126.

Experimental Section

Chapter 1. Section 1:

General

Natural Ir powder (99.9%, d_{50} = 22.560 μm [median size]) was purchased from Furuya Metal (Tokyo, Japan), enriched ^{193}Ir powder (>98%) was purchased from ATOX (Tokyo, Japan), and sodium peroxide (95%) was purchased from Hayashi Pure Chemical Industry (Osaka, Japan). Other chemicals and reagents were purchased from FUJIFILM Wako Pure Chemical (Osaka, Japan), Tokyo Chemical Industry (Tokyo, Japan), Kanto Chemical (Tokyo, Japan), Otsuka Pharmaceutical Factory (Tokyo, Japan), or Sigma-Aldrich (St. Louis, MO, USA), and were used in experiments without further purification. Milli-Q ultrapure water was used for dilution in all experiments.

Analysis

HPGe γ-ray spectrometry was used for radioactivity measurements. The HPGe detector (EGC 15–185-R, Eurisys Measures, Strasbourg, France) was coupled with a 4096 multi-channel analyzer (RZMCA, Laboratory Equipment, Ibaraki, Japan), and calibrated using a mixed standard source (^{109}Cd, ^{57}Co, ^{139}Ce, ^{51}Cr, ^{85}Sr, ^{137}Cs, ^{54}Mn, ^{88}Y, and ^{60}Co; Japan Radioisotope Association, Tokyo, Japan) at QST. The HPGe detector at TUNL was calibrated using a mixed standard source (^{241}Am, ^{109}Cd, ^{57}Co, ^{139}Ce, ^{203}Hg, ^{113}Sn, ^{137}Cs, ^{54}Mn, ^{65}Zn, ^{134}Cs, and ^{88}Y). The efficiencies of each chemical separation process were defined as the ratio of ^{191}Pt radioactivity after separation to before separation.

The HPLC system (PU-4080i; MD-4010, Jasco, Tokyo, Japan) was equipped with a 100–1000 μL sample loop and a radiation detector (US-3000; Universal Giken, Odawara, Japan and model 2200/44-10; Ludlum Measurements, Sweetwater, TX, USA). The analysis of radio-$Pt^{II}Cl_4^{2-}$ was performed using a Nucleosil SB anionic exchange column (Chemco Plus Scientific, Osaka, Japan) at a flow rate of 1.5 mL/min, and eluted with perchlorate solution (CH_3CN/H_2O = 40/60 (v/v) containing 0.1 M $NaClO_4$ and 0.04 M $HClO_4$). Nonradioactive reference samples, $K_2Pt^{II}Cl_4$ prepared in 0.1 M HCl (0.5 mg/mL) in saline solution (0.5 mg/mL) were also analyzed to identify respective retention times.

Chapter 1. Section 2:

General

Chemicals and reagents were purchased from FUJIFILM Wako Pure Chemical (Osaka, Japan), Tokyo Chemical Industry (Tokyo, Japan), Kanto Chemical (Tokyo, Japan), Otsuka Pharmaceutical Factory

(Tokyo, Japan), Kanto Chemical (Tokyo, Japan), Tanaka Metal (Tokyo, Japan), Furuya Metal (Tokyo, Japan), Hayashi Pure Chemical Industry (Osaka, Japan), Fuso Pharmaceutical Industry (Osaka, Japan), or Merck (Darmstadt, Germany). Milli-Q ultrapure water or diluted water was used for dilution in all experiments.

HPGe γ-ray spectrometry (details were in the above section) was performed to measure the radioactivity of radio-cisplatin in saline before all *in vitro* experiments. A gamma counter (Wizard2 2-Detector Gamma Counter; PerkinElmer, Waltham, MA, USA) was used to measure the radioactivity in biological samples. The X-rays and gamma-rays from both ^{191}Pt and ^{189}Pt were counted together under the energy window from 356 keV to 800 keV. Using an aliquot of the injection solution as a control for measurement, uptake was calculated from the radioactivity ratio of samples to the control.

Synthesis of carrier-free radio-cisplatin

Platinum-189 and -191 were produced as described in section 1 of *Chapter 1*. The mixed $^{189, 191}$Pt, described as radio-Pt, were used because ^{189}Pt ($T_{1/2}$ = 10.87 h, EC) is co-produced along with ^{191}Pt ($T_{1/2}$ = 2.83 d, EC) from a natural Ir target. The total radionuclidic purity of $^{189, 191}$Pt was 90–95% (described as radio-Pt), containing small amounts of ^{188}Pt. After purification with the QMA column, the volume of the collected solution was decreased by solvent evaporation, and the radio-$Pt^{II}Cl_4^{2-}$ product was prepared in HCl and KCl solution (< 300 μL). Radio-cisplatin was synthesized from radio-$PtCl_4^{2-}$ and prepared in a saline solution.

The synthesis scheme was shown in **Fig. 1-2-1**. About 900 μL of 3 M ammonia solution was added to the radio-$Pt^{II}Cl_4^{2-}$ solution until the pH reached a value of 8–9, as determined using a pH meter (D-72LAB; 9618S-10D, HORIBA, Kyoto, Japan). The mixed solution was heated in hot water at 60°C for 10 min, and then cooled in ice water. To isolate radio-cisplatin, preparative HPLC was performed using a polymer-based aqueous size exclusion chromatography (SEC) column (OHpak SB-2004, Shodex, Showa Denko, Tokyo, Japan) at a flow rate of 3.0 mL/min, eluted with physiological saline solution. Radio-cisplatin solution (300–2300 kBq/mL, ^{189}Pt; 160–1500 kBq/mL, ^{191}Pt) was used in all experiments, and the radioactivity ratio of ^{189}Pt/^{191}Pt at EOS was 0/1–2/1, depending on the cooling time. The radiochemical yield (RCY) was defined as the ratio of the radio-Pt activity of the isolated product to the total crude samples before preparative HPLC.

The analysis of radio-cisplatin was performed using a polymer-based aqueous SEC column (OHpak SB-804 HQ, Shodex, Showa Denko, Tokyo, Japan) at a flow rate of 1.0 mL/min, eluted with saline solution. Nonradioactive reference samples, nonradioactive cisplatin and transplatin in saline solution (0.5 mg/mL) were also analyzed to identify respective retention times. The radiochemical purity (RCP) was defined as the area ratio of the specified product peak to the total peaks in analytical HPLC chromatographs.

Cell culture

The human mesothelioma cell line NCI-H226 (H226) was obtained from ATCC (Manassas, VA, USA), and the human glioma cell line LN319 was from AddexBio Technologies (San Diego, CA, USA). The human lung cancer cell line NCI-H460 was obtained from ATCC (Manassas, VA, USA). The cell line stably expressing both 53BP1-EGFP and PCNA-DsRed fusion proteins (U2RDP-LE53-21) was established from the human osteosarcoma cell line U2OS via a two-step sequential transfection and blasticidin selection,[1] and gifted by Prof. Akihiro Kurimasa at Tohoku Medical and Pharmaceutical University. The cells were cultured at 37°C in a humidified atmosphere containing 5% CO_2 in a medium containing 10% FBS (Thermo Fisher Scientific, Waltham, MA, USA). The medium was RPMI-1640 (FUJIFILM Wako Pure Chemical) for H226, NCI-H460, and U2RDP-LE53-21, and D-MEM (FUJIFILM Wako Pure Chemical) for LN319.

Cellular uptake

H226 (4×10^4 cells/well) and LN319 (1×10^5 cells/well) cells were seeded onto a 24-well plate and incubated overnight at 37°C in a humidified atmosphere containing 5% CO_2. After the medium was removed, FBS-free medium containing n.c.a. or c.a. (2.5 μg of nonradioactive cisplatin) radio-cisplatin (medium/saline=9/1, 31 kBq (^{189}Pt) and 25 kBq (^{191}Pt)) was added to the cells. After incubating for 0.5–24 h, the cells were washed with PBS and dissolved in 0.1 M NaOH. The radioactivity was measured using a gamma counter, and the protein concentration was determined with the Bradford reagent (Quick Start Bradford Protein Assay kit; Bio-Rad Laboratories, Hercules, CA, USA) for the calculation of the uptake value.

Intracellular distribution

H226 (1.7×10^6 cells/dish) and LN319 (3×10^6 cells/dish) cells were seeded onto a 6-cm dish and incubated overnight at 37°C in a humidified atmosphere containing 5% CO_2. N.c.a. radio-cisplatin in saline (1.8 MBq, ^{189}Pt; 1.6 MBq, ^{191}Pt) was directly added to the cells in a medium containing FBS, and the cells were incubated for 6–48 h. The cells were washed with PBS and collected using a cell scraper. The cells were separated into four fractions: F1 (cytosolic fraction), F2 (membrane/organelle protein fraction), F3 (nucleic protein fraction), and F4 (cytoskeletal fraction), using a ProteoExtract® Subcellular Proteome Extraction kit (Merck, Darmstadt, Germany), followed by radioactivity measurements conducted for each fraction.

DNA binding

LN319 (6.3×10^5 cells/well) cells were seeded onto a 6-well plate and incubated overnight at 37°C in

a humidified atmosphere containing 5% CO_2. N.c.a. radio-cisplatin in saline (920 kBq, ^{189}Pt; 530 kBq, ^{191}Pt) was added to the cells. After incubating for 1 d, genomic DNA was isolated from the cells using a NucleoSpin Tissue DNA extraction kit (Takara Bio, Kusatsu, Japan). Radioactivity of the collected solution containing genomic DNA was measured using a gamma counter, and quantitative analysis was performed using a Microvolume UV-Vis Spectrophotometer NanoDrop One (Thermo Fisher Scientific). The DNA binding rate was calculated based on the measured values.

Sulforhodamine B (SRB) assay

H226 (2×10^3 cells/well) and LN319 (3×10^3 cells/well) cells were seeded onto a 96-well plate and incubated overnight at 37°C in a humidified atmosphere containing 5% CO_2. N.c.a. radio-cisplatin (58–120 kBq, ^{189}Pt; 34–70 kBq, ^{191}Pt), nonradioactive cisplatin (1 μg, 1 ng), or saline was added to the cells, and the cells were incubated for 2 d. After the medium was removed and the cells were washed with PBS, the cells were immobilized with 50% trichloroacetic acid and stained with Sulforhodamine B dye (In Vitro Toxicology Assay Kit, Sulforhodamine B based, TOX6; Merck). After solubilizing the cells with Tris Base solution, absorbance at 565 nm was measured using a plate reader (Synergy HTX Multi-Mode Reader; BioTek, Winooski, VT, USA).

Live/Dead viability/cytotoxicity assay

LN319 (2×10^4 cells/well) cells were seeded onto a 24-well plate and incubated overnight at 37°C in a humidified atmosphere containing 5% CO_2. N.c.a. radio-cisplatin (75 kBq, ^{189}Pt; 50 kBq, ^{191}Pt), nonradioactive cisplatin (2.5 ng), or saline was added to the cells, and the cells were incubated for 2 d. After the medium was removed and the cells were washed with PBS, reduced-serum medium (Opti-MEM; Thermo Fisher Scientific) containing calcein/ethidium homodimer-1 (LIVE/DEAD Viability/Cytotoxicity Kit for mammalian cells; Thermo Fisher Scientific) was added to stain the cells. After incubating for 30 min, fluorescence was measured on a microplate reader (Spectra Max M5; Molecular Devices, San Jose, CA, USA).

Immunofluorescence staining of γH2AX

LN319 (4×10^5) cells were seeded on coverslips (BioCoat collagen I 22-mm coverslips; Corning, Corning, NY, USA) and incubated overnight at 37°C in a humidified atmosphere containing 5% CO_2. Saline containing n.c.a. radio-cisplatin (1200 kBq, ^{189}Pt; 600 kBq, ^{191}Pt), nonradioactive cisplatin (7.5 ng), or none was added to the cells, and the cells were incubated for 3 h. After the medium was removed and the cells were washed with PBS, the cells were immobilized with ice-cold MeOH, incubated in 0.25% Triton X-100/PBS for permeabilization, and then incubated in 1% BSA/PBST for blocking. Immunofluorescence staining was conducted using a gamma-H2A.X antibody (phospho

S139; Abcam, Cambridge, UK) as the primary antibody, with Alexa Fluor 594 anti–rabbit IgG (A-11012; Thermo Fisher Scientific) as the secondary antibody. Coverslips were placed on glass slides using a mounting medium containing DAPI (Vector Laboratories, Burlingame, CA, USA). Fluorescence images were taken with a BZ-X800 fluorescence microscope (KEYENCE, Osaka, Japan) and analyzed using the BZ-Z800 Analyzer software (KEYENCE), under the same conditions for each. In image analysis, setting the lower limits of fluorescence intensity to remove small foci as background, a nucleus with γH2AX foci was defined as a γH2AX-positive nucleus. Total nuclei and γH2AX-positive nuclei were counted, and the fluorescence intensity of nuclear γH2AX foci was quantified.

Gel electrophoresis of plasmid DNA

pcDNA3.1/Hygro (5597 nucleotides) was obtained from Thermo Fisher Scientific. The plasmids were transformed into competent *Escherichia coli* (DH5*α*; TOYOBO, Osaka, Japan). Transformed *E. coli*, were cultured, and plasmid was purified using QIAprep Mini Kit (QIAGEN, Venlo, Netherlands). Isolated plasmids were dissolved in TE buffer (0.01 M Tris and 0.0001 M EDTA) at a concentration of 100–200 ng/μL and stored at −20°C. Plasmid samples were prepared at a DNA concentration of 5 ng/μL in 300 μL (1.5 μg = 0.4 pmol) of 0.2 M phosphate buffer solution with or without 0.2 M DMSO. Samples contained no cisplatin (control), [^{191}Pt]cisplatin (1.62 MBq = 0.9 pmol), or nonradioactive cisplatin (0.18 ng = 0.6 pmol). After mixing, plasmid samples were incubated at 37°C for 1 h, and then stored at <10°C for 34 d. Original plasmid, cloned plasmid, and plasmid digested with the restriction enzyme *Hin*dIII (New England Biolabs, Ipswich, MA, USA) were also prepared at the same concentration (5 ng/μL) in TE buffer. Ten microliters of sample solution (50 ng of plasmid) was mixed with 2 μL of loading dye (sucrose red) and loaded in a gel lane. The gel consisted of 0.8% agarose and ethidium bromide (EtBr) solution (2.5 μg/mL; NIPPON GENE, Tokyo, Japan) in 0.5×TBE buffer (0.0445 M Tris, 0.0445 M borate, and 0.001 M EDTA). DNA ladder (1 kb) was obtained from (New England Biolabs). The gels were run at 100 V for 80 min, and then scanned on an image analyzer (ImageQuant LAS 500; Cytiva, Tokyo, Japan).

Time-lapse imaging of U2RDP-LE53-21 cells

U2RDP-LE53-21 (1.5×10^5 cells/well) cells were seeded onto a glass-based 6-well culture plate (EZVIEW culture plates LB; AGC Techno Glass, Shizuoka, Japan) and incubated overnight at 37°C in a humidified atmosphere containing 5% CO_2. After the medium was replaced with fresh Opti-MEM™ (without phenol red; Thermo Fisher Scientific) containing 10% FBS, pre-time-lapse imaging of the cells was conducted every 15 min for 6 h for background measurements. A saline solution containing radio-cisplatin (886 kBq, ^{189}Pt; 759 kBq, ^{191}Pt), nonradioactive cisplatin (0.5 ng, 0.8 nM),

or none (only saline) was added to the cells, and then time-lapse imaging of the cells was conducted every 15 min for 40 h. Fluorescent microphotographs and brightfield images were acquired using an inverted fluorescence microscope (BZ-X800 fluorescence microscope; KEYENCE, Osaka, Japan) in combination with the Z-stack mode of 4.9/0.7 μm. The fluorescence microscope was equipped with a 20× objective lens (Plan Apochromat; Nikon Solutions, Tokyo, Japan) and a fluorescence filter (EGFP: 49020-UF1-BLA, excitation 480/20, emission 510/20; M SQUARE, Fukuoka, Japan. DsRed: TexasRed, excitation 560/40, emission 630/75; KEYENCE). Because the focused Z-stack points for raw images slightly differed, each original image (1,920 × 1,440) was divided into six sections (1,024 × 768): three vertically and two horizontally. Focused images were selected automatically, and time-lapse images for each section were concatenated and used in the subsequent analyses, where duplicate nuclei were excluded.

The image analysis included the following four main steps (**Fig. 5-1**):[1] (1) extraction of nuclei from raw images using deep learning-based segmentation; (2) concatenation of the extracted nucleus of each time-lapse image; (3) analysis of the fluorescent appearance of each nucleus over time; and (4) determination of the cell cycle on the basis of the fluorescent and morphological features.

Step 1: Extraction of nuclei from raw images

Depending on the cell cycle, the fluorescent intensity might be insufficient to enable precise extraction of nuclei from images in the segmentation process. In the present work, a deep learning-based segmentation was used to handle a large number of nuclei data. First, training image data were prepared by manual segmentation (>100 images, 20–50 nuclei per image) using an ImageJ macro (Fiji, ImageJ 1.53f51; Java 1.8.0.66; 64-bit) combined with the LOCI plugin. Second, nuclei segmentation of images was conducted simultaneously using StarDist Fluorescence Nuclei Segmentation (https://bioimage.io/#/, 10.5281/zenodo.6348084) [accessed 26 November 2021] and the free, open-source toolbox ZeroCostDL4Mic,[2] which is a collection of Jupyter Notebooks provided by Google Colaboratory to implement deep learning in microscopy imaging.

Step 2: Concatenation of the extracted nucleus of each time-lapse image

Using the R language (platform: x86_64-apple-darwin15.6.0 [64-bit]; RStudio, Boston, MA, USA), each nucleus was tracked automatically on the basis of the location information of the segmented nuclei. The two-dimensional (2D) position of a nucleus center was determined, and that of a nearby one was sequentially extracted. In the M phase of the dividing cell, a nucleus expanded to become elliptical. The two spirited nuclei were located along its long axis, and their location information was acquired. The trajectories of extracted nuclei were obtained. Some nuclei were not tracked, in which case their information was corrected manually. Each nucleus with location information was labeled as the cell number in the segmented nuclei. Consequently, four different movies (53BP1-EGFP, PCNA-

DsRed, segmentation, and bright-field images) were created for each identified nucleus from the images concatenated using ImageJ.

Step 3: Analysis of the fluorescent appearance of each nucleus over time

The movie set (53BP1-EGFP, PCNA-DsRed, segmentation, and bright-field images) for an individual nucleus was automatically analyzed. The number of 53BP1-EGFP and PCNA-DsRed foci was counted using the Find Maxima process in ImageJ. For the output, the point selection type was set; for the noise tolerance parameter, 1 and 3 were used for PCNA and 53BP1, respectively. Other image parameters (e.g., brightness, shape, and objectivity) for each cell nucleus were also extracted using an ImageJ macro.

Step 4: Determination of the cell cycle of each cell

Three experts manually determined the cell cycle. The fluorescent appearance of PCNA-DsRed is related to the cell cycle;[3] numerous PCNA foci appear in the S phase (DNA synthesis). The transition of the G1 → S phase and S → G2 phase was judged on the basis of the PCNA-DsRed feature of time-lapse movies. PCNA foci appeared at the beginning of the S phase and disappeared at the end of the S phase. Other phase transitions were determined via a change in the morphological features. The nucleus size returned to normal, and the nuclear membrane appeared clear at the beginning of the G1 phase. The nucleus expanded immediately at the beginning of the M phase and thereafter split into two.

Thus, each nucleus was tracked over time, counted the number of foci, and judged the cell cycle. The cell-cycle data for nuclei in the same treatment was summed (none, nonradioactive cisplatin, and radio-cisplatin), and the average length of each phase was calculated. The number of 53BP1 foci at each time point was found to correspond over time and is discussed in the Results and Discussion sections.

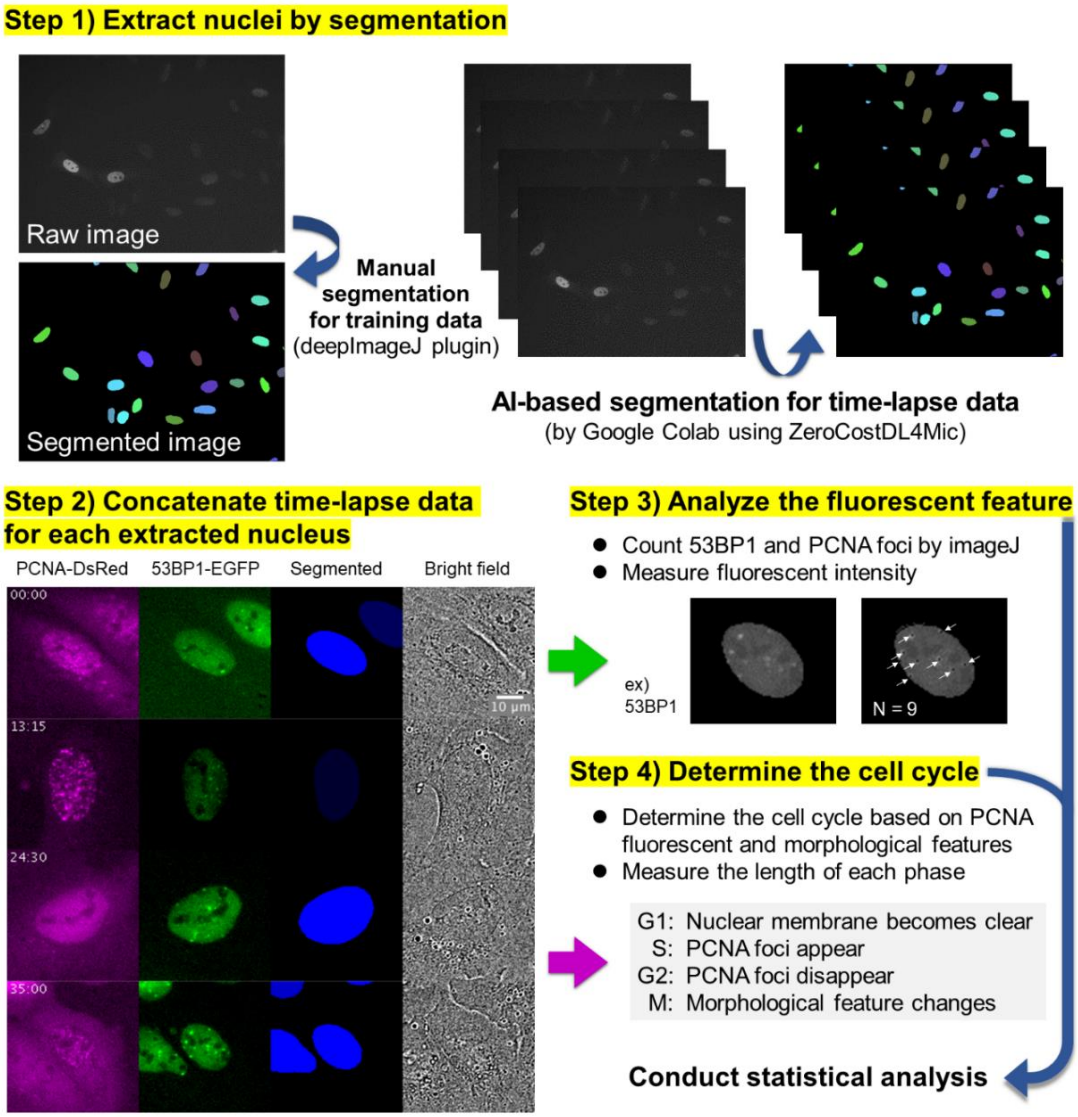

Figure 5-1. Outline of the image analysis process used in the present imaging.

Animal studies on the human tumor xenograft model

The protocol for the animal experiments was approved by the Animal Care and Use Committee of the National Institutes for Quantum and Technology (13–1022, 26 May 2016), and all animal experiments were conducted following the institutional guidelines regarding animal care and handling. H460 cells were suspended in 1 mL PBS (2×10^7 cells/mL), and 2×10^6 cells in 100 µL were subcutaneously injected into the flank of male BALB/c-nu/nu mice (6 weeks old; CLEA Japan, Tokyo, Japan) under isoflurane anesthesia. Tumor volumes reached 100–400 mm^3 2–3 weeks after inoculation. For the biodistribution study, 100 µL of saline solution containing radio-cisplatin (50 kBq, ^{189}Pt; 35 kBq, ^{191}Pt) and 50 µg of nonradioactive cisplatin (2 mg/kg BW) were intravenously injected into mice when tumor volumes reached 100–400 mm^3 (n = 4 for each time-point). The mice were sacrificed by isoflurane

inhalation at 2, 15, 60 min, 1, 3, 5, and 7 d after injection. Blood was obtained from the heart, and then tumor, lung, liver, pancreas, stomach, intestine, kidney, bone, and muscle were dissected. Uptake in tissues was represented as a percentage of the injected dose (radioactivity) per gram of tissue (%ID/g) and that for the whole body as a percentage of the injected dose (%ID). These values were corrected to those in the body weight of 20 g. Uptake in the whole body was calculated from the total radioactivity of dissected tissues and residual bodies.

Red blood cell partitioning and plasma protein binding of cisplatin

The red blood cell partitioning and the plasma protein binding of ^{191}Pt were evaluated for the blood of mice. At 2 min, 60 min, and 1 d after the intravenous injection of cisplatin, blood was obtained from the heart and mixed with heparin (Mochida Pharmaceutical Factory, Tokyo, Japan). The whole blood was centrifuged and divided into blood cells and plasma. The red blood cell partitioning rate of ^{191}Pt was calculated on the basis of the activity of blood and plasma, defined as $(A_{blood} - A_{plasma}) \times (1 - Hct) \times 100/A_{blood}) \times 100$, where A_{blood} is the radioactivity of 20 μL whole blood, A_{plama} is the radioactivity of a 20 μL plasma fraction, and Hct is the hematocrit value (0.43). The plasma was ultrafiltered with Amicon Ultra (10K, 0.5 mL Centrifugal Filters for DNA and Protein Purification and Concentration, Merck). The protein binding rate of ^{191}Pt was calculated based on the activity of each separated fraction, defined as $(A_{con} - A_{fil})/A_{con} \times 100$, where A_{con} is the radioactivity of a 50 μL concentrated fraction and A_{fil} is the radioactivity of a 50 μL filtered fraction.

Statistical analysis

The data of cellular uptake in **Fig. 1-2-4** were evaluated by two-way ANOVA, and the data from the cell proliferation assay in **Table 1-2-2** and γH2AX assay in **Fig. 1-2-7** were evaluated by one-way ANOVA with multiple comparisons using the GraphPad Prism 9 software (GraphPad Software, San Diego, CA, USA). $p < 0.05$ was considered statistically significant. The error of DNA binding was calculated from both counting errors and error propagation. The data in **Fig. 1-2-10** were evaluated by two-way analysis of variance (ANOVA) multiple comparisons, and those in **Fig. 1-2-13** were evaluated by one-way ANOVA with multiple comparisons using R programming and RStudio; $p < 0.05$ was considered statistically significant.

Chapter 2. Section 1:

General

Chemicals and reagents were purchased from FUJIFILM Wako Pure Chemical (Osaka, Japan),

Nacalai Tesque (Kyoto, Japan), DOJINDO Laboratories (Kamimashiki, Japan), Tokyo Chemical Industry (Tokyo, Japan), Macrocyclics (Plano, TX, USA), WATANABE Chemical Industries (Hiroshima, Japan), Cayman Chemical (Ann Arbor, MI, USA), Otsuka Pharmaceutical Factory (Tokyo, Japan), AdipoGen Life Sciences (San Diego, CA, USA), Medchemexpress (Monmouth Junction, NJ, USA), MP Biomedicals (Santa Ana, CA, USA), or Merck (Darmstadt, Germany). Milli-Q ultrapure water or diluted water was used for dilution in all experiments.

^{191}Pt was produced as described above. The radionuclidic purity of the ^{191}Pt precursor was 90–95%, and it contained small amounts of $^{188, 189}$Pt. A collected fraction of $^{191}PtCl_4^{2-}$ was evaporated to dryness and re-dissolved in 0.2 M phosphate buffer solution (pH: 7–8). The obtained ^{191}Pt solution contained KCl (0.2–0.4 M) and phosphate ion (0.2 M), and the concentration of ^{191}Pt activity was 50–1000 kBq/μL.

Reactivity evaluation of multidentate ligands or cysteine for n.c.a. ^{191}Pt

The following chemical agents were considered as ligands for n.c.a. ^{191}Pt (**Fig. 2-1-1**): multidentate ligands: diethylenetriaminepentaacetic acid (DTPA) and ethylenedithiodiacetic acid (EDDA); amino acids: L-cysteine (Cys), L-methionine (Met), L-serine (Ser), and L-glutamine (Gln); protected Cys analogs: *N*-(*tert*-butoxycarbonyl)-*S*-trityl-L-cysteine (Boc-Cys(Trt)-OH) and *S*-trityl-L-cysteine (H-Cys(Trt)-OH). The reaction mixture containing ^{191}Pt was prepared in 40 mM PB (H_2O/DMSO = 1/1) solution containing each agent (5 mM) and 10^{-2} M KCl. The mixed solution (1 MBq of ^{191}Pt in 100–150 μL) was heated at 45–60°C for 60 min. Thin-layer chromatography (radio-TLC) analysis of the reaction mixture of ^{191}Pt was conducted on a silica-gel plate (TLC Silica Gel 60 F_{254}; Merck, Darmstadt, Germany) with a solvent of 100% MeOH.

The protein binding of ^{191}Pt was evaluated after ^{191}Pt was reacted with each agent. The reaction mixture was diluted with the 10% FBS-containing RPMI-1640 medium (reaction mixture/medium = ¼) and incubated at 37°C for 3 h. The mixture was ultrafiltered with Amicon Ultra (10K, 0.5 mL Centrifugal Filters for DNA and Protein Purification and Concentration; Merck). The protein-binding rate of ^{191}Pt was calculated on the basis of the activity of each separated fraction, defined as $(A_{con} - A_{fil})/A_{con} \times 100$ (A_{con}: radioactivity of a 50 μL concentrated fraction, A_{fil}: radioactivity of a 50 μL filtered fraction).

Synthesis of Cys-Hoechst33258 and DTPA-Hoechst33258

The DNA-targeting conjugates based on Hoechst33258 (Cys-Hoechst33258 and DTPA-Hoechst33258) were synthesized as illustrated in **Fig. 2-1-3**; details were provided in the following subsections.

*tBu-DTPA-Hoechst33258 amide analog (**1**) for ^{191}Pt*

Hoechst33258 analog ($C_{29}H_{30}N_6O_3$, 5.7 mg, 0.011 mmol), hexafluorophosphate benzotriazole tetramethyl uronium (HBTU, 5.0 mg, 0.013 mmol), and NH_2-DTPA-*t*Bu ($C_{41}H_{70}N_4O_{10}$, 8.8 mg, 0.011 mmol) were dissolved in dimethylformamide (DMF, 1.5 mL) containing *N*,*N*-diisopropylethylamine (DIPEA, 100.5 μL, 0.59 mmol), and the resultant mixture was stirred at room temperature for 2 h. The reaction mixture was concentrated and purified by column chromatography (silica gel, hexane/EtOAc/TEA = 50/50/1 to CH_2Cl_2/MeOH/TEA = 90/10/1). The collected fraction was evaporated to dryness under reduced pressure, and *t*Bu-DTPA-Hoechst33258 (**1**) was obtained (12.6 mg, 90% yield). ESI calcd for $C_{70}H_{99}N_{10}O_{12}^+$ $[M+H]^+$ 1271.7438; found 1271.7454.

*Boc-C_4-Hoechst33258 (**3**)*

Hoechst33258 ($C_{25}H_{24}N_6O{\cdot}3HCl$, 120 mg, 0.225 mmol), 4-(Boc-amino)butyl bromide (79.4 mg, 0.315 mmol), and K_2CO_3 (156 mg, 1.13 mmol) were suspended in super-dehydrated DMF (6 mL), and the reaction mixture was heated at 80°C for 24 h. After filtering, the reaction mixture was concentrated and purified by column chromatography (silica gel, CH_2Cl_2/MeOH/TEA = 100/1/1 to 100/10/1). The collected fraction was evaporated to dryness under reduced pressure, and Boc-C_4-Hoechst33258 (**3**) was obtained (67 mg, 50% yield). FAB calcd for $C_{34}H_{42}N_7O_3^+$ $[M+H]^+$ 596.33; found 596.

*tBu-DTPA-Hoechst33258 thiourea analog (**5**) for ^{111}In*

NH_2-DTPA-*t*Bu ($C_{41}H_{70}N_4O_{10}$, 80 mg, 0.103 mmol) and 1,1′-thiocarbonyldi-2(1*H*)-pyridone ($C_{11}H_8N_2O_2S$, 24.5 mg, 0.105 mmol) were dissolved in super-dehydrated DMF (5 mL) with TEA (45 μL, 0.323 mmol). The reaction mixture was replaced with dry N_2 gas and stirred at room temperature for 4 h. The solution was concentrated and purified by column chromatography (silica gel, hexane/EtOAc/TEA = 80/40/1). The collected fraction was evaporated to dryness under reduced pressure, and isothiocyanated DTPA-*t*Bu was obtained (NCS-DTPA-*t*Bu (**4**), 50 mg, 60% yield). APCI calcd for $C_{42}H_{69}N_4O_{10}S^+$ $[M+H]^+$ 821.4729; found 821.4718.

Boc-C_4-Hoechst33258 (**3**) (31.5 mg, 0.053 mmol) was suspended in CH_2Cl_2 (4 mL) and dissolved by adding droplets of MeOH. TFA (1 mL) was added to the solution, and the reaction mixture was stirred at room temperature for 30 min. After the mixture was evaporated to dryness under reduced pressure, the residue (NH_2-C_4-Hoechst33258) was co-evaporated with toluene (2 mL × 2). The obtained NH_2-C_4-Hoechst33258 was dissolved in super-dehydrated DMF (1 mL), and DIPEA (200 μL, 1.2 mmol) was added to the solution until the pH reached 9–10. NCS-DTPA-*t*Bu (**4**) (39 mg, 0.047 mmol) was dissolved separately in super-dehydrated DMF (1 mL) and DIPEA (20 μL, 0.12 mmol). Both solutions were mixed and stirred overnight at room temperature. The reaction mixture was concentrated and purified by column chromatography (silica gel, CH_2Cl_2/MeOH/TEA = 100/1/1 to 90/10/1). The collected fraction was evaporated to dryness under reduced pressure, and *t*Bu-DTPA-

Hoechst33258 (**5**) was obtained. APPI calcd for $C_{71}H_{102}N_{11}O_{11}S^+$ $[M+H]^+$ 1316.7475; found 1316.7476.

*DTPA-Hoechst33258 (**2**, **6**)*

A batch of *t*Bu-DTPA-Hoechst33258 (**1** or **5**) (1–3 mg) was dissolved in TFA (500 μL) and stored at room temperature for 3 h. After the mixture was evaporated, the residue was co-evaporated with toluene (1 mL × 2). A batch of DTPA-Hoechst33258 (**2** or **6**) was evaporated to dryness under reduced pressure and stored at −10°C. ESI calcd for (**2**) $C_{50}H_{59}N_{10}O_{12}^+$ $[M+H]^+$ 991.4308; found 991.4320. APPI calcd for (**6**) $C_{51}H_{62}N_{11}O_{11}S^+$ $[M+H]^+$ 1036.4345; found 1036.4355.

*Boc-Cys(Trt)-Hoechst33258 (**7**)*

Boc-C_4-Hoechst33258 (**3**) (11.9 mg, 0.020 mmol) was suspended in CH_2Cl_2 (1 mL) and dissolved by adding droplets of MeOH. TFA (0.25 mL) was added to the solution, and the reaction mixture was stirred at room temperature for 30 min. After the mixture was evaporated to dryness under reduced pressure, the residue (NH_2-C_4-Hoechst33258) was co-evaporated with toluene (2 mL × 2). The obtained NH_2-C_4-Hoechst33258 was dissolved in super-dehydrated DMF (1 mL), and DIPEA (67 μL, 0.39 mmol) was added to the solution until the pH reached 9–10. *N*-(*tert*-Butoxycarbonyl)-*S*-trityl-L-cysteine (Boc-Cys(Trt)-OH, 8.8 mg, 0.019 mmol) and HBTU (9.5 mg, 0.025 mmol) were dissolved separately in a mixture of super-dehydrated DMF (0.5 mL) and DIPEA (33 μL, 0.19 mmol). Both solutions were mixed and stirred at room temperature for 2 h. The reaction mixture was concentrated and purified by column chromatography (silica gel, CH_2Cl_2/MeOH/TEA = 100/1/1 to 100/10/1). The collected fraction was evaporated to dryness under reduced pressure, and Boc-Cys(Trt)-Hoechst33258 (**3**) was obtained (11 mg, 60% yield). ESI calcd for $C_{56}H_{61}N_8O_4^+$ $[M+H]^+$ 941.4531; found 941.4541.

*Cys-Hoechst33258 (**8**)*

A batch of Boc-Cys(Trt)-Hoechst33258 (**7**) (5–10 mg) was dissolved in a mixed solution (TFA/H_2O / Triisopropylsilane (TIPS) = 950/25/25 μL) and stored at room temperature for 1 h. Ice-cold diethyl ether was added to the mixture in an ice bath, and the supernatant was removed after centrifugation. After this process was repeated three times, a batch of Hoechst-Cys was evaporated to dryness under reduced pressure and stored at −30°C. APPI calcd for (**8**) $C_{32}H_{39}N_8O_2S^+$ $[M+H]^+$ 599.2911; found 599.2919.

The protected conjugates Boc-Cys(Trt)-Hoechst33258 (**2**) and *t*Bu-DTPA-Hoechst33258 (**4**, **7**) were >95% pure, as determined by HPLC (conditions: column, COSMOSIL 5C18-MS-II (Nacalai Tesque, Kyoto, Japan); gradient elution, A/B = 0.1% TEA in H_2O/CH_3CN = 80/20 (0–5 min) → 0/100 (15–30 min)).

Lipophilicity evaluation (log $D_{7.4}$)

The log $D_{7.4}$ values of Hoechst33258 (–OH), DTPA-Hoechst33258 (**2**, **6**), and Cys-Hoechst33258 (**8**) were determined as the logarithm of the distribution coefficient in 1-octanol/PBS by the shaking flask method (pH = 7.4 at room temperature). The concentration of compounds for each phase was measured using a NanoDrop One microvolume UV–Vis spectrophotometer (Thermo Fisher Scientific).

Labeling DTPA- and Cys-Hoechst33258 with ^{191}Pt, and purification of the labeled samples.

A batch of DTPA/Cys-Hoechst33258 was dissolved in DMSO (0.45–4.5 mM). The reaction mixture consisting of a DTPA/Cys-Hoechst33258 solution (20 μL), DMSO (80 μL), Tween 80 (0.2 μL), ethanol (0.8 μL), and a ^{191}Pt solution (100 μL) was prepared and heated at 45–80°C for 60 min. Both reaction mixtures were purified by HPLC; the column was a COSMOSIL 5C18-MS-II (5 μm, 4.6 mm × 250 mm; Nacalai Tesque, Kyoto, Japan), the eluent was A/0.1% TFA in H_2O, B/0.1% TFA in CH_3CN, gradient: A/B = 90/10 in 0 min – 50/50 in 20 min – 95/5 in 30 min, and the flow rate was 1.0 mL/min. A solution containing [^{191}Pt]Pt-DTPA/Cys-Hoechst33258 was collected in a vial with Tween 80 added beforehand. The solution was evaporated to remove CH_3CN and neutralized with 10× PBS and 1 M NaOH. [^{191}Pt]Pt-DTPA/Cys-Hoechst33258 was finally prepared in a 1× PBS solution containing 0.2% Tween 80 and 0.2% TFA. After purification, the product was analyzed by HPLC under the same conditions used in the preparation.

An indium chloride injection ($^{111}InCl_3$) was purchased from Nihon Medi-Physics (Tokyo, Japan). The reaction mixture consisting of a 4.5 mM DTPA-Hoechst33258 solution (20 μL), DMSO (30 μL), Tween 80 (0.2 μL), ethanol (0.8 μL), and a ^{111}In solution (150 μL) was prepared. After being stored at room temperature for 30 min, the reaction mixture was injected into a preparative HPLC system and purified similarly. The product solution containing [^{111}In]In-DTPA-Hoechst33258 was prepared under the same conditions used to prepare [^{191}Pt]Pt-DTPA/Cys-Hoechst33258.

A $^{111}InCl_3$ solution was diluted with 1× PBS containing 0.2% Tween 80, which was used as free ^{111}In in the *in vitro* experiments. The $^{191}PtCl_4^{2-}$ solution was also used in labeling and was loaded onto a QMA light cartridge (AccellPlus QMA; Waters, Milford, MA, USA) and eluted with 10× PBS. The eluted ^{191}Pt was diluted with water containing 0.2% Tween 80 and used as free ^{191}Pt.

Cell culture

The human neuroblastoma cell line NB69 was obtained from the European Collection of Authenticated Cell Cultures (Public Health England, London, UK). The cells were cultured at 37°C in a humidified atmosphere containing 5% CO_2 in RPMI-1640 (FUJIFILM Wako Pure Chemical, Osaka, Japan)

containing 10% FBS (Thermo Fisher Scientific, Waltham, MA, USA).

Cellular uptake and intracellular behavior

U2OS-53BP1 cells ((0.5–1) × 10^6 cells/dish) were seeded onto a 6 cm dish or 6-well plate and incubated overnight at 37°C in a humidified atmosphere containing 5% CO_2. Free/labeled ^{191}Pt (54–180 kBq) or ^{111}In (900–1000 kBq) was added to the cells. After incubating for 1 d, the cells were washed with PBS and collected using a cell scraper. The cells were separated into four fractions—F1 (cytosolic fraction), F2 (membrane/organelle protein fraction), F3 (nucleic protein fraction), and F4 (cytoskeletal fraction)—using a ProteoExtract® Subcellular Proteome Extraction kit (Merck, Darmstadt, Germany), followed by measurements of the radioactivity of each fraction. The protein concentration was determined using the Bradford reagent (Quick Start Bradford Protein Assay kit; Bio-Rad Laboratories, Hercules, CA, USA). The cellular uptake was obtained from the value of the sum of the four fractions.

DNA-binding.

U2OS-53BP1 ((3–5) × 10^5 cells/well) and NB69 ((2–3) × 10^5 cells/well) cells were seeded onto a 6-well plate and incubated overnight at 37°C in a humidified atmosphere containing 5% CO_2. Free/labeled ^{191}Pt (27–58 kBq) or ^{111}In (300–370 kBq) was added to the cells. After the cells were incubated for 1 d, genomic DNA was isolated from the cells using a NucleoSpin Tissue DNA extraction kit (MACHEREY-NAGEL, Düren, Germany). The radioactivity of the collected solution containing genomic DNA was measured using a gamma counter (Wizard2 2-Detector Gamma Counter; PerkinElmer, Waltham, MA, USA), and quantitative analysis was performed using a NanoDrop One microvolume UV–Vis spectrophotometer (Thermo Fisher Scientific). The DNA-binding rate was calculated on the basis of the measured values.

Fluorescent imaging of 53BP1-EGFP in U2OS-53BP1 cells.

U2OS-53BP1 ((3–5) × 10^5 cells/well) cells were seeded on a glass-based 6-well culture plate (EZVIEW® culture plates LB; AGC Techno Glass, Shizuoka, Japan) and incubated overnight at 37°C in a humidified atmosphere containing 5% CO_2. A solution containing free/labeled ^{191}Pt (360–420 kBq), free /labeled ^{111}In (430–440 kBq), or none was added to the cells. The cells were incubated in the medium containing each agent overnight, and the medium was replaced with fresh Opti-MEM™ (no phenol red; Thermo Fisher Scientific) containing 10% FBS. After the cells were incubated for an additional 1 d to allow for ^{191}Pt decay, fluorescent microphotographs for 53BP1-EGFP of the cells were acquired with an inverted fluorescence microscope (BZ-X800 fluorescence microscope; KEYENCE, Osaka, Japan). The fluorescence microscope was equipped with a 20× objective lens

(Plan Apochromat; Nikon Solutions, Tokyo, Japan) and a fluorescent filter for EGFP (49020-UF1-BLA, excitation 480/20, emission 510/20; M SQUARE, Fukuoka, Japan). The brightness and contrast of images were analyzed using its software (BZ-Z800 Analyzer software; KEYENCE). The quantitative analysis of images was performed using the "hybrid cell count" method of the software under the same conditions for each image. The nuclei and 53BP1-EGFP foci were extracted from the images semi-automatically and were used as the basis for the calculations of both the number and area.

Statistical analysis

The data in **Fig. 2-1-11** were evaluated by one-way ANOVA with multiple comparisons using the GraphPad Prism 9 software (ver. 9.2.0; GraphPad Software, San Diego, CA, USA); $p < 0.05$ was considered statistically significant.

Chapter 2. Section 2:

General

Chemicals and reagents were purchased from FUJIFILM Wako Pure Chemical (Osaka, Japan), Nacalai Tesque (Kyoto, Japan), Tokyo Chemical Industry (Tokyo, Japan), Otsuka Pharmaceutical Factory (Tokyo, Japan), or Merck (Darmstadt, Germany). Milli-Q ultrapure water or distilled water was used for dilution in all experiments. Mixtures of $^{191}PtCl_4^{2-}$ and $[^{191}PtCl_{4-n}(H_2O)_n]^{(2-n)-}$ were referred to as "free ^{191}Pt"; they were used as the precursor. Free ^{191}Pt was also used in *in vitro* experiments as a control and was prepared in a PBS solution containing 0.2% Tween 80.

Synthesis of [^{191}Pt]Pt-MYCN-Cys-R3-coumarin and [^{191}Pt]Pt-GCC-Cys-R3-coumarin

The MYCN-Cys-R3-coumarin and GCC-Cys-R3-coumarin were provided by the Chemical Biology Lab at Kyoto University. MYCN-PIP: MALDI-TOF MS: *m/z* calcd. for $C_{120}H_{157}N_{50}O_{25}S^+$ $[M+H]^+$ 2730.2, found 2730.6. GCC-PIP: MALDI-TOF MS: *m/z* calcd. for $C_{81}H_{114}N_{33}O_{17}S^+$ $[M+H]^+$ 1852.9, found 1853.4. MYCN-PIP and GCC-PIP were >95% pure, as determined by HPLC.

Two hundred and thirty microliters of the reaction mixture consisting of DMSO (76 μL), ^{191}Pt solution (3.7–93 MBq, 150 μL), MYCN/GCC-Cys-R3-coumarin (2 mM, 3 μL), 0.09% Tween 80 (0.2 μL), and 0.3% ethanol (0.8 μL) was prepared and heated at 45°C for 60 min. The reaction mixture was purified by HPLC; the column was a COSMOSIL 5C18-MS-II (5 μm, 4.6 mm × 250 mm; Nacalai Tesque, Kyoto, Japan), the eluent was A/0.1% TFA in H_2O, B/0.1% TFA in CH_3CN, gradient: A/B = 95/5 in 0 min → 30/70 in 25 min, and the flow rate was 1.0 mL/min. A solution

containing [^{191}Pt]Pt-MYCN/GCC-Cys-R3-coumarin was collected in a vial with Tween 80 added beforehand. The solution was evaporated to remove CH_3CN and neutralized with 10× PBS and 1 M NaOH. [^{191}Pt]Pt-MYCN/GCC-Cys-R3-coumarin was finally prepared in a 1× PBS solution containing 0.2–0.4% Tween 80 and 0.2% TFA for *in vitro* experiments or containing 0.75% Tween 80 and 0.2% TFA for *in vivo* experiments. After purification, the product was analyzed by HPLC under the same conditions used in the preparation. Because the product solution of ^{191}Pt-MYCN-PIP contains nonlabelled MYCN-PIP, the following *in vitro*/*in vivo* experiments involving the treatment of nonlabelled MYCN-PIP with approximately the same concentration as the ^{191}Pt-MYCN-PIP solution (1–20 μM for an incubation or injection solution) were conducted for comparison.

Gel electrophoretic mobility shift assay

Oligonucleotides (30 bp: forward, 5'-CCTAACCACAAGA**AGGCTCCC**AAGTTAACC-3'; reverse, 3'-GGATTGGTGTTCT**TCCGAGGG***T*TCAATTGG-5') were designed and obtained from Sigma-Aldrich. The oligonucleotides were dissolved in Tris buffer (10 mM, pH = 7.5) at a concentration of 100 μM and were formed as double strands by heating at 90°C for 5 min. The oligonucleotide samples were prepared at a DNA concentration of 5 μM in a buffer solution containing 1% DMSO, 0.5% Tween 80, 10 mM $(CH_3)_2AsO_2Na$, 10 mM Tris-HCl, 10 mM NaCl, and nonradioactive GCC/MYCN-PIP (30–55 μM) with/without ^{191}Pt-MYCN-PIP (90 kBq). After the samples were mixed, they were incubated at 37°C overnight (15 h). Samples of only ^{191}Pt-MYCN-PIP without oligonucleotides or only oligonucleotides were also prepared as a control in the same buffer. Ten microliters of sample solution was mixed with 2 μL of loading dye (Gel Loading Dye, Purple 6×, New England Biolabs) and loaded into a gel lane. The gel purchased from ATTO (15%/e-PAGEL; Tokyo, Japan) was run in 1× TG buffer (0.025 M Tris base and 0.192 M glycines) at 20 mA for 60 min at 4°C and then stained with 2.5 μg/mL ethidium bromide in 0.5× TBE buffer solution (0.0445 M Tris base, 0.0445 M borates, and 0.001 M EDTA). The EtBr-stained gel was scanned on an image analyzer (ImageQuant LAS 500; Cytiva, Tokyo, Japan). After the gel was dried, its autoradiograph was obtained using an imaging plate.

Cell culture

The human neuroblastoma cell lines Kelly, SK-N-DZ, and SK-N-AS were obtained from ECACC (Salisbury, UK). The cells were cultured at 37°C in a humidified atmosphere containing 5% CO_2 in RPMI-1640 (FUJIFILM Wako Pure Chemical) containing 10% FBS (Thermo Fisher Scientific, Waltham, MA, USA).

Cellular uptake

Kelly or SK-N-AS cells ((8–9) × 10^5 cells/6-well, 1 × 10^5 cells/24-well) were seeded onto a 6-well or

24-well plate and incubated at 37°C in a humidified atmosphere containing 5% CO_2. No carrier-added free ^{191}Pt, ^{191}Pt-GCC-PIP, or ^{191}Pt-MYCN-PIP (80–90 kBq) was added to the cells (nonradioactive MYCN-PIP or GCC-PIP: 0.03–1 nmol/well). After the cells had incubated for 3–42 h, they were washed with PBS and dissolved in 0.1 M NaOH. The radioactivity was measured using a gamma counter, and the protein concentration was determined using the Bradford reagent (Quick Start Bradford Protein Assay Kit; Bio-Rad Laboratories, Hercules, CA, USA) for the calculation of the uptake value.

DNA-binding assay

Kelly or SK-N-AS cells ((8–10) × 10^5 cells/well) were seeded onto a 6-well plate and incubated. ^{191}Pt-MYCN-PIP (80 kBq) or ^{191}Pt-GCC-PIP (65 kBq) was added to the cells (nonradioactive MYCN-PIP or GCC-PIP: 0.1 nmol/well). After the cells were incubated for 1 d (22 h), genomic DNA was isolated from the cells using a NucleoSpin Tissue DNA Extraction Kit (MACHEREY-NAGEL, Düren, Germany). The radioactivity of the collected solution containing genomic DNA was measured using a gamma counter (Wizard2 2-Detector Gamma Counter; PerkinElmer, Waltham, MA, USA), and quantitative analysis was performed using a NanoDrop One microvolume UV–Vis spectrophotometer (Thermo Fisher Scientific). The DNA-binding rate was calculated on the basis of the measured values.

Cell viability assay

Kelly, SK-N-AS, and SK-N-DZ (1 × 10^5 cells/well) were seeded onto a collagen I coated 24-well plate (Corning, Corning, NY, USA) and incubated. ^{191}Pt-MYCN-PIP (457 kBq) and nonradioactive MYCN-PIP (0.05 nmol), only nonradioactive MYCN-PIP (0.05 nmol), or PBS was added to the cells, and the cells were incubated for 1.5 d (39–40 h). After the medium was removed and the cells were washed with PBS, the cells were stained in a reduced-serum medium (Opti-MEM; Thermo Fisher Scientific) containing calcein (LIVE/DEAD Viability/Cytotoxicity Kit for mammalian cells; Thermo Fisher Scientific). The fluorescence was measured using a microplate reader (Spectra Max M5; Molecular Devices, San Jose, CA, USA).

Quantitative reverse transcription PCR (RT-qPCR)

Kelly, SK-N-DZ (1 × 10^5 cells/24-well), and SK-N-AS (1 × 10^6 cells/24-well) were seeded onto a 24-well or 6-well plate and incubated. ^{191}Pt-MYCN-PIP (457 kBq for 24-well, 732 kBq for 6-well) and nonradioactive MYCN-PIP (0.05 nmol for 24-well, 0.08 nmol for 6-well), only nonradioactive MYCN-PIP (0.05 nmol for 24-well, 0.08 nmol for 6-well), or PBS was added to the cells, and the cells were incubated for 2 d (42–50 h). After the medium was removed, the cells were dissolved in a lysis buffer. Complementary DNA (cDNA) was prepared using a Fastlane Cell cDNA Kit (QIAGEN,

Limburg, Netherlands) from the cell lysates. The quantitative PCR for the synthesized cDNA was performed using a StepOne Real-Time PCR system (Applied Biosystems, Thermo Fisher Scientific). TaqMan Gene Expression assays (MYCN, Hs00232074_m1; IFNα1, Hs00256882_s1; IFNBβ1, Hs01077958_s1; Thermo Fisher Scientific) and Eukaryotic 18S rRNA Endogenous Control (VIC™ probe; Applied Biosystems, Thermo Fisher Scientific) were used for RT-qPCR.

Fluorescence in situ hybridization (FISH) analysis

Kelly cells (6×10^4) were seeded onto a slide chamber (Corning® BioCoat® Collagen I 8-well Culture Slide; Corning, Corning, NY, USA) and incubated. ^{191}Pt-MYCN-PIP (274 kBq) and nonradioactive MYCN-PIP (0.03 nmol), only nonradioactive MYCN-PIP (0.03 nmol), or PBS was added to the cells, and the cells were incubated for 1.5 d (38 h). After the medium was removed and the cells were washed with PBS, the cells were immobilized with an ice-cold Carnoy solution (acetic acid/methanol = 1/3). The immobilized cells were denatured with a denaturing solution containing 70% formamide and 2× saline sodium citrate buffer (SSC) and then dehydrated with 70, 85, and 100% ethanol. The prepared cells were treated with a MYCN FISH probe solution for hybridization (MYCN FISH Probe Red-dUTP; Empire Genomics, Buffalo, NY, USA) at 37°C for 16 h in a humidified atmosphere containing 5% CO_2. Cover glasses were placed on glass slides using a mounting medium containing DAPI (Vector Laboratories, Burlingame, CA, USA). Fluorescence images were taken with a BZ-X800 fluorescence microscope (KEYENCE, Osaka, Japan) and analyzed using the BZ-Z800 Analyzer software (KEYENCE). Fluorescence intensity data were obtained from five different images with 30−80 nuclei per image and were expressed as the ratio of the total fluorescence intensity of the MYCN gene to the nucleus area.

Immunofluorescence staining of double-stranded DNA (dsDNA)

Kelly cells (1×10^6) were seeded on coverslips (BioCoat collagen I 22-mm coverslips; Corning, Corning, NY, USA) and incubated. ^{191}Pt-MYCN-PIP (836 kBq) and nonradioactive MYCN-PIP (0.1 nmol), ^{191}Pt-GCC-PIP (872 kBq) and nonradioactive GCC-PIP (0.1 nmol), free ^{191}Pt (899 kBq), only nonradioactive MYCN-PIP (0.1 nmol), or PBS was added to the cells, and the cells were incubated for 2 d (45 h). After the medium was removed and the cells were washed with PBS, the cells were immobilized with ice-cold MeOH, incubated in 0.25% Triton X-100/PBS for permeabilization, and then incubated in 1% BSA/PBST (phosphate-buffered saline with Tween 20) for blocking. Immunofluorescence staining was conducted using a dsDNA antibody (ab27156; Abcam, Cambridge, UK) as the primary antibody, with Alexa Fluor 594 anti-mouse IgG (Thermo Fisher Scientific) as the secondary antibody. Coverslips were placed on glass slides using a mounting medium containing DAPI (Vector Laboratories, Burlingame, CA, USA). Fluorescence images were acquired with a BZ-

X800 fluorescence microscope (KEYENCE, Osaka, Japan) and analyzed using the BZ-Z800 Analyzer software (KEYENCE). Fluorescence intensity data were obtained from four different images with 20−60 nuclei per image and were expressed as the ratio of the total fluorescence intensity of dsDNA to the nucleus area.

Fluorescent imaging of 53BP1-EGFP in U2OS-53BP1 cells

U2OS-53BP1 (U2RDP-LE53-21) cells stably expressing tumor-suppressor p53-binding protein 1 (53BP1) linked to a green fluorescent protein (EGFP) were established and gifted by Prof. Akihiro Kurimasa at Tohoku Medical and Pharmaceutical University. The cells were cultured at 37°C in a humidified atmosphere containing 5% CO_2 in RPMI-1640 (FUJIFILM Wako Pure Chemical, Osaka, Japan) with 10% FBS (Thermo Fisher Scientific, Waltham, MA, USA). U2OS-53BP1 (6×10^5 cells/well) cells were seeded onto a glass-based 6-well culture plate (EZVIEW® culture plates LB; AGC Techno Glass, Shizuoka, Japan) and incubated overnight at 37°C in a humidified atmosphere containing 5% CO_2. A solution containing nonradioactive MYCN-PIP (1.5 nmol) with or without ^{191}Pt-MYCN-PIP (290 kBq) was added to the cells. The cells were incubated in the medium containing each agent after 16 h of incubation, and the medium was replaced with fresh Opti-MEM™ (no phenol red; Thermo Fisher Scientific) containing 10% FBS. After 0 d and 1 d of incubation, fluorescence microphotographs for 53BP1-EGFP of the cells were acquired with an inverted fluorescence microscope (BZ-X800 fluorescence microscope; KEYENCE, Osaka, Japan). The fluorescence microscope was equipped with a 20× objective lens (Plan Apochromat; Nikon Solutions, Tokyo, Japan) and a fluorescent filter for EGFP (49020-UF1-BLA, excitation 480/20, emission 510/20; M SQUARE, Fukuoka, Japan).

Animal studies on the human tumor xenograft models

The protocol for the animal experiments was approved by the Animal Care and Use Committee of the National Institutes for Quantum and Radiological Science and Technology (13–1022, 26 May 2016), and all animal experiments were conducted following the institutional guidelines regarding animal care and handling. Kelly or SK-N-AS cells were suspended in a mixture of Matrigel and PBS (1:1), and 5×10^6 cells in 100 μL were subcutaneously injected into the flank of female BALB/c-nu/nu mice (4 weeks old for Kelly, 6 weeks old for SK-N-AS; CLEA Japan, Tokyo, Japan) under isoflurane anesthesia. Tumor volumes reached approximately 100–500 mm^3 after 3–4 weeks for Kelly and 2–3 weeks for SK-N-AS after injection.

For the biodistribution study, ^{191}Pt-MYCN-PIP (168–229 kBq, 0.1 nmol of nonradioactive MYCN-PIP) was intravenously or intratumorally injected into mice (Kelly and SK-N-AS) when tumor volumes reached approximately 100–500 mm^3 ($4 \leq n \leq 5$ for each time-point). The mice were

sacrificed by isoflurane inhalation at 1, 2, 4, or 7 days after injection. Blood was obtained from the heart, and then tumor, lung, liver, spleen, intestine, kidney, bone, and muscle were dissected. The uptake was represented as a percentage of the injected dose (radioactivity) per gram of tissue (%ID/g). These values were corrected to those in the body weight of 20 g.

For the experimental therapy, ^{191}Pt-MYCN-PIP (690–975 kBq, 0.3–0.4 nmol of nonradioactive MYCN-PIP) was intravenously or intratumorally injected into mice (Kelly) when tumor volumes reached approximately 100–300 mm^3 ($4 \leq n \leq 5$ for each time-point). As a control, a 1× PBS solution containing 0.75% Tween 80 and 0.2% TFA and a 1× PBS solution containing 0.75% Tween 80, 0.2% TFA, and nonradioactive MYCN-PIP (0.3–0.4 nmol) were prepared and administrated into mice. The tumor volume ((width^2 × length)/2) and body weight were measured every 2 days. The mice were sacrificed when the tumor volume reached 1000 mm^3.

Red blood cell partitioning and plasma protein binding

The red blood cell (RBC) partitioning and the plasma protein binding of ^{191}Pt were evaluated using the blood of mice. At 60 min, 1 d, and 4 d after intravenous injection of ^{191}Pt-MYCN-PIP (229 kBq, 0.1 nmol of nonradioactive MYCN-PIP), the blood was obtained from the heart and mixed with heparin (Mochida Pharmaceutical Factory, Tokyo, Japan). The whole blood was centrifuged and divided into RBCs and plasma. The RBC partitioning rate of ^{191}Pt was calculated on the basis of the activity of blood and plasma, defined as $(A_{blood} - A_{plasma}) \times (1 - Hct) \times 100/A_{blood}) \times 100$, where A_{blood} is the radioactivity of 20 µL whole blood, A_{plama} is the radioactivity of a 20 µL plasma fraction, and Hct is the hematocrit value (0.43). The plasma (50 µL) was put onto a spin column packed with Sephadex G-50 column (GE Healthcare, Chicago, IL, USA) eluted with 0.1 M sodium acetate solution. The protein binding rate of ^{191}Pt was calculated on the basis of the activity of the gel filtered fraction and the column, defined as $A_{sol}/(A_{col} + A_{sol}) \times 100$, where A_{col} is the radioactivity of a column and A_{sol} is the radioactivity of a filtered fraction.

DNA extraction from tumor tissue

Tumors were excised 10 days after injection of ^{191}Pt-MYCN-PIP. Twenty-five milligrams of tumor tissues was homogenized in PBS using a homogenizer (BioMasher I; Nippi, Tokyo, Japan) and dissolved in a lysis buffer. The genomic DNA was isolated from tumor tissues under the same protocol used for the DNA-binding assay. The concentration of RNA and DNA was determined using a NanoDrop One microvolume UV–Vis spectrophotometer (Thermo Fisher Scientific).

Histological analysis (immunohistochemical staining)

Tumors were excised 1 or 4 days after the intratumoral injection or 8 days after the intravenous

injection (2–3 mice per group). The excised tumors were fixed in 10% neutral-buffered formalin overnight, embedded in paraffin, and sliced 1 μm thick. For detection of DNA DSBs, the tumor sections were deparaffinized and immunohistochemically stained with anti-gamma H2A.X (γH2AX) (ab11174, Abcam) as a primary antibody and goat anti-rabbit IgG (ab214880, Abcam) as a secondary antibody and counterstained with hematoxylin (Sakura Finetek Japan, Tokyo, Japan). The images for γH2AX were acquired using a slide scanner (NanoZoomer S60; HAMAMATSU PHOTONICS, Hamamatsu, Japan). To detect dsDNA of replication stress, the tumor sections were deparaffinized and immunohistochemically stained with anti-dsDNA (ab27156, Abcam) as a primary antibody and Alexa Fluor 488 anti-mouse IgG (Thermo Fisher Scientific) as a secondary antibody and mounted with a mounting medium with DAPI (Vector Laboratories). The fluorescence images for dsDNA were acquired with a BZ-X800 fluorescence microscope (KEYENCE, Osaka, Japan) and analyzed using the BZ-Z800 Analyzer software (KEYENCE). The number of γH2AX-positive nuclei was counted from five different images including about 500 nuclei per image from each of two mice, and quantitative data were expressed as the ratio of positive nuclei to total nuclei.

Statistical Analysis

The data were expressed as means ± standard deviation (SD). The RT-qPCR data were evaluated by *t*-test; other data were evaluated via one-way analysis of variance with multiple comparisons using the GraphPad Prism 9 software (ver. 9.0.2, GraphPad Software, San Diego, CA, USA); $p < 0.05$ was considered statistically significant. The DNA binding error was calculated from both counting errors and error propagation.

Chapter 3. Section 1:

General

Chemicals and reagents were purchased from FUJIFILM Wako Pure Chemical (Osaka, Japan), Nacalai Tesque (Kyoto, Japan), Tokyo Chemical Industry (Tokyo, Japan), Otsuka Pharmaceutical Factory (Tokyo, Japan), Chemscene (Monmouth Junction, NJ, USA), AstaTech (Bristol, PA, USA), DOJINDO Laboratories (Kamimashiki, Japan), WATANABE Chemical Industries (Hiroshima, Japan), or Merck (Darmstadt, Germany). Milli-Q ultrapure water or distilled water was used for dilution in all experiments.

Synthesis of Nap-Cys-PSMA and Nap-Cys-RGD

The tumor-targeting conjugates were synthesized as illustrated in **Fig. 3-1-1**; details were provided in

the following subsections. The conjugates Nap-Cys-PSMA (**2**) and Nap-Cys-RGD (**3**) were >95% pure, as determined by HPLC (conditions: column, COSMOSIL 5C18-MS-II (Nacalai Tesque, Kyoto, Japan); gradient elution, A/B = 0.1% TFA in H_2O/CH_3CN = 90/10 (0 min) → 0/100 (15 min)).

*Nap-Cys(Trt) (**1**)*

2-Naphthaleneacetic acid ($C_{12}H_{10}O_2$, 380 mg, 2.04 mmol) and *N*,*N*,*N*',*N*'-tetramethyl-*O*-(*N*-succinimidyl)uronium tetrafluoroborate (TSTU, $C_9H_{16}BF_4N_3O_3$, 600 mg, 1.99 mmol) were dissolved in CH_3CN (10 mL) containing *N*,*N*-diisopropylethylamine (DIPEA, 348 μL, 2.00 mmol), and the reaction mixture was stirred at room temperature for 5 h. The resultant mixture was evaporated to dryness under reduced pressure. The mixture was dissolved in CH_2Cl_2 and washed with water and a saturated NaCl solution. The separated CH_2Cl_2 solution was dehydrated with $MgSO_4$ powders, and then the filtered solution was evaporated to dryness under reduced pressure. The obtained white powders (340 mg, 1.20 mmol) and *S*-trityl-L-cysteine (H-Cys(Trt)-OH, 431 mg, 1.19 mmol) were suspended in CH_3CN (10 mL) and DIPEA (1043 μL, 5.99 mmol), and dissolved by adding droplets of MeOH. The reaction mixture was stirred at room temperature for 2 h. The reaction mixture was concentrated and purified by column chromatography (silica gel, CH_2Cl_2/MeOH/TEA = 100/1/1 to 90/10/1), and Nap-Cys(Trt) (**1**) (500 mg, 0.94 mmol) was obtained. ESI calcd for $C_{34}H_{28}O_3NS^-$ $[M-H]^-$ 530.1795; found 530.1805.

*Nap-Cys-PSMA (**2**)*

Nap-Cys(Trt) (**1**) ($C_{34}H_{29}O_3NS$, 7.8 mg, 0.0147 mmol), (*S*)-di-*tert*-butyl 2-(3-((*S*)-6-amino-1-(*tert*-butoxy)-1-oxohexan-2-yl)ureido)pentanedioate ($C_{24}H_{45}N_3O_7$, 5.05 mg, 0.0104 mmol), and HBTU (5.7 mg, 0.0150 mmol) were dissolved in super-dehydrated DMF (1 mL) with TEA (1.787 μL, 0.0128 mmol), and the reaction mixture was stirred at room temperature for 3 h. The resultant mixture was evaporated to dryness under reduced pressure and purified by column chromatography (silica gel, CH_2Cl_2/MeOH/TEA = 100/1/1). The obtained Nap-Cys(Trt)-PSMA was dissolved in a mixed solution (TFA/H_2O/TIPS = 950/25/25 μL) and stored at room temperature for 1 h. Ice-cold diethyl ether was added to the mixture in an ice bath, and the supernatant was removed after centrifugation. After this process was repeated three times, Nap-Cys-PSMA (**2**) was evaporated to dryness under reduced pressure and stored at −80°C. ESI calcd for $C_{27}H_{33}N_4O_9S^-$ $[M-H]^-$ 589.1974; found 589.1987

*Nap-Cys-RGD (**3**)*

Nap-Cys(Trt) (**1**) ($C_{34}H_{29}O_3NS$, 13.1 mg, 0.0246 mmol), 1-(3-Dimethylaminopropyl)-3-ethylcarbodiimide hydrochloride (EDCI・HCl, 3.9 mg, 0.0203 mmol), and 1-Hydroxy-1H-benzotriazole monohydrate ($C_6H_5N_3O \cdot H_2O$=153.14, 3.0 mg, 0.0196 mmol) were dissolved in super-dehydrated DMF (1 mL) with TEA (3.14 μL, 0.0225 mmol) and stirred for 0.5 h on ice. Cyclo(RGDfK)

peptide ($C_{27}H_{41}N_9O_7$, 10.0 mg, 0.0166 mmol) was added to the reaction mixture and the mixture was stirred for 4 h at room temperature. The resultant mixture was evaporated to dryness under reduced pressure. The crude Nap-Cys(Trt)-RGD was dissolved in a mixed solution (TFA/H_2O/TIPS = 950/25/25 μL) and stored at room temperature for 1 h. Ice-cold diethyl ether was added to the mixture in an ice bath, and the supernatant was removed after centrifugation. After this process was repeated three times, the crude Nap-Cys-RGD product was purified using HPLC (conditions: column, COSMOSIL 5C18-MS-II (Nacalai Tesque, Kyoto, Japan); gradient elution, A/B = 0.1% TFA in H_2O/CH_3CN = 90/10 (0 min) → 0/100 (15 min)). The fractionated Nap-Cys-RGD (**2**) was freeze-dried and stored at −80°C. ESI calcd for $C_{42}H_{55}N_{10}O_9S^+$ $[M+H]^+$ 875.3869; found 875.3881.

Labeling Nap-Cys-PSMA and Nap-Cys-RGD with ^{191}Pt, and purification of the labeled samples.

Nap-Cys-PSMA/RGD was dissolved in DMSO (1 mM). The reaction mixture consisting of a Nap-Cys-PSMA/RGD solution (10 μL), Tween 80 or 20 (0.2 μL), ethanol (0.8 μL), and a ^{191}Pt solution (90 μL) was prepared and heated at 45°C for 60 min. Both reaction mixtures were purified by HPLC; the column was a COSMOSIL 5C18-AR-II (5 μm, 4.6 mm × 250 mm; Nacalai Tesque, Kyoto, Japan), the eluent was A/0.1% TFA in H_2O, B/0.1% TFA in CH_3CN, gradient: A/B = 70/30 in 0 min → 20/80 in 10 min → 0/100 in 15 min, and the flow rate was 1.0 mL/min. A solution containing ^{191}Pt-labeled Nap-Cys-PSMA/RGD was collected in a vial with Tween added beforehand. The solution was evaporated to remove CH_3CN and neutralized with 10× PBS and 1 M NaOH. ^{191}Pt-labeled Nap-Cys-PSMA/RGD was finally prepared in a 1× PBS solution containing 0.2% Tween and 0.2% TFA.

Labeling Trithiol with ^{191}Pt, and purification of the labeled samples.

A trithiocyanate-protected trithiol ligand, 5-(3-Thiocyanate-2,2-bis(thiocyanatomethyl)-propoxy)isophthalic Acid ($C_{16}H_{13}N_3O_5S_3$) was previously established,[4] and provided from Prof. Silvia S. Jurisson *et al.* at University of Missouri. 5-(3-Thiocyanate-2,2-bis(thiocyanatomethyl)-propoxy)isophthalic Acid (0.42 mg, 0.001 mmol) was dissolved in H_2O (0.5 mL) and CH_3CN (0.5 mL) containing 10 mM TCEP. After heating the reaction mixture at 55°C for 2 h, the ligand was deprotected to 5-(3-Mercapto-2,2-bis(mercaptomethyl)propoxy)-isophthalic Acid. ESI found for $C_{13}H_{15}O_5S_3^-$, $[M-H]^-$; 347.1. A crude solution of the deprotected trithiol ligand (1 mM) was used for ^{191}Pt labeling. The reaction mixture consisting of the precursor solution (10 μL), Tween 80 (0.2 μL), ethanol (0.8 μL), and a ^{191}Pt solution (90 μL) was prepared and heated at 45°C for 60 min. The reaction mixtures were purified by HPLC; the column was a COSMOSIL 5C18-AR-II (5 μm, 4.6 mm × 250 mm; Nacalai Tesque, Kyoto, Japan), the eluent was A/0.1% TFA in H_2O, B/0.1% TFA in CH_3CN,

gradient: A/B = 95/5 in 0 min → 60/40 in 10 min → 0/100 in 15 min, and the flow rate was 1.0 mL/min. A solution containing ^{191}Pt-labeled Trithiol was collected in a vial with Tween 80 added beforehand. The solution was evaporated to remove CH_3CN and neutralized with 10× PBS and 1 M NaOH. ^{191}Pt-labeled Nap-Cys-PSMA/RGD was finally prepared in a 1× PBS solution containing 0.2% Tween 80 and 0.2% TFA.

Cell culture

The human prostate cancer cell lines PC3-PIP and PC3-FLU were gifted by Prof. Martin G. Pomper at Johns Hopkins University. The human neuronal glioblastoma cell line U87MG was obtained from ATCC (Manassas, VA, USA). The cells were cultured at 37°C in a humidified atmosphere containing 5% CO_2 in RPMI-1640 (FUJIFILM Wako Pure Chemical) containing 10% FBS (Thermo Fisher Scientific, Waltham, MA, USA) for PC3-FLU and U87MG; RPMI-1640 containing 10% FBS, 1% Penicillin-Streptomycin (Sigma-Aldrich, St. Louis, MO, USA), 10 mg/500 mL puromycin (Thermo Fisher Scientific, Waltham, MA, USA), and 25 mg/500 mL Plasmocin® (ant-mpp, Invivogen, San Diego, CA, USA) for PC3-PIP.

Cellular uptake and Internalization assay

PC3-PIP, PC3-FLU, or U87MG cells (1×10^5 cells/12-well) were seeded onto a 12-well plate and incubated overnight at 37°C in a humidified atmosphere containing 5% CO_2. No carrier-added free ^{191}Pt, ^{191}Pt-labeled Nap-Cys-PSMA, or ^{191}Pt-labeled Nap-Cys-RGD (1–2 kBq) was added to the cells. After the cells had incubated for 3–24 h, they were washed with fresh FBS-free medium twice. The cells were incubated in an acidic buffer consisting of 50 mM glycine-HCl/0.1 M NaCl (pH 2.83, 4°C) and the solution was collected as a membrane-bound fraction. The residual cells were dissolved in a 1% SDS solution as an internalized fraction. The radioactivity was measured using a gamma counter (1480 Wizard 3 Gamma Counter: PerkinElmer, Waltham, MA, USA). The X-rays and gamma-rays from ^{191}Pt were counted together under the energy window from 15 keV to 1000 keV. Using an aliquot of the injection solution as a control for measurement, the uptake was calculated from the radioactivity ratio of samples to the control.

Animal studies on the human tumor xenograft models

The protocol for the animal experiments was approved by the Animal Care and Use Committee of the National Institutes for Quantum and Radiological Science and Technology (13–1022, 26 May 2016) or the Duke University IACUC, and all animal experiments were conducted following the institutional guidelines regarding animal care and handling. PC3-PIP, PC3-FLU, or U87MG cells were suspended in a mixture of Matrigel and PBS (1:1), and $2–5 \times 10^6$ cells in 100 µL were subcutaneously injected

into the flank of male BALB/c-nu/nu mice (4 weeks old; CLEA Japan, Tokyo, Japan) under isoflurane anesthesia. Tumor volumes reached approximately 100–500 mm^3 after 1–2 weeks for PC3-PIP and PC3-FLU and 2–3 weeks for U87MG after injection.

For the biodistribution study, ^{191}Pt-labeled Nap-Cys-PSMA, Nap-Cys-RGD, Trithiol (70–340 kBq) was intravenously injected into mice when tumor volumes reached approximately 100–500 mm^3 ($4 \leq n \leq 5$ for each time-point). The mice were sacrificed by isoflurane inhalation at 2 min, 1 h, or 1 day after injection. Blood was obtained from the heart, and then tumor, lung, liver, spleen, stomach, intestine, kidney, prostate, bone, and muscle were dissected. The uptake was represented as a percentage of the injected dose (radioactivity) per gram of tissue (%ID/g). These values were corrected to those in the body weight of 20 g.

For the experiment data in **Table 3-1-1**, a gamma counter (Wallace 1282 Compugamma CS Universal Gamma Counter; LKB Instruments, Victoria, Australia) was used to measure radioactivity in biological samples. The X-rays and gamma-rays from ^{191}Pt were counted together under the energy window from 40 keV to 250 keV. Using an aliquot of the injection solution as a control for measurement, the uptake was calculated from the radioactivity ratio of samples to the control. For the other data, the gamma counter described in the above subsections was used.

Red blood cell partitioning and plasma protein binding

The red blood cell (RBC) partitioning and the plasma protein binding of ^{191}Pt were evaluated using the blood of mice. At 2 min, 1 h, and 24 h after intravenous injection of ^{191}Pt-labeled compounds, the blood was obtained from the heart and mixed with heparin (Mochida Pharmaceutical Factory, Tokyo, Japan). The whole blood was centrifuged and divided into RBCs and plasma. The RBC partitioning rate of ^{191}Pt was calculated on the basis of the activity of blood and plasma, defined as $(A_{blood} - A_{plasma}) \times (1 - Hct) \times 100/A_{blood}) \times 100$, where A_{blood} is the radioactivity of 20 µL whole blood, A_{plama} is the radioactivity of a 20 µL plasma fraction, and Hct is the hematocrit value (0.43). The plasma (50 µL) was put onto a spin column packed with Sephadex G-50 column (GE Healthcare, Chicago, IL, USA) eluted with 0.1 M sodium acetate solution. The ^{191}Pt solution was also filtered using the column. The protein binding rate of ^{191}Pt was calculated on the basis of the activity of the gel filtered fraction and the column, defined as $(1 - A_{col}/((A_{col} + A_{sol})*(B_{col}/(B_{col} + B_{sol})))) \times 100$, where A_{col}, the radioactivity of a column for plasma sample; B_{col}, that for ^{191}Pt solution; A_{sol}, the radioactivity of a filtered fraction for plasma sample; B_{sol}, that for ^{191}Pt solution.

Appendix:

General

Chemicals and reagents were purchased from Mallinckrodt Pharmaceuticals (Dublin, Ireland), AdipoGen Life Sciences (San Diego, CA, USA), Macron Fine Chemicals (Radnor, PA, USA), J.T.Baker (Radnor, PA, USA), or Merck (Darmstadt, Germany). Milli-Q ultrapure water or distilled water was used for dilution in all experiments. [^{125}I]NaI in 0.1 M NaOH was purchased from PerkinElmer (Waltham, MA, USA). A [^{125}I]NaI (<1 μL) was diluted with 1 mL of a 1× PBS solution containing 0.2% Tween 20 and used in the *in vitro* experiments.

Synthesis of [^{125}I]VK290Lu

The trimethyl tin precursor VK290Lu was developed,[5] and was provided by Professor Michael R Zalutsky *et al*. at Duke University. [^{125}I]VK290Lu were obtained as illustrated in **Fig. 4-2**; details were provided in the following.

Fifty micrograms of the tin precursor VK290Lu were dissolved in a methanol solution consisting of 0.2 mg/mL of N-Chlorosuccinimide (NCS) and 6–10 μL/mL of acetic acid (AcOH). A [^{125}I]NaI solution (<10 μL) was added to the precursor solution. The reaction mixture was mixed and left at room temperature for 30 min. The solution was evaporated with dry Ar gas and co-evaporated with an EtOAc/hexane solution (=30/70 (v/v)) (100 μL × 3). The residue was dissolved in a CH_3CN/H_2O solution (=20/80 (v/v)) and purified by preparative C18 HPLC; the column was InfinityLab Poroshell (120 EC-C18, 2.7 μm, 4.6 mm × 50 mm; Agilent Technologies, Santa Clara, CA, USA), the eluent was A/0.1% TFA in H_2O, B/0.1% TFA in CH_3CN, gradient: A/B = 80/20 in 0 min → 60/40 in 8 min → 10/90 in 10 min, and the flow rate was 2.0 mL/min. A solution containing [^{125}I]VK290Lu was collected and evaporated with dry Ar gas to remove CH_3CN. The solution was diluted with 10 mL of H_2O and then loaded onto the Sep-Pak C18 Plus Short Cartridge (Waters, Milford, MA, USA). Thereafter, [^{125}I]VK290Lu was eluted with ethanol and the solution was evaporated with dry Ar gas. [^{125}I]VK290Lu was re-dissolved and finally prepared in a 1× PBS solution containing 0.2% Tween 20.

Synthesis of [^{125}I]1,3,4-SGMIB-Hoechst33258

The trimethyl tin precursor 1,3,4-SGMTB was developed,[6] and was provided by Professor Michael R Zalutsky *et al*. at Duke University. [^{125}I]1,3,4-SGMIB-Hoechst33258 were synthesized as illustrated in **Fig. 4-3**; details were provided in the following.

Fifty micrograms of the tin precursor 1,3,4-SGMTB were dissolved in a methanol solution consisting of 0.2 mg/mL of N-Chlorosuccinimide (NCS) and 6–10 μL/mL of acetic acid (AcOH). A [^{125}I]NaI solution (<10 μL) was added to the precursor solution. The reaction mixture was mixed and left at room temperature for 30 min. The solution was evaporated with dry Ar gas and co-evaporated with an EtOAc/hexane solution (=30/70 (v/v)) (100 μL × 3). The residue was dissolved in an

EtOAc/hexane solution (=30/70 (v/v), 100 μL) and purified by preparative normal-phase HPLC; the column was a ZORBAX Rx-SIL (80Å, 5 μm, 4.6 mm × 250 mm; Agilent Technologies, Santa Clara, CA, USA), the eluent was A/0.2% AcOH in EtOAc, B/0.2% AcOH in hexane (A/B = 70/30), and the flow rate was 1.5 mL/min. A solution containing protected [^{125}I]1,3,4-SGMIB was collected and evaporated with dry Ar gas. The residue was dissolved in TFA (100 μL) and left at room temperature for 10 min. Thereafter, the solution was evaporated with dry Ar gas and co-evaporated with an EtOAc/hexane solution (=30/70 (v/v)) (100 μL × 3); the residue was deprotected [^{125}I]1,3,4-SGMIB (**1**).

Boc-C_4-Hoechst33258 (**2**) was synthesized in the same way described above (section 1 of *Chapter 2*). For deprotection, Boc-C_4-Hoechst33258 (**2**, 0.1 mg) was dissolved in TFA (100 μL) and left at room temperature for 10 min. The solution was evaporated with dry N2 gas and co-evaporated with EtOAc (100 μL × 3). The residue was dissolved in an H_2O/CH_3CN/TEA solution (=49.5/49.5/1 (v/v), 100 μL) and NH_2-C_4-Hoechst33258 was prepared.

The solution containing NH_2-C_4-Hoechst33258 (100 μL) was added to the deprotected [^{125}I]1,3,4-SGMIB (**1**) for a conjugation reaction. The mixed solution was left at room temperature for 30 min, and then AcOH (2 μL) was added to the reaction mixture. The crude solution was purified by preparative C18 HPLC; the column was COSMOSIL 5C18-MS-II (5 μm, 4.6 mm × 250 mm; Nacalai Tesque, Kyoto, Japan), the eluent was A/0.1% TFA in H_2O, B/0.1% TFA in CH_3CN, gradient: A/B = 90/10 in 0 min → 20/80 in 15 min → 0/100 in 20 min, and the flow rate was 1.0 mL/min. A solution containing [^{125}I]1,3,4-SGMIB-Hoechst33258 was collected and evaporated with dry Ar gas to remove CH_3CN. The solution was diluted with 10 mL of H_2O and then loaded onto the Sep-Pak C18 Plus Short Cartridge (Waters, Milford, MA, USA). Thereafter, [^{125}I]1,3,4-SGMIB-Hoechst33258 was eluted with ethanol and the solution was evaporated with dry Ar gas. [^{125}I]1,3,4-SGMIB-Hoechst33258 was re-dissolved and finally prepared in a 1× PBS solution containing 0.2% Tween 20.

Cell culture

The human prostate cancer cell lines PC3-PIP were gifted by Prof. Martin G. Pomper at Johns Hopkins University. The cells were cultured at 37°C in a humidified atmosphere containing 5% CO_2 in RPMI-1640 containing 10% FBS, 1% Penicillin-Streptomycin (Sigma-Aldrich, St. Louis, MO, USA), 10 mg/500 mL puromycin (Thermo Fisher Scientific, Waltham, MA, USA), and 25 mg/500 mL Plasmocin® (ant-mpp, Invivogen, San Diego, CA, USA) for PC3-PIP.

Cellular uptake and Internalization assay

PC3-PIP cells (1×10^5 cells/12-well) were seeded onto a 12-well plate and incubated overnight at 37°C in a humidified atmosphere containing 5% CO_2. [^{125}I]NaI, [^{125}I]VK290Lu, or [^{125}I]1,3,4-

SGMIB-Hoechst33258 (55–62 kBq) was added to the cells. After the cells had incubated for 3–24 h, they were washed with fresh FBS-free medium twice. The cells were incubated in an acidic buffer consisting of 50 mM glycine-HCl/0.1 M NaCl (pH 2.83, 4°C) and the solution was collected as a membrane-bound fraction. The residual cells were dissolved in a 1% SDS solution as an internalized fraction. The ^{125}I radioactivity was measured using a gamma counter (1480 Wizard 3 Gamma Counter: PerkinElmer, Waltham, MA, USA). Using an aliquot of the injection solution as a control for measurement, the uptake was calculated from the radioactivity ratio of samples to the control.

DNA binding

PC3-PIP cells (5×10^5 cells/well) were seeded onto a 6-well plate and incubated overnight at 37°C in a humidified atmosphere containing 5% CO_2. [^{125}I]NaI, [^{125}I]VK290Lu, or [^{125}I]1,3,4-SGMIB-Hoechst33258 (555–568 kBq) was added to the cells. After incubating for 1 d, genomic DNA was isolated from the cells using a NucleoSpin Tissue DNA extraction kit (Takara Bio, Kusatsu, Japan). Radioactivity of the collected solution containing genomic DNA was measured using a gamma counter (1480 Wizard 3 Gamma Counter: PerkinElmer, Waltham, MA, USA), and quantitative analysis was performed using a Microvolume UV-Vis Spectrophotometer NanoDrop One (Thermo Fisher Scientific). The DNA binding rate was calculated based on the measured values.

MTT assay

PC3-PIP cells (2×10^3 cells/well) were seeded onto a 96-well plate and incubated overnight at 37°C in a humidified atmosphere containing 5% CO_2. [^{125}I]NaI, [^{125}I]VK290Lu, or [^{125}I]1,3,4-SGMIB-Hoechst33258 (7.4–807 kBq) was added to the cells, and the cells were incubated for 3 d. The MTT assay was conducted using an assay kit (Cell Proliferation Kit I (MTT): Roche, Basel, Switzerland) and absorbance at 550 nm was measured using a plate reader (Spectra Max ABS; Molecular Devices, San Jose, CA, USA).

References:

1 Obata H, Kurimasa A, Muraoka T, Tsuji AB, Kondo K, Kuwahara Y, Minegishi K, Nagatsu K, Ogawa M, Zhang MR. Dynamic imaging analysis reveals Auger electron-emitting radio-cisplatin induces DNA damage depending on the cell cycle. *BBRC* **2022**; 637: 286–293.

2 Chamier L, Laine RF, Jukkala J, Spahn C, Krentzel D, Nehmen E, Lerche M, Hernández-pérez S, Mattila P, Karinou E, Holden S, Solak AC, Krull A, Buchholz TO, Jones ML, Royer LA, Leterrier C, Shechtman Y, Jug F, Heilemann M, Jacquemet G, Henriques R. Democratising deep learning for microscopy with ZeroCostDL4Mic. *Nat Commun* **2021**; 12: 2276.

3 Kelman Z. PCNA: structure, functions and interactions, *Oncogene* **1997**; 14: 629e640.

4 Olson AP, Ma L, Feng Y, Khosroshahi FN, Kelley SP, Sarduy EA, Barnhart TE, Hennkens HM, Ellison PA, Jurisson SS, Engle JW. A third generation potentially bifunctional trithiol chelate, its ^{nat,1XX}Sb(III) complex, and selective chelation of radioantimony (^{119}Sb) from its Sn target. *Inorg Chem* **2021**; 60(20): 15223–15232.

5 Mease RC, Kang CM, Kumar V, Banerjee SR, Minn I, Brummet M, Gabrielson KL, Feng Y, Park A, Kiess AP, Sgouros G, Vaidyanathan G, Zalutsky MR, Pomper MG. An improved ^{211}At-labeled agent for PSMA-targeted α-therapy. *J Nucl Med* 2022; 63(2): 259−267.

6 Vaidyanathan G, McDougald D, Choi J, Koumarianou E, Weitzel D, Osada T, Lyerly HK, Zalutsky MR. Preclinical evaluation of ^{18}F-labeled anti-HER2 nanobody conjugates for imaging HER2 receptor expression by immuno-PET. *J Nucl Med* **2016**; 57(6): 967−73.

Acknowledgements

I would like to express my sincere gratitude to my supervisor, Professor Mikako Ogawa of Hokkaido University for her constructive and thoughtful guidance during my Ph.D. time.

I would like to thank Professor Shigeki Matsunaga and Dr. Tatsuhiko Yoshino of Hokkaido University for their careful direction and kind help in reviewing my Ph.D. dissertation.

I am deeply grateful to Dr. Ming-Rong Zhang of National Institutes for Quantum Science and Technology for his continuous support of my research up to today.
I would like to express my best appreciation to Dr. Kotaro Nagatsu of National Institutes for Quantum Science and Technology for his kind encouragement and continuous support during my research life, and for giving me an opportunity for radio-Pt research at QST, and to Dr. Atsushi B. Tsuji for his kind guidance on all biological experiments, continuous support during my Ph.D. time, and a great help in reviewing all of my publications.
I would like to express my heartfelt thanks to Mr. Katsuyuki Minegishi, Dr. Hitomi Sudo, and Ms. Aya Sugyo for a lot of their continuous technical support for all of the experiments of this dissertation and warm encouragement during my Ph.D. time.

I would like to express my deepest gratitude to Professor Michael R Zalutsky, Dr. Yutian Feng, and Prof. Werner Tornow of Duke University for giving me an opportunity and a lot of help to do my Ph.D. research on radio-Pt at Duke University. I am deeply grateful to Duke members, particularly Ms. Rebecca Meshaw, Dr. Thao Truc Huynh, Dr. Ganesan Vaidyanathan, Dr. Xiao-Guang Zhao, Mr. Shawn Murphy, Dr. Sean Finch, and Mr. Darryl McDougald for their technical support and kind help.

I would like to express my appreciation to Professor Akihiro Kurimasa of Tohoku Medical and Pharmaceutical University for allowing me to do time-lapse imaging of U2RDP-LE53-21 cells, and for kind guidance on image analysis and careful discussion of the results. I am grateful to Professor Katsuya Kondo of Tottori University, Dr. Yoshikazu Kuwahara, and Mr. Tadanori Muraoka of Tohoku Medical and Pharmaceutical University for their fruitful discussion on time-lapse imaging of U2RDP-LE53-21 cells.

A special gratitude I give to the cyclotron staffs at QST and CYRIC, for operating the AVF-930 cyclotrons. I particularly would like to thank Takashi Wakui of National Institutes for Quantum Science and Technology, Dr. Hayato Ikeda, and Professor Masatoshi Ito of Tohoku University for supporting me to use the cyclotrons.

I would like to thank Professor Hiroshi Sugiyama, Dr. Toshikazu Bando, and Ms. Kaori Hashiya for providing me with the MYCN-PIP and GCC-PIP precursors.

I would like to appreciate Professor Martin Pomper and Mr. James Engles of Johns Hopkins University for providing me with PC3-PIP and PC3-FLU cells.

I am grateful to Professor Silvia S. Jurisson, Dr. Heather M. Hennkens, and Ms. Chathurya Munindradasa of University of Missouri for providing me with the trithiol ligand precursor.

I would like to thank Ms. Sayaka Kado of Chiba University for her support of MS analysis.

I would like to express my appreciation to all members of the Dept. of Advanced Nuclear Medicine Sciences and the Dept. of Molecular Imaging and Theranostics for their kindness and continuous support. I am particularly grateful to Mr. Hisashi Suzuki, Mr. Akihito Abe, Mr. Katsushi Kumata, Dr. Masayuki Hanyu, Ms. Wakana Mori, Ms. Ayumi Kadoma, and Dr. Maki Okada.

I would like to thank all members of Laboratory for Bioanalysis and Molecular Imaging at Hokkaido University, particularly Dr. Hideo Takakura, Dr. Kohei Nakajima, and Ms. Kayo Watanabe, for their kind help and thoughtful discussion during my Ph.D. time. I appreciate all staff of Laboratory of Biomolecular Science at Hokkaido University for supporting my research abroad at Duke University.

I acknowledge Japan Society for the Promotion of Science (Grant number JP20J20518), Japan Science and Technology Agency (Grant number JPMJAX2223), the Ito foundation, and the Global Institution for Collaborative Research and Education at Hokkaido University for their financial support. This research was also supported by the Platform Project for Supporting Drug Discovery and Life Science Research from AMED (Grant number JP21am0101101) and the Supply Platform of Short-lived Radioisotopes for Fundamental Research from JSPS (Grant number 16H06278).

Finally, I would like to express my best thanks to my family and friends for their heartfelt and kind encouragement, and a lot of support throughout the time of my Ph.D.